

Supramolecular Self-Assembly of Pyrene-Modified Amphiphilic DNA Nanostructures

Inauguraldissertation
der Philosophisch-naturwissenschaftlichen Fakultät
der Universität Bern

vorgelegt von

Jan Thiede

von Luzern

Leiter der Arbeit:

Prof. Dr. Robert Häner

Departement für Chemie, Biochemie und Pharmazie der Universität Bern

Original document saved on the web server of the University Library of Bern



This work is licensed under the CC BY-NC-ND 2.5 CH License. To view a copy of this license, visit <http://creativecommons.org/licenses/by-nc-nd/2.5/ch/> or send a letter to Creative Commons, PO Box 1866, Mountain View, CA 94042, USA.

Supramolecular Self-Assembly of Pyrene-Modified Amphiphilic DNA Nanostructures

Inauguraldissertation
der Philosophisch-naturwissenschaftlichen Fakultät
der Universität Bern

vorgelegt von

Jan Thiede

von Luzern

Leiter der Arbeit:

Prof. Dr. Robert Häner

Departement für Chemie, Biochemie und Pharmazie der Universität Bern

Von der Philosophisch-naturwissenschaftlichen Fakultät angenommen.

Bern, 05. April 2024

Der Dekan:
Prof. Dr. Marco Herwegh

Acknowledgments

I would like to start by thanking Prof. Dr. Robert Häner for his consistent encouragement, guidance, and for providing me with the opportunity to explore the intriguing research area of DNA-constructed self-assemblies. Robert's rigorous scientific approach and attention to detail have enabled me to become a much-improved scientist and writer, for which I am extremely grateful. Furthermore, I would like to thank Prof. Dr. Stefan Vogel and Prof. Dr. Philippe Renaud for their valuable assessment of my work.

I would like to show my gratitude to the cryo-EM specialists, Prof. Dr. Benoît Zuber and Dr. Ioan Iacovache, for their significant contributions to this work. Their expertise in cryo-EM experiments provided valuable insights into the assembly of DNA nanostructures.

Deep gratitude goes to all current and former members of the Häner research group for their valuable input and support throughout my research journey. Special thanks are extended to Dr. Simon Langenegger for his helpful advice and constructive discussions. Whenever I encountered challenges with interpreting my results, designing experiments, or needing guidance in my writing, he was available to offer his insights and advice. In addition, I thank Thomas Schneeberger for his contribution during the completion of his Master's thesis. Last but certainly not least, I would like to thank Dr. Simon Langenegger and Isabelle Kolly for proofreading this thesis.

I also would like to thank all DCBP staff members, including all in-house services, for their assistance and support. I would like to show my gratitude to the Swiss National Science Foundation (SNF) and the University of Bern, whose financial support made this research possible.

Lastly, I am very thankful to my family and friends for their consistent support, encouragement, and love throughout the years.

Contents

1	Introduction	3
1.1	Supramolecular Polymers in Aqueous Medium	3
1.2	Structure of DNA	6
1.3	Solid-Phase Synthesis of Oligomers	8
1.4	DNA Nanostructures	13
1.5	Light-Harvesting and Energy Transfer	18
2	Aim of the Thesis	23
3	Supramolecular Self-Assembly of 3'-End Modified Pyrene-DNA Conjugates: Influence of Pyrene Substitution Pattern and Light-Harvesting	25
3.1	Results and Discussion	26
3.1.1	Spectroscopic Characterization of 1,6-, 1,8- and 2,7-Dialkynyl Pyrene Diol	26
3.1.2	3'-End Modified Pyrene-DNA Conjugates	27
3.1.3	Spectroscopic Characterization	28
3.1.4	Atomic Force Microscopy	29
3.1.5	Transmission Electron Microscopy	30
3.1.6	Cryo-Electron Microscopy	31
3.1.7	Dynamic light scattering	33
3.1.8	Summary of Self-Assembly	33
3.1.9	Light-Harvesting Experiments	34
3.2	Conclusions and Outlook	41
3.3	Appendix - Chapter 3	42
3.3.1	Organic Synthesis	42
3.3.2	NMR Spectra	50
3.3.3	Synthesis of Oligonucleotides	57
3.3.4	Spectroscopic Measurements	62
3.3.5	Additional Microscopic Measurements	63
3.3.6	DLS Measurement Conditions and Results	66
3.3.7	Additional Light-Harvesting Experiments	67
4	Influence of Sticky-End Length and Spermine & Ethanol Concentration on Supramolecular Assembly of Pyrene-DNA Conjugates	69
4.1	Results and Discussion	70
4.1.1	Influence of Spermine and Ethanol Concentration on the Supramolecular Assembly	70
4.1.2	Influence of Length of Sticky Ends on the Supramolecular Assembly	74
4.2	Conclusions and Outlook	78
4.3	Appendix - Chapter 4	79
4.3.1	Synthesis and Characterization of Oligonucleotides	79
4.3.2	DLS Measurement Conditions and Results	84

5	Supramolecular Assembly of 3'- and 5'-end modified Pyrene-DNA Conjugates: Influence of Number of Pyrene Modifications	85
5.1	Results and Discussion	86
5.1.1	Self-Assembly of 2,7-Dialkynyl Pyrene-DNA Conjugate	87
5.1.2	Self-Assembly of 1,6-Dialkynyl Pyrene-DNA Conjugate	92
5.2	Conclusions and Outlook	97
5.3	Appendix - Chapter 5	98
5.3.1	Synthesis and Characterization of Oligonucleotides	98
5.3.2	Additional AFM	106
5.3.3	Additional Cryo-EM Images	108
5.3.4	DLS Measurement Conditions and Results	110
6	Supramolecular Self-Assembly of Terminal Functionalized 3'- and 5'-End Modified Pyrene-DNA Conjugates	111
6.1	Results and Discussion	112
6.1.1	Alkyne Functionalization	114
6.1.2	Effect of PEGylation	114
6.1.3	Influence of a Branched GalNAc Moiety	116
6.2	Conclusions and Outlook	117
6.3	Appendix - Chapter 6	118
6.3.1	Organic Synthesis	118
6.3.2	Synthesis and Characterization of Oligonucleotides	120
6.3.3	Additional Spectroscopic Measurements	124
7	Supramolecular Assembly of Highly Modified Phenanthrene-DNA Conjugates with Light-Harvesting Capabilities	125
7.1	Results and Discussion	126
7.1.1	Self-Assembly of Highly Modified Phenanthrene-DNA Conjugates	126
7.1.2	Light-Harvesting Experiments of Highly Modified Phenanthrene-DNA Conjugates	128
7.2	Conclusions and Outlook	131
7.3	Appendix - Chapter 7	132
7.3.1	Organic Synthesis	132
7.3.2	Synthesis and Characterization of Oligonucleotides	134
7.3.3	Spectroscopic Characterization of Pyrene and Phenanthrene Diols	138
7.3.4	Additional Spectroscopic and Microscopic Measurements	139
7.3.5	Additional Light-Harvesting Experiments	142
8	Overall Conclusions and Outlook	143
	Abbreviations	145
	General Methods	147
	Bibliography	153
	Curriculum Vitae	168

Summary

In the first chapter, topics related to this thesis are introduced. Supramolecular polymers in aqueous medium, general aspects and structural features of deoxyribonucleic acid (DNA), the preparation of synthetic oligomers *via* solid-phase synthesis, nanostructures built by DNA, and light harvesting and energy transfer in supramolecular systems are introduced.

In the second chapter, the aim of the thesis is described. The subsequent chapters describe the results, discussion, conclusion, and outlook of the experimental work.

In the third chapter, the supramolecular self-assembly of amphiphilic 3'-end modified pyrene-DNA conjugates is described. Modifications of DNA with three pyrene isomers are compared, and their light-harvesting capabilities are explored. The supramolecular assembly of pyrene-DNA conjugates decorated with the three isomers yielded nanostructures with different morphologies. All assemblies exhibit light-harvesting properties. Interestingly, the 2,7-dialkynyl pyrene isomer exhibited a non-FRET energy transfer.

In the fourth chapter, the supramolecular assembly of pyrene-DNA conjugates is further investigated. The influence of spermine and ethanol concentrations, as well as the impact of the number of pyrene modifications on the sticky ends, is examined.

In the fifth chapter, the supramolecular assembly of the 3'-/5'-end modified pyrene-DNA conjugates paired with a complementary unmodified DNA strand is presented. Pyrene-DNA conjugates bearing sticky ends with one, two, and three 2,7-dialkynyl and 1,6-dialkynyl pyrene are compared. The morphologies of the nanostructures formed by the two isomers are similar. They assemble into single vesicles and aggregates of vesicles. Switching from three to two pyrene modifications in the sticky ends reduces the size of the formed nanostructures.

In the sixth chapter, the supramolecular self-assembly of terminal functionalized 3'-/5'-end modified pyrene-DNA conjugates is described. This chapter describes the functionalizations of the pyrene-DNA conjugate with an alkyne, polyethylene glycol, or a branched N-acetyl galactosamine. Interestingly, these modifications influence the morphologies of the supramolecular assemblies only marginally.

In the seventh chapter, the supramolecular assembly of highly modified phenanthrene-DNA conjugates is presented. The conjugates presented in this chapter contain phenanthrene modifications in the middle of the strand and at the 3'-ends form filled spherical nanostructures. A doping experiment with a pyrene-containing phenanthrene-DNA conjugate proved their light-harvesting capabilities.

In the eighth chapter, overall conclusions are drawn, and future perspectives are outlined.

Chapter 1

Introduction

1.1 Supramolecular Polymers in Aqueous Medium

The complex and fascinating structures found in nature are often constructed from small and simple subunits that are held together by weak and reversible non-covalent intermolecular forces.¹ Inspired by nature, researchers started to focus on the study of non-covalently bound constructs, giving rise to the field of supramolecular polymers.² Supramolecular polymers are formed from monomeric units that self-assemble through non-covalent interaction.³ Hydrogen bonds, the hydrophobic effects, metal coordination, Coulomb and/or van der Waals interactions are among the non-covalent interactions that drive the self-assembly of supramolecular polymers in aqueous medium.^{4–6} These intermolecular interactions are much weaker compared to covalent bonds found in classical polymers. However, the non-covalent nature makes supramolecular polymers dynamic, reversible, self-healable, adaptive, or stimuli-responsive.^{7–15} As the chemistry of living things generally takes place in aqueous environments, supramolecular polymers formed in aqueous media are of particular interest.¹⁶ A recent publication by Stupp *et al.* illustrates the manifold way of assembly of supramolecular polymers in aqueous media.¹⁷ Depending on pH an amphipathic naphtho-p-quinodimethane self-assembled into three different morphologies, ribbons, helical rolled ribbons, and twisted filaments (Figure 1.1).

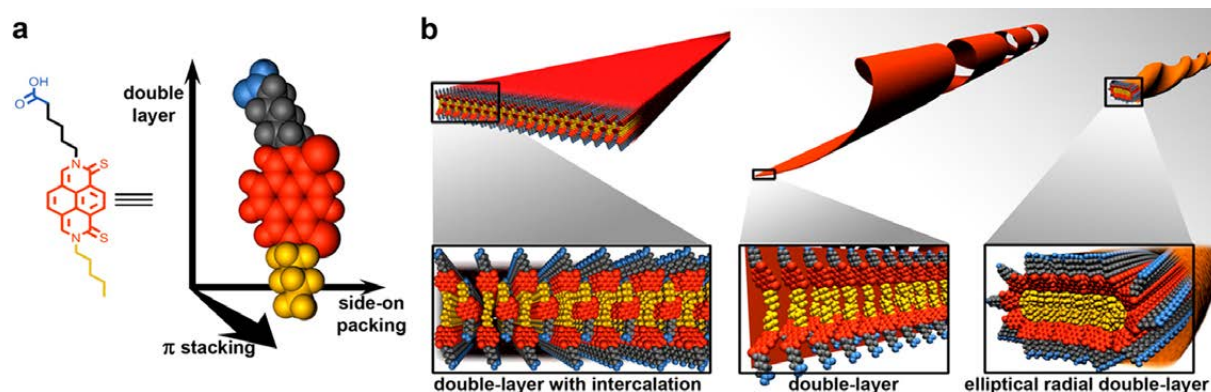


Figure 1.1: (a) Chemical structure and model representation of amphipathic naphtho-p-quinodimethane with the proposed axis of intermolecular packing. (b) Illustration of stacked amphiphiles, depending on the pH, the amphiphile self-assembles into different supramolecular assemblies (left to right: ribbon at 0.70–0.85 eq. NaOH, helical rolled ribbons at 0.9–1.0 eq. NaOH, and twisted filaments at more than 2.0 eq. NaOH). Figure adapted from ref.¹⁷

The driving forces for the formation of the nanostructures are the π - π interactions of the aromatic core, the hydrophobicity, and the dipole-dipole interactions between the monomers. In the presented example, the hydrophobic part of the amphiphile, the pentyl chains are located

inside the assemblies, whereas the hydrophilic carboxylates point to the aqueous medium. It was found that the charges on the carboxylated head groups are the main reason for the formation of different aggregates. Elevating the pH increases the number of negatively charged deprotonated carboxylate head groups. The deprotonation of these head groups amplifies the repelling forces among them, thus giving rise to distinct nanostructures depending on the extent of deprotonation.

Our research group focuses on the supramolecular assembly of diverse types of phosphodiester-linked amphiphilic polyaromatic oligomers. Different polycyclic aromatic hydrocarbons (PAHs) have been investigated, such as phenanthrene,^{18,19} pyrene,^{20–26} anthracene,^{27,28} squaraine,^{29,30} anthanthrene,³¹ and azobenzene³² (Figure 1.2). The amphiphilic oligomers were self-assembled *via* thermal assembly. Various morphologies were observed for the different PAHs. The formation of these assemblies is mainly driven by the π -stacking forces and dipole-dipole interactions between the hydrophobic PAHs in aqueous medium.

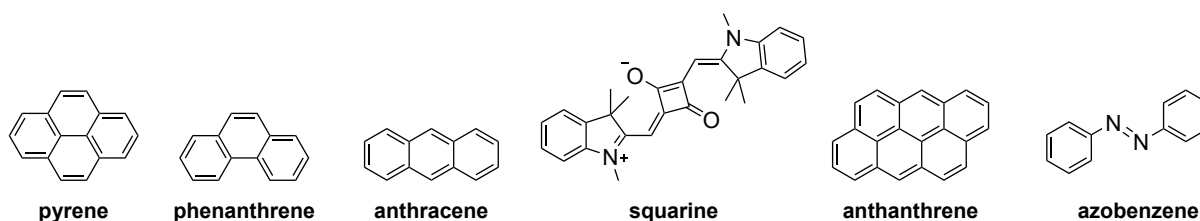
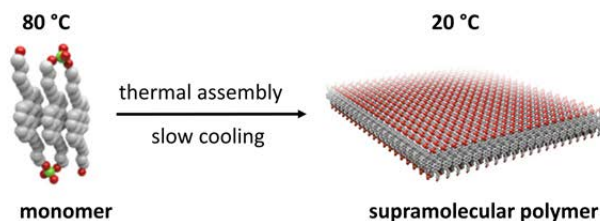


Figure 1.2: Various polycyclic aromatic hydrocarbons (PAHs) studied by our group.

Before, thermal assembly solutions containing monomers are heated to elevated temperatures (75–80 °C). Heating is required to ensure complete disaggregation of the monomeric units. Then, the monomers are self-assembled by slowly cooling the solution with a defined cooling gradient (*e.g.*, 0.5 °C/min). During the slow cooling, the supramolecular polymers are formed from the monomers (Scheme 1.1).²⁴ When the applied cooling gradient is sufficiently slow, the thermodynamically most stable supramolecular assembly is formed.²³



Scheme 1.1: Thermal assembly of a monomer forming a supramolecular polymer. Adapted from ref.²³

Here, the supramolecular assembly of a 1,6-disubstituted phosphodiester-linked pyrene trimer **Py₃** is described in more detail (Figure 1.3a).²³ **Py₃** aggregates into 2D supramolecular assemblies. In the supramolecular assembly, the hydrophobic dialkynyl pyrenes are π -stacked, while the charged phosphate groups point toward the aqueous medium, comparable to the work described by Stupp *et al.* above. Supramolecular assembly by slow and fast cooling were compared: slow cooling (0.1 °C/min) yielded large and highly regular sheets (Figure 1.3a left), whereas fast cooling (20 °C/min) formed a large number of smaller sheets (Figure 1.3a right). Fast cooling yields the kinetic products, whereas slow cooling forms the thermodynamic products. To determine the mechanism of supramolecular assembly of **Py₃**, temperature dependent fluorescence spectroscopy was conducted (Figure 1.3b). In the first phase of supramolecular assembly, above 63 °C, the intensity of the excimer fluorescence remained

unchanged, and the amphiphiles are in the monomeric form. Then, at 63 °C, the intensity of the excimer fluorescence drops abruptly and steadily decreases until it plateaus, and the supramolecular assembly is formed. The shape of the curve is an indication that the supramolecular polymerization follows a cooperative growth mechanism. The different growth mechanisms are described below.

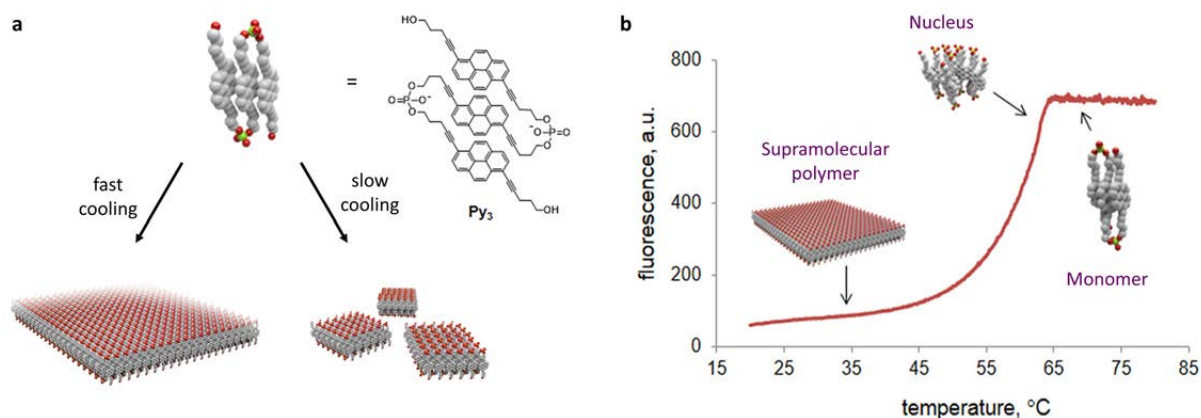


Figure 1.3: (a) Illustration of the self-assembly of a pyrene-trimers by fast and slow cooling and chemical structure of Py_3 . (b) Temperature-dependent excimer fluorescence of Py_3 in aqueous solution. Conditions: λ_{em} , 520 nm, λ_{ex} , 365 nm, cooling 0.1 °C/min. Figure adapted from ref.²³

There are two predominant growth mechanisms in supramolecular polymerization, namely, isodesmic and cooperative growth (Figure 1.4).³³ The main difference between the two mechanisms is the requirement for a nucleation phase. In an isodesmic growth, the association constant of the monomer to the supramolecular polymer is independent of the polymer length. In contrast, cooperative polymerization is divided into two distinct stages: nucleation and elongation. The nucleation step requires the creation of a nucleus or molecular cluster from which the supramolecular polymers grow. Consequently, the cooperative polymerization is dependent on two association constants: the nuclei association constant (K_N) and association constant for elongation (K_E) of the supramolecular assembly, whereas K_N must be larger than K_E (Figure 1.4a). As cooperative polymerization is dependent on two constants, it follows a non-sigmoidal growth with a critical point (Figure 1.4b, blue curve). On the other hand, the dependence on only one association constant leads to a sigmoidal growth in an isodesmic polymerization (Figure 1.4b, green curve).

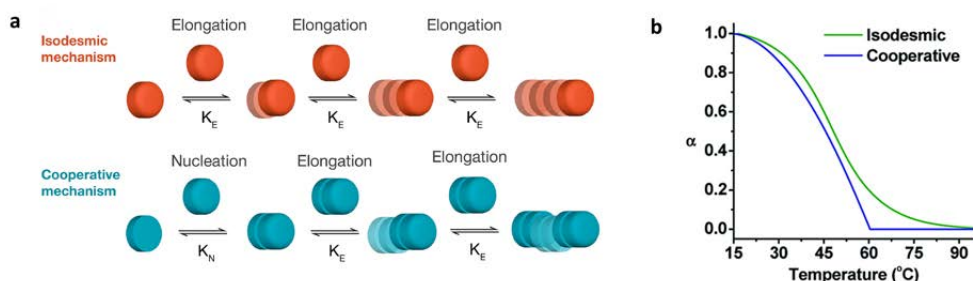


Figure 1.4: (a) Isodesmic supramolecular self-assembly process, with a single association constant (K_E). And a cooperative self-assembly, which is divided into two phases: the nucleation phase, where nuclei are formed with the association constant (K_N) and the elongation phase, with the association constant (K_E). (b) Graphic illustration of the difference between the isodesmic and cooperative growth mechanisms. Figures adapted from.^{34,35}

1.2 Structure of DNA

One of the most notable accomplishments of the previous century was the discovery of the double-helical structure of DNA in 1953 by Watson, Crick, Franklin, and Wilkins (depicted in Figure 1.5).³⁶⁻³⁸ For their contributions, Watson, Crick, and Wilkins were honored with the Nobel Prize in Medicine in 1962. This event marked the initiation of a period characterized by extensive exploration of nucleic acids within the realms of chemistry, biochemistry, and biology. A crucial aspect of this advancement was the chemical synthesis of nucleic acids. Notably, during the 1980s, Caruthers and Köster pioneered the development of automated DNA synthesis, employing the innovative phosphoramidite chemistry approach (described in more detail in 1.3).³⁹ Over time, this methodology underwent refinements, leading to the capability to automate the synthesis of a diverse array of modified nucleic acid variants.

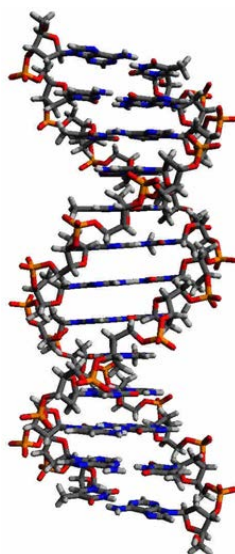


Figure 1.5: Model of a regular DNA duplex.

DNA consists of a linear polynucleotide structure, wherein each deoxyribonucleoside is connected to the subsequent one through a 3'-to-5' phosphodiester linkage. Nucleotides, the building blocks of DNA, consist of three essential components: the four principal nucleobases (adenine, thymine, guanine, and cytosine), 2'-deoxy-D-ribose sugar, and a phosphate residue (Figure 1.6).⁴⁰ The sequential covalent bonding occurs between the 5'-hydroxyl group of one nucleoside and the 3'-hydroxyl group of another nucleoside through a phosphodiester bond, giving rise to individual nucleic acid single strands.

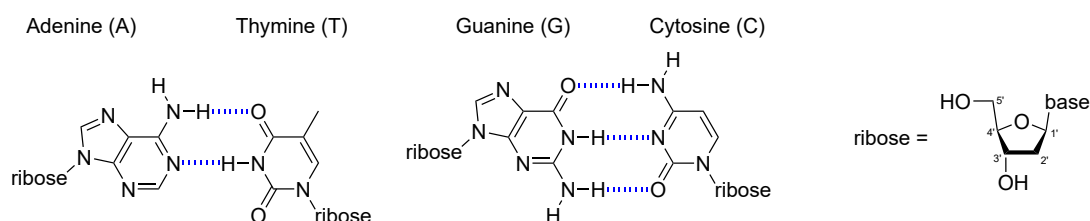


Figure 1.6: Watson-Crick base pairs for A–T and G–C (left) and 2'-deoxy-D-ribose sugar (right)

Through hydrogen bonds, two separate DNA single strands can hybridize in an anti-parallel fashion to create a duplex structure. In this arrangement, the bases of one strand pair specifically with the bases of the other strand (adenine with thymine and guanine with cytosine). Various

conformations of the DNA double helix contingent on the surrounding aqueous conditions and base composition have been reported. Three major DNA conformers exist: A-DNA, B-DNA, and Z-DNA (Figure 1.7). In Table 1.1, key geometrical differences between the three DNA forms are summarized.^{41,42} A-DNA is commonly observed when DNA is dehydrated. Z-DNA can emerge in DNA sequences with alternating G/C bases and under conditions of high salt concentration. The B-DNA structure is the prevailing conformation under high humidity and low salt concentration.⁴³⁻⁴⁶

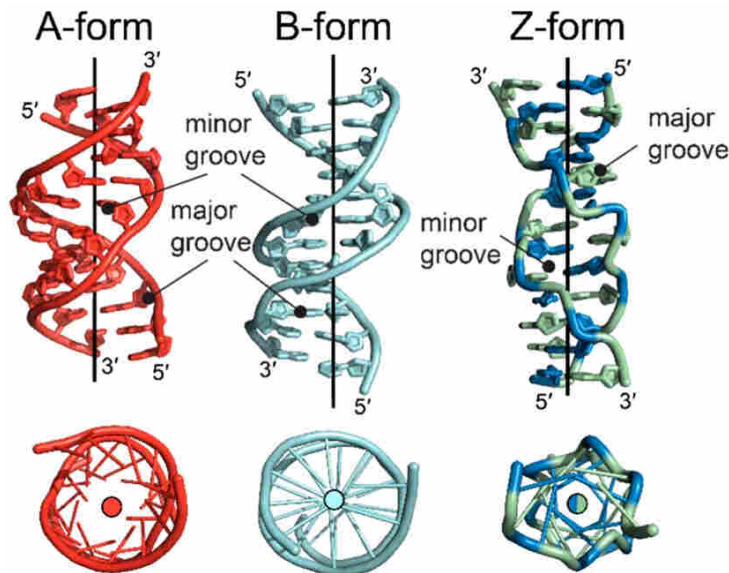


Figure 1.7: Comparison of A-, B-, and Z-DNA, side (top) and top-down (bottom) views. Adapted from ref.⁴⁷

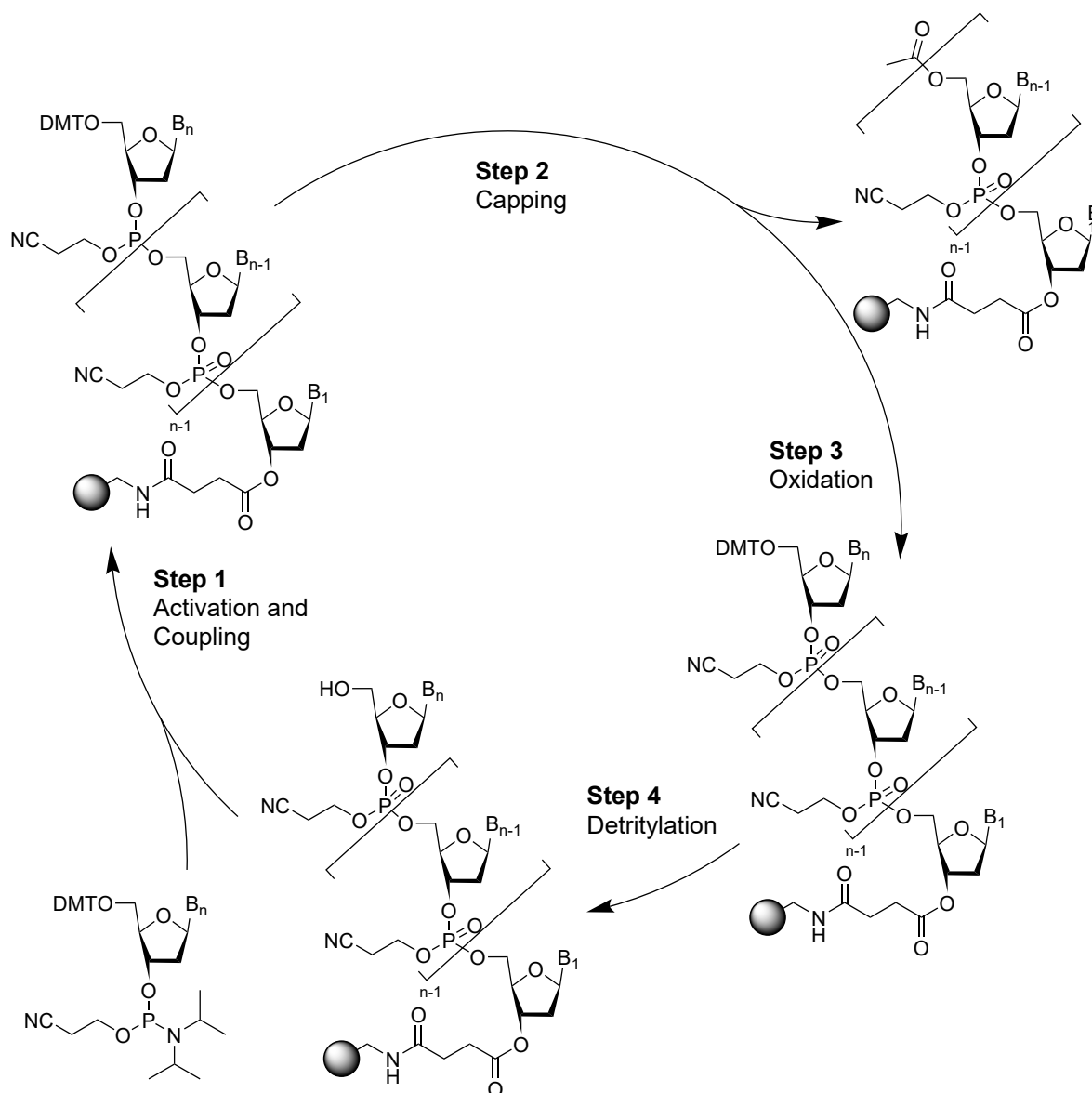
The distinctive structural properties of DNA have inspired numerous researchers to take advantage of the organizational potential of the DNA scaffold. The DNA scaffold has been used to assemble multi-chromophore arrays,⁴⁸⁻⁵⁹ to position functional groups at specific interchromophore distances,⁶⁰⁻⁶³ and explore excitation energy transfer processes,⁶⁴⁻⁷⁴ among other applications. In the examples stated above, chemically modified oligonucleotides were used. The incorporation of artificial nucleotide substitutes into oligonucleotides has significantly broadened DNA's realm beyond its traditional role in biological systems as a genetic information carrier.⁷⁵⁻⁷⁸ These synthetic building blocks bring forth supplementary functionalities that hold relevance for applications within the domains of DNA nanotechnology and materials sciences.⁷⁹⁻⁸³ However, this expansion necessitated the establishment of a reliable method to synthesize oligonucleotides synthetically.

Table 1.1: Comparison of important key helix parameters.⁸⁴

	A-DNA	B-DNA	Z-DNA
Helical Sense	Right-handed	Right-handed	Left-handed
Helical Diameter	26 Å	20 Å	18 Å
Number of Bases per Turn	11	10	12
Rise per Base Pair	2.9 Å	3.4 Å	3.7 Å
Rise per Turn (Pitch)	32 Å	34 Å	45 Å
Tilt of Base	20	-6	7
Major Groove	Narrow, Deep	Wide, Deep	Convex Surface
Minor Groove	Wide, Shallow	Narrow, Deep	Narrow, Deep

1.3 Solid-Phase Synthesis of Oligomers

Although short fragments of oligomer can be synthesized in a flask, more commonly, they are synthesized with a solid-phase DNA/RNA synthesizer.⁸⁵ Without a doubt, the invention of solid-phase chemical synthesis in the 1960s by Bruce Merrifield, for which he later received the Nobel Prize for Chemistry in 1984, was of immense importance.⁸⁶ Solid-phase synthesis, in comparison to solution-phase synthesis, brings many advantages. Solid-phase synthesis can be automated. In addition to that, side products and excess reagents can be easily washed away, mitigating the need for purification after each step. Furthermore, large excesses of reagents can be used to drive the reactions more quickly to completion. In summary, solid-phase synthesis of oligomers using a computer-controlled synthesizer has proven superior to solution-phase synthesis.



Scheme 1.2: Solid-phase oligomer synthesis: cycle of oligomer elongation by activation, coupling, capping, oxidation, and detritylation.

The synthesis of oligomers using a DNA synthesizer is quite simple (Scheme 1.2). A nucleoside bearing one reactive 3'-phosphorous group is coupled to the 5'-hydroxyl of the existing solid-

support-bound nucleoside. Between each coupling, the following additional steps are necessary to prepare the growing chain: capping, oxidation, detritylation, and activation. When the last building block is coupled to the chain, the oligomer must be cleaved from the support and deprotected. In the following pages, the solid-phase synthesis of oligomers is described in detail.

It is crucial to select a suitable solid support to perform solid-phase synthesis of oligomers. The following key features are required for a successful synthesis. The solid support must be available in uniformly sized particles. At the same time, it must be insoluble in water and other commonly used organic solvents to hinder it from diffusing through the filters. In addition to that, a uniform and sufficiently large surface without functionalities is necessary, as such functionalities could lead to unwanted side reactions with reagents. Since the 1960s, different candidates have been tested, such as polystyrene, polyamide, polyamide bonded to silica gel, cellulose, silica gel, and controlled pore glass (CPG).^{85,87–89} Out of all candidates, CPG-beads were successfully used in a broad range of applications and have shown to be very reliable. For most applications, CPG-beads sized 125 to 177 μm with 500 to 2000 \AA -sized pores proved to be suitable.

Importantly, it is unfavorable that the first building blocks are directly coupled to the solid supports. Direct coupling is disadvantageous because this would result in very crowded beads, hindering the access of reagents and, therefore, reducing the coupling yields of solid-phase synthesis. Usually, solid supports are equipped with long linkers on which the oligomers are synthesized to circumvent this problem. Different kinds of long linker arms have been assessed for different kinds of beads.⁸⁵ Typically, long-chain alkylamino (LCAA) linkers featuring 17-atom-long arms containing primary amino groups at their ends are employed. To attach the solid supports to 5'-protected nucleosides (including cytosine, thymine, adenine, or guanine), the 3'-hydroxy groups of the nucleosides undergo a reaction with succinic anhydride. The resulting carboxylic acid then reacts with the amino groups of the solid supports. Covalently binding the solid supports and the initial nucleosides through base-labile ester bonds is essential for subsequent cleaving after synthesis (see Figure 1.8 left).

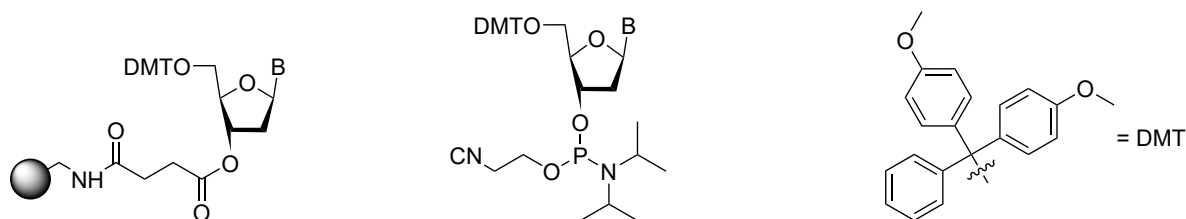


Figure 1.8: DMT-protected nucleoside with base B (cytosine, thymine, adenine, or guanine) bound to solid-phase support (black sphere) *via* succinyl linker (left) and corresponding DMT- and 2-cyanoethyl-protected phosphoramidites (middle).

To avoid unwanted side reactions of the reactive groups on the DNA-building blocks, they are protected with acid- or base-labile protecting groups, allowing selective deprotection. The 5'-OH groups of all building blocks are protected with acid-labile 4,4'-dimethoxytrityl (DMT) protecting groups, and the phosphoramidites on the 3'-OH of the DNA-building-blocks are protected by base-labile 2-cyanoethyl groups (Figure 1.8). In addition to that, the amines in the nucleobases are protected with base-labile protecting groups (Figure 1.9).

Solid-phase oligomer synthesis is performed in four steps: activation, coupling, capping, oxidation, and detritylation. First, the 5'-OH of the nucleosides attached to the solid supports must be deprotected by detritylation. The detritylation, depicted in Scheme 1.3,

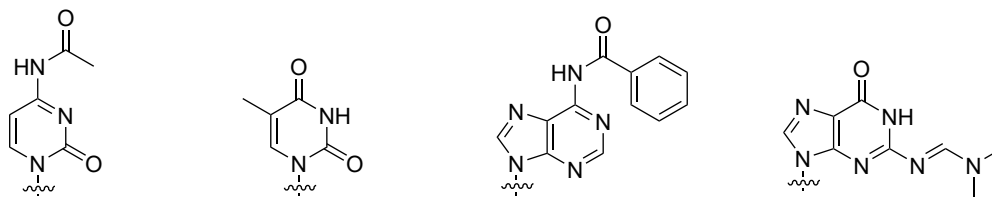
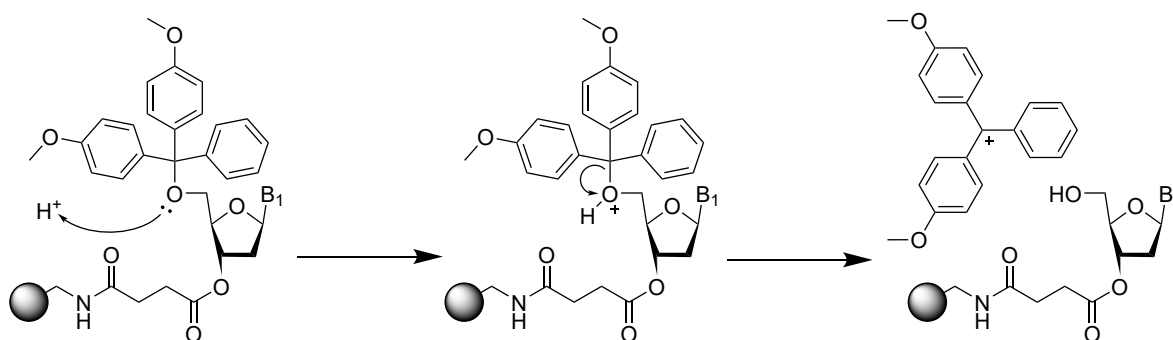


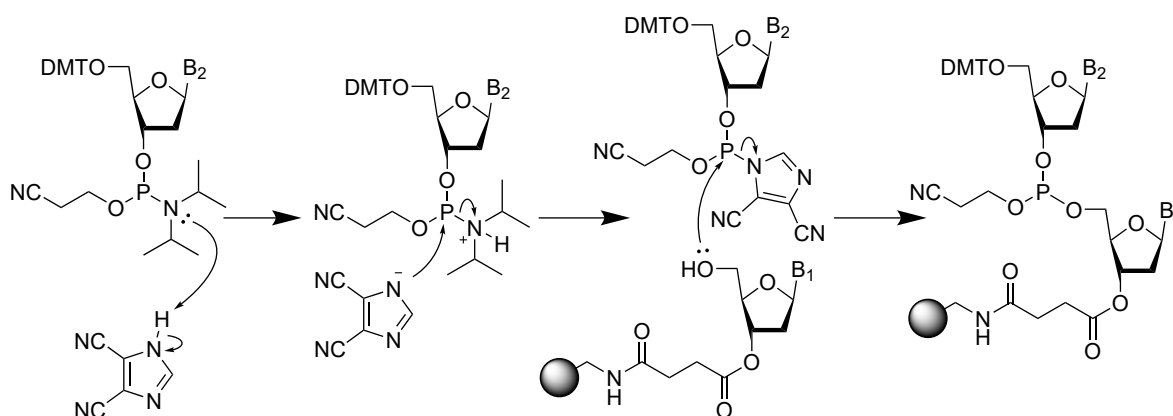
Figure 1.9: From left to right: the four nucleobases used for solid-phase synthesis: acetyl-protected cytosine, thymine, benzoyl-protected adenine, and dimethylformamidinium-protected guanine.

is performed under acidic conditions, for example, 3% trichloroacetic acid in DCM. Under these conditions, the DMTs are cleaved. The resulting 5'-hydroxyl groups then react with the activated phosphoramidites of the second building block.



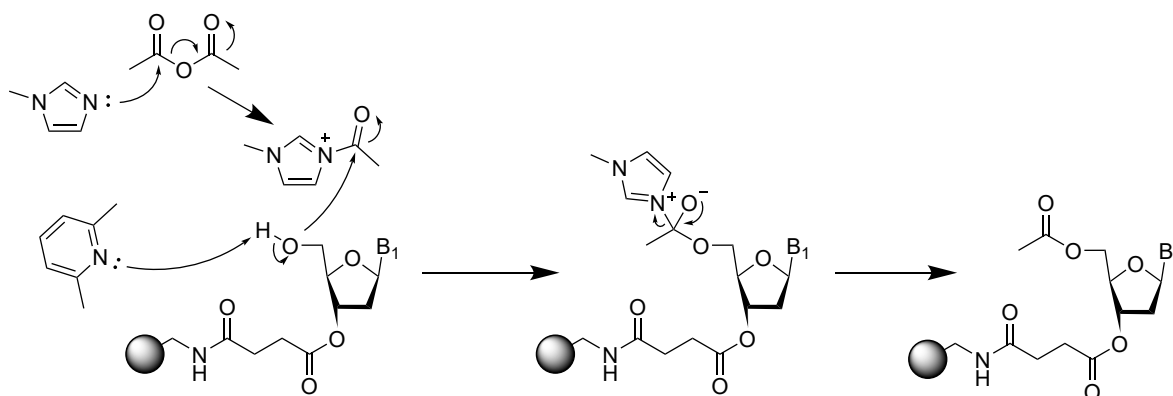
Scheme 1.3: Detritylation step: Protonation of the DMT-protected solid support-bound building block, followed by the cleaving of DMT, yielding a free 5'-hydroxy group.

The cyclic oligomer synthesis starts with the activation of the phosphoramidites, followed by their coupling to the 5'-hydroxy groups of the preceding oligomers on the solid supports. Overall, in the first step, the monomers are activated and linked to the existing oligomer chains (Scheme 1.4). First, a solution of DMT-protected phosphoramidite is added to the solid supports. Then, the phosphoramidites are activated by replacing the diisopropylamines with azoles such as 4,5-dicyanoimidazole (DCI) or 1-*H*-tetrazole. The azole-activated intermediates then couple with the 5'-OHs of the chains on the solid supports.



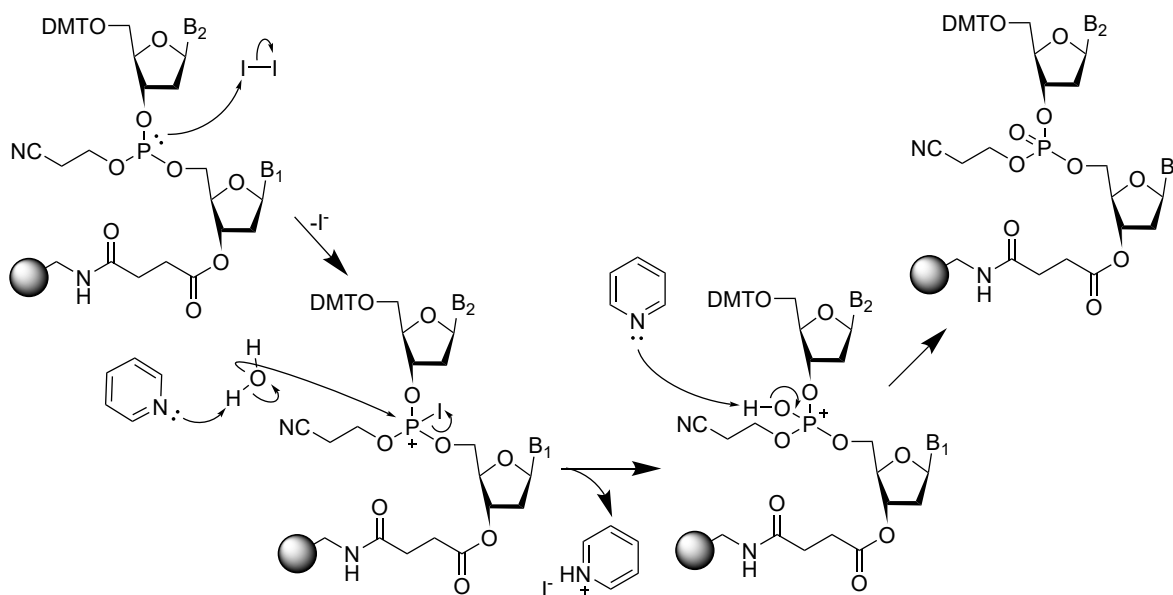
Scheme 1.4: Step 1 the activation and coupling: Activation of DMT-protected phosphoramidite with 4,5-dicyanoimidazole (DCI); first protonation of the amine by DCI, followed by a nucleophilic attack of the deprotonated DCI forming the DCI-activated intermediate. Then, coupling of the activated phosphoramidite to solid support bound oligomer chain by the attack of the 5'-oxygen.⁹⁰

After completion of step 1, the remaining unreacted 5'-OH groups are deactivated to prevent them from intervening with the following additions. Therefore, the unreacted 5'-hydroxy groups are capped by acetylation. As illustrated in Scheme 1.5, the capping is performed by mixing acetic anhydride and the bulky base 2,6-lutidine with the catalyst 1-methylimidazole. Importantly, the two reagents must be mixed *in situ* because the active acetylating agent is unstable.



Scheme 1.5: Step 2 the capping: 1-Methylimidazole mixed with acetic anhydride form 3-acetyl-1-methyl-1H-imidazol-3-ium that is attacked by the deprotonated oxygen atom of the 5'-OH forming acetyl-capped side-products upon recovery of the 1-methylimidazole catalyst.

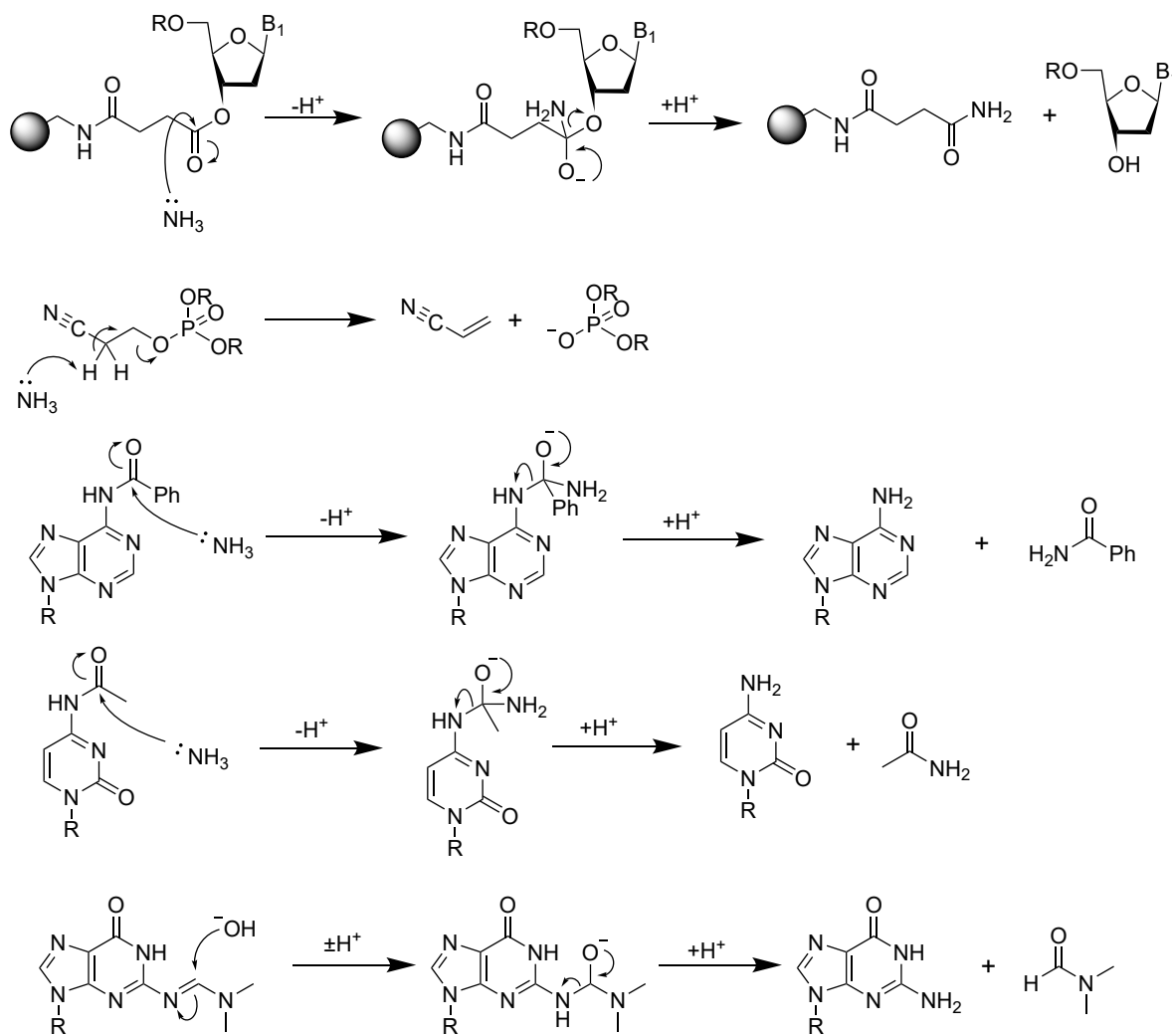
In the third step, the newly formed phosphite triesters are oxidized to pentavalent phosphate triesters. The oxidation is usually performed with iodine in a mixture of tetrahydrofuran (THF), water, and pyridine. Iodine acts as a mild oxidant, and water is the oxygen donor. The process of oxidation is explained in detail in Scheme 1.6.



Scheme 1.6: Step 3 the oxidation: Phosphite triester is oxidized by iodine in the presence of water and pyridine following the depicted mechanism.

In the fourth step, the 5'-trityls are removed to start another cycle. The detritylation is performed according to the mechanism described above and illustrated in Scheme 1.3.

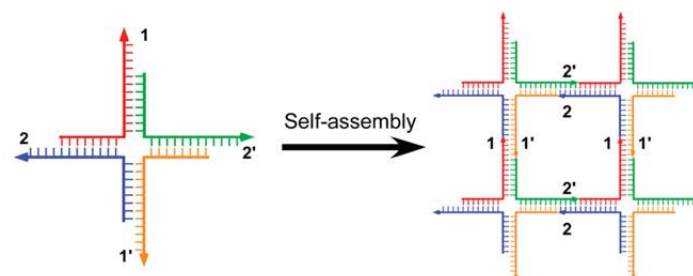
When the oligomers reach the desired lengths, the cyclic process is stopped. The crude oligomers are then deprotected and cleaved from the solid supports by shaking them at 55°C in a concentrated aqueous solution of ammonia overnight. The alkaline conditions lead to the cleavage of the oligomers from the solid supports and the deprotection of the phosphodiester backbones as well as the nucleobases. The mechanism of cleaving and the deprotections are described in Scheme 1.7. After the reaction, the oligomers are lyophilized. Finally, the pure product is afforded by high-performance liquid chromatography (HPLC).



Scheme 1.7: Mechanisms top to bottom: Cleavage of the oligomer from the solid support, deprotection of the phosphotriester, and deprotection of the base-labile protecting groups on the nucleobases with concentrated ammonia solution.

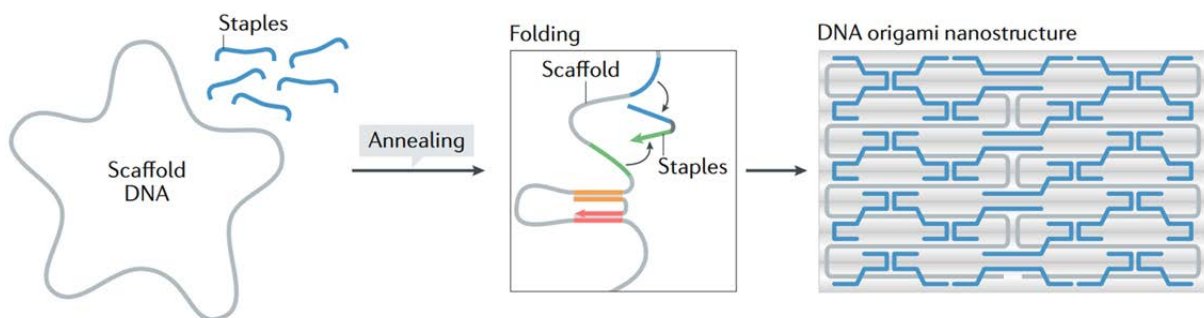
1.4 DNA Nanostructures

The construction of precisely defined DNA nanostructures can be achieved through the assembly of branched, double-stranded DNA featuring terminal single-stranded nucleotide overhangs, commonly referred to as sticky ends. An influential milestone in this field was marked by the seminal theoretical contributions of Nadrian C. Seeman in 1982. Seeman's work delineated the concept of immobile DNA junction motifs and demonstrated their potential for assembly into two-dimensional (2D) or three-dimensional (3D) networks. In these structures, individual DNA fragments are interconnected through the utilization of sticky ends, as illustrated in Scheme 1.8.^{91,92} Shortly after that the formation of a tetrameric junction complex in solution was proven experimentally.⁹³ The pioneering work of Nadrian C. Seeman during this period might have sparked the exploration and development of the entire DNA nanotechnology research field.⁹⁴⁻¹⁰⁴



Scheme 1.8: Self-assembly of a 2D lattice, from a four-arm Holliday-junctions with DNA bearing complementary sticky-ends *via* sticky-end interactions. Numbers indicate base pairing strategies between sticky ends (1 is complementary to 1', etc.). Figures adapted from ref.¹⁰⁵

In 2006, Paul W. K. Rothemund published a method for the bottom-up fabrication of intricate DNA nanostructures named DNA origami.¹⁰⁶ The fundamental success of this assembly strategy hinges on the dependability of nucleobase pairing and the programmability inherent in the folding of nucleic acids. 2D and 3D structures are formed by DNA origami by annealing a long single-stranded scaffold strand with multiple distinct short single-stranded staple strands (Scheme 1.9 and Figure 1.10a).



Scheme 1.9: Principle of DNA origami: A long single-stranded scaffold of DNA (grey) is annealed with short staples (blue). Folding occurs during the annealing as the staples can bring together distant regions of the scaffold via base pairing to form the DNA origami nanostructures. Figures adapted from ref.¹⁰⁷ Reproduced with permission from Springer Nature.

The folding process of a 7-kilobase scaffold strand into a specified 2D configuration was achieved through the annealing of a collection of over 200 staple strands to the scaffold strand. These staple strands undergo hybridization with complementary fragments of the scaffold strand, thereby ensuring the scaffold stays in place. Through the systematic design of the staple strands, DNA origami nanostructures with anticipated dimensions and shapes can be engineered (Figure 1.10b).

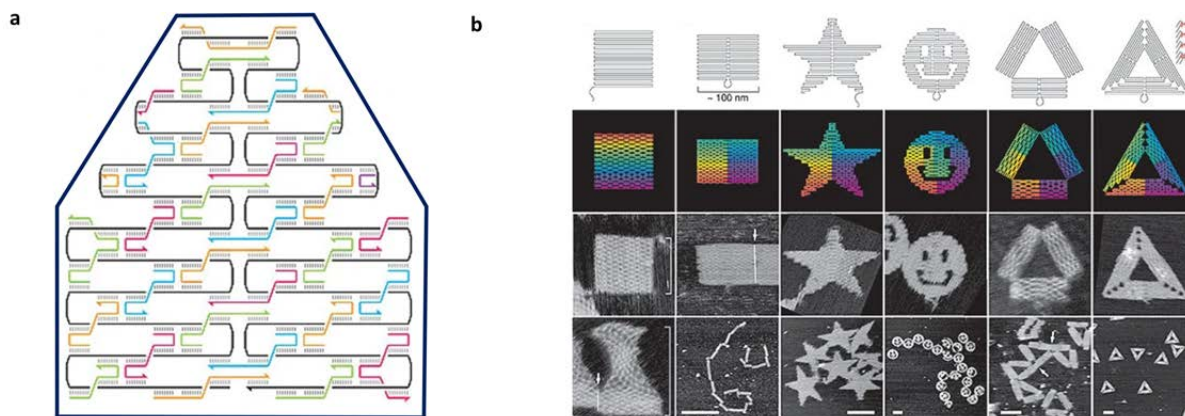
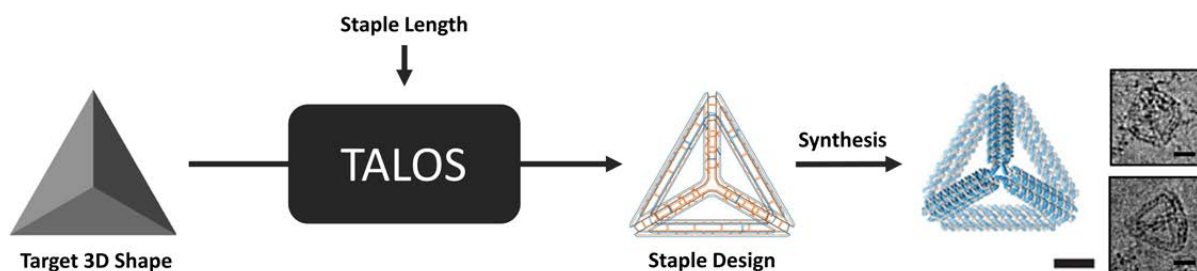


Figure 1.10: (a) DNA origami design for a desired shape (dark blue), the scaffold strand (black), and the numerous staple strands (in different colors). (b) Different shapes formed by DNA origami, with the corresponding folding paths (top to rows) and atomic force microscopy (AFM) images of them (bottom two rows). Figures adapted from ref.¹⁰⁶ Reproduced with permission from Springer Nature.

To create the vast number of desired nanostructures thorough understanding of sequence design principles is needed.^{108–110} Therefore, numerous computer-aided design software tools were developed over the years.^{111–121} These tools significantly streamline the workflow, enabling the straightforward fabrication of intricate DNA shapes. An example of a state-of-the-art top-down sequence design procedure three-dimensional algorithmically generated library of DNA Origami Shapes (TALOS) is illustrated in Scheme 1.10.¹²¹ The proof of principle for TALOS was demonstrated by the formation of a variety of 3D DNA origami structures verified experimentally by cryo-electron microscopy (cryo-EM).



Scheme 1.10: Simplified scheme of the operating principle of TALOS: Starting from a target polyhedron, TALOS generates, with the user-defined staple length, a staple design for the desired structure. Subsequent synthesis generates the desired polyhedron experimentally proven by cryo-EM images (scale bar 20 nm). Figures adapted from ref.¹²¹

In the work described above, the nanostructures assemble entirely *via* the Watson-Crick base pairing of the DNA nucleotides. The scope of DNA architecture is vastly expanded by combining the Watson-Crick base pairing with orthogonal supramolecular interactions.^{122–128} It was found that the incorporation of artificial building blocks has substantial effects on the assembly.^{129–134} Particular interest emerged in equipping the hydrophilic DNA with hydrophobic functionalities,

forming amphiphilic DNA conjugates.^{135–145} In most of these amphiphilic conjugates, self-assembly results from the inter-molecular interaction between the artificial building blocks rather than the DNA part.

Previous work in our research group demonstrated the formation of supramolecular nanostructures in aqueous medium composed of 3'-modified phenanthrene-DNA conjugates (Figure 1.11).¹⁴⁶ Atomic force microscopy (AFM) and Transmission electron microscopy (TEM) revealed the supramolecular self-assembly of the phenanthrene-DNA conjugates into vesicles (Figure 1.11c). The self-assembly of the amphiphilic phenanthrene-DNA conjugates was enabled by the supramolecular interactions of the hydrophobic phenanthrene stick ends. For a successful assembly, the addition of spermine tetrahydrochloride (Figure 1.12) was essential. The supramolecular assembly was conducted in a buffered system at pH 7.0. At this pH, spermine is positively charged (Figure 1.12). It is assumed that the repulsion between the negatively charged backbone of the DNA duplexes inside the supramolecular assemblies is reduced by the positive charges of the spermine.

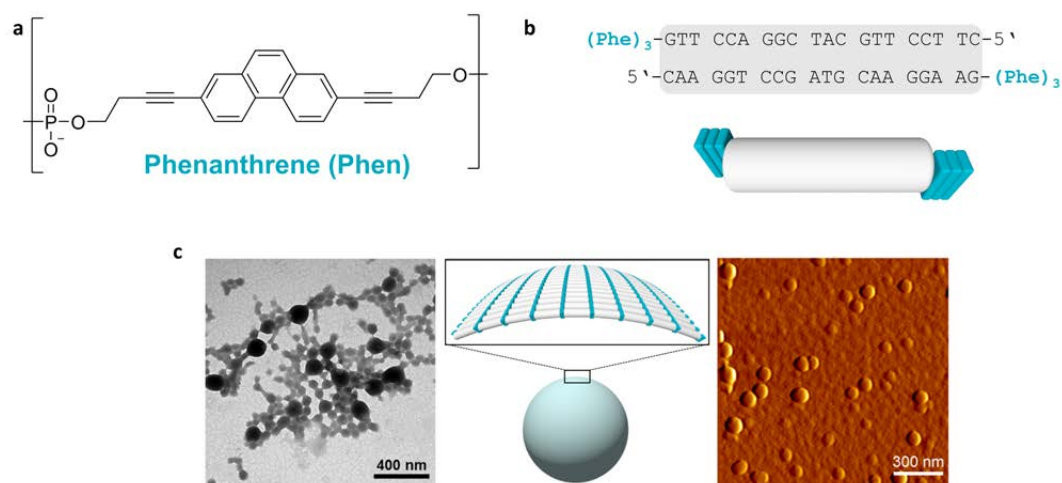


Figure 1.11: (a) Structure of the phenanthrene sub-unit, (b) sequence and illustration of the 3'-phenanthrene-modified DNA duplex, and (c) TEM image, schematic representation, and AFM image of the resulting supramolecular after self-assembly. Conditions: 5 μ M phenanthrene-DNA conjugate, 10 mM sodium phosphate buffer pH 7.0, 0.1 mM spermine tetrahydrochloride, 20 vol% ethanol. Figures adapted from ref.¹⁴⁶

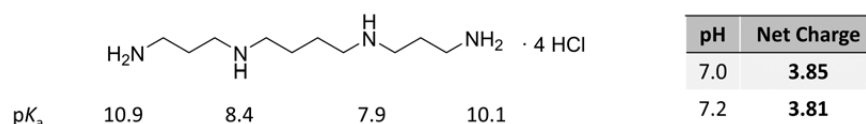


Figure 1.12: Molecular structure of spermine tetrahydrochloride, pK_a value of the four amines, and net charge of spermine at pH values discussed here (calculated with the Henderson–Hasselbalch equation).¹⁴⁷

Spermine is an abundant natural polycation found in elevated levels in conditions characterized by high cell division, such as in tumor cells.^{148,149} This polyamine is associated with diverse cellular functions, although the precise mechanism of action remains still unclear.^{150–156} Nevertheless, it is hypothesized that spermine plays a crucial role in facilitating DNA packaging and stabilizing chromatin, primarily through electrostatic attraction to the negatively charged phosphate backbone of the DNA.^{157,158} The non-specific electrostatic Coulomb interaction between nucleic acids and polyamines has led to the application of synthetic polymeric polycations as transfection agents for delivering therapeutic nucleic acids to cells.^{159–162}

More recently, our group has published the self-assembly of 3'-end modified tetraphenylethylene (TPE)-DNA conjugates (Figure 1.13).¹⁶³ The nanostructures were formed under identical conditions, as described for the phenanthrene-DNA conjugates above. The amphiphilic TPE-DNA conjugate self-assembled *via* the hydrophobic interactions of the TPE-sticky ends in the presence of spermine. Interestingly, cryo-EM measurements revealed the assembly of two different vesicular morphologies. An extended alignment (rugby-balls) and a compact columnar arrangement of the duplexes were observed. The proposed aggregation-induced emission (AIE) of the TPE units was confirmed (Figure 1.13d).

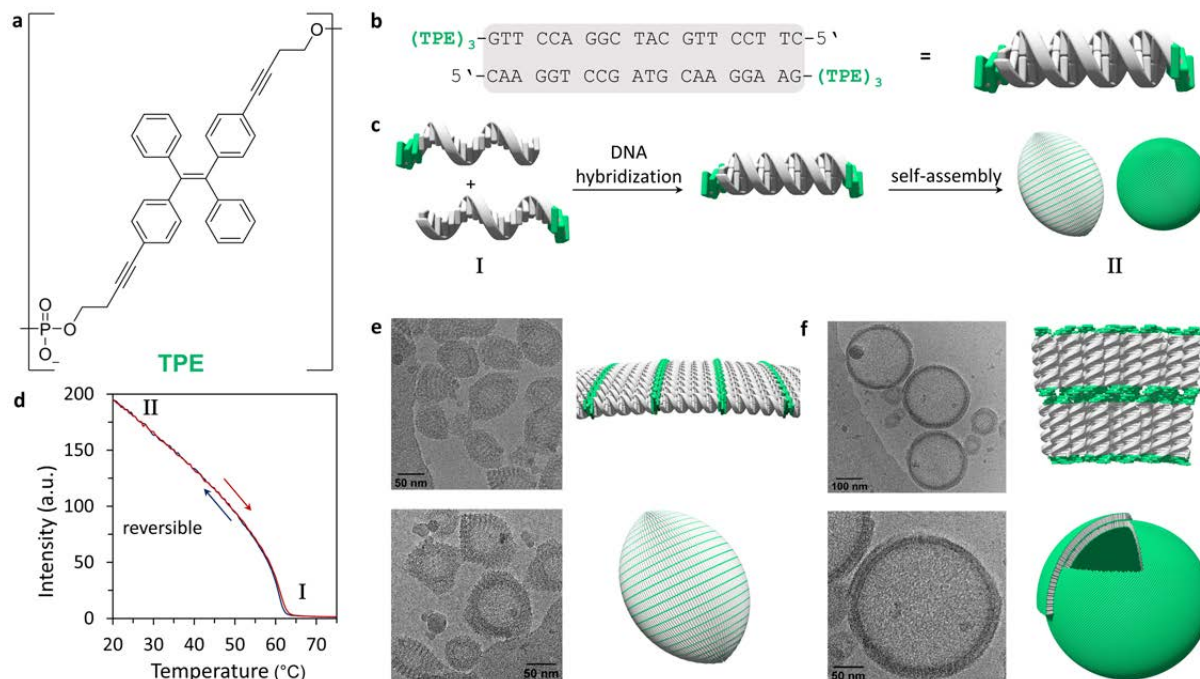


Figure 1.13: (a) Chemical structure of the tetraphenylethylene (TPE) building block; (b) sequence of the 3'-end modified DNA duplex and schematic representation; (c) schematic illustration of the assembly process starting from two single strands at 75 °C (I), DNA hybridization upon controlled cooling, and self-assembly to supramolecular assemblies (II) at 20 °C; (d) temperature-dependent fluorescence emission highlighting the aggregation-induced emission (AIE) upon assembly (heating in red and cooling in blue, $\lambda_{\text{ex.}}$: 335 nm, $\lambda_{\text{em.}}$: 490 nm, 0.5 °C·min⁻¹) and reversibility of the self-assembly; and (e and f) cryo-EM images and schematic illustrations of self-assembled TPE-DNA conjugates (e) into prolate, ellipsoidal vesicle (rugby-like) and (f) columnar-packed vesicles. Conditions: 1 μM TPE-DNA conjugate, 10 mM sodium phosphate buffer pH 7.2, 0.1 mM spermine tetrahydrochloride, 20 vol% ethanol. Figures adapted from ref.¹⁶³

A weakness of the two DNA conjugates described above is the limited ability to modify them, as the TPE or phenanthrene modifications are on two opposing strands. Therefore, our group modified a single DNA strand on the 3'- and 5'-end with TPE, leaving the opposing strand open for modification (Figure 1.14).^{164,165} It was found that a minimum of two TPE units on each side of the duplex are required to form vesicles. Vesicles formed by TPE-DNA conjugates with three units on each side started to agglomerate on AFM (Figure 1.14a). Cryo-EM of the conjugates bearing a total of 6 units showed that the vesicles are packed in a columnar fashion, and on top of the columnar arranged duplexes, a second layer of extended DNA arrangement is present (Figure 1.14b).

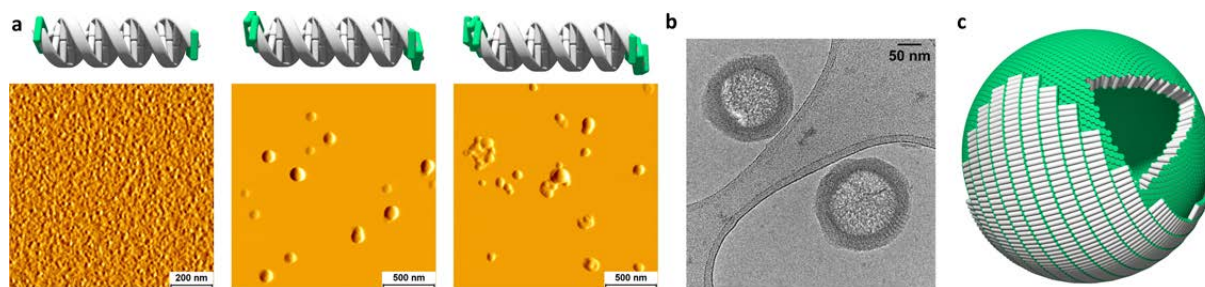


Figure 1.14: (a) Schematic representation and AFM images of 3'- and 5'-modified TPE-DNA conjugates bearing 1 TPE on each side (left), 2 TPEs (middle), and 3 TPE (right), (b) cryo-EM image of columnar packed TPE-DNA conjugate with 3 TPEs on each side, and (c) schematic representation of the assemblies observed in cryo-EM. Conditions: 1 μM each strand, 10 mM sodium phosphate buffer pH 7.2, 0.1 mM spermine tetrahydrochloride, 20 vol% ethanol. Figures adapted from ref.¹⁶⁴

Another publication of our group focused on the introduction of modifications.¹⁶⁵ 3'- and 5'-modified TPE-DNA strands were hybridized with complementary DNA-20-mers that were modified with polyethylene glycol (PEG) of different chain lengths or a carbohydrate moiety. The impact on the self-assembly of the modifications was tested by cryo-EM. The modification led to the formation of various architectures (Figure 1.15). A duplex bearing a short PEG chain of only six units formed vesicles. However, with the increasing length of the PEG chain, the morphology changes from vesicles to ribbons. Astoundingly, the attachment of the *N*-acetyl galactosamine carbohydrate led to the formation of star-shaped morphology.

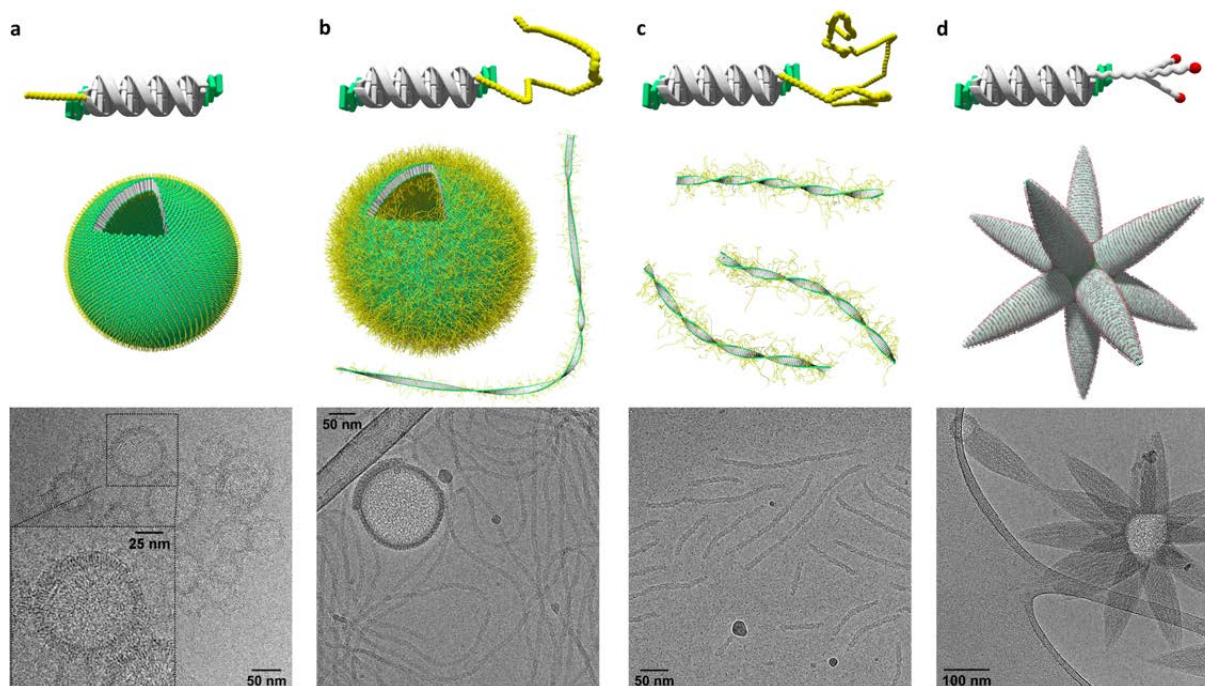


Figure 1.15: Schematic representations of the duplexes (top), representation of the supramolecular assemblies (middle), and cryo-EM images (bottom) of the 3'- and 5'-modified TPE-DNA conjugates with addition modifications on the complementary strand: (a) PEG₆ modification, (b) PEG₂₀₀₀ modification (M_w 2000 Da), (c) PEG₅₀₀₀ modification (M_w 5000 Da), and (d) *N*-acetyl galactosamine carbohydrate modification. Conditions: 1 μM each strand, 10 mM sodium phosphate buffer pH 7.2, 0.1 mM spermine tetrahydrochloride, 30 vol% ethanol. Figures adapted from ref.¹⁶⁵

1.5 Light-Harvesting and Energy Transfer

In the previous section, DNA-based supramolecular assemblies were introduced. The possibility of precisely arranging units on the nanometer scale in the DNA-constructed assemblies was highlighted. This distinctive feature of DNA can be exploited for energy transfer and light-harvesting by introducing chromophores into such systems. First, the light-harvesting and excitation energy transfer is described. Followed by examples of excitation energy transfer in DNA-constructed assemblies.

The capture of light energy involved in photosynthesis is one of the most intensively studied area of research. In photosynthesis, an organism adeptly captures and stores light energy for subsequent utilization in cellular processes. In these organisms, the light energy is captured by light-harvesting complexes (LHCs) that consist of several chromophores. In LHCs, a light-harvesting antenna collects the incoming light and transfers it to the photosynthetic reaction center. At the photosynthetic reaction center, light energy is converted to chemical energy through the transfer of electrons from a donor to an acceptor, resulting in charge separation. In a biological sense, LHCs produce oxygen and sugar using water and CO_2 with the energy of sunlight.^{166,167} This process is illustrated graphically in Figure 1.16.

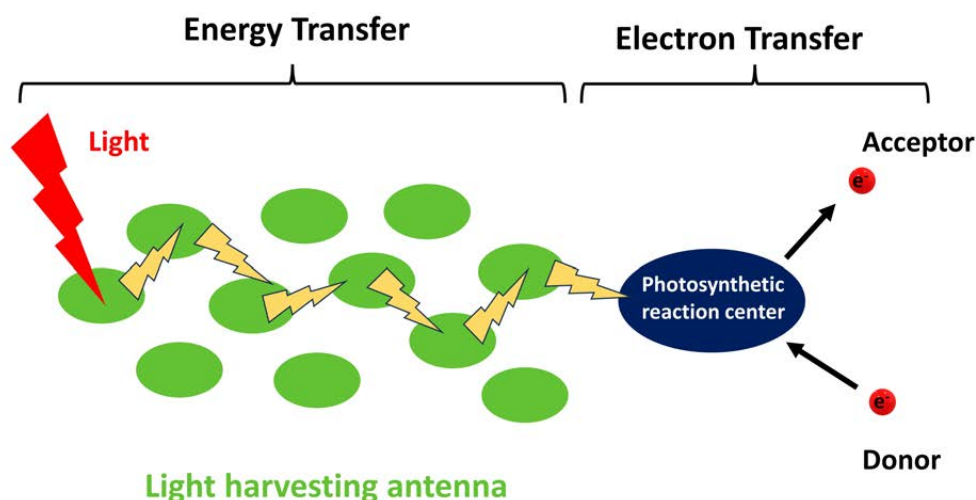
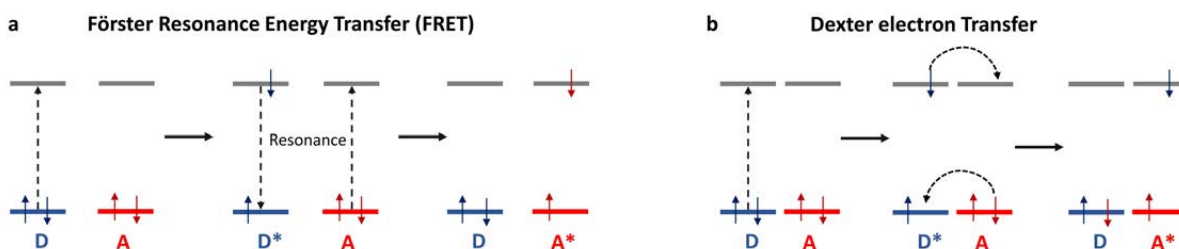


Figure 1.16: Graphical illustration of a light-harvesting complex in organisms. Light is absorbed by multiple chromophores (green), followed by the energy transfer (flashes) throughout the light-harvesting antenna system until it reaches the photosynthetic reaction center (blue). There, the electron transfer takes place.

The natural LHCs are constructed using chromophores, namely chlorophylls and carotenoids. To better understand the complex nature of natural light harvesting, researchers started to simplify systems found in nature. Therefore, artificial light-harvesting complexes were designed that contain different electron donors and acceptors that mimic the charge separation in the natural photosynthetic proteins.^{168–174} With these artificial light-harvesting complexes, scientists started investigating the different energy transfer pathways in such systems, discussed in more detail below.

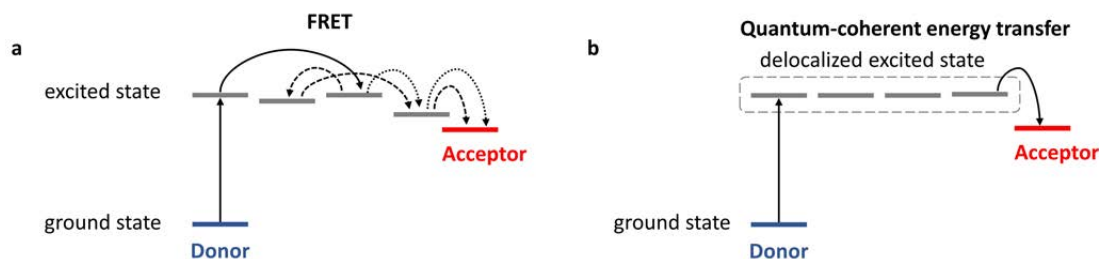
Excitation energy transfer (EET) describes the energy transfer between two light-sensitive chromophores. EET is mainly observed in multichromophoric systems over reasonably large distances by a series of energy hops.¹⁷⁵

When the electronic coupling among chromophores is weak, the EET can be described by Förster resonance energy transfer (FRET).¹⁷⁶ The Förster model is based on electric dipole-dipole interactions, where excitation transitions from the donor to the acceptor. The rate of energy transfer is dependent on the sixth power of the distance between chromophores, the orientation of the chromophores in relation to each other, the donor's fluorescence quantum yield, the refractive index of the medium, and the overlap of the donor's fluorescence and acceptors absorption bands.^{177,178} FRET usually occurs when donors and acceptors are separated by 1.0–10 nm. At lower interchromophore distances, the ideal dipole approximation of the Förster theory breaks down.¹⁷⁹ For donor-acceptor distances smaller than 1.0 nm, the energy transfer is better explained by Dexter electron transfer that requires a wave-function overlap between the donor and acceptor (Scheme 1.11).¹⁸⁰



Scheme 1.11: Illustration of non-radiative excitation energy transfer mechanism. (a) FRET: excitation energy transfer from excited Donor (D^*) to acceptor (A) *via* dipole-dipole coupling (Interchromophore distance 1.0–10 nm) and (b) Dexter electron transfer: excited electron transfer from an excited donor (D^*) to acceptor (A) requiring a wavefunction overlap between donor and acceptor (Interchromophore distance < 1.0 nm).

As described above, in light-harvesting complexes, several donor chromophores transmit energy to the acceptor. In systems where excitation energy transfer occurs through FRET, the weak electronic coupling among the chromophores results in the incoherent hopping of excitation energy between donor chromophores, resembling a random walk pattern (Scheme 1.12a). In contrast, when there is strong electronic coupling among the chromophores, the electronic excitation can be spread coherently. The electronic states of the donor and acceptor mix and generate a quantum mechanically coupled delocalized excited state that is shared among multiple chromophores. In this delocalized excited state, the energy is transferred wave-like from the donor to the acceptor (Scheme 1.12b).¹⁸¹ Recent theories and models developed to describe and understand light-harvesting in nature incorporate the concept of quantum coherent energy transfer.^{182–185}



Scheme 1.12: Difference between the classical (incoherent) and quantum coherent EET. (a) FRET: The excitation energy hops randomly from chromophore to chromophore until it reaches the acceptor and (b) quantum-coherent energy transfer: the excitation is delocalized over several quantum-mechanically coupled chromophores, and it travels wave-like to the acceptor.

An example where a DNA duplex was used in a light-harvesting application was outlined by our group in 2011 (Figure 1.17).⁴⁹ The DNA-based light-harvesting antenna described consists of an array of π -stacked phenanthrene chromophores serving as the light-collecting antenna, an exciplex-forming pyrene functioning as the acceptor, and a DNA double helix acting as the supramolecular scaffold (Figure 1.17a). The light collection involved up to eight phenanthrene units. The emitted photons by the phenanthrene–pyrene exciplex are directly proportional to the quantity of light-absorbing chromophores present (Figure 1.17b). This example showed that up to 8 phenanthrene units in a DNA scaffold can donate their excitation energy to the phenanthrene–pyrene exciplex (Figure 1.17c).

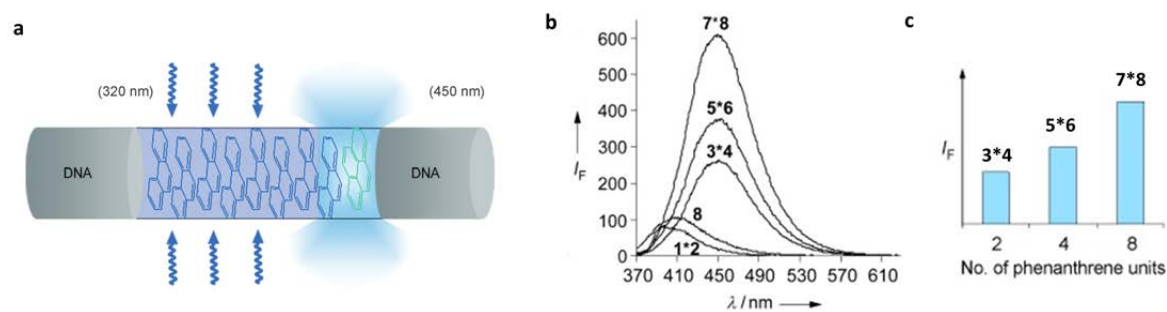


Figure 1.17: (a) Supramolecular scaffold of precisely arranged chromophores inside a DNA duplex (phenanthrene donor array in blue and pyrene acceptor in green). (b) fluorescence emission after excitation of the phenanthrene array at 320 nm of DNA duplexes containing one pyrene donor and different numbers of phenanthrene units: 0 (**1*2**), 2 (**3*4**), 4 (**5*6**), and 8 (**7*8**) and the control single strand **8** containing 4 pyrenes. (c) Integrated fluorescence emission after excitation at 320 nm of **3*4**, **5*6**, and **7*8**. Adapted from ref.⁴⁹

In a follow-up paper, the limit of chromophore segmentation in DNA-organized artificial LHCs was assessed (Figure 1.18).⁷² The DNA-organized artificial LHCs are comprised of multi-segmental duplexes featuring alternating DNA and phenanthrene sections (Figure 1.18a). The assembly of phenanthrenes within the DNA duplex functions as a collective light-harvesting antenna. Despite the interruption in the phenanthrene stack due to intervening DNA base pairs, absorbed light efficiently transfers to a pyrene acceptor chromophore. All segmented constructs demonstrate efficiency as light-harvesting systems. The efficiency of the LHCs initially rises with the number of phenanthrenes until reaching a maximum after three to four

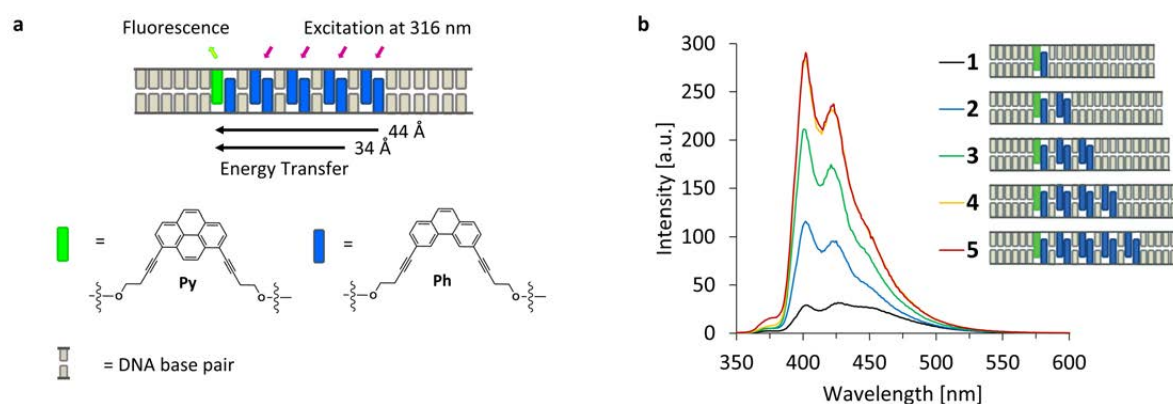


Figure 1.18: (a) illustration of phenanthrene antenna in DNA-organized artificial LHCs with an alternating arrangement of base pairs and phenanthrene units and chemical structure of phenanthrene donor (**Ph**) and pyrene acceptor (**Py**) units. (b) Fluorescence emission spectra after excitation of the phenanthrene antenna at 316 nm in DNA-organized LHCs **1–5** containing 1–9 phenanthrene units. Adapted from ref.⁷²

chromophore segments (Figure 1.18b). These findings highlight the tolerance of constructing artificial light-harvesting systems by integrating functionally non-related components, such as DNA base pairs, into the multi-chromophore array.

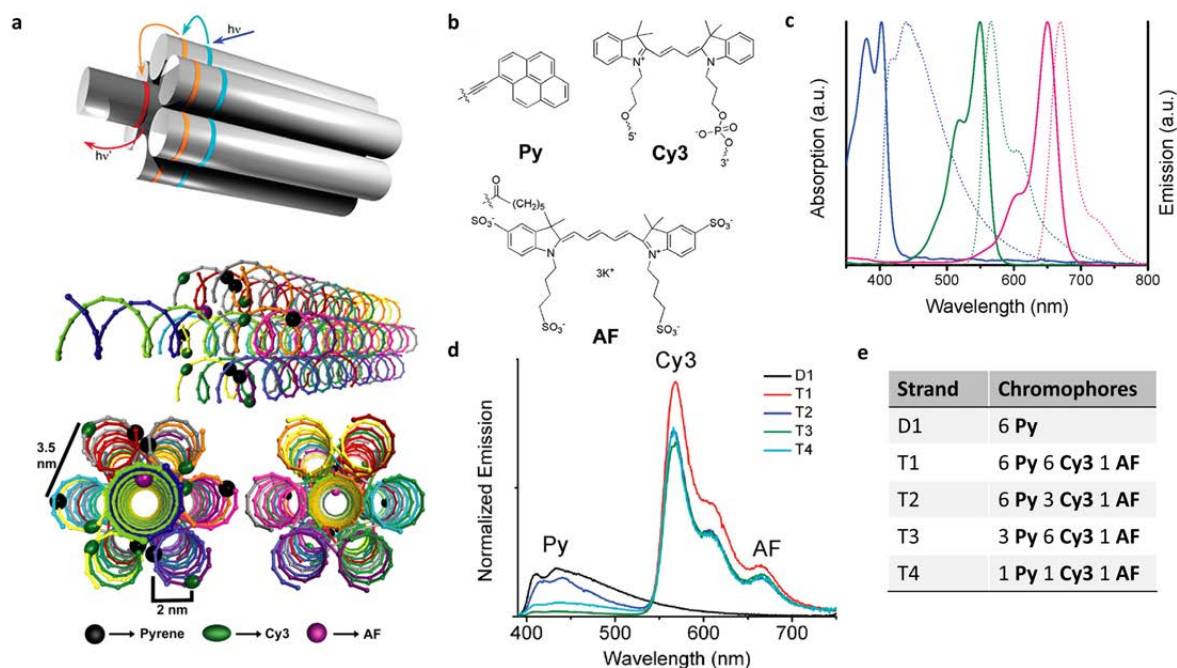


Figure 1.19: (a) Schematic representation of seven self-assembled DNA duplexes with precisely arranged chromophores, excitation of **Py** (blue), followed by FRET cascade over **Cy3** (orange), to **AF** (red) and side, front, and rear view of **T1**. (b) Chemical structures of the chromophores. (c) Normalized absorption (solid line) and emission (dotted line) spectra for **Py** (blue), **Cy3** (green), and **AF** (pink) modified DNAs showing the optical spectral overlap. (d) Normalized emission spectra of **D1** and **T1–T4**, all with excitation of the **Py** at 380 nm. (e) Table of strands **D1** and **T1–T4** with the corresponding chromophore compositions. Adapted from ref. ¹⁸⁶

Liu *et al.* have utilized DNA origami to construct a well-defined, DNA-templated artificial light-harvesting antenna (Figure 1.19). Three distinct chromophore arrays were organized into configurations, ensuring precise inter-chromophore distances and well-defined donor-acceptor ratios (Figure 1.19a). Steady-state and time-resolved fluorescence analyses demonstrated efficient, step-wise FRET from a primary donor (**Py**) array to an acceptor (**AF**) through an intermediate donor (**Cy3**) array upon excitation of the primary donor (Figure 1.19d). Exclusively, unidirectional energy transfer to the final acceptor was observed. This example illustrates the possibilities of DNA nanotechnology in light-harvesting applications.

Chapter 2

Aim of the Thesis

Previous work in our group focused on assembling chromophores within DNA scaffolds. The chromophores were organized within DNA duplexes, triplexes, as well as three-way and four-way junctions. More recently, the focus of our group has shifted to chromophore modifications on the ends of DNA, forming DNA duplexes with hydrophobic sticky ends on each side. These chromophore-DNA conjugates formed supramolecular nanostructures upon self-assemblies. The supramolecular assembly of the conjugates is enabled by a combination of orthogonal supramolecular interaction, *i.e.*, hydrophobic interaction between the sticky ends and DNA hybridization. Furthermore, spermine tetrahydrochloride is required to form supramolecular polymers, as it reduces the repulsion between the negatively charged DNA backbone. Our group has examined the supramolecular assembly of phenanthrene- and TPE-DNA conjugates forming vesicular DNA nanostructures, described in detail in the introduction (section 1.4).^{146,163–165}

The aim of the thesis was to synthesize and examine the self-assembly properties of pyrene-DNA conjugates modified with pyrene at the 3'- and 3'/5'-ends. A key focus was laid on examining the influence of the pyrene substitution pattern on the morphology of the assemblies. In addition, we aimed to evaluate the effect of changes in the number of pyrenes on the sticky ends. Another objective was to determine the impact of further terminal functionalizations on the supramolecular assembly. Furthermore, we aimed to investigate if 3'-end phenanthrene-DNA conjugates bearing additional modification in the middle of the strand self-assemble into nanostructures. Finally, we aimed to explore the potential of the pyrene- and phenanthrene-DNA conjugates for light-harvesting applications.

Chapter 3

Supramolecular Self-Assembly of 3'-End Modified Pyrene-DNA Conjugates: Influence of Pyrene Substitution Pattern and Light-Harvesting

In this chapter, the supramolecular self-assembly of 3'-end modified pyrene-DNA conjugates is described. The self-assembled nanostructures formed by three differently substituted pyrene units in pyrene-DNA conjugates are compared. The conjugates assembled into nanostructures *via* the hydrophobic pyrene sticky ends and spermine-mediated interactions. Different morphologies were observed by cryo-EM for the three isomers. 1,6- and 1,8-isomers formed multilamellar vesicles, whereas conjugates of the 2,7-isomer exclusively assemble into spherical nanoparticles. Artificial light-harvesting complex (LHC) systems were evaluated with the pyrene isomers as donors and Cy3 or Cy5 as energy acceptors.

Part of this work has been published:

Supramolecular Assembly of Pyrene-DNA Conjugates: Influence of Pyrene Substitution Pattern and Implications for Artificial LHCs

J. Thiede, S. Rothenbühler, I. Iacovache, S. M. Langenegger, B. Zuber, and R. Häner, *Org. Biomol. Chem.* **2023**, 21, 7908–7912.

3.1 Results and Discussion

3.1.1 Spectroscopic Characterization of 1,6-, 1,8- and 2,7-Dialkynyl Pyrene Diol

First, the spectroscopic properties of 2,7-, 1,6-, and 1,8-dialkynyl pyrene diols **1**, **4**, and **5** (Figure 3.1a) were determined. The three pyrene isomers were characterized by ultraviolet-visible (UV-vis) and fluorescence spectroscopy.

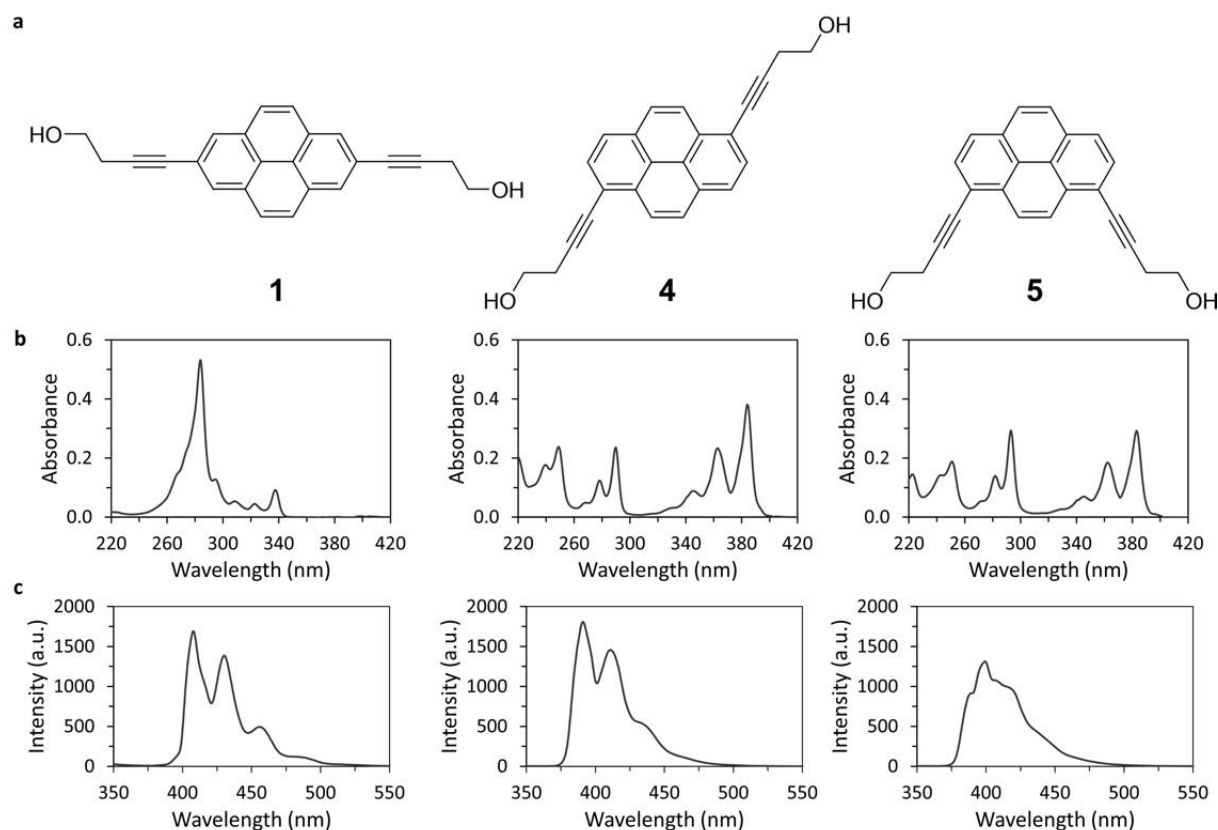


Figure 3.1: (a) Molecular structures of 2,7-, 1,6-, and 1,8-dialkynyl pyrene diols **1**, **4**, and **5**. (b) UV-vis absorption and (c) fluorescence emission spectra of **1** (left), **4** (middle), and **5** (right). Conditions: 6 μM pyrene diol in ethanol, 20 $^{\circ}\text{C}$, λ_{ex} for **1**; 285 nm, **4**; 290 nm, and **5**; 293 nm, excitation slit width for **1**; 2.5 nm and for **4** and **5**; 1.0 nm, emission slit width; 2.5 nm for all isomers.

The UV-vis absorption spectra of **1**, **4**, and **5** in ethanol at 20 $^{\circ}\text{C}$ are shown in Figure 3.1b. As the substitution of pyrene strongly affected the absorption spectra,¹⁸⁷ of the three isomers exhibit distinct absorption bands (Table 3.1). The linearly substituted pyrene **1** exhibited a very weak absorption maximum at 399 nm and a strong absorption band with a maximum at 284 nm. Substitutions at the 1, 6, and 8 positions of pyrene lead to vastly different absorptions. The absorption profiles of **4** (384 nm, 290 nm, and 249 nm) and **5** (383 nm, 293 nm, and 251 nm) are similar, only their maxima are slightly shifted.

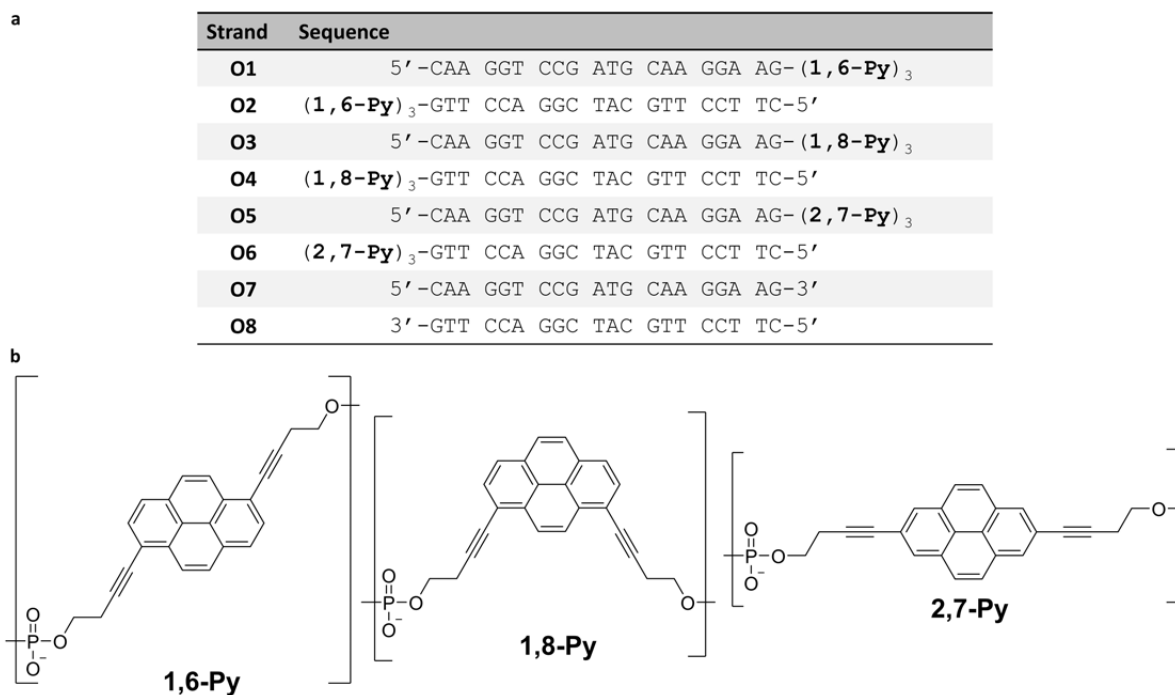
The pyrene diols **1**, **4**, and **5** exhibit monomer fluorescence after excitation (Figure 3.1c). The substitution effects fluorescence emission, **1** and **4** displayed resolved vibronic fine structure, whereas **5** showed broader and more structureless bands. Additionally, **1** expressed a more pronounced bathochromic shift compared to **4** and **5**.

Table 3.1: Pyrene-absorption maxima of pyrene in cyclohexane (adapted from ref.),¹⁸⁷ **1**, **4**, and **5** in ethanol.

λ_{\max} pyrene, nm (ϵ , mol ⁻¹ cm ⁻¹ L)	λ_{\max} 1 , nm (ϵ , mol ⁻¹ cm ⁻¹ L)	λ_{\max} 4 , nm (ϵ , mol ⁻¹ cm ⁻¹ L)	λ_{\max} 5 , nm (ϵ , mol ⁻¹ cm ⁻¹ L)
372 (510)	399 (450)	384 (63000)	383 (49000)
334 (55000)	338 (15000)	346 (15000)	345 (12000)
272 (54000)	284 (88000)	290 (39000)	293 (49000)
243 (8000)	-	249 (40000)	251 (31000)

3.1.2 3'-End Modified Pyrene-DNA Conjugates

The modified DNA strands used in this chapter are listed in Figure 3.2a. **O1** to **O6** were prepared *via* solid-phase synthesis using the phosphoramidite approach explained in the general introduction (1.3) and subsequently purified by HPLC. Detailed experimental procedures are provided in the appendix (chapter 3.3). The six oligomers consist of 20 DNA nucleotides and three differently substituted phosphodiester-linked pyrene units at their 3'-ends (Figure 3.2). The two complementary unmodified DNA strands **O7** and **O8** were purchased commercially and serve as a reference.

**Figure 3.2:** (a) DNA sequences **O1–O8** and (b) molecular structures of the pyrene modifications.

The self-assembly characteristics of the DNA duplexes modified either with 1,6-dialkynyl pyrene (**O1*O2**), 1,8-dialkynyl pyrene (**O3*O4**), and 2,7-dialkynyl pyrene (**O5*O6**) were compared, we aimed to determine the effects of the different substitution patterns. Recently, our group has explored the effect of substitution in a TPE-DNA conjugate.¹⁸⁸ Interestingly, only minute differences were observed between the *E*- and *Z*-TPE. Our group previously reported that the substitution pattern in phosphodiester bridge trimers alters the morphology of their self-assembled supramolecular polymer.^{22–24} Therefore, pyrene is a more promising candidate to observe isomeric effects in supramolecular assemblies.

3.1.3 Spectroscopic Characterization

The temperature-dependent UV-vis absorption spectra of the pyrene-DNA conjugates **O1*O2**, **O3*O4**, and **O5*O6** are shown in Figure 3.3. At 75 °C, the spectrum of **O1*O2** displays the distinctive absorption peaks for 1,6-dialkynyl pyrene at 365 nm and 387 nm.^{22,189} Within the range of 220 nm to 320 nm, the pyrene absorption bands overlap with those of DNA nucleobases. Upon controlled cooling at a rate of 0.5 °C per minute from 75 °C to 20 °C, the pyrene absorption peaks above 320 nm exhibit a slight shift toward longer wavelengths (1–2 nm), while a small decrease in absorption intensity is observed for the band between 220 and 300 nm. Additionally, there is a minor presence of light scattering, suggesting some level of aggregation of the pyrene-DNA conjugates. The absorption spectra of **O3*O4** closely resemble those of **O1*O2**.^{189,190} The spectrum of 2,7-dialkynyl pyrene-DNA conjugates **O5*O6** at 75 °C consists of two maxima. The weaker maximum at 342 nm arises from the pyrene units, while the one at 270 nm originates from both the pyrene and the DNA nucleobases.^{19,187,191} Upon cooling to 20 °C, the 342 nm maximum shifts to longer wavelengths (2 nm), the 270 nm band shifts to shorter wavelengths, and scattering is again observed, indicating some level of aggregation of the pyrene-DNA conjugates.¹⁶⁴

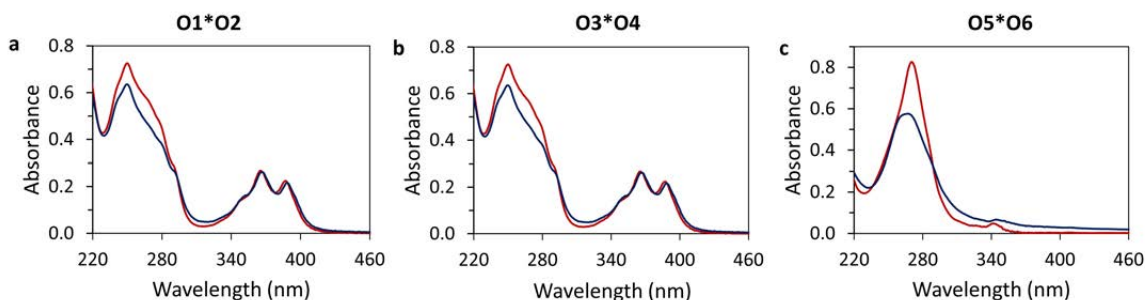


Figure 3.3: Temperature-dependent UV-vis absorption spectra of (a) **O1*O2**, (b) **O3*O4**, and (c) **O5*O6** (red 75 °C and blue 20 °C after self-assembly). Conditions: 1 μ M each single strand, 10 mM sodium phosphate buffer pH 7.2, 0.03 mM spermine \cdot 4 HCl, 20 vol% ethanol.

To gain a further understanding of the aggregation process, the absorbance at 260 nm was measured while heating and cooling the sample (Figure 3.4). The shapes of the heating-cooling curves show a self-assembly mechanism of **O1*O2**, **O3*O4**, and **O5*O6**. The form of the curves strongly suggests a nucleation-elongation growth mechanism.^{192–196} The points at which the absorbance starts to decrease pronounceable, also called nucleation temperatures, of **O1*O2**, **O3*O4**, and **O5*O6** were observed between 58 °C and 60 °C. The increase of the absorbance close to 20 °C emerges from the scattering of the self-assemblies. A minor

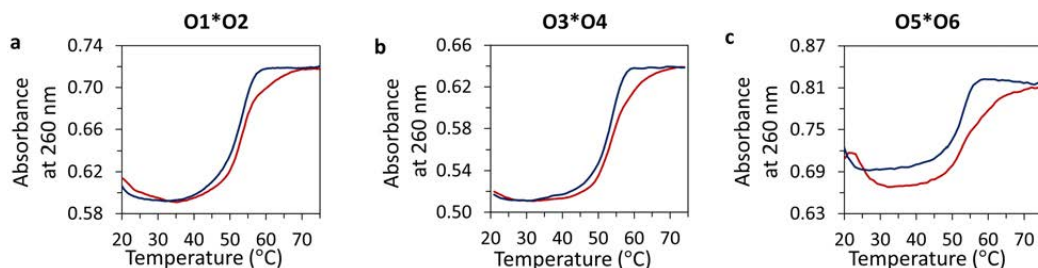


Figure 3.4: Temperature-dependent UV-vis absorbance at 260 nm (cooling-heating curves) of (a) **O1*O2**, (b) **O3*O4**, and (c) **O5*O6** (red heating and blue cooling). Conditions: 1 μ M each single strand, 10 mM sodium phosphate buffer pH 7.2, 0.03 mM spermine \cdot 4 HCl, 20 vol% ethanol.

hysteresis was observed in the heating and cooling profiles of all hybrids. Control experiments of **O1*O2** in the absence of spermine tetrahydrochloride (depicted in the appendix Figure 3.40) and the presence of 100 mM NaCl (illustrated in the appendix Figure 3.41) showed sigmoidal heating-cooling curves. Indicating the formation of a DNA duplex and highlighting the necessity of spermine tetrahydrochloride for supramolecular assemblies.

Temperature-dependent fluorescence excitation and emission spectra of the pyrene-DNA conjugates were conducted (Figure 3.5 and interval scan illustrated in the appendix Figure 3.43). Hybrids **O1*O2** and **O3*O4** exhibit pyrene excimer fluorescence with a maximum around 525 nm. Upon cooling, a bathochromic and hypochromic shift in the emission is observed. Hybrid **O5*O6** displayed both monomer fluorescence (410–450 nm) and excimer fluorescence (450–625 nm). Interestingly, in this hybrid cooling induced a hyperchromic shift for both monomer and excimer emissions. The quantum yields of the self-assembled **O1*O2** ($34.0 \pm 3.1\%$) and **O3*O4** ($31.3 \pm 0.8\%$) are significantly higher than the one of **O5*O6** ($3.1 \pm 0.1\%$). Importantly, the scattering observed in the UV-vis absorption spectra strongly affects the measured quantum yield. The scattering was most pronounced in **O5*O6**, one of the reasons for the decreased quantum yield measured in this hybrid.

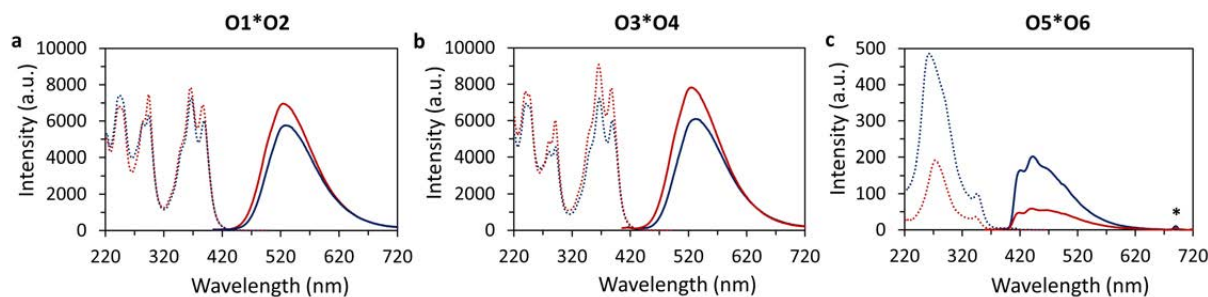


Figure 3.5: Temperature-dependent fluorescence emission (solid line) and excitation (dotted line) spectra of (a) **O1*O2**, (b) **O3*O4**, and (c) **O5*O6** (red 75 °C and blue 20 °C after self-assembly). Conditions: 1 μ M each single strand, 10 mM sodium phosphate buffer pH 7.2, 0.03 mM spermine · 4 HCl, 20 vol% ethanol, for **O1*O2** and **O3*O4**: λ_{ex} . 388 nm, λ_{em} . 525 nm and for **O5*O6**: λ_{ex} . 345 nm, λ_{em} . 415 nm.

3.1.4 Atomic Force Microscopy

Atomic force microscopy (AFM) was performed to visualize the nanostructures formed by **O1*O2**, **O3*O4**, and **O5*O6** after thermal assembly (Figure 3.6). The AFM measurements were conducted on (3-aminopropyl)triethoxysilane (APTES) modified mica. Individual and agglomerated vesicles were observed with **O1*O2** and **O3*O4**, while round-shaped aggregates were measured with **O5*O6**. **O1*O2** self-assembled into vesicles with a diameter of 108 ± 50 nm. The pyrene-DNA conjugate with the 1,8-dialkynyl pyrene stereoisomer **O3*O4** exhibited slightly larger vesicles with an average diameter of 134 ± 47 nm. The 2,7-dialkynyl pyrene-modified DNA **O5*O6** self-assembled into spherical aggregates with a diameter of 182 ± 55 nm. AFM measurements of the unmodified DNA duplex **O7*O8** after thermal assembly were conducted as a control (depicted in the appendix Figure 3.44). AFM images of **O7*O8** showed small structures with heights of less than 7 nm, indicating randomly deposited DNA duplexes. Similarly, AFM measurements of **O1*O2** in the absence of spermine tetrahydrochloride and the presence of 100 mM NaCl revealed no large nanostructures (illustrated in the appendix Figure 3.45).

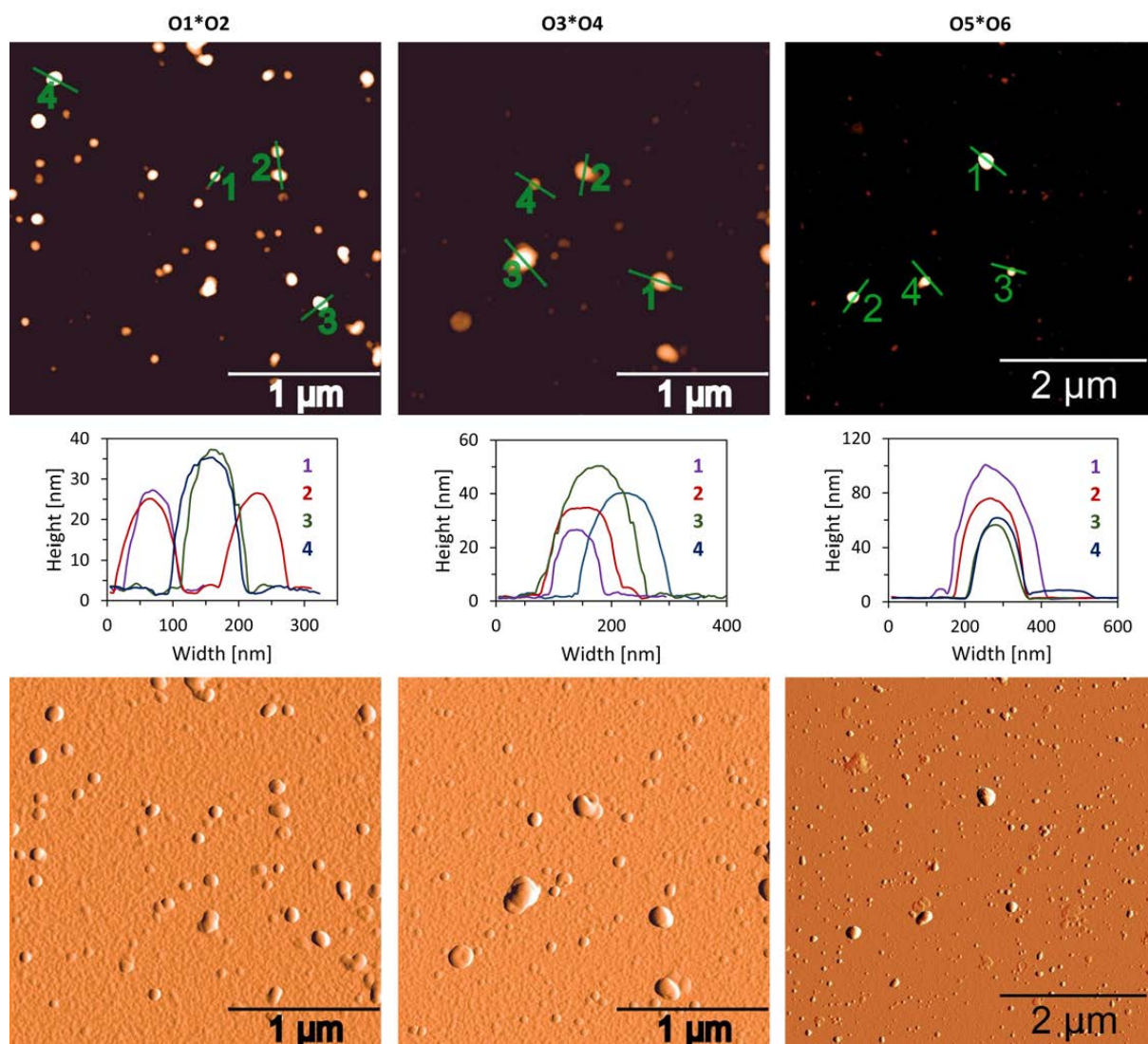


Figure 3.6: AFM scan (top) with corresponding cross sections (middle) and deflection scan of assembled (bottom) **O1*O2** (left), **O3*O4** (middle), and **O5*O6** (right). Conditions: 1 μM **O1*O2**, **O3*O4**, or **O5*O6**, 10 mM sodium phosphate buffer pH 7.2, 0.03 mM spermine \cdot 4 HCl, 20 vol% ethanol.

3.1.5 Transmission Electron Microscopy

To confirm the findings of the AFM measurements, transmission electron microscopy (TEM) of the three hybrids was conducted (Figure 3.7). All TEM samples were stained with a commercially available UA-zero stain to visualize the nanostructures. TEM results confirmed the size of the nanostructures. Diameters of 50–200 nm were measured for all three isomers, respectively. TEM images of **O1*O2** revealed an exciting feature, namely a regular pattern (Figure 3.7 left). The distance between the regular dark bands is around 7–8 nm, which corresponds well with the length of a single DNA duplex. In contrast, patterns were absent in TEM measurements of **O3*O4** and **O5*O6**. To get deeper insights into the arrangement of the molecular units in the supramolecular assemblies cryo-electron microscopy (cryo-EM), in collaboration with Prof. Dr. Benoît Zuber and Dr. Ioan Iacovache from the Institute of Anatomy of the University of Bern, was performed.

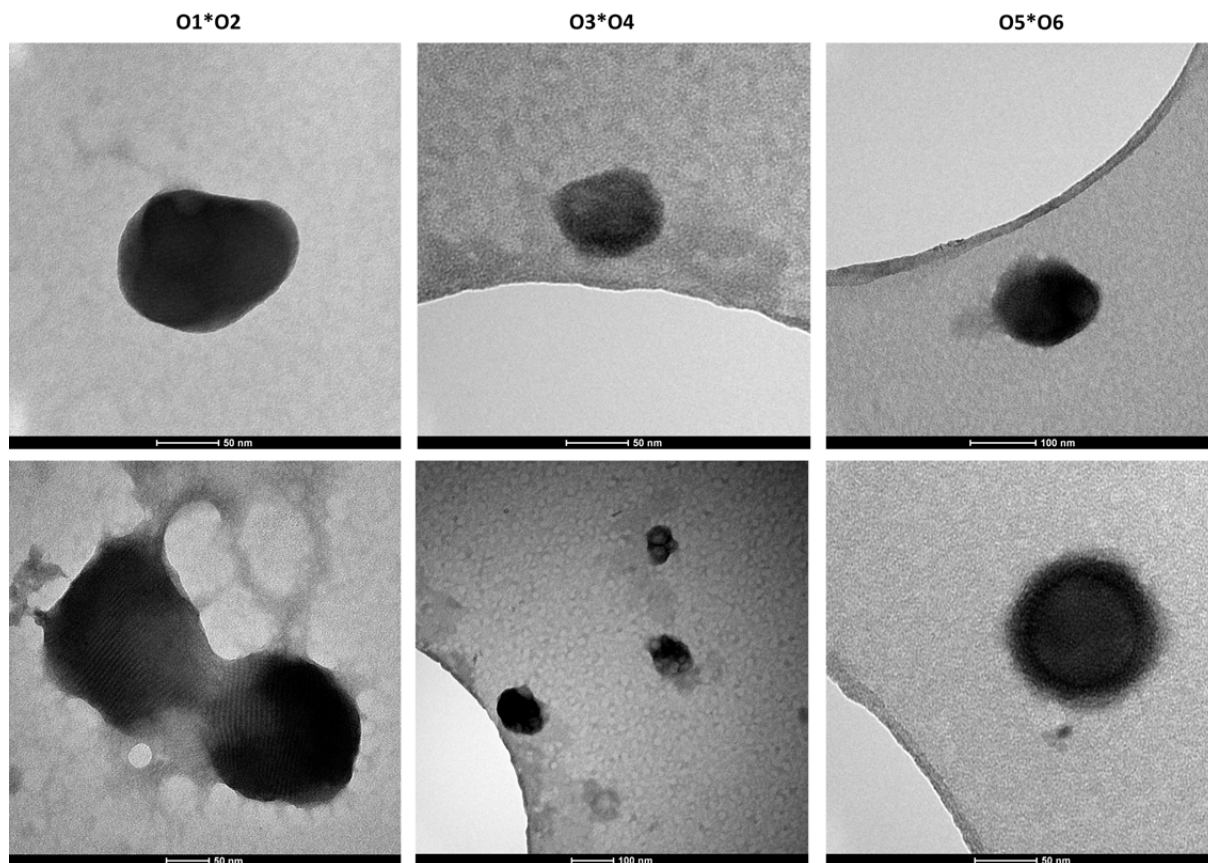


Figure 3.7: TEM image of self-assembled **O1*O2** (left), **O3*O4** (middle), and **O5*O6** (right) on holey carbon films on copper grids; UA-zero staining. Conditions: 1 μM **O1*O2**, **O3*O4**, or **O5*O6**, 10 mM sodium phosphate buffer pH 7.2, 0.03 mM spermine \cdot 4 HCl, 20 vol% ethanol.

3.1.6 Cryo-Electron Microscopy

In AFM and TEM, the nanostructures are exposed to drying effects and surface adsorption processes. These effects and processes are not present in cryo-EM. In cryo-EM imaging, the samples are vitrified, allowing the visualization of the nanostructures in their actual morphology in solution.^{197–199} In contrast to TEM, staining is not necessary for cryo-EM, and thus, potential artifacts due to the staining agent and interaction of the stain with the sample can be excluded.^{200,201} However, the nanostructures possess a high vulnerability to the electron beam. Hence, the electron dose had to be adjusted to less than $20 \text{ e}^-/\text{\AA}^2$.

Cryo-EM images of **O1*O2** reveal a distinctive vesicular morphology in the aggregates (Figure 3.8a, Figure 3.9a, and additional images in the appendix Figure 3.46). Vesicles formed from **O1*O2** exhibited diameters of $105 \pm 46 \text{ nm}$. Interestingly, **O1*O2** formed multilamellar vesicles and agglomerates of several vesicles. In the lamellae, a regular pattern with an interlamellar distance of $7.5 \pm 0.5 \text{ nm}$ was found, similar to the observations in TEM (Figure 3.8b). This specific interlamellar distance aligns closely with the length of the pyrene-modified DNA duplex, suggesting that the multilamellar vesicles originate from columnar arranged layers of organized pyrene–DNA duplexes. The interactions between individual layers in these vesicles are facilitated by the hydrophobic interactions of pyrene overhangs and the stabilizing properties of spermine, illustrated in the schematic representation Figure 3.8c and d. Interestingly, the observed number of lamellae varies among different vesicles, with some displaying up to 7 layers. The outer lamellae exhibit an open-shell appearance.

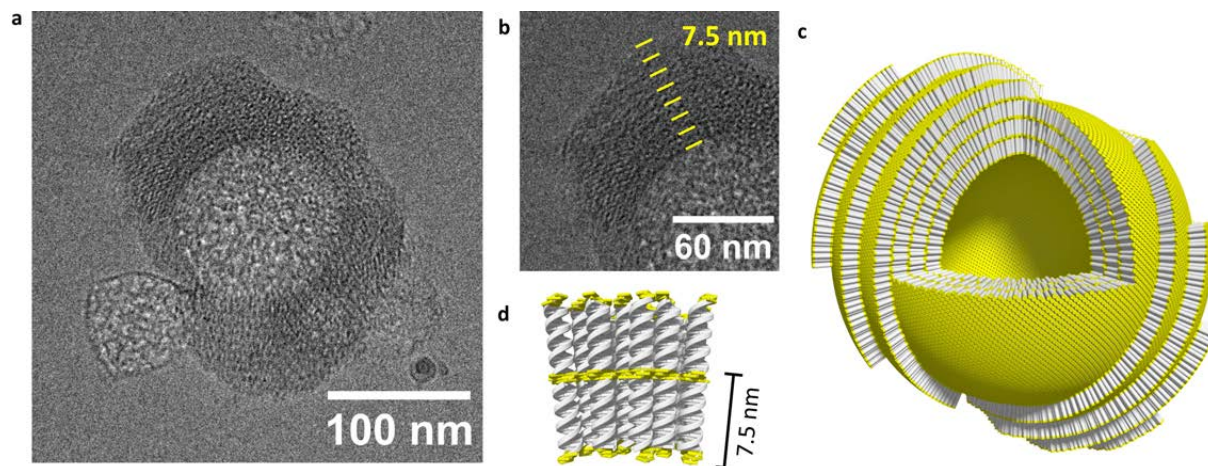


Figure 3.8: Cryo-EM image of (a) self-assembled $\text{O1}^*\text{O2}$, (b) zoom-in, and schematic illustrations of (c) the assemblies and (d) the stacked pyrene-DNA conjugates. Conditions: 1 μM $\text{O1}^*\text{O2}$, 10 mM sodium phosphate buffer pH 7.2, 0.03 mM spermine \cdot 4 HCl, 20 vol% ethanol.

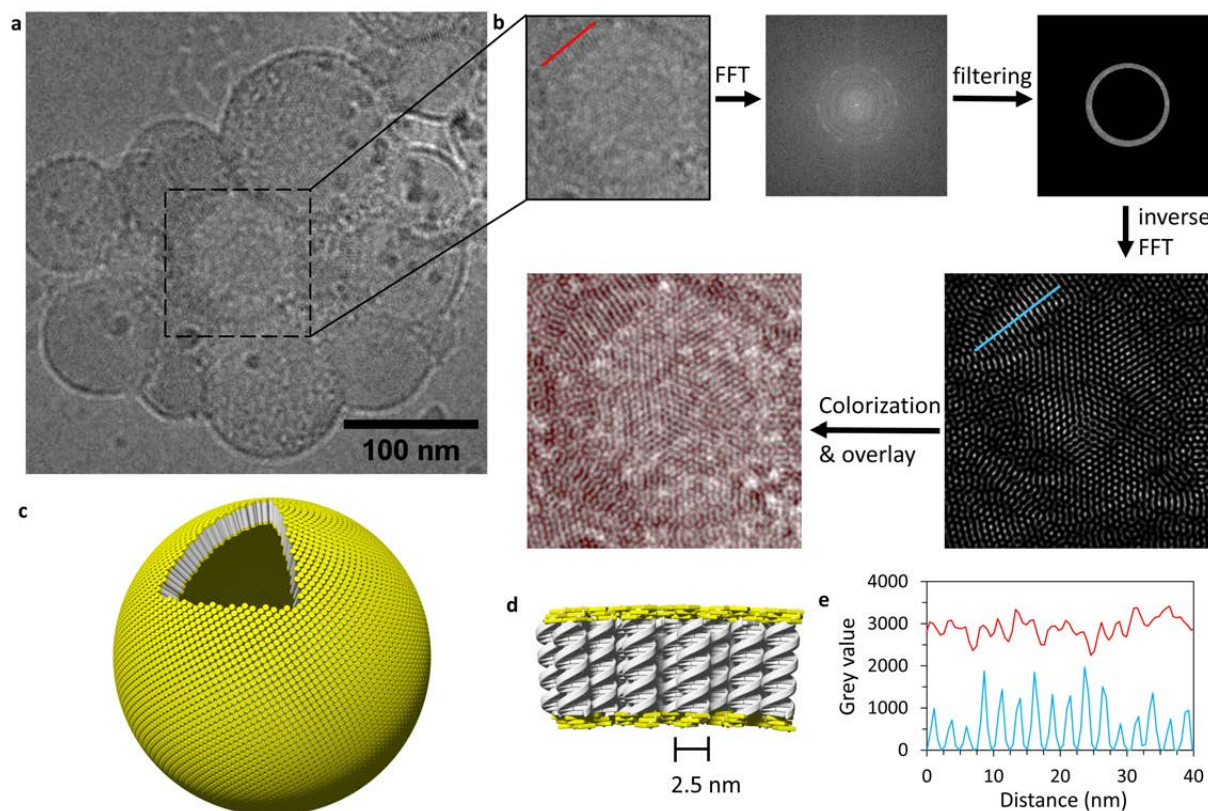


Figure 3.9: (a) Cryo-EM image of self-assembled $\text{O1}^*\text{O2}$, (b) workflow of the image manipulations (FFT, filtering of low and high frequencies, inverse FFT, and colorization & overlay), (c) schematic representation of the columnar packed vesicles, (d) detailed visualization of the packing, and (e) graph of the gray values of the original cryo-EM image (red) and the extracted image (light blue). Conditions: 1 μM $\text{O1}^*\text{O2}$, 10 mM sodium phosphate buffer pH 7.2, 0.03 mM spermine \cdot 4 HCl, 20 vol% ethanol.

In cryo-EM images, an interesting pattern was observed (Figure 3.9a). Therefore, the following image manipulations were performed (Figure 3.9b). First, a fast Fourier transform (FFT) of the image was conducted. The resulting FFT image was then filtered by excluding high and low frequencies. An inverse FFT of the filtered FFT image yielded the underlying pattern. This pattern was then colored and overlaid with the original cryo-EM image. In the graph

of the gray values of the original and extracted image clearly highlights the advantages of the FFT manipulations (Figure 3.9e). The manipulated image reveals the hexagonal pattern with a distance of 2.5 nm present in the original cryo-EM image. The distance of 2.5 nm fits well with the width of a DNA duplex. Assuring the columnar packing of the vesicles as illustrated in the schematic representation of Figure 3.9c and d.

Cryo-EM measurements of **O3*O4** showed comparable multilamellar vesicles (Figure 3.10 left and Figure 3.47). The vesicles formed by **O3*O4** had diameters of 121 ± 29 nm. They were observed in clusters of two or more vesicles. In contrast, cryo-EM images of **O5*O6** showed spherical assemblies without a cavity (Figure 3.10 right and Figure 3.48). These nano-spheres exhibited a diameter of 220 ± 60 nm. Intriguingly, cryo-EM observations of **O5*O6** revealed only single spheres and no agglomeration was observed.

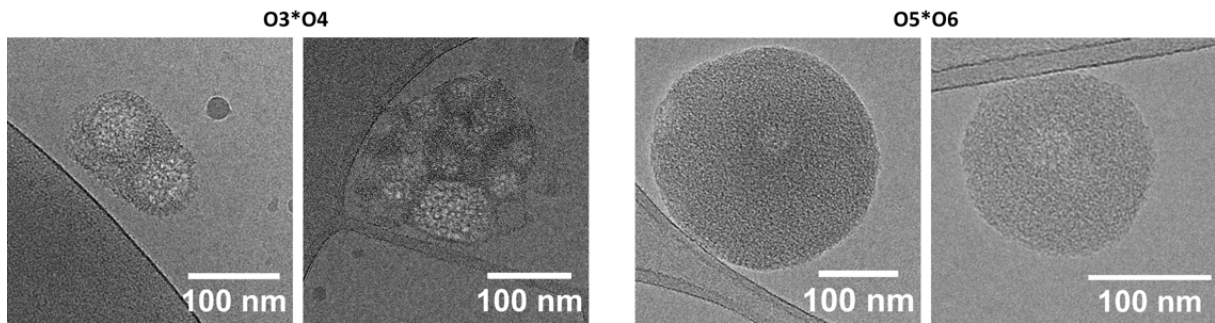


Figure 3.10: Cryo-EM image of self-assembled **O3*O4** (left) and **O5*O6** (right). Conditions: 1 μ M **O3*O4** or **O5*O6**, 10 mM sodium phosphate buffer pH 7.2, 0.03 mM spermine \cdot 4 HCl, 20 vol% ethanol.

3.1.7 Dynamic light scattering

To further characterize the nanostructures dynamic light scattering (DLS) experiments were conducted. Average diameters of 192 ± 60 nm for **O1*O2**, 196 ± 67 nm for **O3*O4**, and 186 ± 62 nm for **O3*O4** were measured (appendix: Table 3.6 and Figure 3.49). These findings are in good agreement with the cryo-EM, TEM, and AFM measurements.

3.1.8 Summary of Self-Assembly

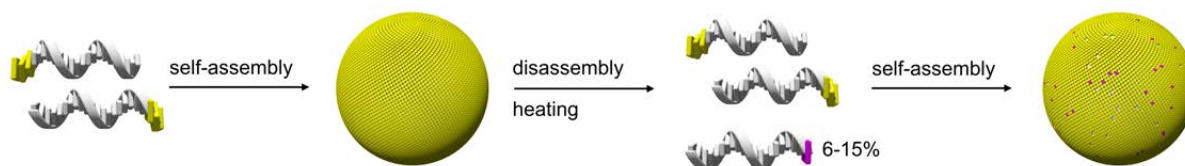
Cryo-EM, AFM, and DLS measurements revealed that **O1*O2**, **O3*O4**, and **O5*O6** self-assemble *via* controlled cooling into nanostructures of a defined size and shape. The diameters of the assemblies determined by the different techniques, are in good agreement (Table 3.2).

Table 3.2: Summary of diameters measured of **O1*O2**, **O3*O4**, and **O5*O6** in cryo-EM, AFM, and DLS experiments. The reported distances are mean values with the corresponding standard deviation, and the number of measurements (n) is indicated in the brackets.

Duplex	Cryo-EM		AFM		DLS	
	Size	Diameter (nm)	Size	Diameter (nm)	Size	Diameter (nm)
O1*O2	105 ± 46	($n = 288$)	108 ± 50	($n = 57$)	192 ± 60	
O3*O4	121 ± 29	($n = 68$)	134 ± 47	($n = 63$)	196 ± 67	
O5*O6	220 ± 60	($n = 36$)	182 ± 55	($n = 61$)	186 ± 62	

3.1.9 Light-Harvesting Experiments

To investigate the light-harvesting properties of the self-assembled nanostructures formed by **O1*O2**, **O3*O4**, and **O5*O6**, we doped them with complementary DNA strands containing a Cy3 (**O9**) or Cy5 (**O11**) acceptor moiety, the two cyanines modified non-complementary single strand **O10** and **O12** serve as controls (Scheme 3.1 and Figure 3.11). Cy3 and Cy5 were chosen as acceptors, as they are reported to be suitable for excitation energy transfer *via* Förster resonance energy transfer (FRET)¹⁷⁶ with pyrene as a donor.^{202–204} One of the main reasons for the excellent suitability is the pronounced spectral overlap of the absorption band of Cy3 and Cy5 and the emission band of the pyrene (Figure 3.12).



Scheme 3.1: Scheme of procedure of light-harvesting measurement: self-assembly of complementary pyrene-DNA conjugates, addition of acceptor modified DNA strand, and reassembly to form the doped nanostructures.

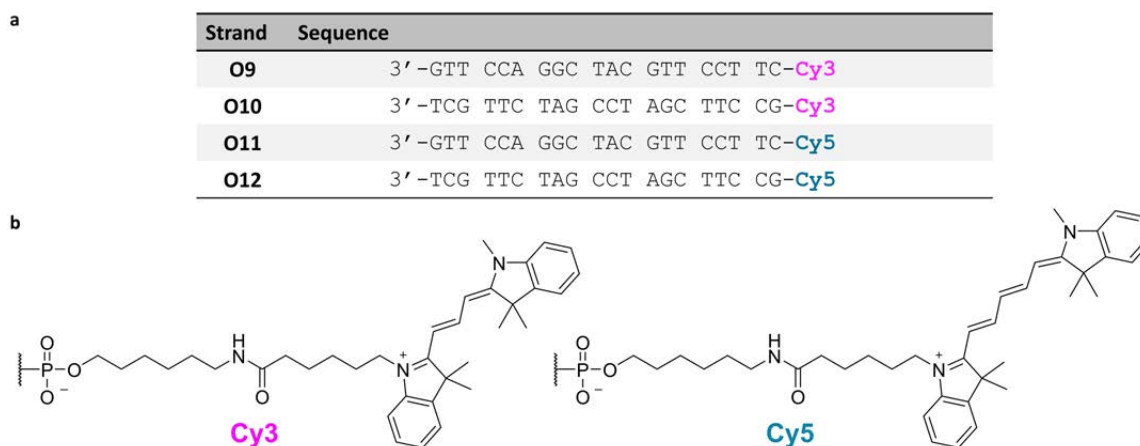


Figure 3.11: (a) Sequence of the complementary Cy3 (**O9**), non-complementary Cy3 (**O10**), complementary Cy5 (**O11**), and non-complementary Cy5 (**O12**), and (b) chemical structure of Cy3 and Cy5 modification.

When assemblies of the pyrene-DNA conjugates are doped with **O9** or **O11**, excitation energy transfers from the pyrene to the cyanine units are expected. To determine this light-harvesting ability of the supramolecular assemblies, fluorescence emission spectroscopy of undoped and Cy3 (Figure 3.13a–c), as well as Cy5 (Figure 3.13d–f) doped nanostructures were compared.

In comparison to undoped assemblies, the fluorescence emission is altered. In doped nanostructures, the pyrene excimer emission is slightly reduced, and a new emission with a maximum around 580 nm emerges. The emission at 580 nm is attributed to the Cy3 emission and indicates an excitation energy transfer from the pyrene donor to the Cy3 acceptor. Interestingly, the Cy3 emission is red-shifted by 8–11 nm when comparing it to the Cy3-modified single strand **O9** (Figure 3.13a–c; shifts tabulated in the appendix Table 3.7). The red shift indicates a strong interaction between the Cy3 dye and the pyrene-DNA conjugate in the supramolecular assembly.

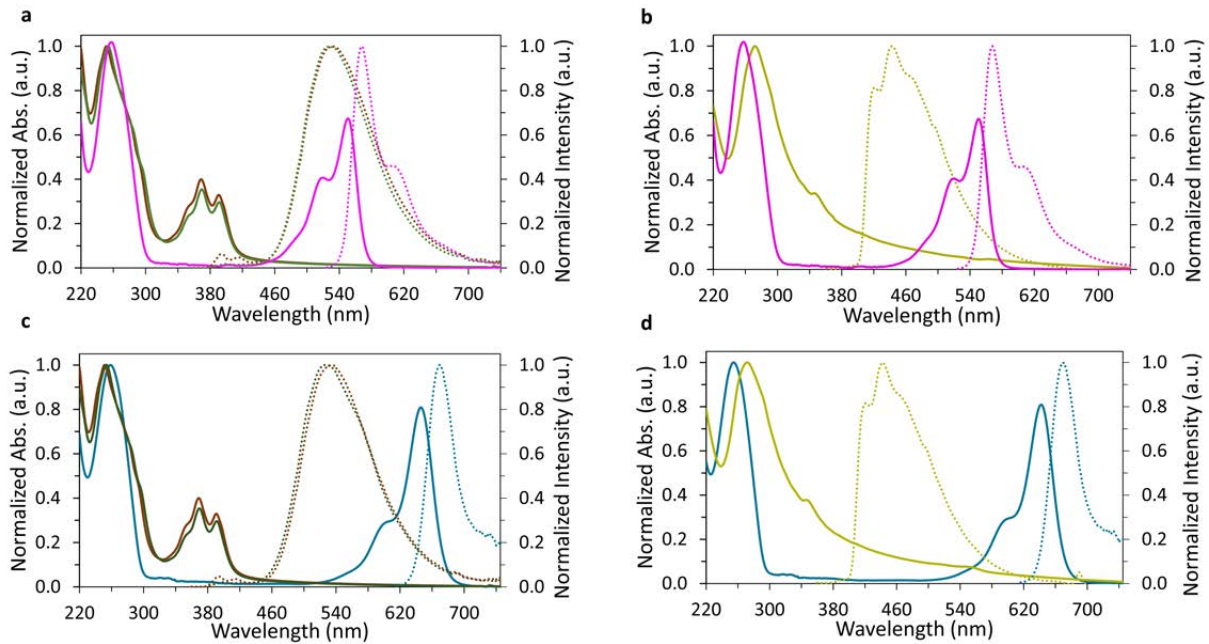


Figure 3.12: Normalized UV-vis absorbance (solid line) and fluorescence emission (dashed) of self-assembled pyrene-DNA conjugates and (a and b) Cy3- and (c and d): (a) **O1*O2** (brown), **O3*O4** (green), and **O9** (pink), (b) **O5*O6** (yellow) and **O9** (pink), (c) **O1*O2** (brown), **O3*O4** (green), and **O11** (cyan) and (d) **O5*O6** (yellow) and **O11** (cyan). Conditions: 1 μM of all single strands, 10 mM sodium phosphate buffer pH 7.2, 0.03 mM spermine \cdot 4 HCl, 20 vol% ethanol, λ_{ex} . 345 nm for pyrene. λ_{ex} . 515 nm for Cy3 and λ_{ex} . 660 nm for Cy5.

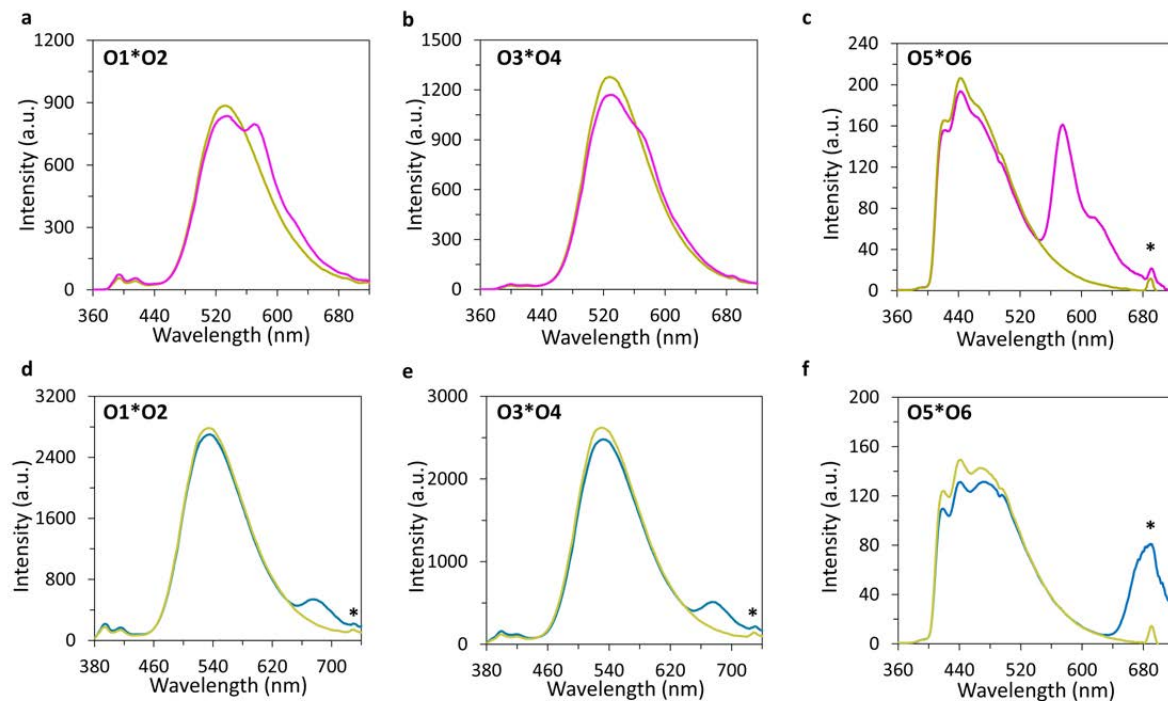


Figure 3.13: Fluorescence emission spectra of undoped (yellow) and Cy3-doped (pink, a–c) or Cy5-doped (cyan, d–f) nanostructures: (a and d) **O1*O2**, (b and e) **O3*O4**, and (c and f) **O5*O6**. Conditions: 1 μM each pyrene-DNA conjugate, (a and b) 0.15 μM **O9**, (c) 0.06 μM **O9**, (d and e) 0.15 μM **O11**, and (f) 0.06 μM **O11**, 10 mM sodium phosphate buffer pH 7.2, 0.03 mM spermine \cdot 4 HCl, 20 vol% ethanol, (a–c) and (f): λ_{ex} . 345 nm, (d) and (e): λ_{ex} . 365 nm, * second-order diffraction.

Excitation energy transfer was also observed in Cy5-doped supramolecular assemblies. After the formation of the nanostructures by controlled cooling from 75 °C to 20 °C, the assemblies were doped with a small quantity of complementary Cy5-modified DNA strand **O11**. Upon excitation of the pyrene units in the doped nanostructures, the pyrene excimer fluorescence is slightly reduced, and a new emission with a maximum around 680 nm distinctive for Cy5 arises. With all three self-assembled pyrene-DNA conjugates, the cyanine fluorescence is red-shifted by 9–13 nm compared to the single strand **O11** (Figure 3.13d–f; shifts tabulated in the appendix Table 3.7). Also, the Cy5 dye seems to interact with the pyrene-DNA conjugate as described with the Cy3 dye. The excitation wavelength was changed from 345 nm to 365 nm with **O1*O2** and **O3*O4** to minimize the interference of the second-order diffraction in the emission spectra.

The integrals of the fluorescence emissions in undoped and **O9**- or **O11**-doped assemblies were compared to gain further information (Table 3.3 and Figure 3.50 in the appendix). Importantly, the total area of fluorescence emission of the assemblies formed by **O1*O2** and **O3*O4** remained comparable after doping. A comparable area of the fluorescence emission is characteristic of quantitative FRET, as in FRET, the increase of the acceptor emission cannot exceed the decrease of the donor emission.^{176,205} In contrast, in assemblies containing **O5*O6**, the total emission area is increased after doping. This increase cannot be explained by excitation energy transfer *via* FRET. Consequently, alternative energy transfer mechanisms beyond FRET, such as quantum coherent energy transfer, are active in these assemblies.

Table 3.3: Fluorescence integrals of **O1*O2**, **O3*O4**, and **O5*O6** with and without **O9** or **O11** and deconvoluted cyanine and pyrene fluorescence emission integrals

Cy3	Fl _{area} ^a			Cy5	Fl _{area} ^b		
	O1*O2	O3*O4	O5*O6		O1*O2	O3*O4	O5*O6
Undoped	100582	138511	20969	Undoped	315783	296152	18396
Cy3 doped	109402	136854	27937	Cy5 doped	324821	295048	20954
Contribution of				Contribution of			
- pyrene	94886	126743	19657	- pyrene	306232	276897	16198
- Cy3	14516	10111	8280	- Cy5	18589	18151	4756

^a Integrals from 360–720 nm

^b Integrals from 380–720 nm except **O5*O6** from 360–720 nm

To gain a better understanding of the excitation energy transfer, we assessed FRET efficiencies, Förster radii, and the number of donors involved in the excitation energy transfer to the acceptor (Table 3.4, equations 8.2, 8.3, and 8.4 in the general methods section chapter 8). Whereas FRET efficiencies represent the probability of an energy transfer event occurring per donor excitation event, and the Förster radii correspond to the donor-acceptor distances at which FRET efficiencies reach 50%.

Table 3.4: FRET efficiencies, Förster radii, and number of pyrene units transferring energy to one cyanine unit of **O9** or **O11** doped **O1*O2**, **O3*O4**, and **O5*O6**.

Cy3 doped	O1*O2	O3*O4	O5*O6	Cy5 doped	O1*O2	O3*O4	O5*O6
FRET Efficiency	5.7%	8.5%	6.3%	FRET Efficiency	3.0%	6.5%	6.8%
Förster Radius	5.5 nm	5.5 nm	3.2 nm	Förster Radius	5.4 nm	5.4 nm	2.7 nm
Pyrenes involved	2.3	3.4	6.3	Pyrenes involved	1.2	2.6	6.8

The FRET efficiencies of the measurements with Cy3 and Cy5 are comparable (3.0%–8.5%). **O1*O2** and **O3*O4** expressed Förster radii of 5.4–5.5 nm with Cy3 and Cy5. Calculations based on the FRET efficiencies proposed that up to 3–4 individual pyrene units participate in FRET. As described in the previous sections, **O1*O2** and **O3*O4** assemble into columnar packed vesicles. In such vesicles, more than three pyrene units are present in the calculated Förster radii. Hence, the data calculated for **O1*O2** and **O3*O4** are in good agreement.

These calculations showed that in nanostructures formed by **O5*O6**, a larger number of pyrene units (6–7 pyrenes) participate in contrast to **O1*O2** and **O3*O4**, despite the smaller Förster radii of 3.2 nm for Cy3 and 2.7 nm for Cy5. However, additional information on the exact assembly of **O5*O6** cannot be derived from the calculations presented here, as **O5*O6** also exhibits non-FRET excitation energy transfer properties, as indicated above. Importantly, it is possible that a portion of the excitation energy in supramolecular assemblies of **O5*O6** is still transferred through FRET. Therefore, the presented data are still significant.

To prove that **O9** and **O11** are incorporated into the supramolecular nanostructures. Control experiments with non-complementary Cy3- (**O10**) and Cy5-modified DNA strands (**O12**) were conducted (Figure 3.14).

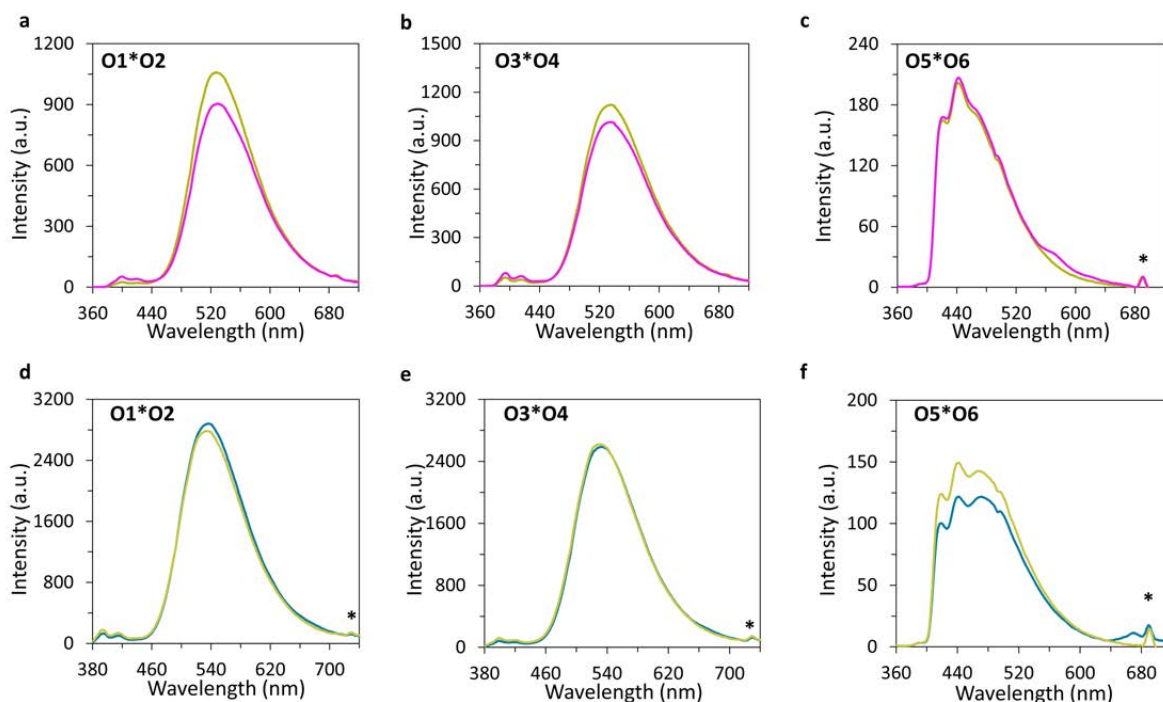


Figure 3.14: Control experiment of nanostructures doped with non-complementary Cy3- and Cy5-modified DNA strands **10** and **12**. Fluorescence emission spectra of undoped (yellow) and Cy3-doped (pink, **a–c**) or Cy5-doped (cyan, **d–f**) nanostructures (**a** and **d**) **O1*O2**, (**b** and **e**) **O3*O4**, and (**c** and **f**) **O5*O6**. Conditions: 1 μM each pyrene-DNA conjugate, (**a** and **b**) 0.20 μM **O10**, (**c**) 0.06 μM **O10**, (**d** and **e**) 0.20 μM **O12**, and (**f**) 0.06 μM **O12**, 10 mM sodium phosphate buffer pH 7.2, 0.03 mM spermine \cdot 4 HCl, 20 vol% ethanol, (**a–c**) and (**f**): λ_{ex} . 345 nm, (**d**) and (**e**): λ_{ex} . 365 nm, * second-order diffraction.

The fluorescence emission of assemblies formed by **O1*O2**, **O3*O4**, and **O5*O6** were compared to **O10**- and **O12**-doped assemblies. The assemblies were doped by adding **O10** and **O12** and subsequent reassembly. As expected, after the addition of the cyanine-modified non-complementary strands, excitation energy transfer was almost absent. Upon excitation of pyrene, a minute emission of Cy3 (574 nm) and Cy5 (668 nm) was observed in assemblies formed by **O5*O6** (Figure 3.14c and f). Proposing that the pyrene units on assemblies formed by **O5*O6** can interact with the cyanine on the non-complementary stands. Whereas pyrenes on assemblies formed by **O1*O2** and **O3*O4** are not accessible for interaction. Furthermore, these experiments highlight that the light-harvesting ability of the supramolecular assemblies is sequence-specific, and the cyanine dyes have to be incorporated into the assembly for an efficient energy transfer.

In another experiment, we determined the accessibility of the nanostructures by assessing the incorporation-ability of a complementary DNA strand containing an acceptor (**O9**) at 20 °C into the nanostructures. Assemblies formed by **O5*O6** were evaluated in these experiments, as the visibility of the Cy3 emission is superior in nanostructures formed by **O5*O6** to **O1*O2** and **O3*O4**. To determine accessibility and addressability fluorescence emission measurement of the assemblies formed by **O5*O6** before doping, after doping (at 20 °C), and after thermal reassembly (reheating to 75 °C, followed by reassembly by cooling with a gradient of 0.5 °C·min⁻¹ to 20 °C) were compared (Figure 3.15). Excitation energy transfer from pyrene to Cy3 was observed before the reassembly. However, upon reassembly, the fluorescence band attributed to Cy3 increased even more. Hence, directly after doping assemblies of **O5*O6** with **O9**, a part of the Cy3-modified strand was incorporated (30–40%). These results suggest that the supramolecular assemblies are partially accessible at 20 °C, but complete incorporation is only possible upon reassembly. **O1*O2** and **O3*O4** showed similar results. The increase of Cy3 emission was minor after the addition and more pronounced upon reassembly (illustrated in the appendix Figure 3.51). The efficiency of the excitation energy transfer can be increased by reassembling the supramolecular assemblies to fully in-cooperated the Cy3-modified DNA strands.

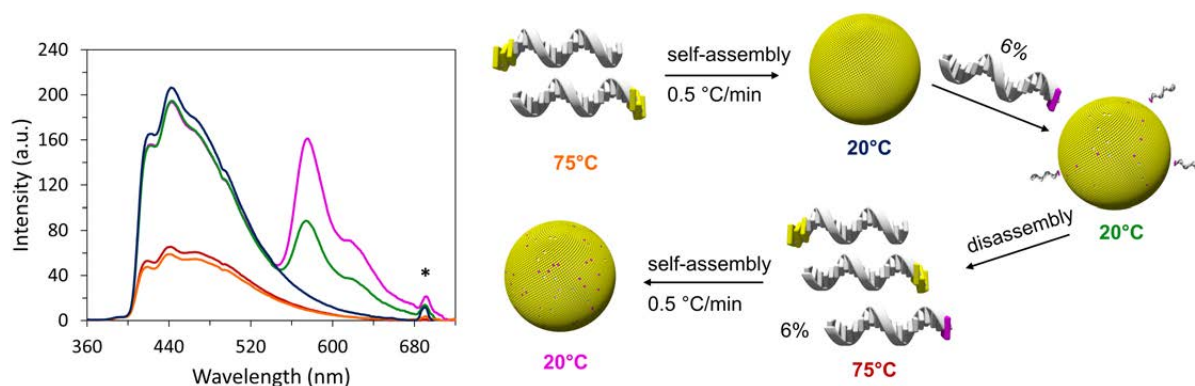


Figure 3.15: Fluorescence emission spectra of **O5*O6** at 75 °C (orange), after controlled self-assembly (blue), after the addition of 6% **O9** at 20 °C (green), after the re-heating to 75 °C (red), and after reassembly by controlled cooling to 20 °C (pink). Conditions: 1 μM **O5*O6** (+ 0.06 μM **O9**), 10 mM sodium phosphate buffer pH 7.2, 0.03 mM spermine · 4 HCl, 20 vol% ethanol, λ_{ex} . 345 nm.

To better understand the excitation energy transfer in **O5*O6**, further light-harvesting experiments were conducted. The effect of doping assemblies of **O5*O6** with different amounts of **O5*O9** was analyzed by UV-vis and fluorescence spectroscopy (Figure 3.16). As expected, the subsequent increase of the concentration of **O5*O9** from 0.010 μM to 0.324 μM led to an increase of the absorption band of DNA and pyrene at 270 nm, as well as the band of

cyanine with a maximum at 557 nm (Figure 3.16 left). To determine if excitation energy is transferred from pyrene to Cy3 in the assemblies, fluorescence emission spectra were conducted at the different concentrations of added **O5*O9**. Excitation of pyrene at 345 nm led to pyrene emission (400–600 nm) and Cy3 emission (540–720 nm) at all concentrations. Interestingly, increasing the concentration of **O5*O9** led to the rise of Cy3 emission, whereas the pyrene emission remained almost unchanged (Figure 3.16 right).

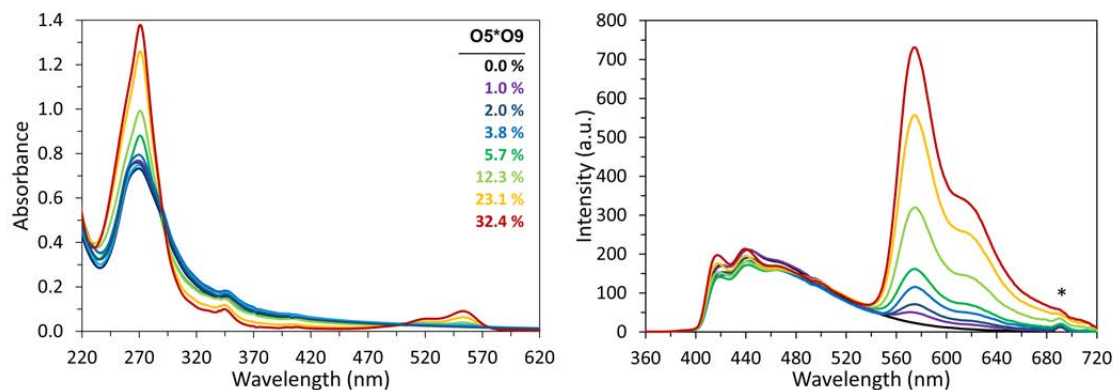


Figure 3.16: UV-vis spectra (left) and fluorescence emission spectra (right) of self-assembled **O5*O6** at 20 °C with the addition of different amounts of **O5*O9** (0.0–32.4%). Conditions: 1 μ M **O6**, 1–1.48 μ M **O5**, 0–0.48 μ M **O9**, 10 mM sodium phosphate buffer pH 7.2, 0.03 mM spermine \cdot 4 HCl, 20 vol% ethanol, λ_{ex} . 345 nm, * second-order diffraction.

As a control experiment, fluorescence emission spectra of the added amounts of **O5*O9** were conducted in parallel (depicted in the appendix Figure 3.52). Exciting the pyrene units in **O5*O9** leads to an excitation energy transfer to the Cy3 (576 nm). To determine the influence of the supramolecular assembly, these spectra and the emission spectra of **O5*O6** were deduced from the measurements of the doped experiments. The resulting fluorescence emissions are denoted here as extracted additional fluorescence.

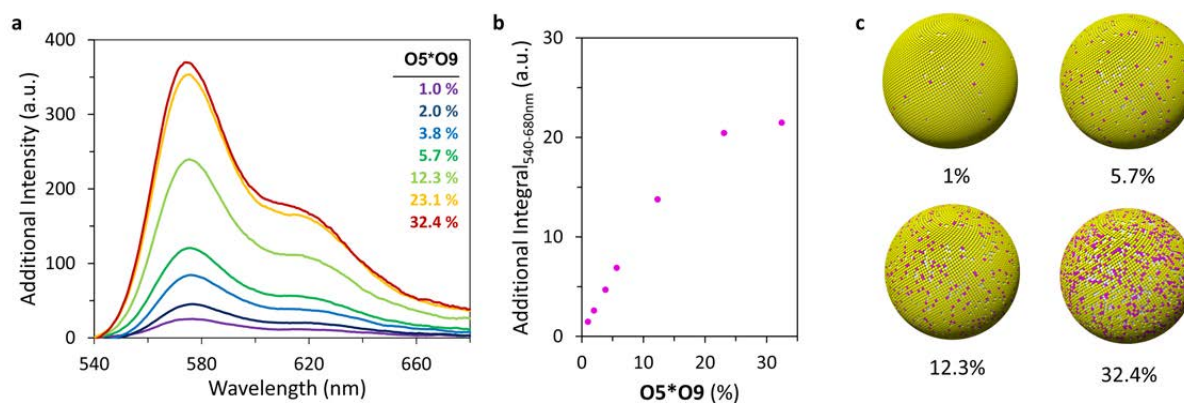


Figure 3.17: (a) additional Cy3 emission after the addition of 1.0–32.4% **O5*O9**, (b) integrals of the additional Cy3 emissions depending on the addition of **O5*O9** and (c) schematic illustration of the nanostructures formed by pyrene-DNA conjugates (DNA gray, pyrene yellow) with different amount of Cy3 (pink).

The extracted additional fluorescence emissions of the supramolecular assembled **O5*O6** containing 1.0% to 32.4% **O5*O9** were analyzed (Figure 3.17a). The extracted additional fluorescence emissions were integrated and plotted against the doping concentrations (Figure 3.17b). The addition of **O5*O9** leads to Cy3 emission, increasing linearly at low doping

concentrations (below 6%) and plateauing at 32.4%. Plateauing of the additional fluorescence arises as all pyrene units participate in the EET. Between 6% and 32.4% of doping, the increase is not linear, as the Cy3 units are unevenly distributed on the assemblies as the acceptors are randomly distributed on the assemblies some Cy3 congest. The uneven distribution leads to a limited amount of pyrene (donor) available per Cy3 (acceptor), as illustrated in the schematic representation below (Figure 3.17c). By extrapolating the linear increase (below 6%) with the maximal additional integral (at 32.4%), an optimal doping of 18.5% was calculated. If the Cy3-containing strands were perfectly distributed on the vesicle, every single pyrene unit would contribute to the emission of Cy3 at 18.5% $\mathbf{O5*O9}$ per $\mathbf{O5*O6}$. The presented data proposes that a maximum of 5–6 $\mathbf{O5*O6}$ duplexes can excite one Cy3. In other words, 33–39 individual pyrenes participate in the excitation energy transfer to one Cy3.

These results are in contrast to the calculations with the FRET model described above, which states that only 6–7 individual pyrene units participate in the excitation energy transfer. Further proving that the excitation energy is not only transferred *via* FRET. In summary, these results show that the supramolecular assemblies formed by the pyrene-DNA conjugate function as light-harvesting complexes, and inside the supramolecular assembly, the excitation energy is transferred from 33–39 individual pyrene units to Cy3.

3.2 Conclusions and Outlook

In this chapter, the self-assembly of amphiphilic 3'-end modified pyrene-DNA conjugates into nanostructures has been demonstrated. Pyrene-DNA conjugates bearing three dialkynyl pyrene isomers have been compared, all three self-assembled into nanostructures with diameters between 50–300 nm. The sizes and morphologies have been confirmed by AFM, DLS, TEM, and cryo-EM. The morphologies proved to be dependent on the pyrene isomer. The pyrene-DNA conjugates with 1,6- and 1,8-dialkynyl pyrene isomers assemble into columnar-packed multilamellar vesicles. In contrast, spherical aggregates are formed by the 2,7-dialkynyl pyrene isomer.

Nanostructures formed by all three pyrene isomers show light-harvesting properties when doping them with a complementary Cy3- or Cy5-modified DNA strand. Upon excitation of the pyrene units, they transfer their excitation energy to the respective cyanine acceptor. The light-harvesting properties of the pyrene-DNA conjugate bearing the 2,7-dialkynyl pyrene have been studied in more detail. Interestingly, a strong increase in the cyanine emission combined with a minute decrease in the pyrene emission has been observed after the incorporation of the dye. Therefore, the excitation energy transfer cannot be explained only by FRET, but other energy transfer mechanisms are also involved, *i.e.*, coherent energy transfer mechanisms. The experiments presented in this chapter showed that the 33-39 individual pyrenes or 11-13 DNA strands in the supramolecular assembly transfer energy to one Cy3 unit.

Other excitation energy acceptors, then Cy3 and Cy5, could be evaluated. Two-pulse fluorescence-detected coherent spectroscopy and four-pulse fluorescence-detected coherent spectroscopy could help to determine if the excitation energy transfer is proceeding *via* quantum coherent energy transfer.²⁰⁶

The formed assemblies could also be evaluated for drug-delivery applications. The incorporation of drug molecules into the vesicular cavity could be tested. A key challenge for incorporating drug molecules is the annealing of the vesicles, as the drug molecules could impact the self-assembly of the supramolecular polymers. Small hydrophobic drug molecules may be most promising, as they could be integrated into the assembly via interaction with the hydrophobic pyrene sticky ends.

In this work, we placed three pyrene units on each side of the pyrene-DNA duplex. It would be interesting to elucidate the required quantity of pyrene units necessary in the overhangs for successful self-assembly. In the following chapter, chapter 4, pyrene-DNA conjugates bearing one, two, and three pyrenes on each side are compared.

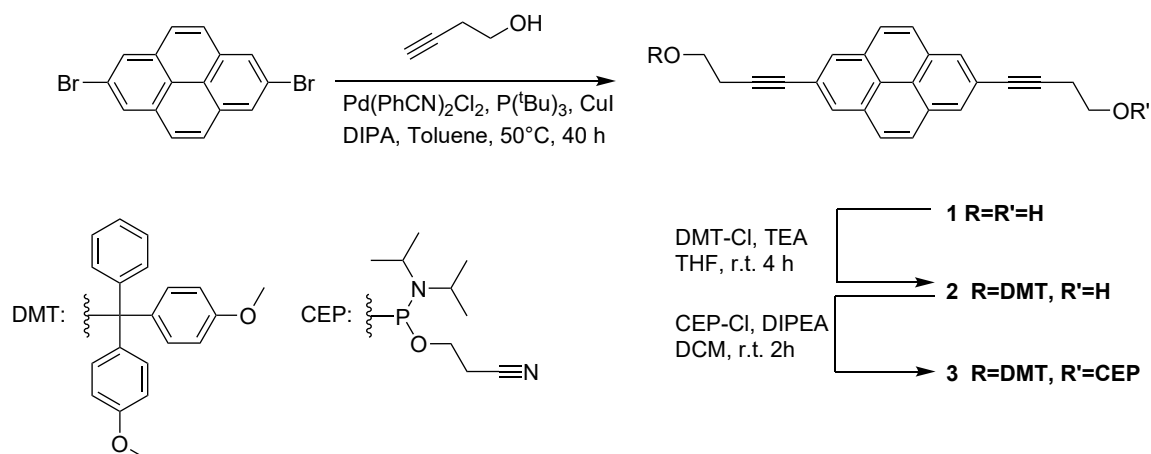
3.3 Appendix - Chapter 3

First, the organic synthesis of 2,7-, 1,6- and 1,8-dialkynyl pyrene phosphoramidites is described, and the corresponding NMR spectra are depicted. Then, the solid phase oligomer synthesis and purification of the pyrene-DNA conjugates are described. After that, additional spectroscopic measurements and supplementary microscopic measurements (AFM and cryo-EM images) are depicted. Finally, additional light-harvesting experiments are displayed.

3.3.1 Organic Synthesis

3.3.1.1 Synthesis 2,7-Substituted Pyrene Phosphoramidite

The 2,7-dialkynyl pyrene phosphoramidite **3** was synthesized in three steps according to published procedures.¹⁹ In the first step, the commercially available 2,7-dibromopyrene was functionalized with 3-butynol through palladium-catalyzed Sonogashira-coupling forming the diol **1** in good yield. In the second step, **1** was tritylated on one side using one equivalent of 4,4'-dimethoxytrityl chloride (DMT-Cl). The mono-protected **2** was isolated in an acceptable yield. In the third step, the **2** was reacted at the remaining alcohol with 2-cyanoethyl N,N-bis(1-methylethyl)phosphoramidite chloride (CEP-Cl), yielding the final product **3**.



Scheme 3.2: A general overview of the synthesis of pre-cursor **1** and **2** and pyrene phosphoramidite **3**.

3.3.1.1.1 4,4'-(pyrene-2,7-diyl)bis(but-3-yn-1-ol) (**1**)

2,7-Dibromopyrene (0.828 g, 2.300 mmol, 1.00 eq.), Pd(PhCN)₂Cl₂ (0.053 g, 0.138 mmol, 0.06 eq.), and CuI (0.026 g, 0.138 mmol, 0.06 eq.) were placed in a three-necked round-bottom flask which was purged with argon three times. To the reaction mixture, anhydrous toluene (50 ml), DIPA (6.7 ml), and a 1 M solution of tri-tert-butylphosphine in toluene (0.36 ml) were added with syringes, and the reaction mixture was heated to 50 °C under vigorous stirring. After 6 h, some solids were formed in the reaction mixture. Therefore, 15 ml of anhydrous THF was added with a syringe. After that, the resulting reaction mixture was left stirring for another 26 h. After letting the reaction cool down to r.t. and removing all solvents by rotary evaporator, the residue was subjected to column chromatography (silica gel (65g), hexane/ethyl acetate 4:6). After that, the solvents of the fraction containing the product were evaporated, the solid residue was redissolved in a minimum amount of DCM and precipitated in ice-cold HPLC grade hexane. The precipitate was filtered off and dried under high vacuum. Finally, the product **1** was isolated as a light-yellow powder in reasonable yield (414 mg, 53%).

^1H NMR (300 MHz, DMSO- d_6): δ 8.32 (s, 4H), 8.17 (s, 4H), 4.98 (t, $J = 5.6$ Hz, 2H), 3.72 – 3.65 (m, 4H), 2.68 (t, $J = 6.8$ Hz, 4H).

3.3.1.1.2 4-(7-(4-(bis(4-methoxyphenyl)(phenyl)methoxy)but-1-yn-1-yl)pyren-2-yl)but-3-yn-1-ol (**2**)

4,4'-(pyrene-2,7-diyl)bis(but-3-yn-1-ol) (**1**) (0.152 g, 0.450 mmol, 1.0 eq.) was submitted to a three-necked round-bottom flask which was purged with argon three times. After that, anhydrous THF (6 ml) and argon-bubbled TEA (1.3 ml) were added with syringes. Then, 4,4'-dimethoxytrityl chloride (152 g, 0.450 mmol, 1.0 eq.) was added in two portions. The second addition was done after letting the reaction mixture stir at r.t. for 30 min. After the second addition, the resulting reaction mixture was left stirring for another 3 h and 30 min. The solvent was reduced to approximately 10 ml *in vacuo*, and 40 ml of ethyl acetate was added. The reaction mixture was washed with aq. 10% citric acid (3×50 mL), with aq. sat. NaHCO_3 (2×50 ml), once with brine (100 ml), dried over MgSO_4 , filtered, and concentrated *in vacuo*. The residue was purified by gradient column chromatography (silica gel (30 g), hexane/ethyl acetate/TEA 2:1:0.01 to 1:1:0.01 to 1:2:0.01) to yield product **2** as a white foam (111 mg, 39%).

^1H NMR (300 MHz, DMSO- d_6): δ 8.32 (s, 4H), 8.17 (s, 4H), 7.49 (d, $J = 7.2$ Hz, 2H), 7.37 – 7.30 (m, 6H), 7.25 (d, $J = 7.2$ Hz, 1H), 6.91 (d, $J = 8.9$ Hz, 4H), 4.98 (t, $J = 5.6$ Hz, 1H), 3.73 (s, 6H), 3.71 – 3.64 (m, 2H), 3.24 (t, $J = 6.5$ Hz, 2H), 2.84 (t, $J = 6.5$ Hz, 2H), 2.68 (t, $J = 6.8$ Hz, 2H).

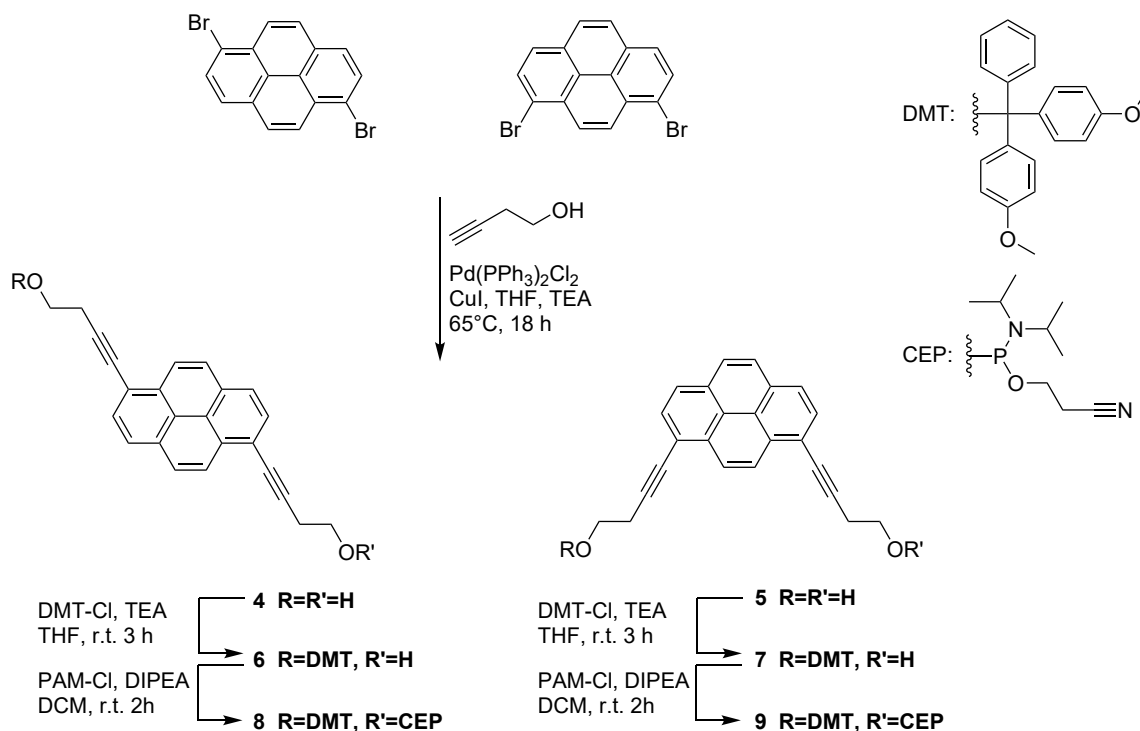
3.3.1.1.3 4-(7-(4-(bis(4-methoxyphenyl)(phenyl)methoxy)but-1-yn-1-yl)pyren-2-yl)but-3-yn-1-yl (2-cyanoethyl) di-tert-butylphosphoramidite (**3**)

The DMT-protected pyrene **2** (0.423 g, 0.660 mmol, 1.0 eq.) was loaded into a round-bottom flask which was purged with argon three times. After that, anhydrous DCM (5.0 ml) and N,N -diisopropylethylamine (DIPEA) (0.57 ml, 3.300 mmol, 5.0 eq.) were added with syringes. Then, 2-cyanoethyl N,N -diisopropylchlorophosphoramidite (CEP) (0.18 ml, 0.726 mmol, 1.1 eq.) was slowly added with a syringe and left stirring vigorously at r.t. for 2.5 h. The solvent was reduced *in vacuo*, and the solid residue was purified by column chromatography (silica gel (15 g), hexane/ethyl acetate/TEA 2:1:0.01, 1:1:0.01, 1:2:0.01) to yield product **3** as a white foam (513 mg, 92%).

^1H NMR (300 MHz, CDCl_3): δ 8.19 (q, $J = 2.0$ Hz, 4H), 7.98 (d, $J = 1.5$ Hz, 4H), 7.56 (d, $J = 7.7$ Hz, 2H), 7.44 (d, $J = 8.7$ Hz, 4H), 7.29 (t, $J = 7.7$ Hz, 2H), 7.25 – 7.19 (m, 1H), 6.84 (d, $J = 8.7$, 4H), 4.04 – 3.79 (m, 4H), 3.78 (s, 6H), 3.69 – 3.60 (m, 2H), 3.39 (t, $J = 6.8$, 2H), 2.88 – 2.78 (m, 4H), 2.67 (td, $J = 6.5, 3.0$ Hz, 2H), 1.23 (t, $J = 6.8$, 11H). ^{31}P NMR (121 MHz, CDCl_3): δ 248.22.

3.3.1.2 Synthesis 1,6 and 1,8-Substituted Pyrene Phosphoramidite

The synthesis of 1,6-pyrene phosphoramidite **8** and 1,8-pyrene phosphoramidite **9** was adapted from published procedures (Scheme 3.3).¹⁸⁹ In the first step, a mixture of 1,6- and 1,8-dibromopyrene was functionalized with 3-butyn-1-ol through palladium-catalyzed Sonogashira-coupling, forming a mixture of **4** and **5** that were separated on multiple silica column chromatography in acceptable yield. In the second step, **4** respectively **5** were on one side tritylated using one equivalent of 4,4'-dimethoxytrityl chloride (DMT-Cl). The mono-protected pyrenes **6** and **7** were isolated in acceptable yield. In the third step, the mono-protected **6** and **7** were reacted with 2-cyanoethyl N,N-bis(1-methylethyl)phosphoramidite chloride (CEP-Cl). The third reaction yielded the final products phosphoramidite **8** and **9**.



Scheme 3.3: Synthesis of 1,6-pyrene phosphoramidite **8** and 1,8-pyrene phosphoramidite **9**.

3.3.1.2.1 4,4'-(pyrene-1,6-diyl)bis(but-3-yn-1-ol) (**4**) and 4,4'-(pyrene-1,8-diyl)bis(but-3-yn-1-ol) (**5**)

A mixture of 1,8- and 1,6-dibromopyrene (3.00 g, 8.33 mmol, 1.00 eq.) was submitted to an argon-flushed round-bottom flask. Then, freshly degassed TEA (40 ml) and THF (80 ml) were added by syringes, and the reaction mixture was heated to 65 °C. After That, 3-butyn-1-ol (2.5 ml, 33.33 mmol, 4.00 eq.) was submitted to the reaction mixture by syringe, followed by the addition of copper iodine (0.063 g, 0.33 mmol, 0.04 eq.) and Pd(PPh₃)₂Cl₂ (0.46 g, 0.21 mmol, 0.025eq.) resulting in a black reaction mixture that was left stirring at reflux for 18 h. After cooling to r.t., the reaction mixture was filtered over celite. The orange reaction mixture obtained was concentrated *in vacuo*, dissolved in ethyl acetate (100 ml), washed with aq. 10% citric acid (3×50 ml), aq. sat. NaHCO₃ (2×50 ml), once with brine (100 ml), dried over MgSO₄, filtered, and concentrated *in vacuo*. The solid residue was absorbed to silica and purified by gradient column chromatography (silica gel (220 g), DCM/toluene/isopropanol 87:10:3 to 85:10:5 to 80:10:10), the chromatography was repeated four times, affording product **4** and **5** as light-yellow powders (757.6 mg, 27% and 790.1 mg, 28%).

4: ^1H NMR (300 MHz, $\text{DMSO-}d_6$): δ 8.53 (d, $J = 9.0$ Hz, 2H), 8.29 (d, $J = 8.0$ Hz, 2H), 8.28 (d, $J = 9.0$ Hz, 2H), 8.14 (d, $J = 8.0$ Hz, 2H), 5.05 (t, $J = 5.5$ Hz, 2H), 3.76 (dt, $J = 6.7, 5.5$ Hz, 4H), 2.81 (t, $J = 6.7$ Hz, 4H).

5: ^1H NMR (300 MHz, $\text{DMSO-}d_6$): δ 8.62 (s, 2H), 8.28 (d, $J = 8.0$ Hz, 2H), 8.21 (s, 2H), 8.14 (d, $J = 8.0$ Hz, 2H), 5.05 (t, $J = 5.5$ Hz, 2H), 3.77 (dt, $J = 5.5$ Hz, 6.7, 4H), 2.82 (t, $J = 6.7$ Hz, 4H).

3.3.1.2.2 4-(6-(4-(bis(4-methoxyphenyl)(phenyl)methoxy)but-1-yn-1-yl)pyren-1-yl)but-3-yn-1-ol (**6**)

4,4'-(pyrene-1,6-diyl)bis(but-3-yn-1-ol) (0.677 g, 2.00 mmol, 1.0 eq.) was submitted to a three-necked round-bottom flask which was purged with argon three times, followed, by addition of freshly degassed TEA (10 ml) and THF (50 ml) by syringe. After that, DMT-Cl (0.678 g, 2.00 mmol, 1.0 eq.) was added in two portions (second addition after 30 min) to the vigorously string reaction mixture, and it was left stirring at r.t. for 3 h. Then, the reaction was worked up according to the procedure described for the 2,7-dialkynly pyrene diol **2** (3.3.1.1.2) to yield product **6** as a yellow foam (539 mg, 42%).

^1H NMR (300 MHz, $\text{DMSO-}d_6$): δ 8.54 (2 \times d, $J = 9.0, 9.0$ Hz, 2H), 8.34 – 8.26 (m, 3H), 8.19 – 8.11 (m, 3H), 7.55 – 7.49 (m, 2H), 7.41 – 7.19 (m, 7H), 6.93 – 6.85 (m, 4H), 5.05 (t, $J = 5.6$ Hz, 1H), 4.03 (d, $J = 7.1$ Hz, 1H), 3.76 (dt, $J = 5.6, 6.6$ Hz, 2H), 3.72 (s, 6H), 3.29 (t, superimposed with water, $J = 6.1$ Hz, 1H), 2.96 (t, $J = 6.1$ Hz, 2H), 2.81 (t, $J = 6.7$ Hz, 2H).

3.3.1.2.3 4-(8-(4-(bis(4-methoxyphenyl)(phenyl)methoxy)but-1-yn-1-yl)pyren-1-yl)but-3-yn-1-ol (**7**)

4,4'-(pyrene-1,8-diyl)bis(but-3-yn-1-ol) (0.677 g, 2.00 mmol, 1.0 eq.) was submitted to an argon-flushed three-necked round-bottom flask. After that, freshly degassed TEA (10 ml) and THF (50 ml) were added by syringe. Then, DMT-Cl (0.678 g, 2.00 mmol, 1.0 eq.) was added in two portions (second addition after 30 min) to the vigorously string reaction mixture, and it was left stirring at r.t. for 3 h, followed by the worked-up of the reaction mixture according to the procedure described for the 2,7-dialkynly pyrene diol **2** (3.3.1.1.2) yielding the product **6** as a yellow foam (544.4 mg, 43%).

^1H NMR (300 MHz, $\text{DMSO-}d_6$): δ 8.65 (d, $J = 9.3$ Hz, 1H), 8.51 (d, $J = 9.3$ Hz, 1H), 8.31 (d, $J = 8.1$ Hz, 1H), 8.28 (d, $J = 7.9$ Hz, 1H), 8.22 (s, 2H), 8.16 (d, $J = 7.9$ Hz, 1H), 8.14 (d, $J = 8.1$ Hz, 1H), 7.50 – 7.57 (m, 2H), 7.41 – 7.23 (m, 7H), 6.93 – 6.86 (m, 4H), 5.05 (t, $J = 5.6$ Hz, 1H), 3.77 (dt, $J = 5.6, 6.8$ Hz, 2H), 3.72 (s, 6H), 3.29 (s, 2H), 2.96 (t, $J = 6.1$ Hz, 2H), 2.82 (t, $J = 6.8$ Hz, 2H).

3.3.1.2.4 4-(6-(4-(bis(4-methoxyphenyl)(phenyl)methoxy)but-1-yn-1-yl)pyren-1-yl)but-3-yn-1-yl (2-cyanoethyl) di-tert-butylphosphoramidite (8)

The DMT-protected pyrene **6** (0.423 g, 0.660 mmol, 1.0 eq.) was put into an argon-flushed three-necked round-bottom flask. After that, anhydrous DCM (5.0 ml) and N,N-diisopropylethylamine (DIPEA) (0.57 ml, 3.300 mmol, 5.0 eq.) were added by syringes. Then, 2-cyanoethyl N,N-diisopropylchlorophosphoramidite (CEP) (0.18 ml, 0.726 mmol, 1.1 eq.) was slowly added with a syringe and left stirring vigorously at r.t. for 2.5 h. The solvent was reduced *in vacuo*, and the solid residue was purified by column chromatography (silica gel (17 g), hexane/ethyl acetate/TEA 2:1:0.01, 1:1:0.01, 1:2:0.01) to yield product **8** as a yellow foam (512 mg, 92%).

R_f 0.49 (silica gel hexane/ethyl acetate/TEA 2:1:0.01); ^1H NMR (300 MHz, CDCl_3): δ 8.60 and 8.58 (2×d, $J = 9.1, 9.1$ Hz, 2H), 8.15 – 8.05 (m, 5H), 7.99 (d, $J = 9.1$ Hz, 1H), 7.60 – 7.54, 7.34 – 7.28 7.24 – 7.18 and 6.87 – 6.79 (4×m, 13H), 4.16 – 3.60 and 3.77 (m and s, 12H), 3.45 (t, $J = 6.7$ Hz, 3H), 2.98 (t, $J = 6.7$ Hz, 2H), 2.93 (t, $J = 7.0$ Hz, 2H), 2.69 – 2.60 (m, 2H), 1.26 – 1.19 (m, 12H); ^{31}P NMR (121.5 MHz, CDCl_3): δ 184.2.

3.3.1.2.5 4-(8-(4-(bis(4-methoxyphenyl)(phenyl)methoxy)but-1-yn-1-yl)pyren-1-yl)but-3-yn-1-yl (2-cyanoethyl) di-tert-butylphosphoramidite (9)

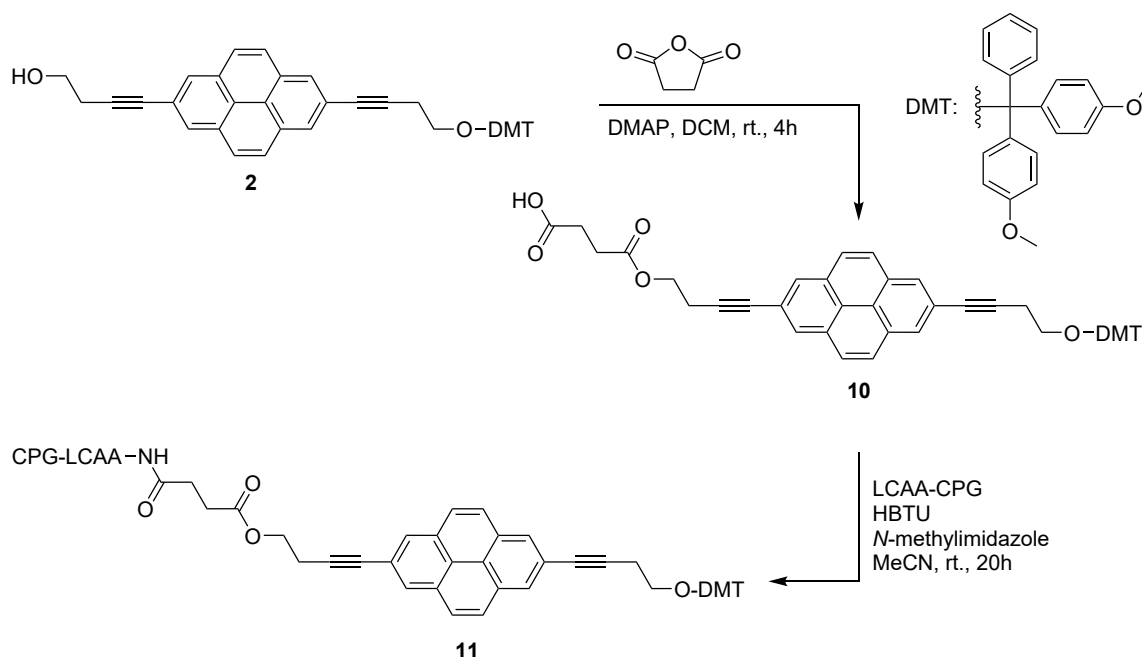
The DMT-protected pyrene **7** (0.310 g, 0.48 mmol, 1.0 eq.) was put into an argon-flushed three-necked round-bottom flask. After that, anhydrous DCM (5.0 ml) and N,N-diisopropylethylamine (DIPEA) (0.42 ml, 2.42 mmol, 5.0 eq.) were added by syringes. Then, 2-cyanoethyl N,N-diisopropylchlorophosphoramidite (CEP) (0.13 ml, 0.53 mmol, 1.1 eq.) was slowly added with a syringe and left stirring vigorously at r.t. for 2.5 h. The solvent was reduced *in vacuo*, and the solid residue was purified by column chromatography (silica gel (17 g), hexane/ethyl acetate/TEA 2:1:0.01, 1:1:0.01, 1:2:0.01) to yield product **9** as a yellow foam (419 mg, quantitative).

R_f 0.59 (silica gel hexane/ethyl acetate/TEA 2:1:0.01); ^1H NMR (300 MHz, CDCl_3): δ 8.66 (d, $J = 9.2$ Hz, 1H), 8.58 (d, $J = 9.2$ Hz, 1H), 8.16 – 8.04 (m, 4H), 8.02 (s, 2H), 7.62 – 7.53, 7.51 – 7.40, 7.35-7.17 and 6.88 – 6.79 (4×m, 13H), 4.15 – 3.68 (m and s, 12H), 3.45 (t, $J = 6.8$ Hz, 2H), 2.99 and 2.93 (2×t, $J = 6.8$ and 6.7 Hz, 4H), 2.67 - 2.58 (m, 2H), 1.23 and 1.21 (2×d, $J = 4.1$ and 4.1 Hz, 12H); ^{31}P NMR (121.5 MHz, CDCl_3): δ 184.3.

3.3.1.3 Synthesis of Pyrene-Modified Solid-Support

The synthesis of 2,7-, 1,6-, and 1,8-solid-support **11**, **13**, and **15** (Scheme 3.4, Scheme 3.5, and Scheme 3.6) was adapted from published procedure.¹⁹

3.3.1.3.1 2,7-Pyrene-Modified Solid-Support (**11**)

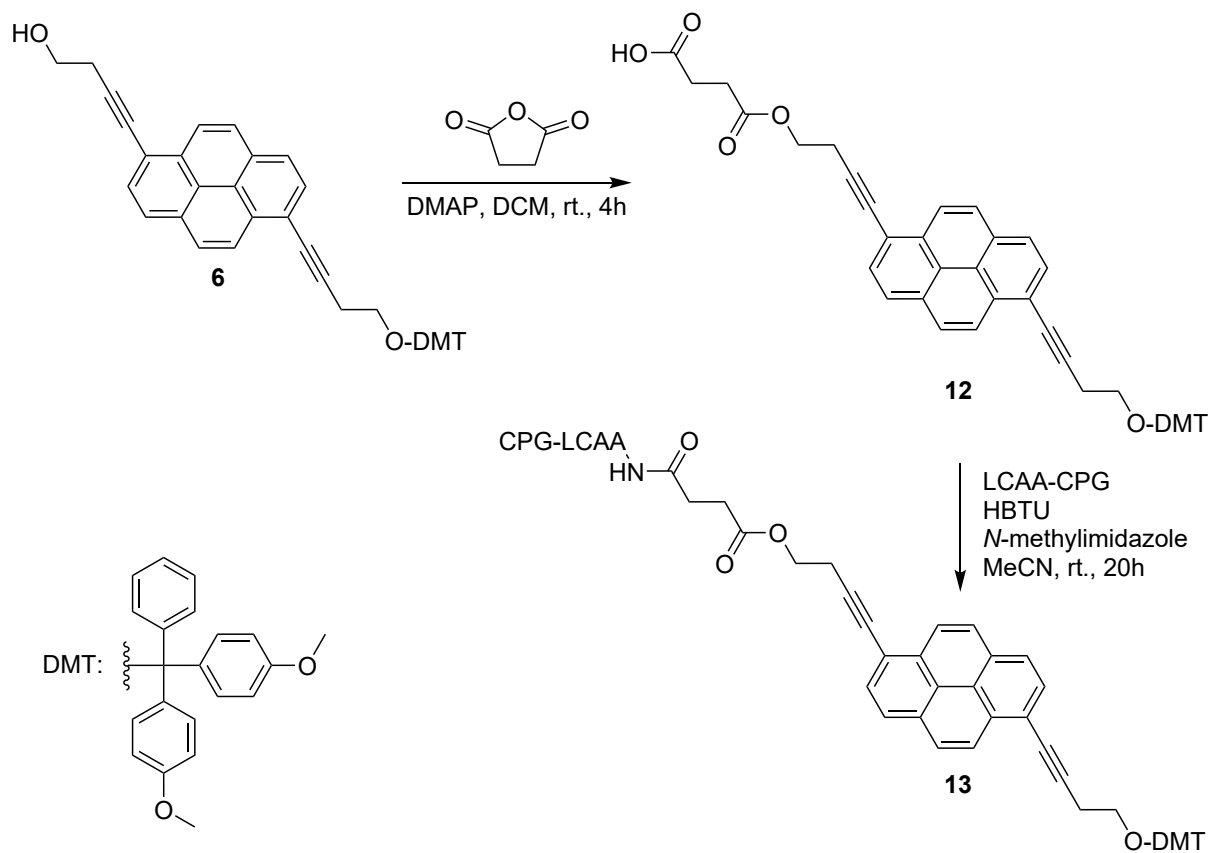


Scheme 3.4: Synthesis of 2,7-pyrene-modified solid-support **11**.

DMT-protected pyrene **2** (0.051 g, 0.08 mmol, 1 eq.) was dissolved in anhydrous DCM (0.4 ml). Succinic anhydride (0.012 g, 0.12 mmol, 1.5 eq.) and DMAP (0.015 g, 0.12 mmol, 1.5 eq.) were added and the reaction mixture was stirred at r.t. for 4 h. Then, the reaction mixture was diluted with 10 ml of DCM, and the organic layer was washed once with aq. 10% citric acid (100 ml), once with brine (100 ml), dried over Na_2SO_4 , filtered, and concentrated *in vacuo* to yield **10**. Compound **10** was dissolved in anhydrous MeCN (6 ml), and to 5.6 ml of this solution LCAA-CPG (0.602 g, 500 Å, amine loading: $110 \mu\text{mol}\cdot\text{g}^{-1}$), HBTU (0.061 g, 0.160 mmol, 2.0 eq.), and *N*-methylimidazole (0.024 ml, 0.304 mmol, 3.8 eq.) were added. The resulting reaction mixture was flushed with argon and shaken (100 min^{-1}) for 20 h (not stirred to avoid decomposition of the glass beads through friction). The solid residue was filtered off and washed with DCM. Then, a solution of pyridine and acetic anhydride (3:1, 7.2 ml) was added to the solid residue. DMAP (64.6 mg, 0.52 mmol, 6.5 eq.) was added, and the suspension was shaken (100 min^{-1}) at r.t. for 2 h. The white solid-support **11** was filtered off and washed with DCM. The loading of **11** was determined according to the Lambert-Beer law: solid-support **11** (2.3 mg) was added to 3% trichloroacetic acid in DCM (10 ml). After a 1:1 dilution, the absorbance was measured at 498 nm. The molar absorptivity ϵ of the DMT cation of $70'000 \text{ l}\cdot\text{mol}^{-1}\cdot\text{cm}^{-1}$ was used to calculate the loading of the solid support **11** ($79 \mu\text{mol}\cdot\text{g}^{-1}$).

10: ^1H NMR (300 MHz, CDCl_3): δ 8.20 – 8.16 (m, 4H), 8.17 (d, $J = 1.6 \text{ Hz}$, 4H), 7.57 – 7.52 (m, 1H), 7.46 – 7.39 (m, 2H), 7.30 – 7.14 (m, 6H), 6.87 – 6.79 (m, 4H), 4.38 (t, $J = 6.8 \text{ Hz}$, 2H), 3.92 (t, $J = 6.2 \text{ Hz}$, 1H), 3.80 (s, 3H), 3.78 (s, 3H), 3.38 (t, $J = 6.8 \text{ Hz}$, 2H), 2.87 (t, $J = 6.8 \text{ Hz}$, 2H), 2.84 – 2.77 (m, 2H), 2.71 (s, 4H).

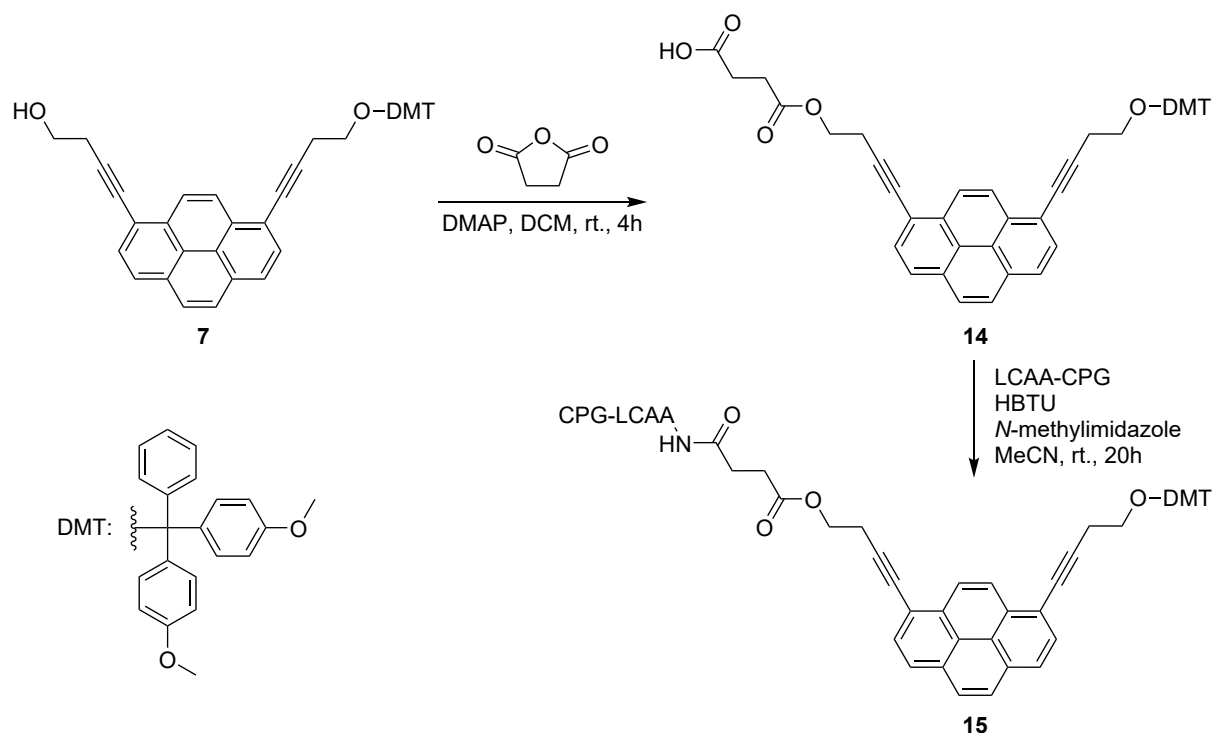
3.3.1.3.2 1,6-Pyrene-Modified Solid-Support (13)

Scheme 3.5: Synthesis of 1,6-pyrene-modified solid-support **13**.

The synthesis and purification of compounds **12** and **13** were done according to **10** and **11** (3.3.1.3.1), starting with 1,6-substituted pyrene **6**. To determine the loading, 2.9 mg of **11** were dissolved in 3% trichloroacetic acid in DCM (10 ml) and diluted 1:1. The loading was calculated to be $75 \mu\text{mol}\cdot\text{g}^{-1}$.

12: $^1\text{H NMR}$ (300 MHz, CDCl_3): δ 8.61 – 8.48 (m, 2H), 8.12 – 7.95 (m, 6H), 7.59 – 7.55 (m, 1H), 7.46 – 7.43 (m, 2H), 7.35 – 7.13 (m, 6H), 6.87 – 6.79 (m, 4H), 4.46 (t, $J = 6.8$ Hz, 2H), 3.98 (t, $J = 6.2$ Hz, 1H), 3.80 (s, 3H), 3.76 (s, 3H), 3.45 (t, $J = 6.5$ Hz, 1H), 3.02 – 2.90 (m, 5H), 2.72 (s, 4H).

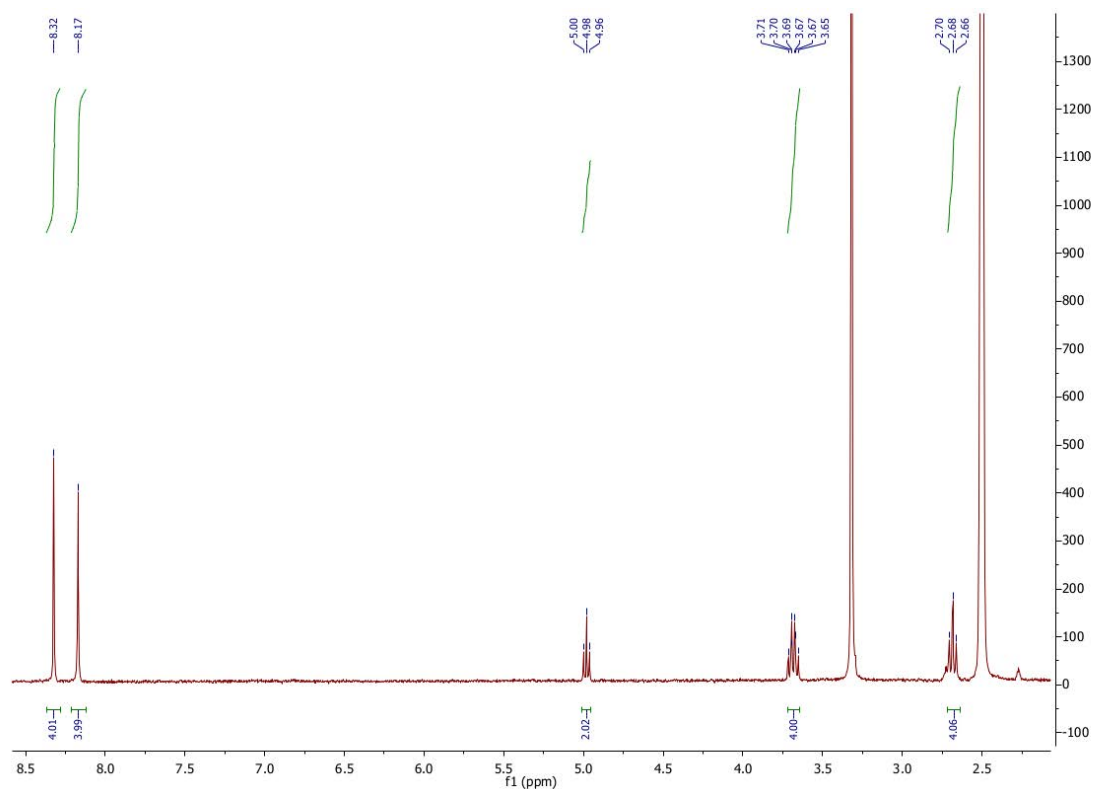
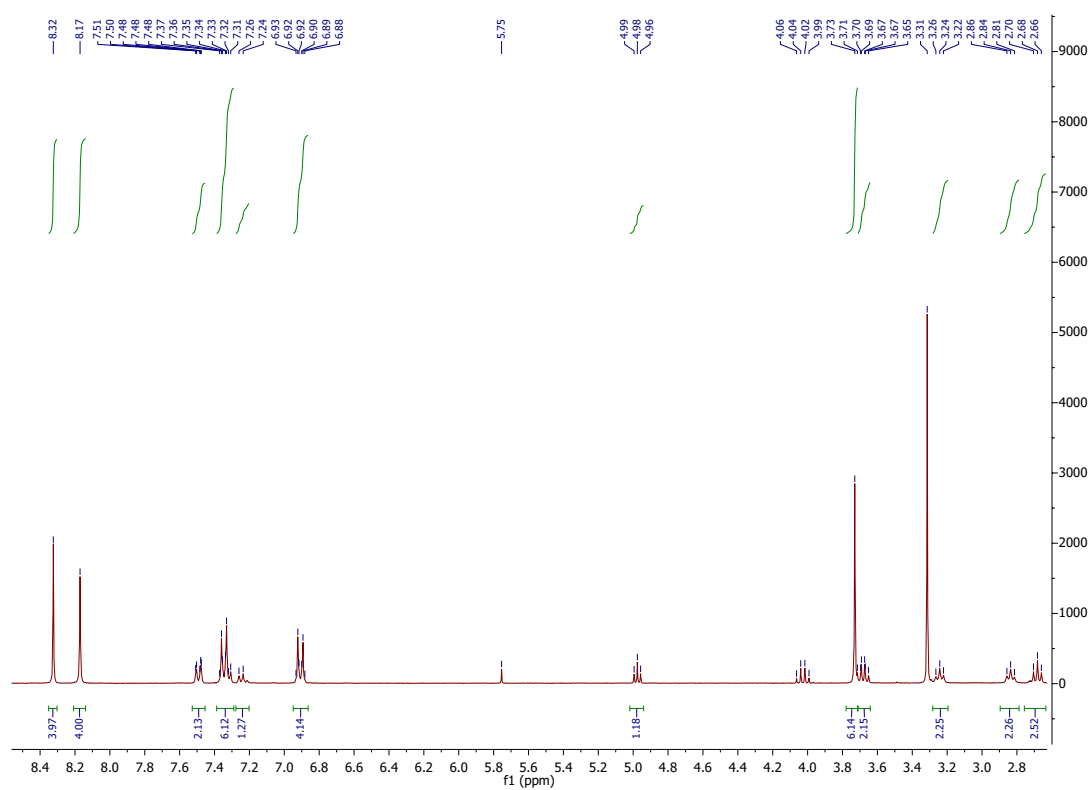
3.3.1.3.3 1,8-Pyrene-Modified Solid-Support (15)

**Scheme 3.6:** Synthesis of 1,8-pyrene-modified solid-support **15**.

The synthesis and purification of compounds **14** and **15** were done corresponding to **10** and **11** (3.3.1.3.1), starting with 1,8-substituted pyrene **7**. To determine the loading, 2.8 mg of **11** were dissolved in 3% trichloroacetic acid in DCM (10 ml) and diluted 1:1. The loading was calculated to be $62 \mu\text{mol}\cdot\text{g}^{-1}$.

14: $^1\text{H NMR}$ (300 MHz, CDCl_3): δ 8.70 – 8.53 (m, 2H), 8.10 – 8.00 (m, 6H), 7.60 – 7.54 (m, 1H), 7.48 – 7.41 (m, 3H), 7.33 – 7.14 (m, 6H), 6.87 – 6.80 (m, 4H), 4.48 (t, $J = 6.8 \text{ Hz}$, 2H), 4.03 (t, $J = 5.8 \text{ Hz}$, 1H), 3.80 (s, 3H), 3.77 (s, 3H), 3.46 (t, $J = 6.5 \text{ Hz}$, 1H), 3.02 – 2.88 (m, 5H), 2.71 (s, 3H).

3.3.2 NMR Spectra

Figure 3.18: $^1\text{H-NMR}$ of compound 1 in $\text{DMSO-}d_6$.Figure 3.19: $^1\text{H-NMR}$ of compound 2 in $\text{DMSO-}d_6$.

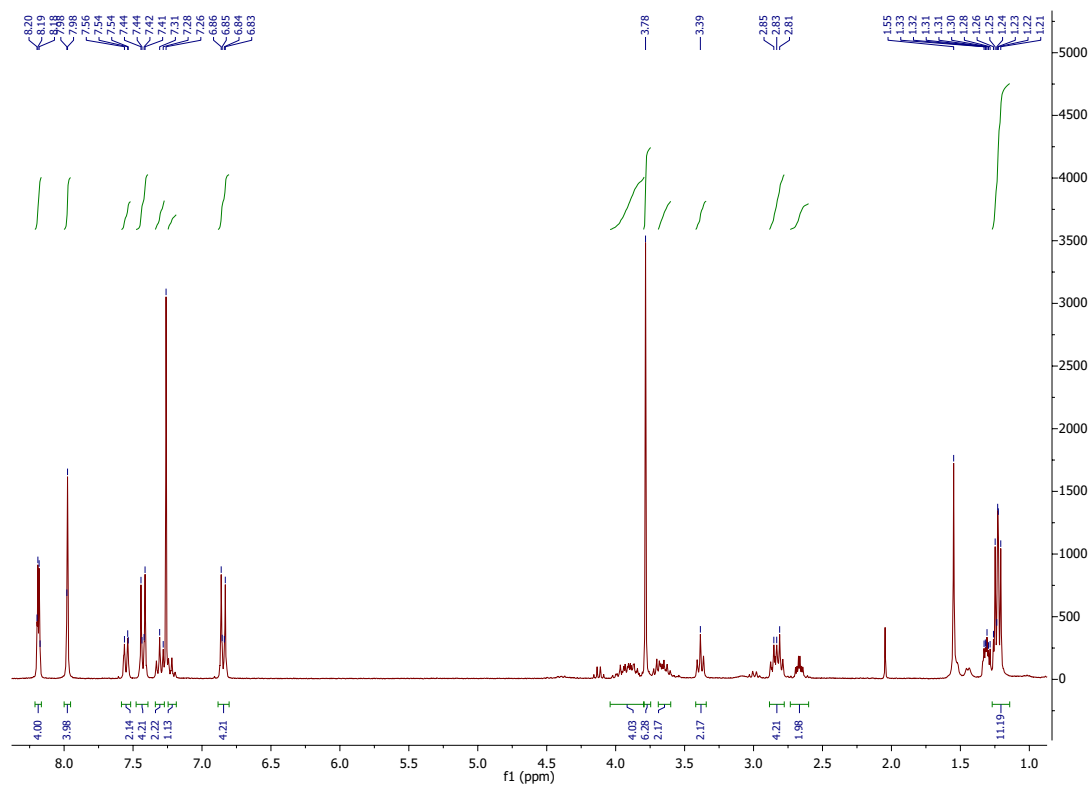


Figure 3.20: ^1H -NMR spectrum of compound **3** in CDCl_3 .

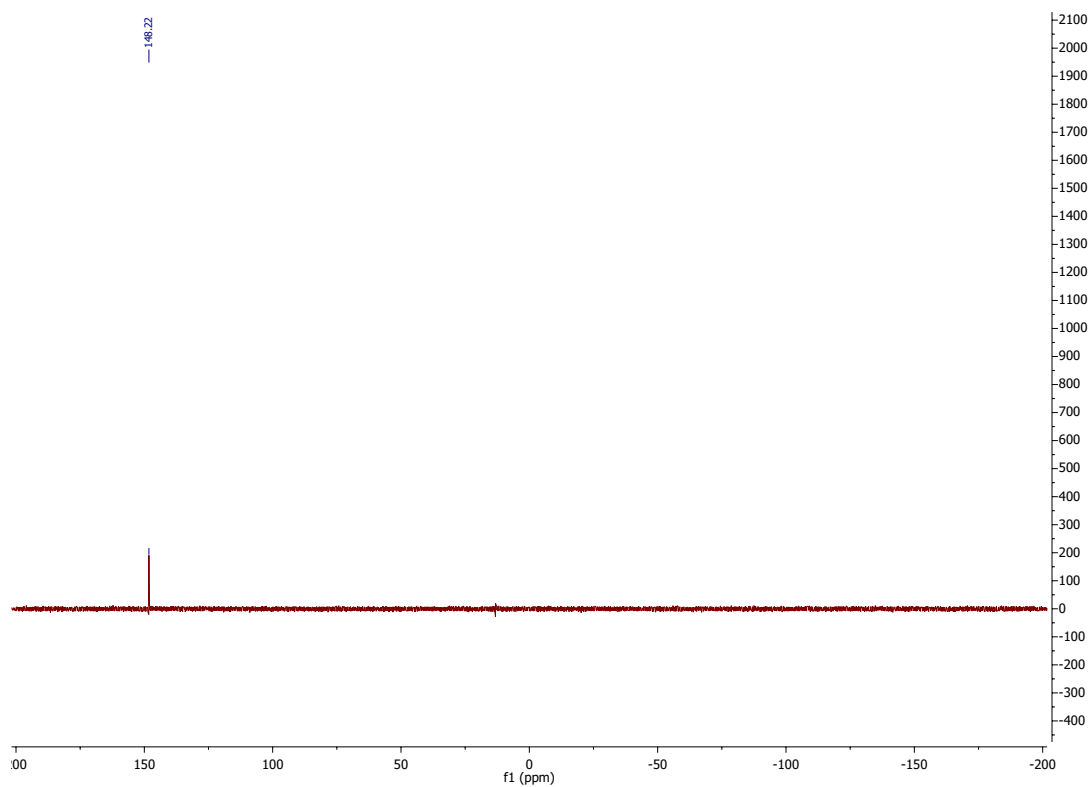


Figure 3.21: ^{31}P -NMR spectrum of compound **3** in CDCl_3 .

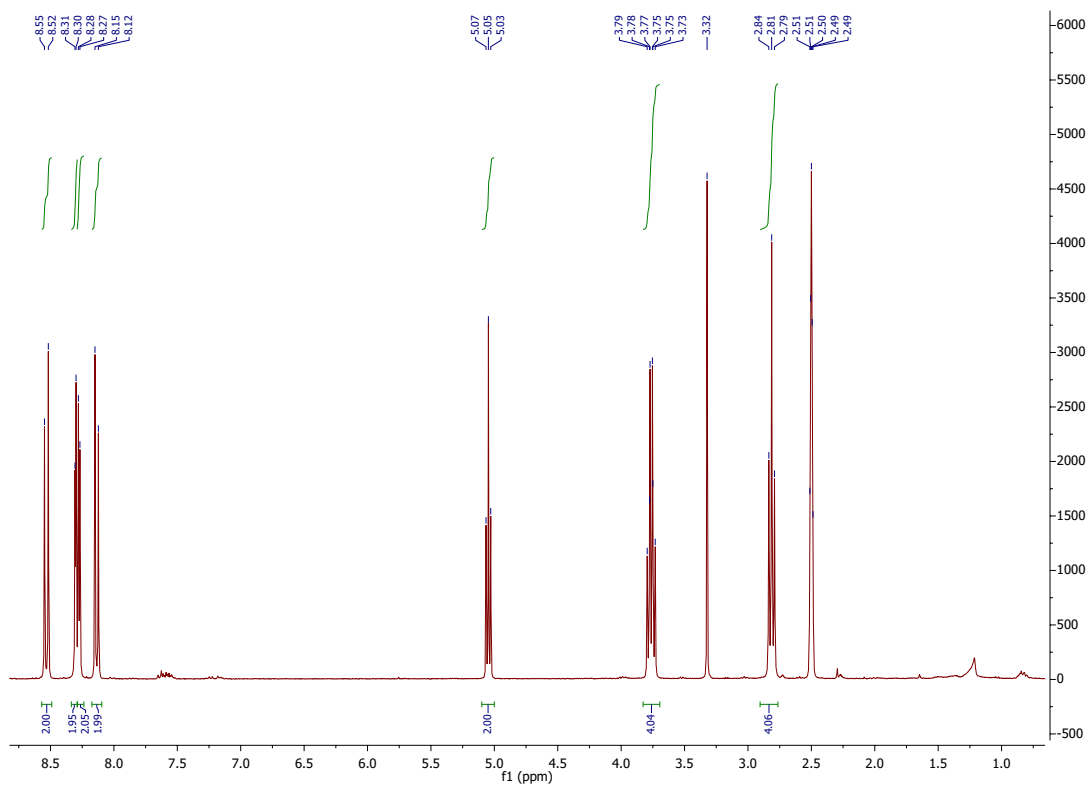


Figure 3.22: $^1\text{H-NMR}$ spectrum of compound 4 in $\text{DMSO-}d_6$.

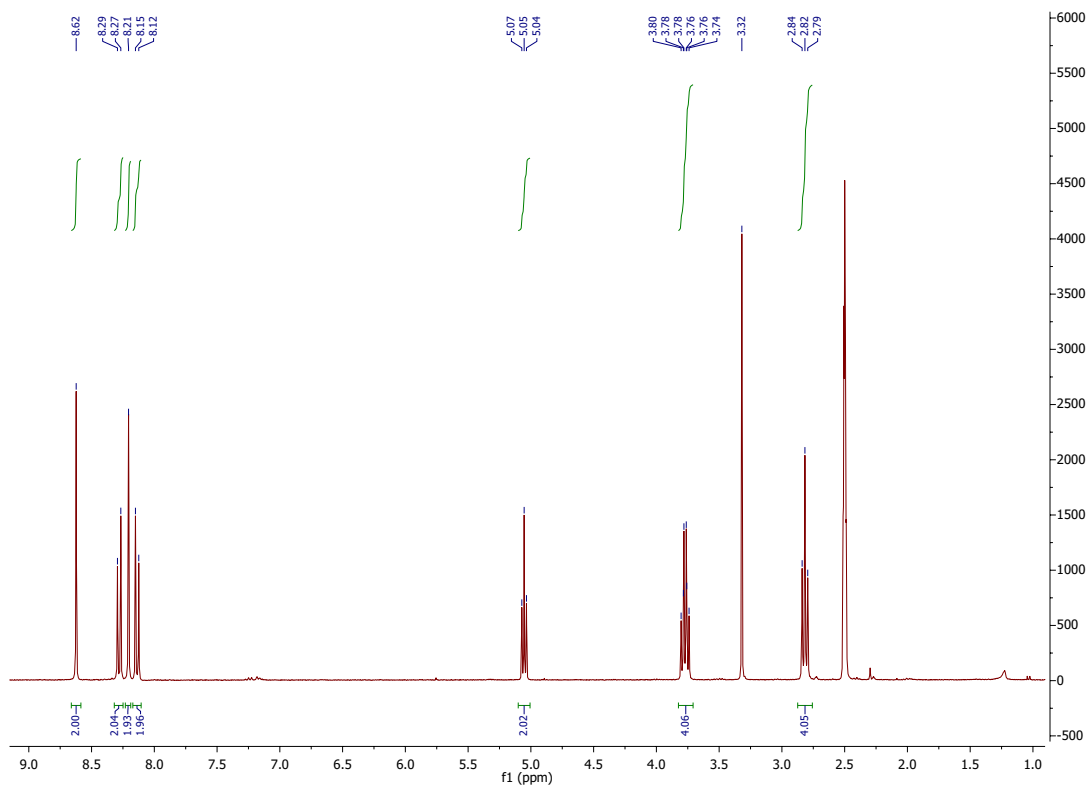


Figure 3.23: $^1\text{H-NMR}$ spectrum of compound 5 in $\text{DMSO-}d_6$.

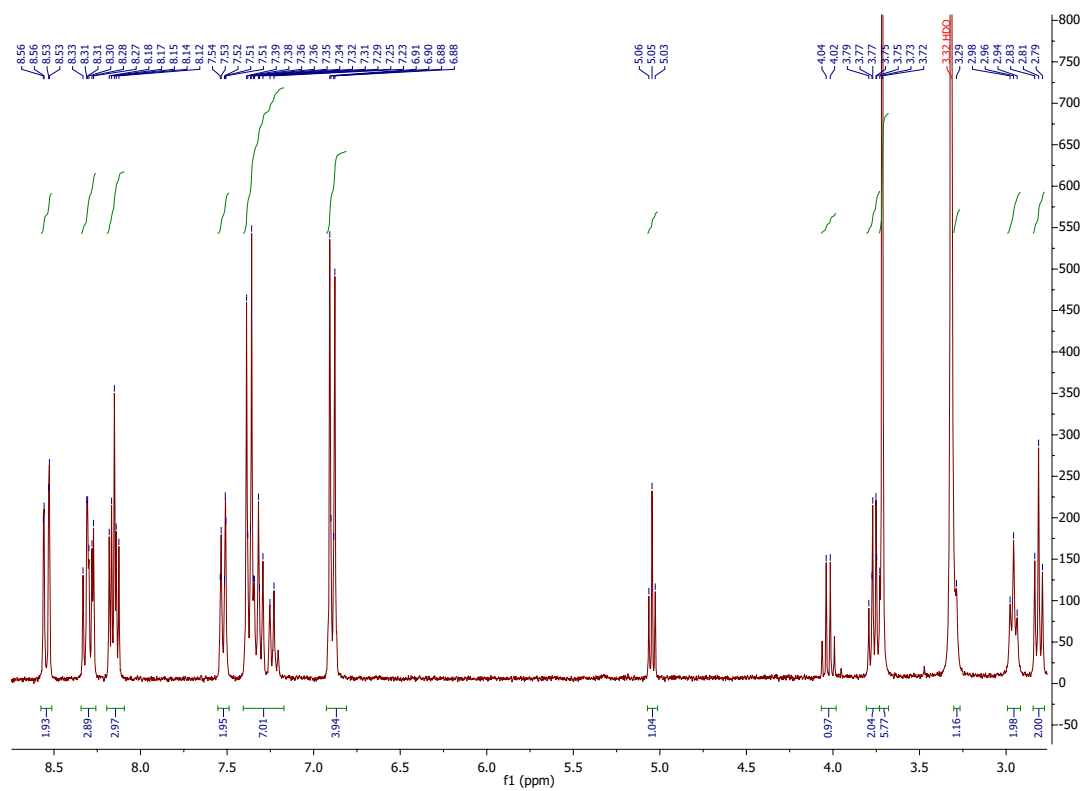


Figure 3.24: $^1\text{H-NMR}$ spectrum of compound **6** in $\text{DMSO-}d_6$.

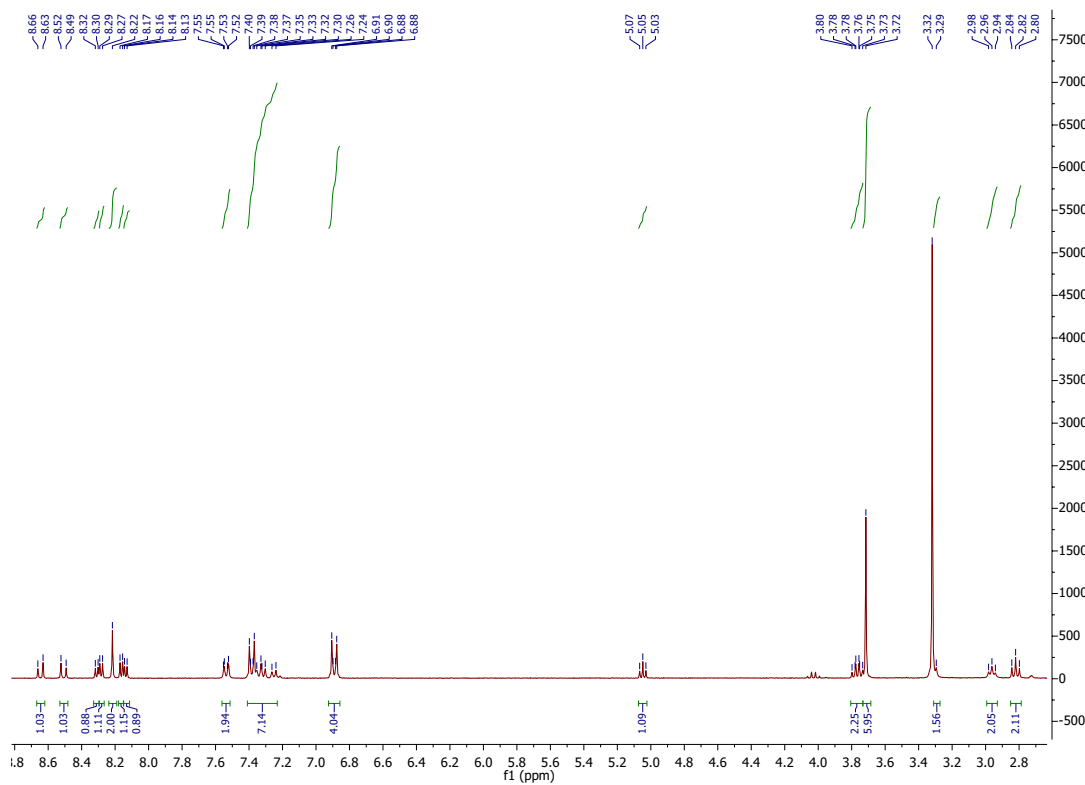


Figure 3.25: $^1\text{H-NMR}$ spectrum of compound **7** in $\text{DMSO-}d_6$.

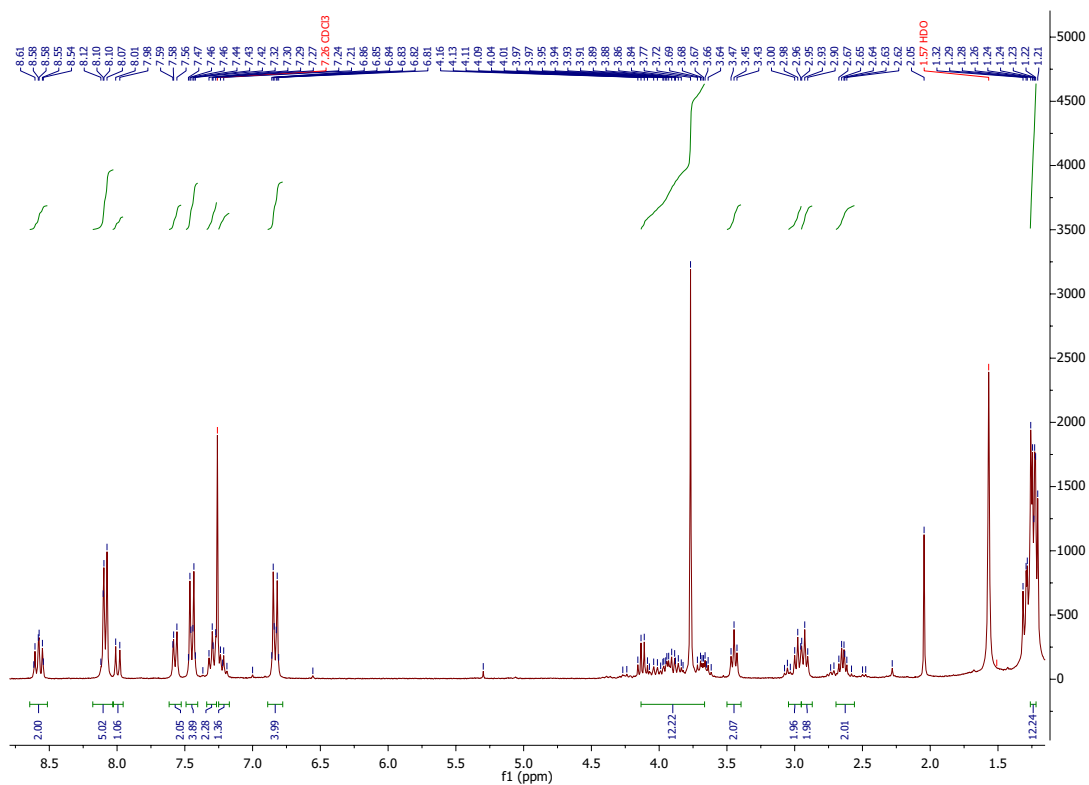


Figure 3.26: ^1H -NMR spectrum of compound **8** in CDCl_3 .

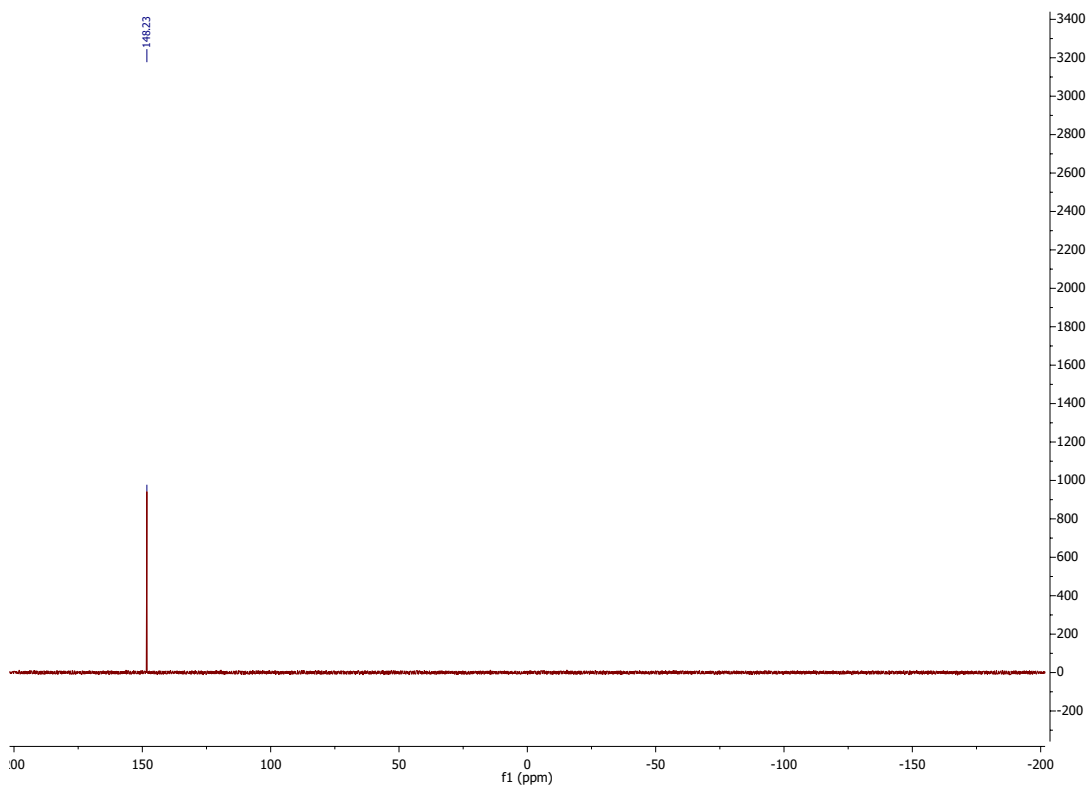


Figure 3.27: ^{31}P -NMR spectrum of compound **8** in CDCl_3 .

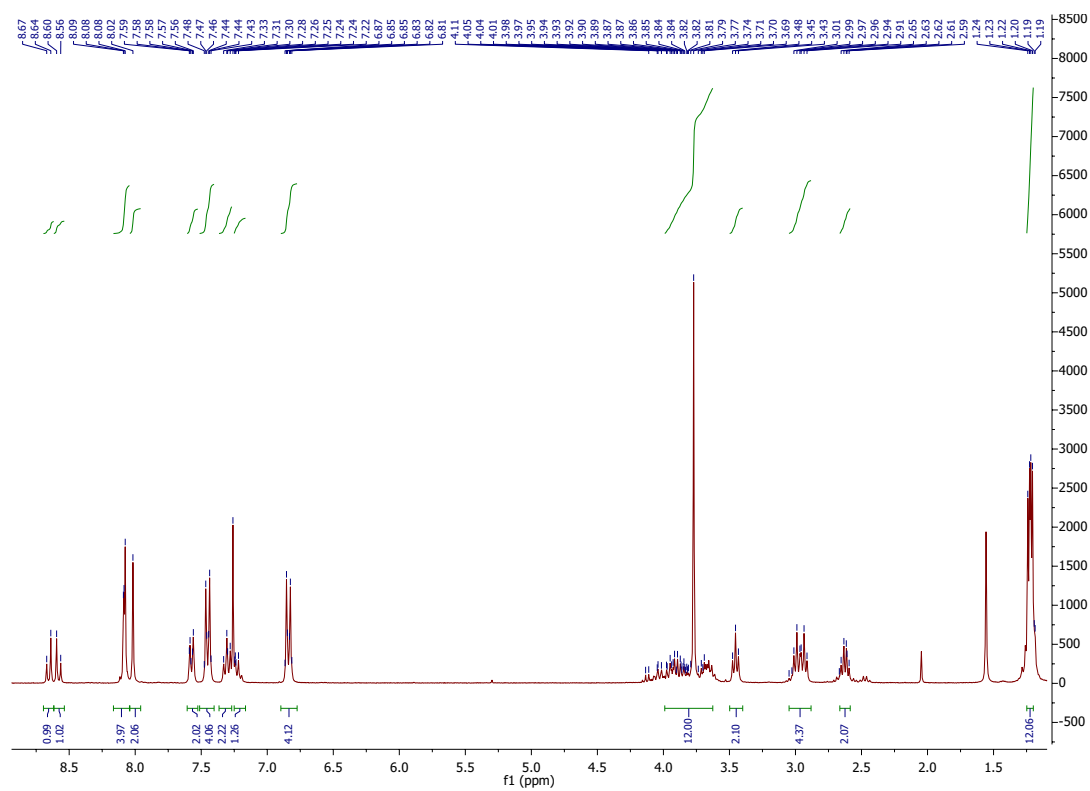


Figure 3.28: $^1\text{H-NMR}$ spectrum of compound **9** in CDCl_3 .

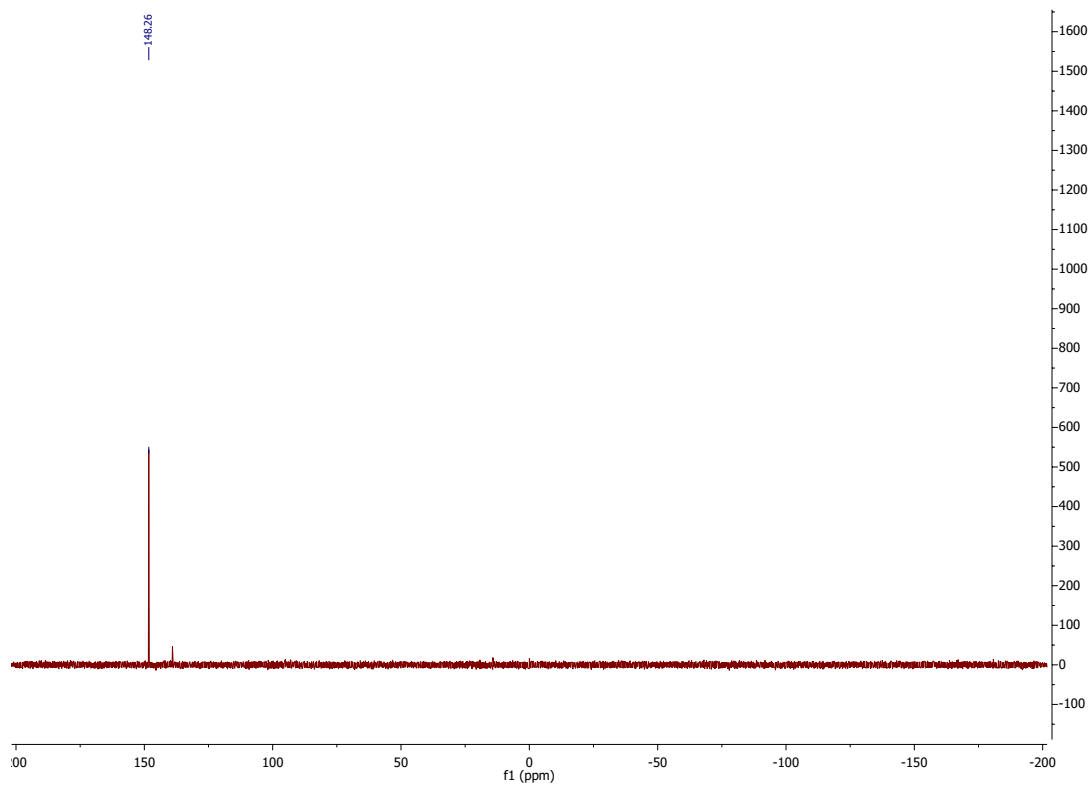


Figure 3.29: $^{31}\text{P-NMR}$ spectrum of compound **9** in CDCl_3 .

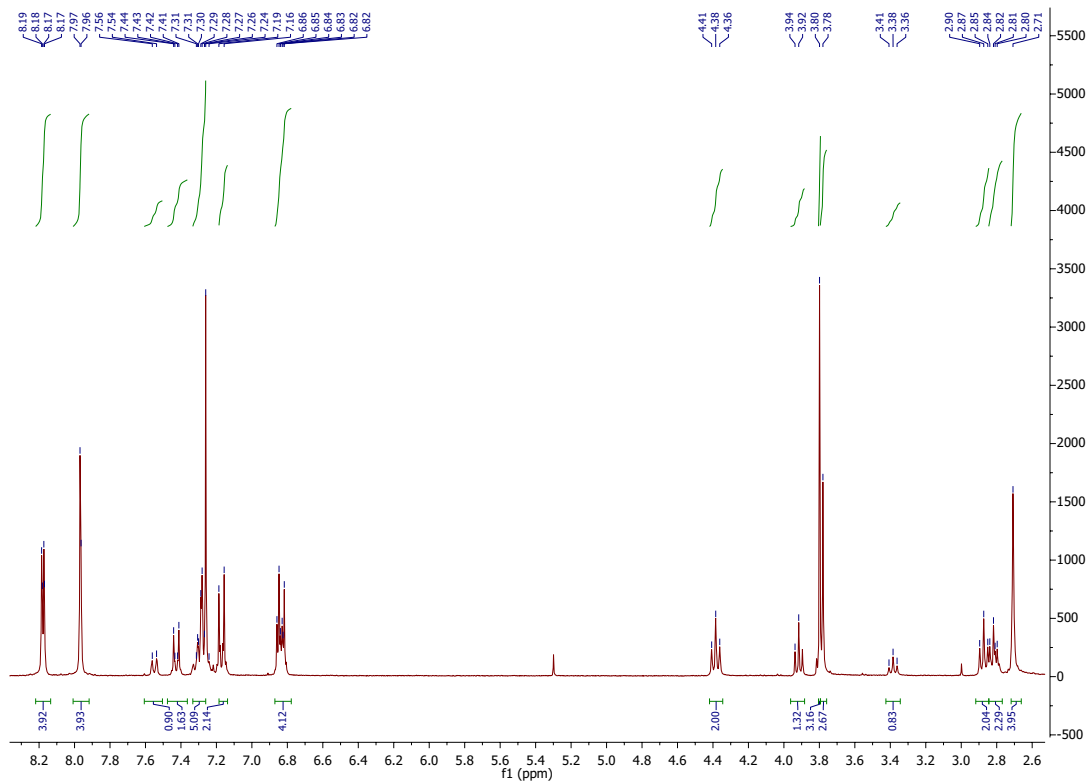


Figure 3.30: $^1\text{H-NMR}$ spectrum of compound **10** in CDCl_3 .

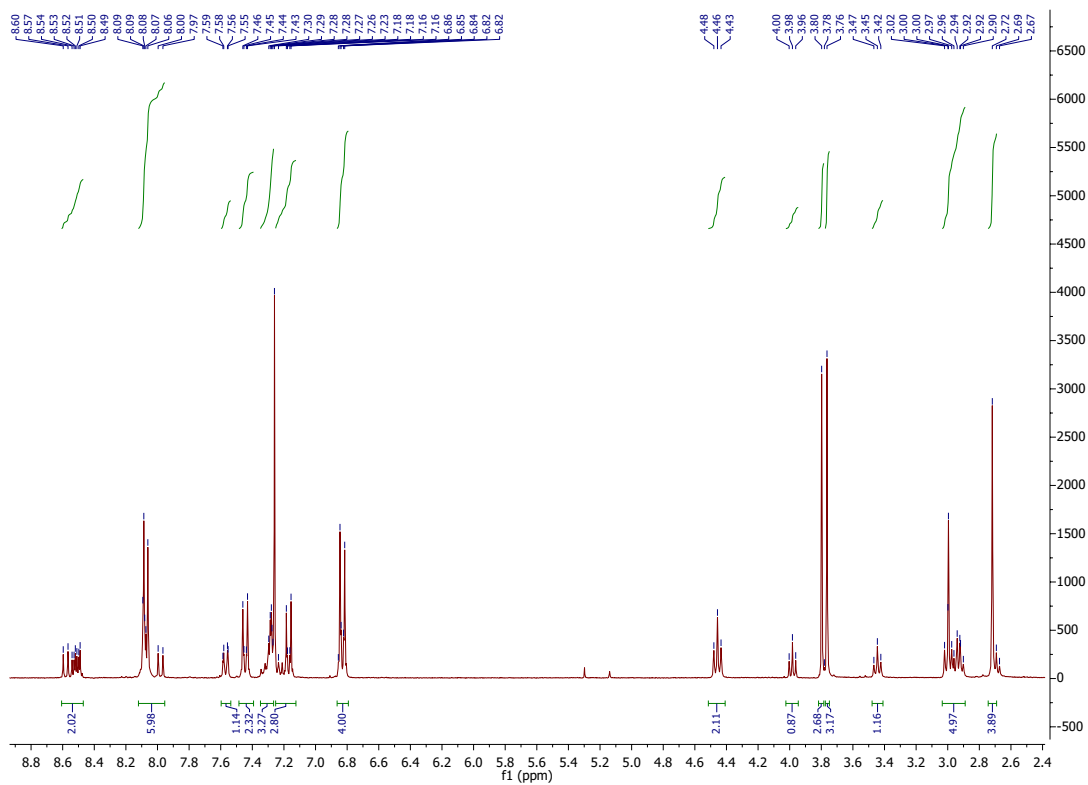


Figure 3.31: $^1\text{H-NMR}$ spectrum of compound **12** in CDCl_3 .

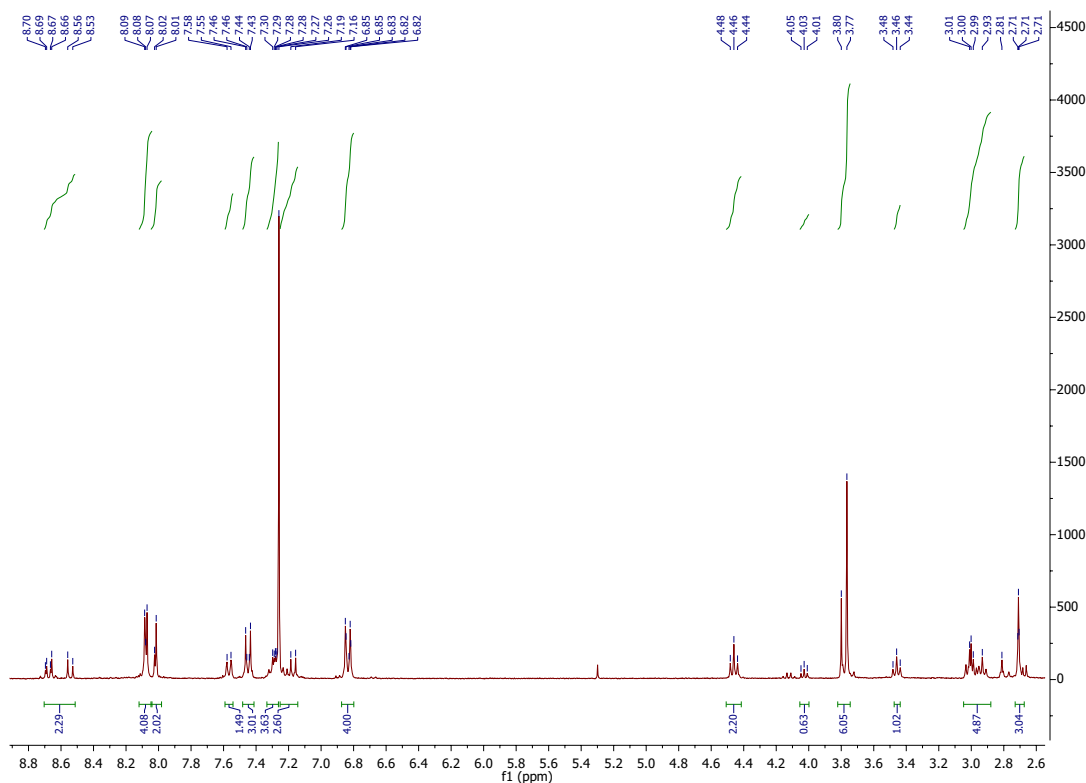


Figure 3.32: $^1\text{H-NMR}$ spectrum of compound **14** in CDCl_3 .

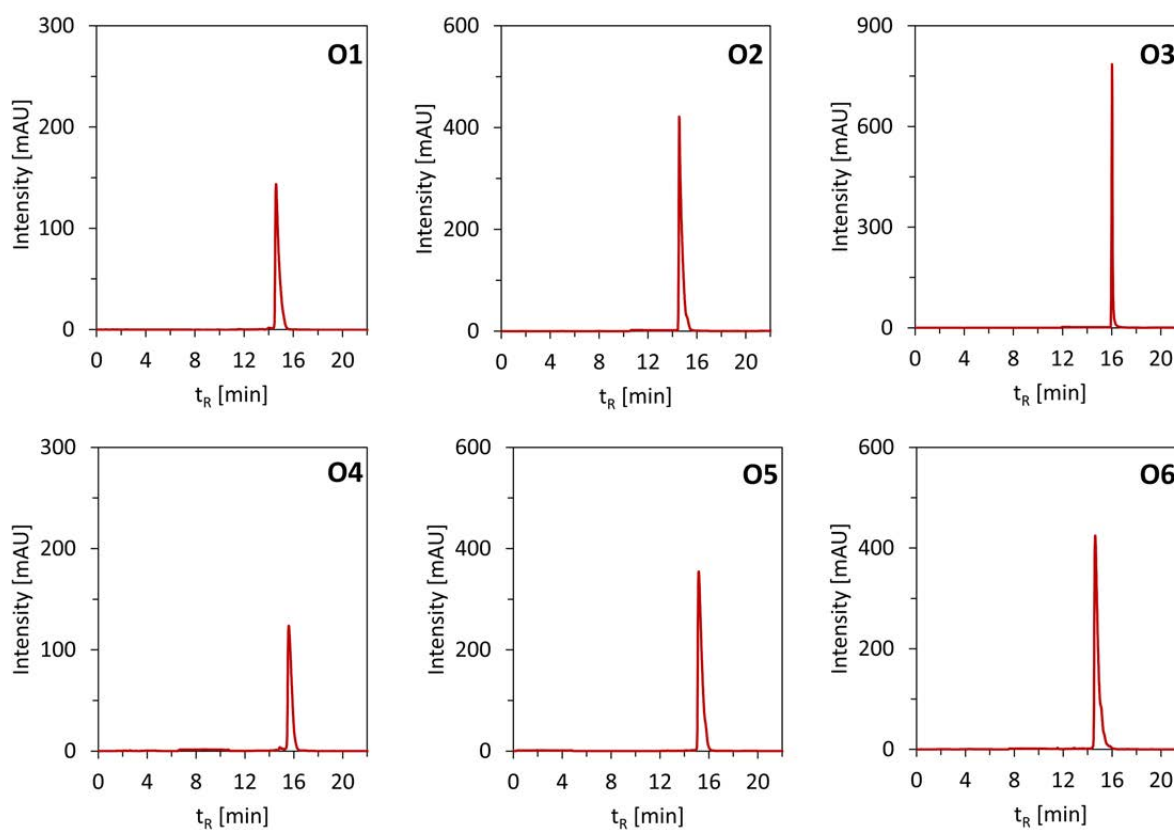
3.3.3 Synthesis of Oligonucleotides

3'-modified pyrene-DNA conjugates **O1–O6** were synthesized on an Applied Biosystems 394 DNA/RNA synthesizer applying a standard cyanoethyl phosphoramidite coupling protocol on a $1\ \mu\text{mol}$ scale. Synthesis and purification are described in detail in chapter 8.

Afterward, the oligomers **O1–O6** were purified by reverse-phase HPLC (Shimadzu LC-20AT, ReproSil 100 C18, $5.0\ \mu\text{m}$, $250\times 4\ \text{mm}$) at $40\ ^\circ\text{C}$ with a flow rate of $1\ \text{ml}/\text{min}$, with a detection wavelength of $260\ \text{nm}$. Solvent A: aqueous $2.1\ \text{mM}$ triethylamine (TEA) / $25\ \text{mM}$ 1,1,1,3,3,3-hexafluoropropan-2-ol (HFIP) pH 8; solvent B: acetonitrile; applying the gradients B [%] (t_{R} [min]) = 5 (0), 20 (24). The purified oligomers **O1–O6** were dissolved in $1\ \text{ml}$ of Milli-Q H_2O . After that, the absorbance of the pyrene-DNA conjugates was measured at $260\ \text{nm}$ to determine the concentration of the stock solutions and yields of **O1–O6**. Their concentrations were determined by applying the Beer-Lambert law. For the DNA nucleobases, the following molar absorptivities (at $260\ \text{nm}$) in $\text{L}\cdot\text{mol}^{-1}\cdot\text{cm}^{-1}$ were used: ϵ_{A} ; $15'300$, ϵ_{T} ; $9'000$, ϵ_{G} ; $11'700$, ϵ_{C} ; $7'400$, $\epsilon_{2,7\text{-pyrene}}$; $32'000$, $\epsilon_{1,8\text{-pyrene}}$; $30'000$, and $\epsilon_{1,6\text{-pyrene}}$; $20'000$. The mass spectra results of **O1–O6** are listed in Table 3.5, the HPLC traces are depicted in Figure 3.33, and the mass spectra are displayed in Figure 3.34–Figure 3.39.

Table 3.5: Pyrene-DNA oligonucleotide sequences of **O1–O6**, calculated and found masses by NSI-MS, and yields.

Oligomer	Sequence (5'→3')	Calcd mass	Found mass	Yield [%]
O1	CAA GGT CCG ATG CAA GGA AG-(1,6-pyrene) ₃	7400.3621	7401.3217	27
O2	CTT CCT TGC ATC GGA CCT TG-(1,6-pyrene) ₃	7235.2858	7235.2415	36
O3	CAA GGT CCG ATG CAA GGA AG-(1,8-pyrene) ₃	7400.3621	7401.3219	18
O4	CTT CCT TGC ATC GGA CCT TG-(1,8-pyrene) ₃	7235.2858	7235.2407	12
O5	CAA GGT CCG ATG CAA GGA AG-(2,7-pyrene) ₃	7400.3621	7401.3151	29
O6	CTT CCT TGC ATC GGA CCT TG-(2,7-pyrene) ₃	7235.2858	7235.2443	36

**Figure 3.33:** HPLC traces of pyrene-DNA conjugates **O1–O6**.

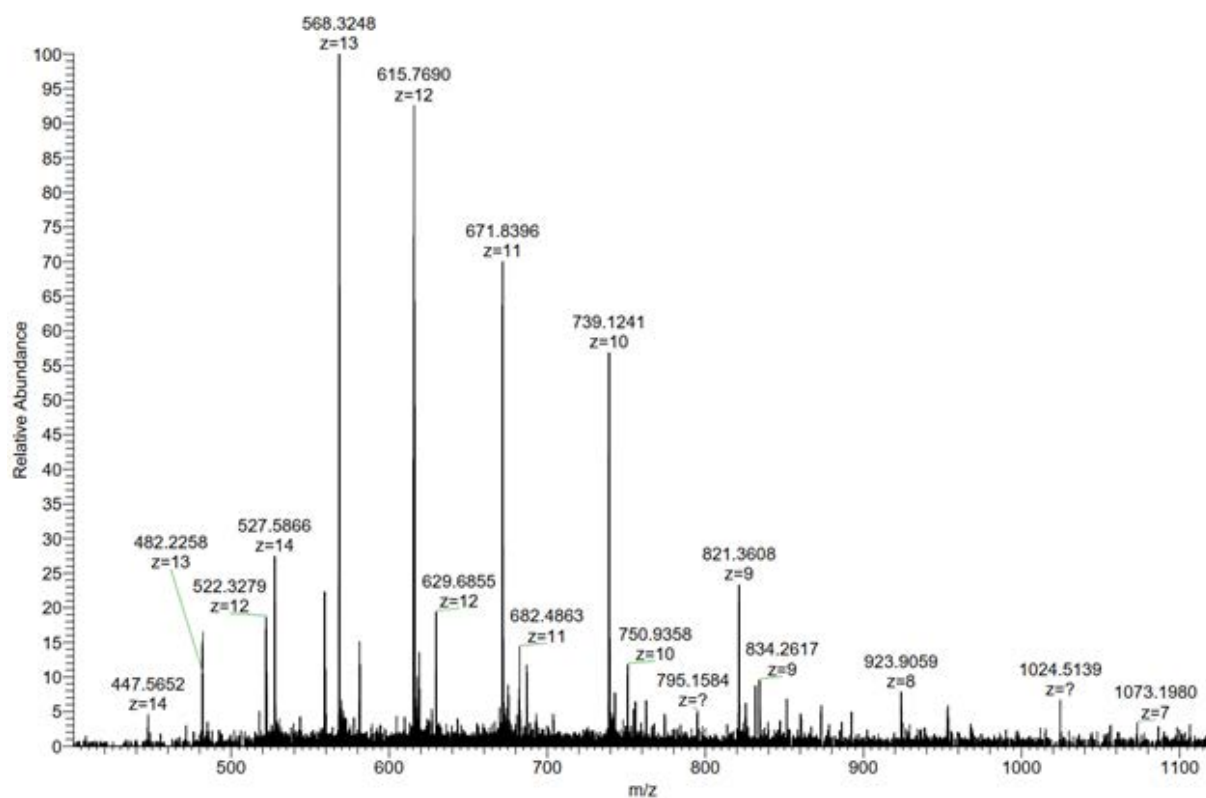


Figure 3.34: MS spectrum of O1.

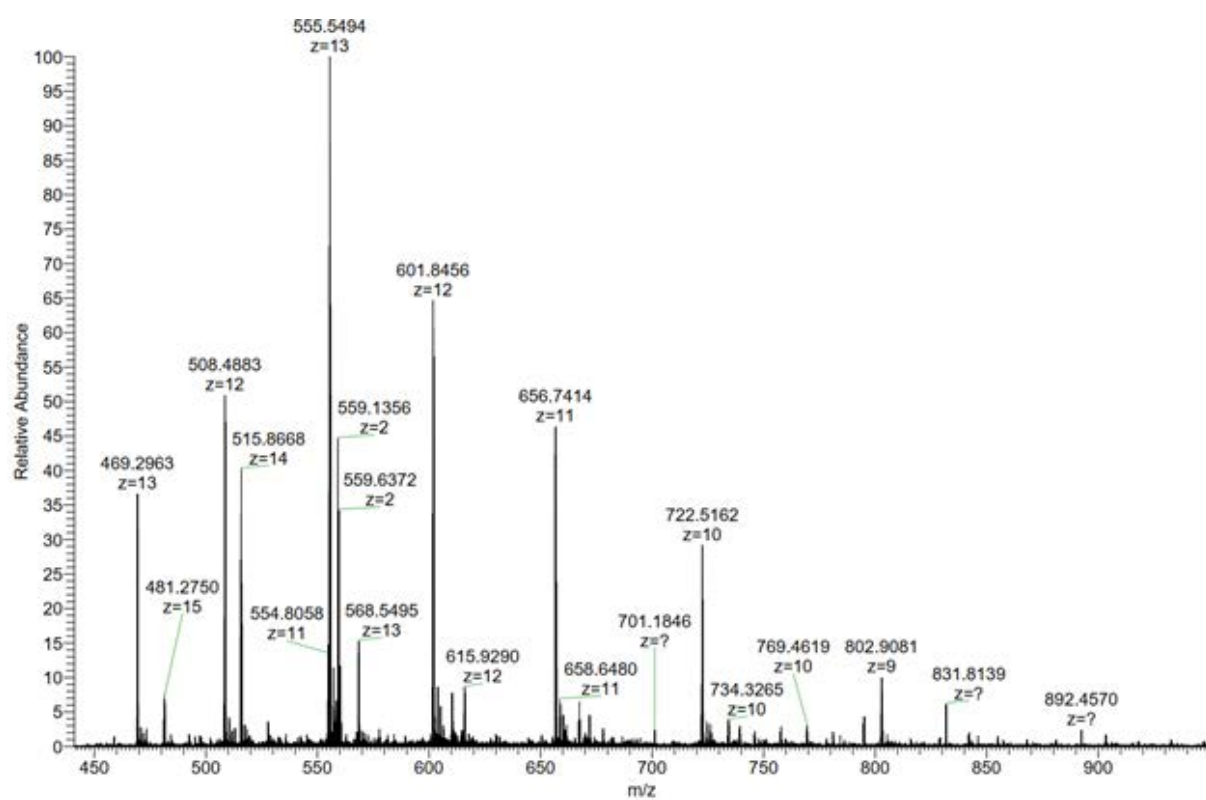
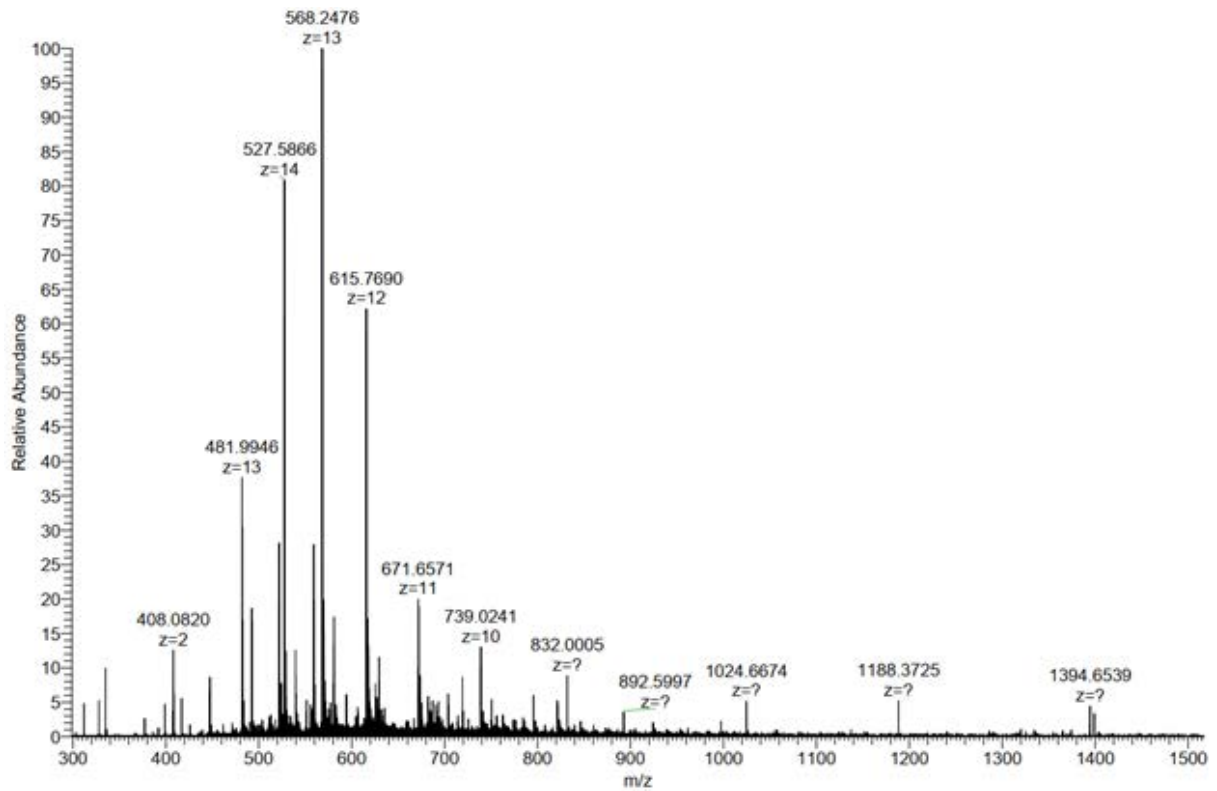
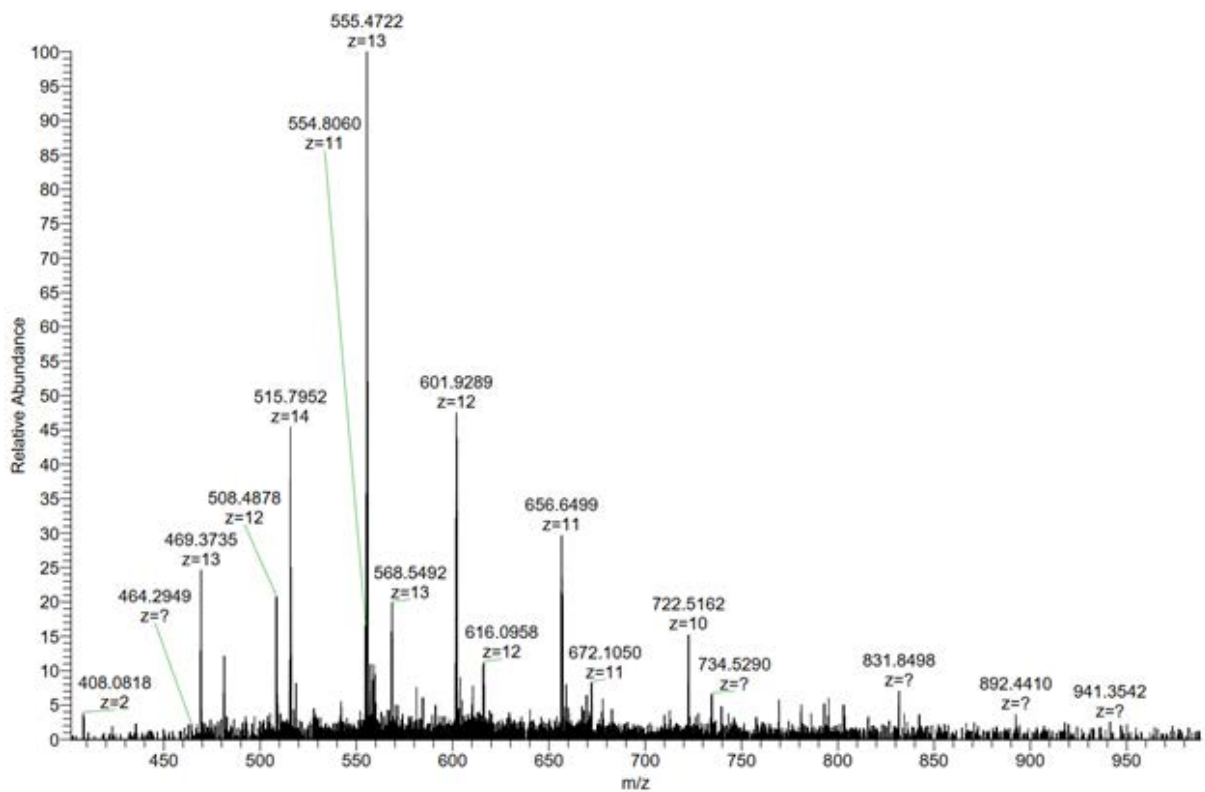


Figure 3.35: MS spectrum of O2.

Figure 3.36: MS spectrum of O₃.Figure 3.37: MS spectrum of O₄.

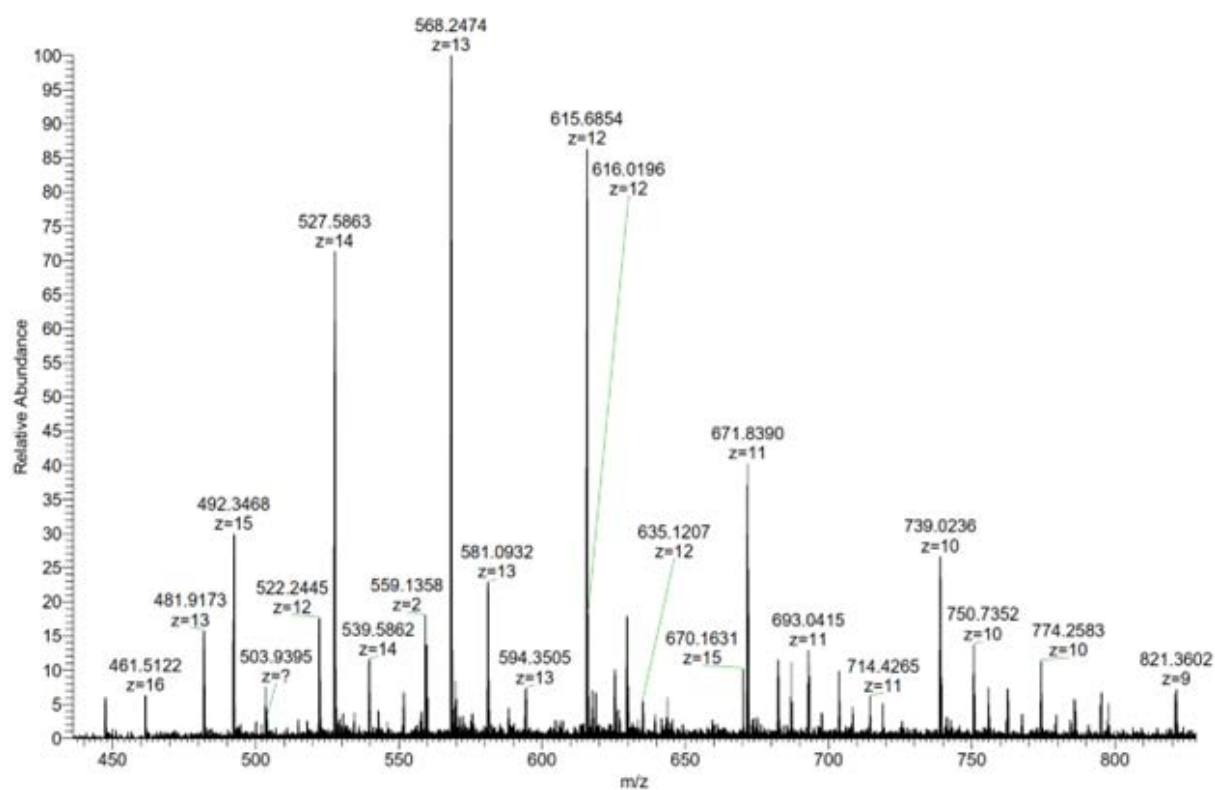


Figure 3.38: MS spectrum of O5.

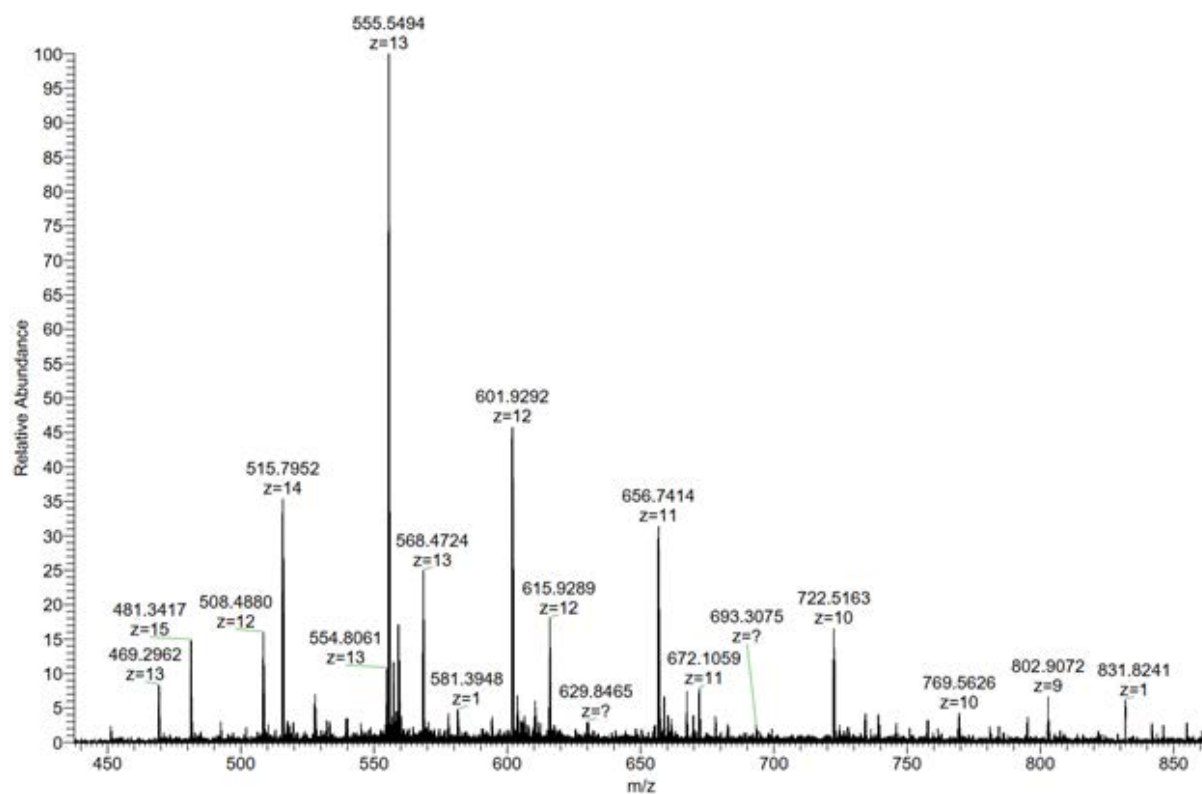


Figure 3.39: MS spectrum of O6.

3.3.4 Spectroscopic Measurements

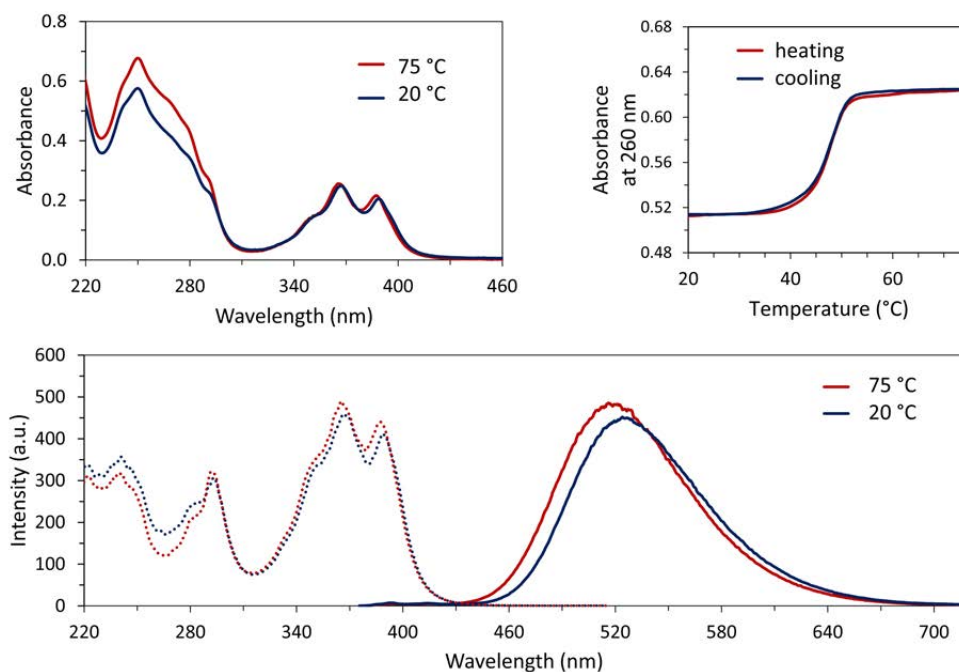


Figure 3.40: Temperature-dependent UV-vis absorption spectra (left), cooling-heating curve at 260 nm (right), and fluorescence emission and excitation spectra of **O1*O2** (bottom). Conditions: 1 μ M each single strand, 10 mM sodium phosphate buffer pH 7.2, 20 vol% ethanol.

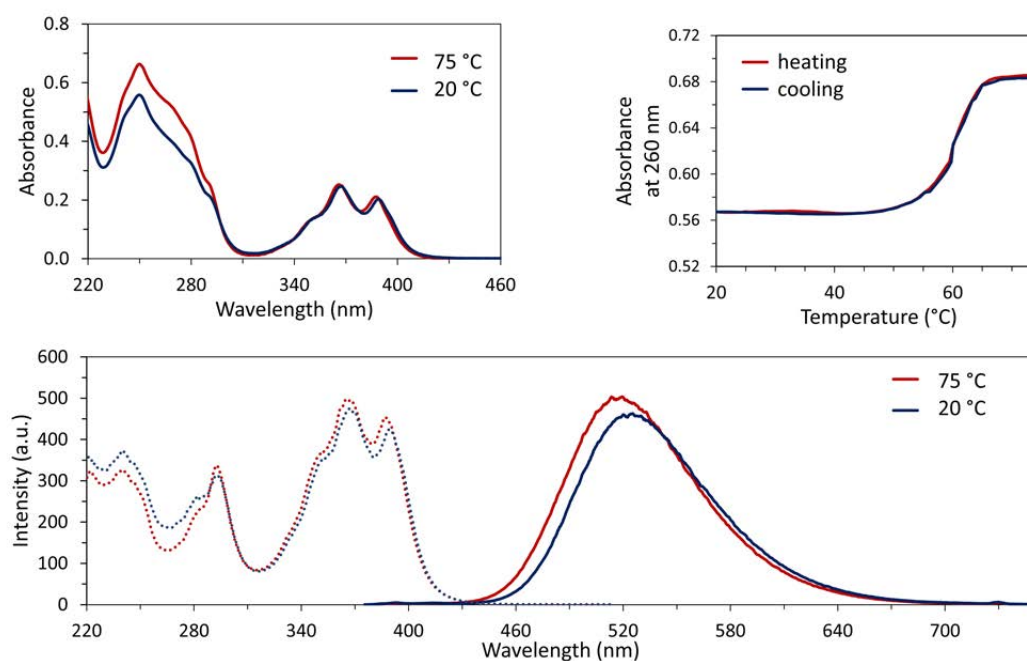


Figure 3.41: Temperature-dependent UV-vis absorption spectra (left), cooling-heating curve at 260 nm (right), and fluorescence emission and excitation spectra of **O1*O2** (bottom). Conditions: 1 μ M each single strand, 10 mM sodium phosphate buffer pH 7.2, 100 mM NaCl, 20 vol% ethanol.

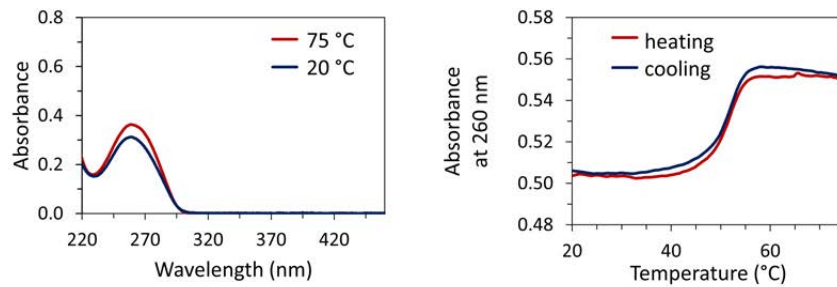


Figure 3.42: Temperature-dependent UV-vis absorption spectra of **O7*O8** (left) and cooling-heating curve at 260 nm (right). Conditions: 1 μM each single strand, 10 mM sodium phosphate buffer pH 7.2, 0.03 mM spermine \cdot 4 HCl, 20 vol% ethanol.

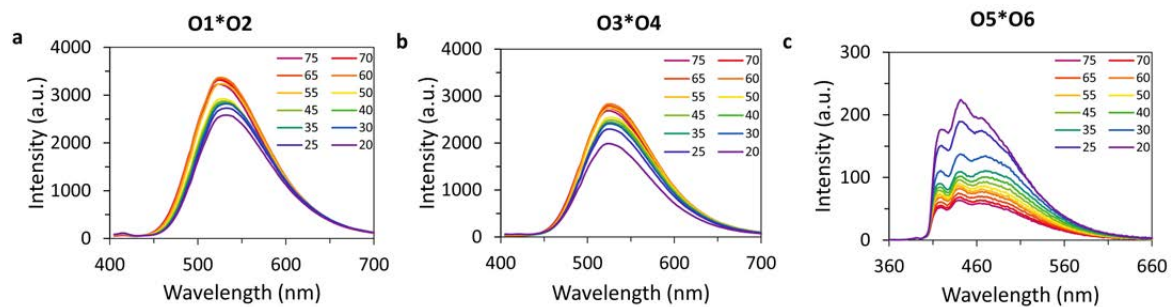


Figure 3.43: Temperature-dependent fluorescence emission spectra of (a) **O1*O2**, (b) **O3*O4**, and (c) **O5*O6** cooling from 75 °C to 20 °C. Conditions: 1 μM each single strand, 10 mM sodium phosphate buffer pH 7.2, 0.03 mM spermine \cdot 4 HCl, 20 vol% ethanol, **O1*O2** and **O3*O4**: λ_{ex} . 388 nm and **O5*O6**: λ_{ex} . 345 nm.

3.3.5 Additional Microscopic Measurements

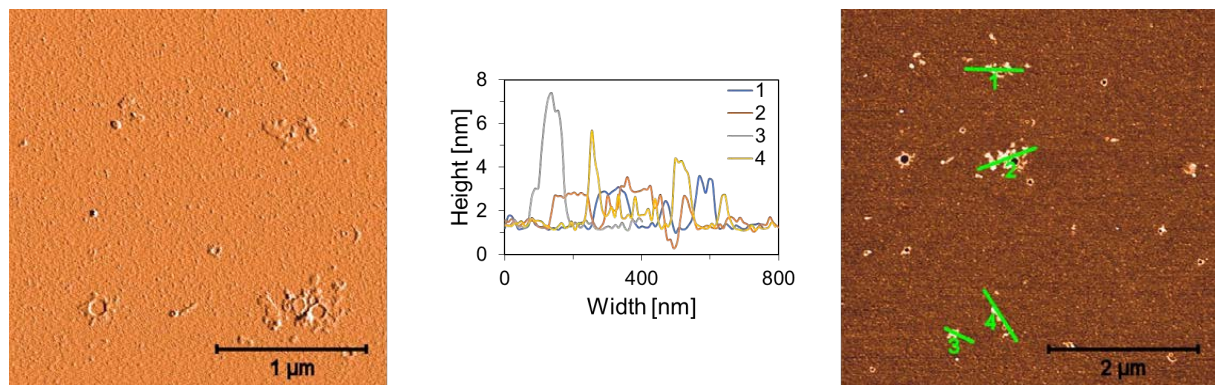


Figure 3.44: AFM deflection scan (left) and scan with corresponding cross sections of assembled **O7*O8** (right). Conditions: 1 μM each single strand, 10 mM sodium phosphate buffer pH 7.2, 0.03 mM spermine \cdot 4 HCl, 20 vol% ethanol.

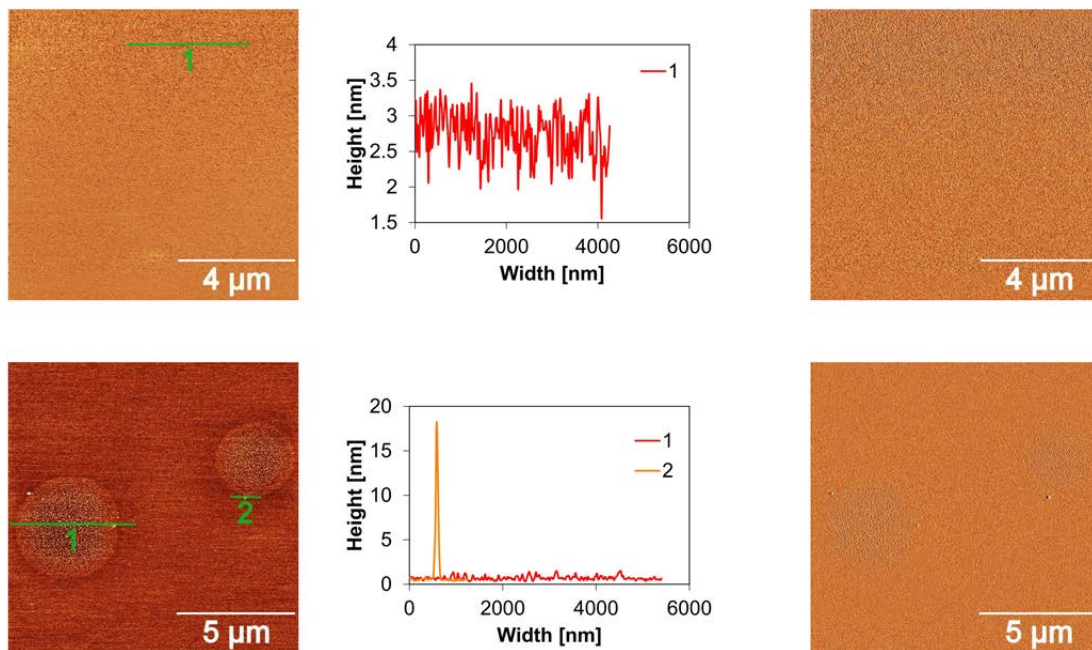


Figure 3.45: AFM scan with corresponding cross sections of assembled **O1*O2** (left) and deflection scan (right): Measurement without spermine · 4 HCl (top) and with 100 mM NaCl (bottom). Conditions: 1 μM each single strand, 10 mM sodium phosphate buffer pH 7.2, 20 vol% ethanol, without (top) and with 100 mM NaCl (bottom).

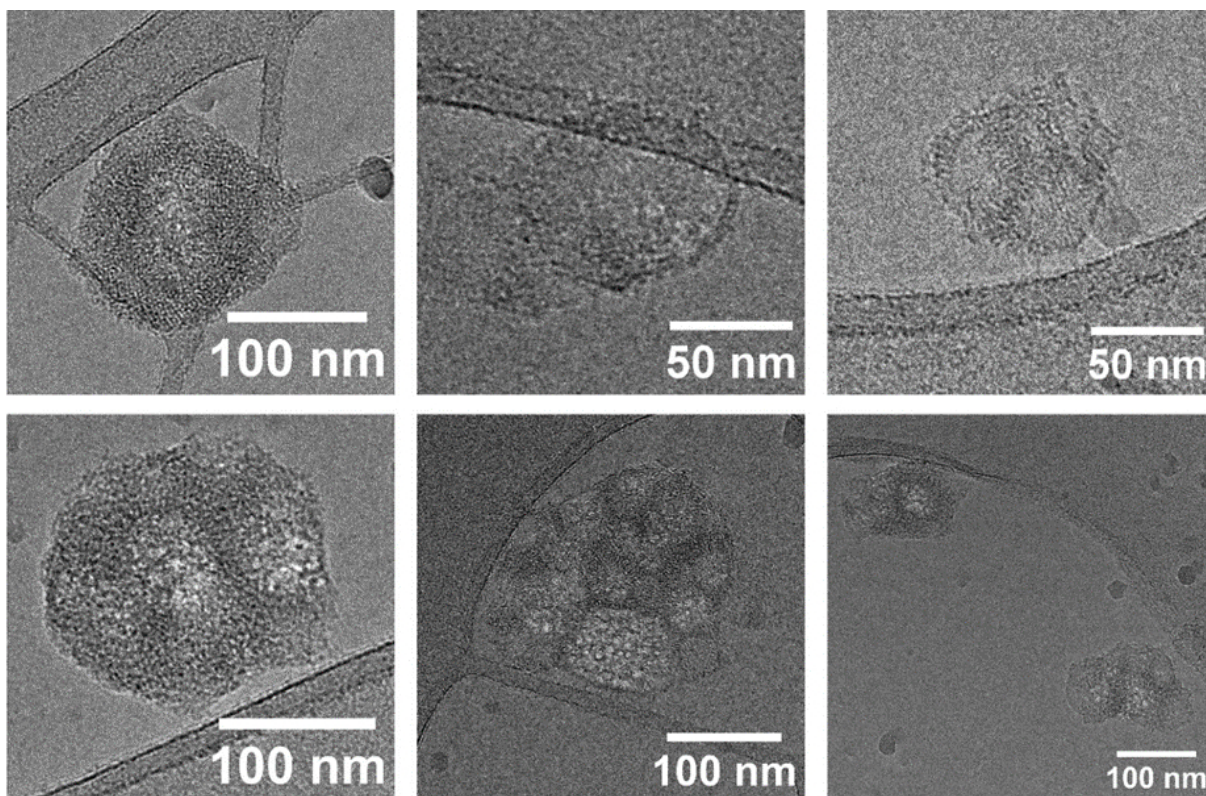


Figure 3.46: Additional cryo-EM image of self-assembled **O1*O2**. Conditions: 1 μM **O1*O2**, 10 mM sodium phosphate buffer pH 7.2, 0.03 mM spermine · 4 HCl, 20 vol% ethanol.

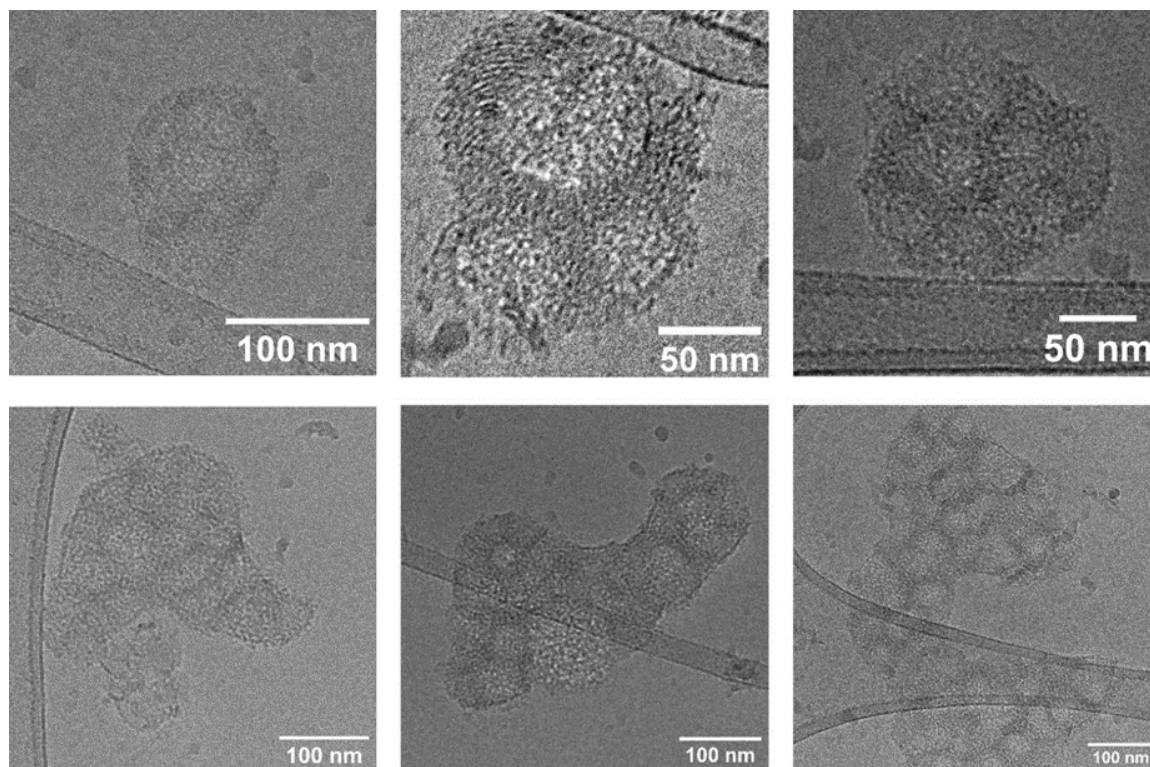


Figure 3.47: Additional cryo-EM image of self-assembled **O3*O4**. Conditions: 1 μ M **O3*O4**, 10 mM sodium phosphate buffer pH 7.2, 0.03 mM spermine \cdot 4 HCl, 20 vol% ethanol.

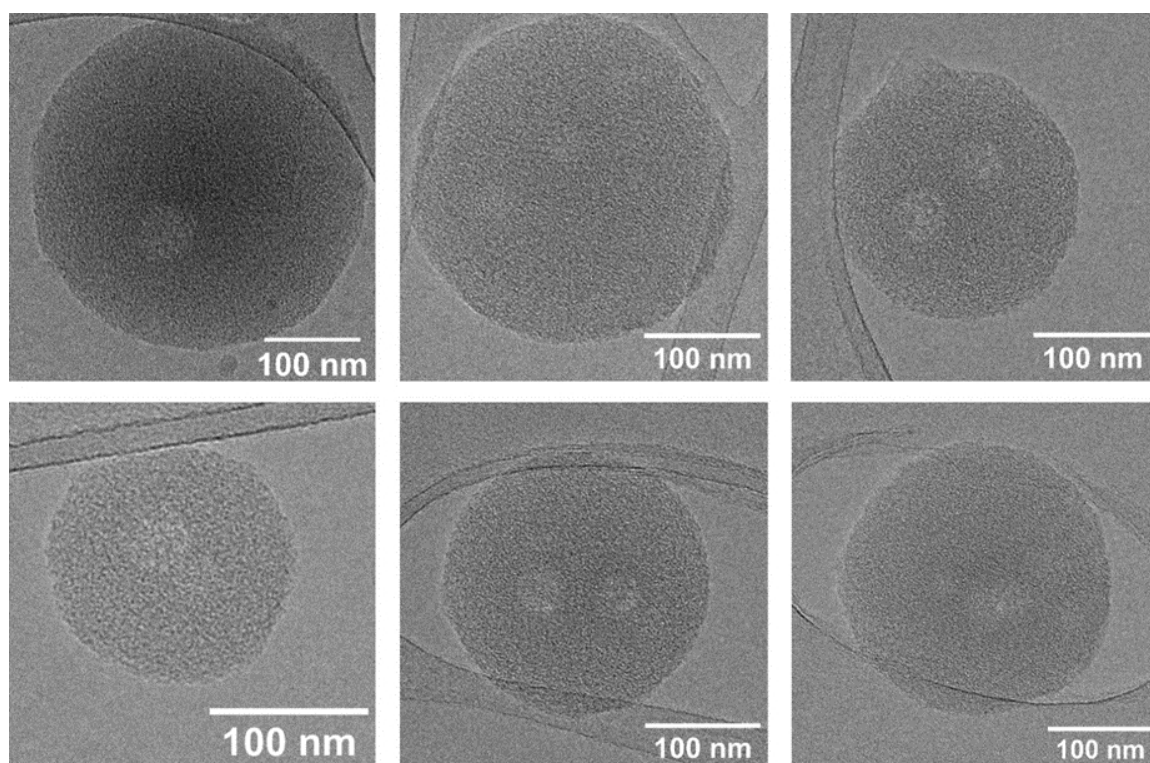


Figure 3.48: Additional cryo-EM image of self-assembled **O5*O6**. Conditions: 1 μ M **O5*O6**, 10 mM sodium phosphate buffer pH 7.2, 0.03 mM spermine \cdot 4 HCl, 20 vol% ethanol.

3.3.6 DLS Measurement Conditions and Results

Table 3.6: Key results and measurement conditions of DLS measurement at 20 °C of a solution of **O1*O2**, **O3*O4**, **O5*O6**, and **O5*O6** with 6% **O9**. Conditions: 1 μ M each single strand, 10 mM sodium phosphate buffer pH 7.2, 0.03 mM spermine \cdot 4 HCl, 20 vol% ethanol.

Duplex	Size Diameter with Error (nm)	Z-Average Size Diameter (nm)	PDI	PDI Width (nm)	Count Rate (kcps)	Attenuator
O1*O2	191.8 \pm 59.5	172.2	0.107	56.38	11446.9	7
O3*O4	196.3 \pm 66.5	174.2	0.113	58.44	16291.0	7
O5*O6	185.9 \pm 62.2	166.1	0.103	53.30	21334.9	7
O5*O6 + 6% O9	188.1 \pm 55.5	171.5	0.095	52.91	7779.5	8

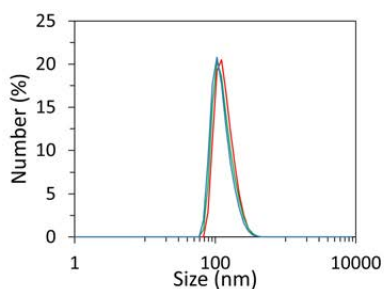


Figure 3.49: DLS measurements of **O1*O2** (red), **O3*O4** (green), and **O5*O6** (blue). Conditions: 1 μ M each single strand, 10 mM sodium phosphate buffer pH 7.2, 0.03 mM spermine \cdot 4 HCl, 20 vol% ethanol.

3.3.7 Additional Light-Harvesting Experiments

Table 3.7: Fluorescence emission maximum of the cyanine emission of **O9**, **O11**, and the **O9** and **O11** doped supramolecular assemblies of **O1*O2**, **O3*O4**, and **O5*O6**. Data retrieved from Figure 3.12 and Figure 3.13.

	FL _{max} of Cy3		FL _{max} of Cy5
O9	568 nm	O11	669 nm
O1*O2 + O9	579 nm	O1*O2 + O11	680 nm
O3*O4 + O9	578 nm	O3*O4 + O11	678 nm
O5*O6 + O9	576 nm	O5*O6 + O11	682 nm

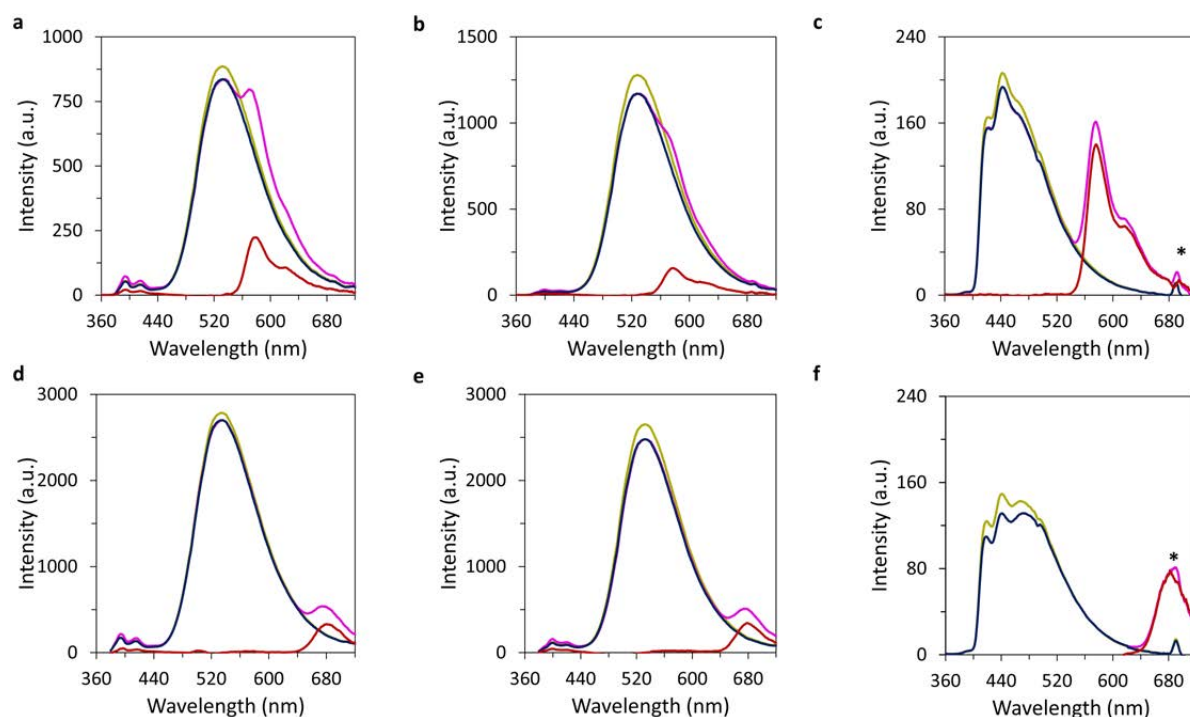


Figure 3.50: Fluorescence emission spectra of undoped (yellow) and Cy3-doped (pink, **a–c**) or Cy5-doped (pink, **d–f**) nanostructures. Extracted parts of the doped emission Cy3 or Cy5 (red) and pyrene (blue). (**a** and **d**) **O1*O2** (**b** and **e**) **O3*O4** and (**c** and **f**) **O5*O6**. Conditions: 1 μM each pyrene-DNA conjugate, (**a** and **b**) 0.15 μM **O9**, (**c**) 0.06 μM **O9**, (**d** and **e**) 0.15 μM **O11**, and (**f**) 0.06 μM **O11**, 10 mM sodium phosphate buffer pH 7.2, 0.03 mM spermine \cdot 4 HCl, 20 vol% ethanol, (**a–c**) and (**f**): λ_{ex} . 345 nm, (**d**) and (**e**): λ_{ex} . 365 nm, * second-order diffraction.

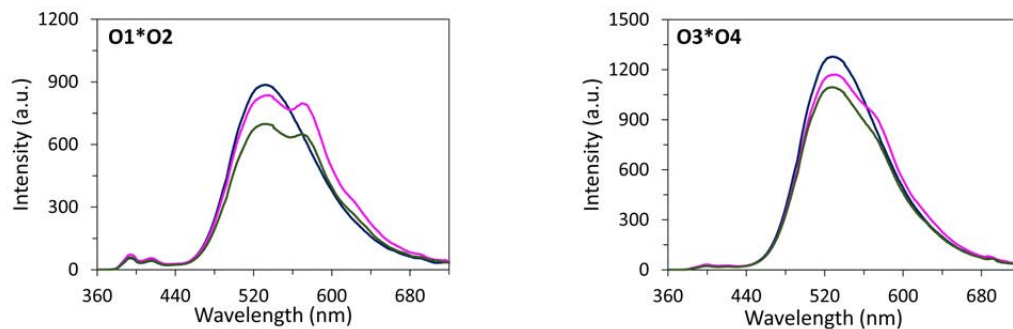


Figure 3.51: Fluorescence emission spectra of **O1*O2** (left) and **O3*O4** (right) after controlled self-assembly (blue), after the addition of 15% **O9** at 20 °C (green), and after reassembly by controlled cooling to 20 °C (pink). Conditions: 1 μM each pyrene-modified single strand (+ 0.15 μM **O9**), 10 mM sodium phosphate buffer pH 7.2, 0.03 mM spermine \cdot 4 HCl, 20 vol% ethanol, λ_{ex} . 345 nm.

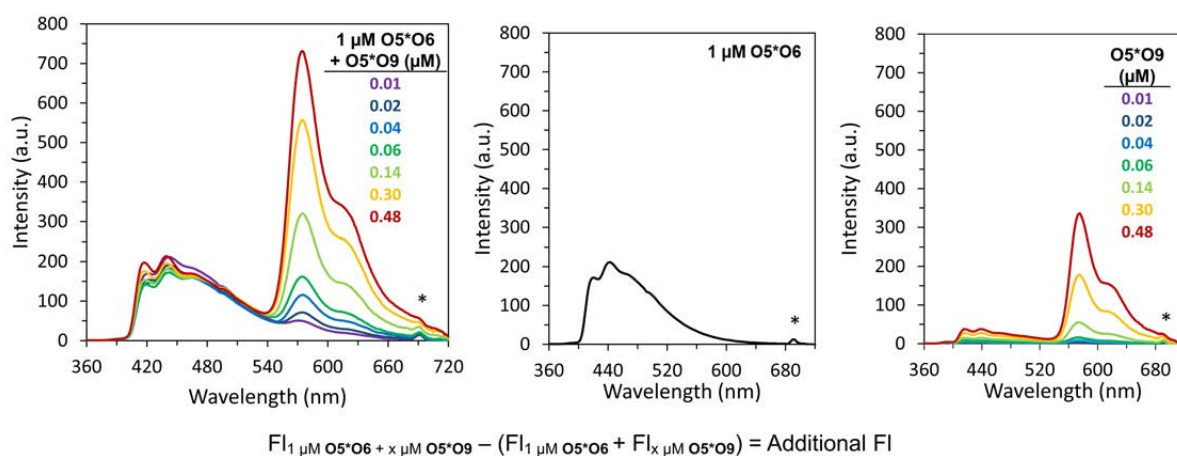


Figure 3.52: Fluorescence emission spectra relevant for the determination of additional Cy3 fluorescence in self-assembled **O5*O6** at 20 °C with the addition of different amounts of **O5*O9** (0.01–0.48 μM) (left), 1 μM **O5*O6** (middle), and **O5*O9** (0.01–0.48 μM) (right). Conditions: 1 μM **O6**, 1.01–1.48 μM **O5**, 0.01–0.48 μM **O9** (left), 1 μM **O5*O6** (middle), and 0.01–0.48 μM **O5*O9** (right), 10 mM sodium phosphate buffer pH 7.2, 0.03 mM spermine \cdot 4 HCl, 20 vol% ethanol, λ_{ex} . 345 nm, * second-order diffraction.

Chapter 4

Influence of Sticky-End Length and Spermine & Ethanol Concentration on Supramolecular Assembly of Pyrene-DNA Conjugates

As described in the general introduction (chapter 1), the self-assembly in aqueous media can be influenced by varying the pH, the concentration of salts, and the concentration of solvent or anti-solvent. Furthermore, altering the chemical composition of the supramolecular monomer also changes the self-assembly properties. In the previous chapter 3, three different substitution patterns on the pyrene units were tested, but all measurements were conducted at the same pH and with the same salt and ethanol concentrations (10 mM sodium phosphate buffer at pH 7.2, 0.03 mM spermine · 4 HCl, and 20 vol% ethanol). In the following chapter, first, the influence of different spermine tetrahydrochloride and ethanol concentrations are investigated, and then the impact of the composition of the supramolecular monomer, namely the number of pyrene modifications on 3'-end modified pyrene-DNA conjugates is evaluated.

4.1 Results and Discussion

The DNA strands used in this chapter are listed in Figure 4.1. **O5** and **O6** were already described in chapter 3, and **O13–O16** were prepared *via* solid-phase synthesis according to the phosphoramidite approach described in the general introduction (section 1.3) and purified by reverse-phase HPLC. Detailed experimental procedures are provided in the appendix of this chapter (section 4.3). The preparation of the 2,7-dialkynyl pyrene phosphoramidites is described in the experimental section of the previous chapter (section 3.3) and was conducted according to literature.¹⁹ All oligomers listed in Figure 4.1 consist of a DNA 20-mer and 2,7-dialkynyl pyrene modifications on the 3'-end (chemical structure of the modification in Figure 4.1b). The amount of phosphodiester-linked pyrene units differs between the oligomers. **O5** and **O6** are equipped with three pyrene units, **O13** and **O14** with two, and **O15** and **O16** with only one pyrene unit. The pyrene-DNA conjugates **O5** and **O6**, **O13** and **O14**, and **O15** and **O16** are complementary.

a

Strand	Sequence
O5	5'-CAA GGT CCG ATG CAA GGA AG-(2,7-Py) ₃
O6	(2,7-Py) ₃ -GTT CCA GGC TAC GTT CCT TC-5'
O13	5'-CAA GGT CCG ATG CAA GGA AG-(2,7-Py) ₂
O14	(2,7-Py) ₂ -GTT CCA GGC TAC GTT CCT TC-5'
O15	5'-CAA GGT CCG ATG CAA GGA AG-(2,7-Py)
O16	(2,7-Py)-GTT CCA GGC TAC GTT CCT TC-5'

b

2,7-Py

Figure 4.1: (a) DNA sequences of the 3'-end modified 2,7-dialkynyl pyrene-DNA conjugates bearing three (**O5** and **O6**), two (**O13** and **O14**), and one (**O15** and **O16**) pyrene units and (b) the molecular structure of 2,7-dialkynyl pyrene.

4.1.1 Influence of Spermine and Ethanol Concentration on the Supramolecular Assembly

The self-assembly of **O5*O6** at different concentrations of spermine tetrahydrochloride (**Sp**, Figure 4.2) with 20 vol% ethanol was tested by UV-vis spectroscopy (Figure 4.3a). At 75 °C, the DNA strands are unaggregated (dashed line in Figure 4.3a). The absorption with a maximum at 273 nm is a combination of DNA absorption and 2,7-pyrene. A second band exhibits a maximum at 338 nm and originates only from the 2,7-dialkynyl pyrene. To test the influence of **Sp** samples with different concentrations of the salt were cooled from 75 °C to 20 °C (0.5 °C·min⁻¹).

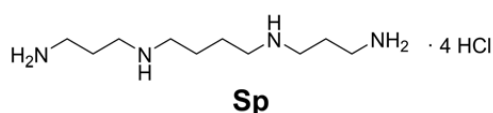


Figure 4.2: Molecular structure of spermine tetrahydrochloride (**Sp**).

Upon cooling, the absorbance around 270 nm decreased in all conditions. This decrease originates mostly from the hybridization of the DNA bases. In addition, the samples started to scatter upon cooling. When monitoring the scattering effect at 420 nm at the different **Sp** concentrations, it increases linearly with increasing amounts of **Sp**. Furthermore, the absorption bands broaden with an increased presence of **Sp** (Figure 4.3c). With 20 vol% ethanol, the scattering starts at a **Sp** concentrations smaller than 0.02 mM. The observed scattering in UV-vis spectroscopy suggests the formation of particles inside the solution. Furthermore, these experiments propose that the size and amount of the particles are influenced by the amount of **Sp** added.

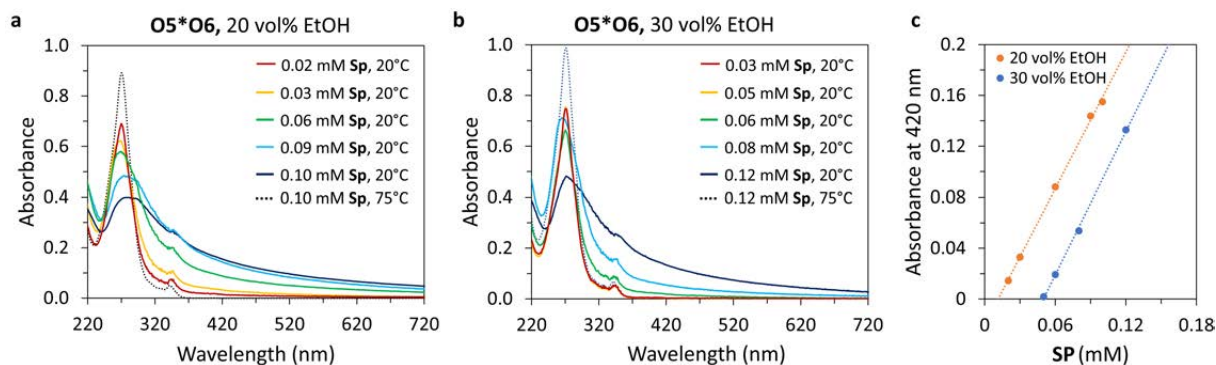


Figure 4.3: Temperature-dependent UV-vis absorption spectra of **O5*O6** at different **Sp** and ethanol concentrations (a) with 20 vol% ethanol, (b) 30 vol% ethanol (for (a and b) dashed line: at 75 °C and solid lines: at 20 °C after self-assembly), and (c) absorbance at 420 nm at 20 °C after cooling with different **Sp** concentrations at 20 vol% ethanol (orange) and 30 vol% ethanol (light blue). Conditions: 1 μ M each single strand, 10 mM sodium phosphate buffer pH 7.2, 0.02–0.12 mM spermine \cdot 4 HCl, 20 or 30 vol% ethanol.

Additionally, the supramolecular assembly of **O5*O6** was evaluated at 30 vol% ethanol. The bands before cooling (75 °C) and after cooling (20 °C) are attributed according to the measurement at 20 vol% ethanol described above. Similarly, scattering was observed in measurements of self-assembled **O5*O6** at 20 °C with elevated **Sp** concentrations. The scattering also increases at higher **Sp** concentrations. This observation suggests the formation of larger and more particles at elevated **Sp** concentrations. UV-vis absorption measurements of sample solutions that contained 30 vol% ethanol began to scatter at **Sp** concentrations of 0.06 mM. In contrast, the measurements with 20 vol% ethanol exhibited scattering at **Sp** concentration of 0.02 mM. Hence, increasing amounts of **Sp** are required at elevated ethanol contents to form more and larger assemblies (Figure 4.3c). These data suggest that ethanol has a destabilizing effect on the assemblies, whereas **Sp** enhances the formation of more and larger aggregates. AFM measurements were performed to prove the formation of nanostructures and to determine their sizes and shapes.

To visualize the self-assembled structures of **O5*O6**, AFM experiments of the self-assembled **O5*O6** at different **Sp** and ethanol concentrations were conducted. The slowly cooled solutions of **O5*O6** were adsorbed on an APTES-modified mica and subsequently measured (detailed experimental conditions in the general methods section 8). First, AFM measurements with 20 vol% ethanol and different **Sp** concentrations are presented (Figure 4.4).

On the AFM image at 0.02 mM **Sp**, spherical nanostructures were observed, but their height and size are not well defined (Figure 4.4, left). An increase in the concentration of **Sp** to 0.03 mM led to more scattering in the UV-vis experiments. In AFM images of this condition, larger nanostructures were observed (Figure 4.4, middle). Upon raising the **Sp** concentration to 0.09 mM, the conditions where pronounced scattering was detected in UV-vis spectroscopy, AFM images displayed the presence of large particles (see Figure 4.4, right). The findings on the AFM images support the results from UV-vis spectroscopy. The increase in **Sp** concentration led to the development of increasingly larger aggregates.

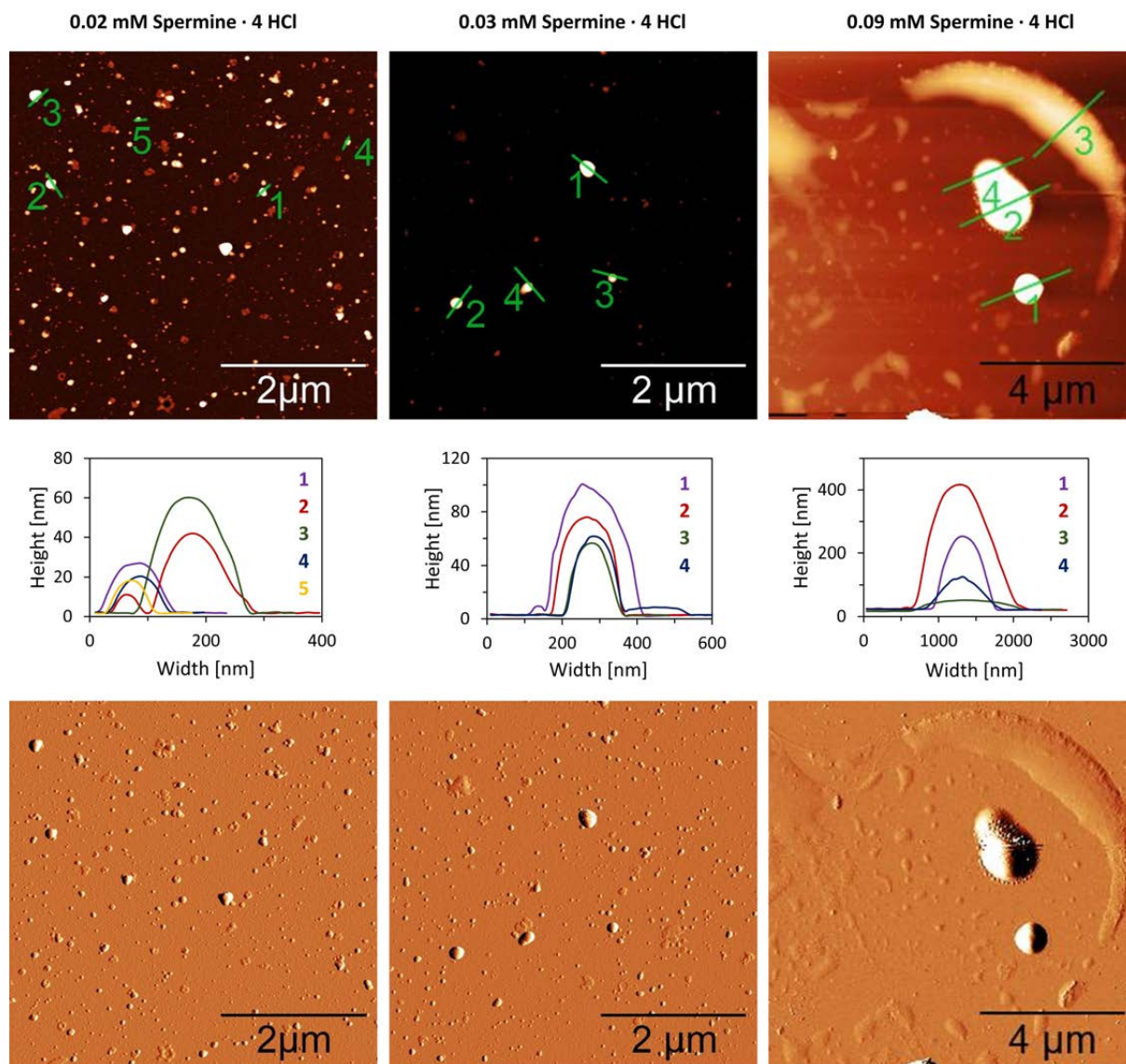


Figure 4.4: AFM scan (top) with corresponding cross sections (middle) and deflection scan of assembled **O5*O6** with 0.02 mM **Sp** (left), 0.03 mM **Sp** (middle), and 0.09 mM **Sp** (right). Conditions: 1 μM **O5*O6**, 10 mM sodium phosphate buffer pH 7.2, 0.02–0.09 mM spermine · 4 HCl, 20 vol% ethanol.

AFM experiments with **O5*O6** in 30 vol% ethanol were also conducted (Figure 4.5). First, AFM images of self-assembled nanostructures with 20 vol% ethanol (Figure 4.5 left) are compared to assemblies formed in a solution containing 30 vol% ethanol (Figure 4.5 middle and right). Increasing the amount of ethanol from 20 vol% to 30 vol% leads to the formation of smaller (Figure 4.5, middle). AFM measurements of **O5*O6** containing 30 vol% ethanol and 0.08 mM **Sp**, a **Sp** concentration at which scattering was observed in UV-vis spectroscopy, revealed the formation of large undefined, and small particles (Figure 4.5, right).

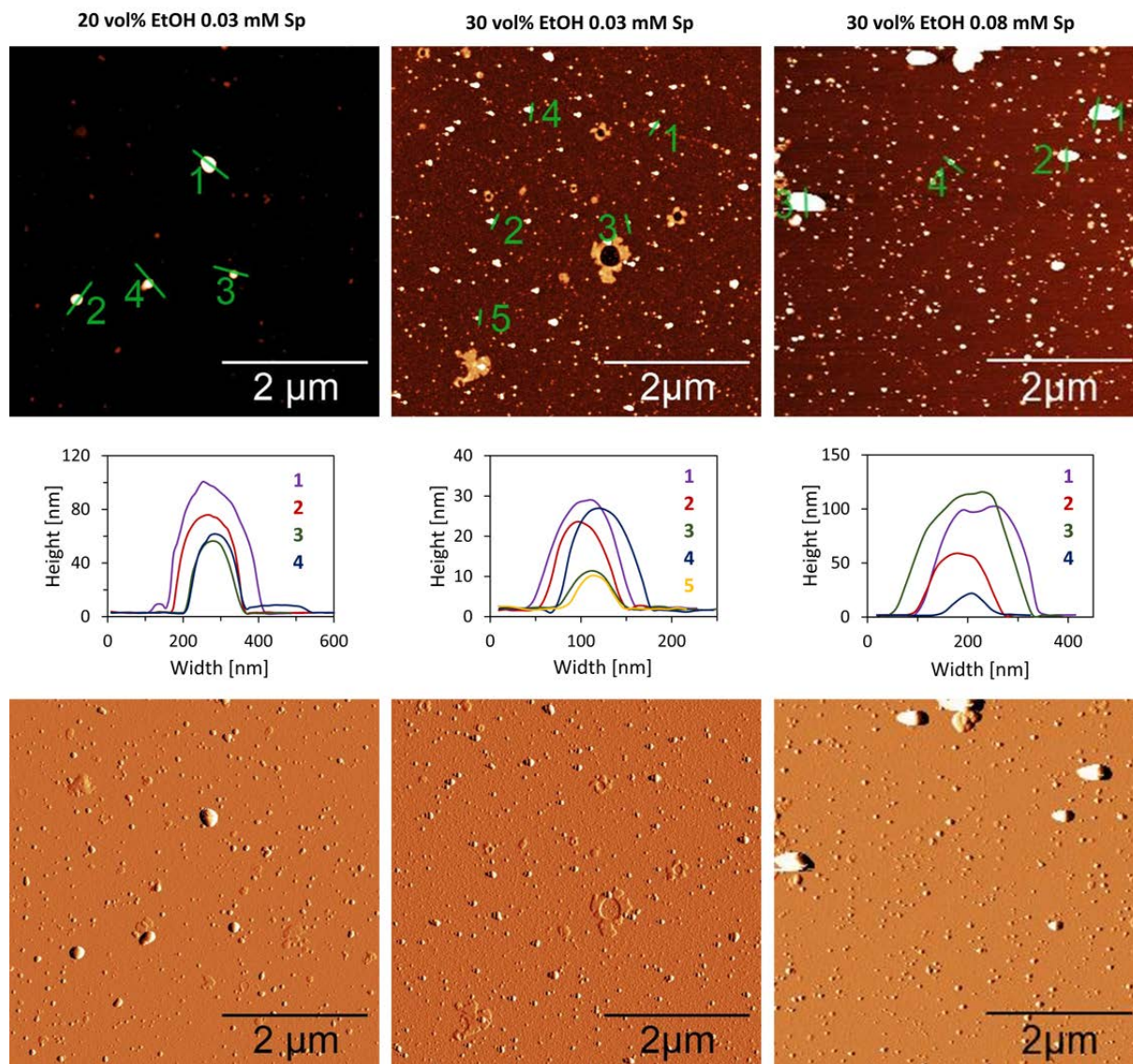


Figure 4.5: AFM scan (top) with corresponding cross sections (middle) and deflection scan of assembled **O5*O6** with 20 vol% ethanol and 0.03 mM **Sp** (left), with 30 vol% ethanol and 0.03 mM **Sp** (middle), and with 30 vol% ethanol and 0.08 mM **Sp** (right). Conditions: 1 μM **O5*O6**, 10 mM sodium phosphate buffer pH 7.2, 0.03 or 0.08 mM spermine · 4 HCl, 20 or 30 vol% ethanol.

In summary, the concentrations of **Sp** and ethanol influence the self-assembly properties of **O5*O6**. Large and less-defined aggregates are formed at elevated **Sp** concentrations. The formation of large structures can either be monitored by UV-vis spectroscopy in the form of scattering or by AFM. At increased ethanol contents, scattering is only observed at more elevated spermine concentrations.

4.1.2 Influence of Length of Sticky Ends on the Supramolecular Assembly

Here, the self-assembly of **O5*O6** is compared to the pyrene-DNA conjugates with two pyrene units on each side (**O13*O14**) and the one, with one pyrene on each side (**O15*O16**). The supramolecular assembly is dependent on the ethanol and **Sp** concentration, as discussed in the last section. Therefore, different conditions were evaluated to assemble **O13*O14** and **O15*O16** successfully. The conditions were optimized with UV-vis spectroscopy (Figure 4.6), and the formation of nano-assemblies was evaluated by AFM (Figure 4.7 and Figure 4.9).

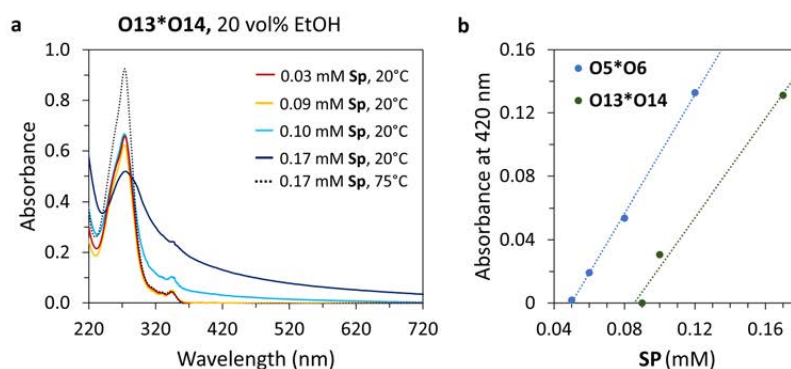


Figure 4.6: Temperature-dependent UV-vis absorption spectra of (a) **O13*O14** at different **Sp** concentrations (dashed line: at 75 °C and solid lines: at 20 °C after self-assembly), (b) absorbance at 420 nm at different **Sp** concentrations at **O5*O6** (light blue) and **O13*O14** (green). Conditions: 1 μ M each single strand, 10 mM sodium phosphate buffer pH 7.2, 0.03–0.17 mM spermine \cdot 4 HCl, 20 vol% ethanol.

Self-assembly of **O13*O14** was assessed at 20 vol% ethanol with different **Sp** concentrations. At 75 °C, when the DNA strands are unaggregated, two absorption bands were observed in the UV-vis measurements (dashed line in Figure 4.6a). The strong absorption band with a maximum at 272 nm is attributed to DNA and 2,7-dialkynyl pyrene. The second band with a maximum at 344 nm originates only from the 2,7-dialkynyl pyrene. After controlled cooling from 75 °C to 20 °C ($0.5 \text{ }^\circ\text{C}\cdot\text{min}^{-1}$), the pyrene band at 344 nm remained the same, and the absorbance around 270 nm decreased. This decrease originates mostly from the hybridization of the DNA bases. In addition, scattering was observed at **Sp** concentrations greater than 0.09 mM.

By measuring the absorption at 420 nm, the increase of the scattering was evaluated at different **Sp** concentrations. The absorption at 420 nm increased linearly with the **Sp** concentration, where scattering was observed (Figure 4.6b). In addition to the rise of the scattering, the absorption bands broadened. This effect is most pronounced at 0.17 mM **Sp**, the sample with the highest amount of **Sp** measured (dark blue curve Figure 4.6a). In UV-vis experiments of self-assembled **O5*O6**, the absorption at 420 nm started to rise at **Sp** concentrations of 0.03 mM. In comparison, scattering occurred only at concentrations higher than 0.09 mM **Sp** in samples containing **O13*O14** (Figure 4.6b). This observation can be explained by the reduced hydrophobic interactions stemming from the reduced number of hydrophobic units on the DNA strands in **O13*O14**. Hence, more **Sp** is required to stabilize the assemblies.

To better understand the self-assembly of **O13*O14**, AFM experiments were performed (Figure 4.7). At the conditions that yield regularly sized nanostructures on AFM in **O5*O6** (0.03 mM **Sp** and 20 vol% ethanol), only small aggregates were observed with **O13*O14** (Figure 4.7, left). In contrast, at 0.09 mM **Sp**, regular and equally sized spherical assemblies with diameters between 100–150 nm were observed (Figure 4.7, middle). AFM images of **O13*O14** with 0.10 mM **Sp** displayed a limited quantity of large agglomerates. These results suggest that the amount of **Sp** is crucial for the successful assembly of **O13*O14**. However, the concentration of **Sp** must be meticulously regulated, as nanostructures produced by **O13*O14** tend to agglomerate at elevated **Sp** concentrations.

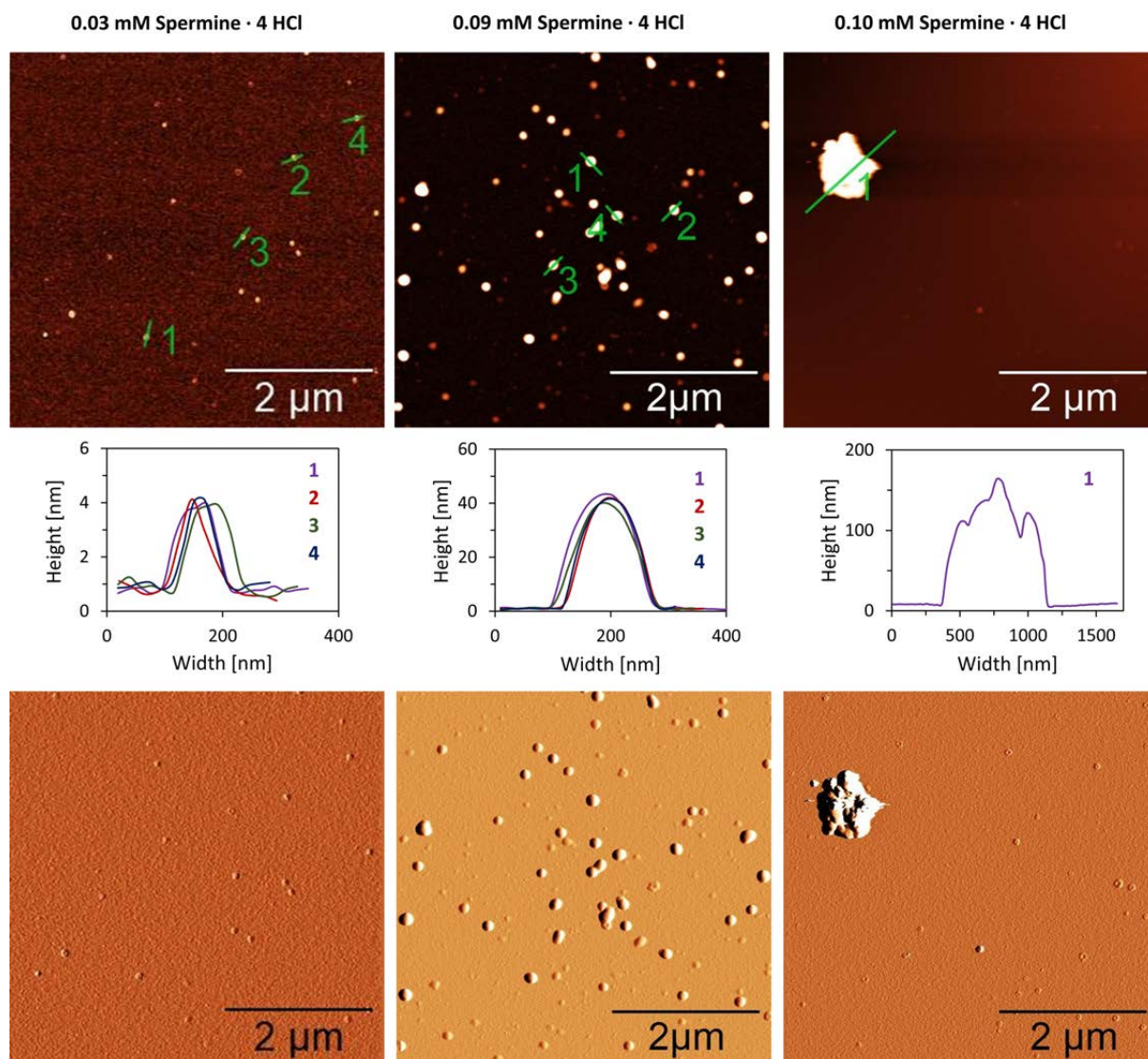


Figure 4.7: AFM scan (top) with corresponding cross sections (middle) and deflection scan of assembled **O13*O14** with 20 vol% ethanol and 0.03 mM **Sp** (left), with 0.09 mM **Sp** (middle), and with 0.10 mM **Sp** (right). Conditions: 1 μM **O13*O14**, 10 mM sodium phosphate buffer pH 7.2, 0.03–0.10 mM spermine · 4 HCl, 20 vol% ethanol.

The self-assembly of **O15*O16**, the pyrene-DNA conjugate with only one pyrene unit at each end, was also assessed by temperature-dependent UV-vis spectroscopy and AFM. Various conditions were examined using UV-vis spectroscopy. No scattering was detected in UV-vis measurements involving ethanol. Hence, the ethanol was entirely removed (Figure 4.8). UV-vis measurements of the **O15*O16** at 75 °C revealed two bands with a maximum around 270 nm

and 340 nm (dashed line in Figure 4.8). The one at 270 nm is attributed to the DNA bases and the 2,7-dialkynyl pyrene, and the one at 340 nm originates from the pyrene. After controlled cooling to 20 °C, the band at 270 nm is reduced because of the hybridization of the two single strands, whereas the band at 340 nm remains unchanged at all concentrations. In experiments with 1.5 mM **Sp**, scattering was observed, a sign of assembly (dark blue graph in Figure 4.8).

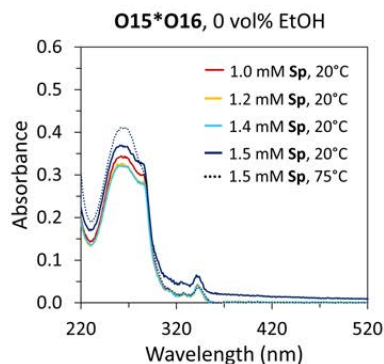


Figure 4.8: Temperature-dependent UV-vis absorption spectra of **O15*O16** at different **Sp** concentrations (dashed line: 75 °C and solid lines: at 20 °C after self-assembly). Conditions: 1 μ M each single strand, 10 mM sodium phosphate buffer pH 7.2, 1.0–1.5 mM spermine \cdot 4 HCl.

AFM images of the pyrene-DNA conjugate with only one pyrene on each side **O15*O16** at 1.5 mM **Sp** revealed the aggregation of the duplexes (Figure 4.9). Mostly sheets with a height of 2 nm and a few larger toroidal aggregates were observed. The height of the sheets correlates well with the thickness of a DNA duplex, suggesting a 2-dimensional sheet-like assembly of the pyrene-DNA conjugates containing one pyrene unit on each side. The present toroidal assemblies express a height of up to 8 nm. In a previous study conducted with phenanthrene-DNA conjugates, initially, sheets were observed on APTES-modified mica.¹⁴⁶ However, upon increase of the oligomer concentration to 5 μ M the formation of vesicles was observed on AFM and TEM. We assume the sheets are only formed once the vesicle interacts with the AFM surface. Therefore, the presence of sheets and toroids here hints at the presence of vesicles in the solution.

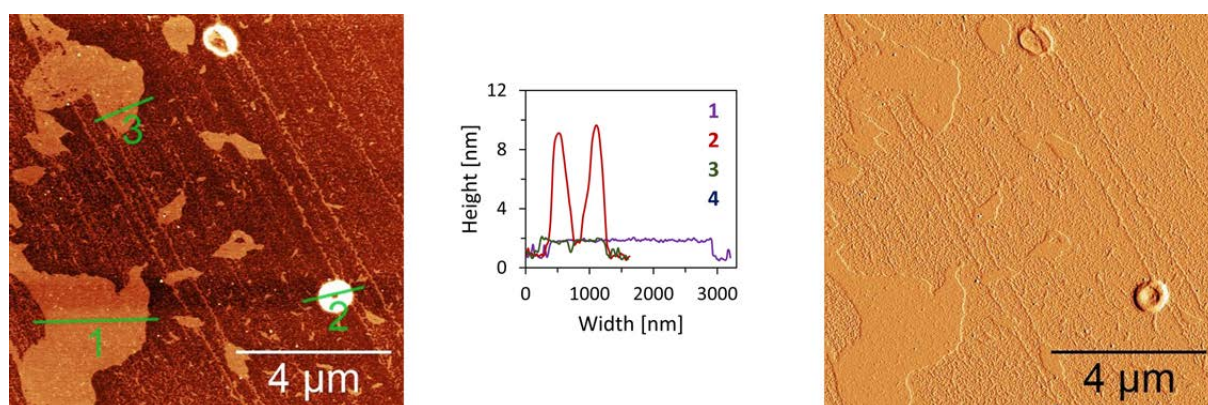


Figure 4.9: AFM scan (left) with corresponding cross sections (middle) and deflection scan of assembled **O15*O16** with 1.5 mM **Sp**. Conditions: 1 μ M **O15*O16**, 10 mM sodium phosphate buffer pH 7.2, 1.50 mM spermine \cdot 4 HCl.

In summary, shortening the pyrene sticky ends has a strong influence on the self-assembly behavior of pyrene-DNA conjugates (Figure 4.10). A decrease in pyrene units in the sticky ends decreases the hydrophobic interactions in the assemblies, which leads to less stable aggregates. One approach to counteract the loss of stability due to the reduced hydrophobic interactions is the decrease of electrostatic repulsion between the backbones of the DNA duplexes. The repulsion between the negatively charged phosphodiester groups of the DNA duplexes can be reduced by increasing the amount of spermine tetrahydrochloride in the aqueous solution. Hence, conjugates with shorter sticky ends require larger quantities of spermine tetrahydrochloride to form assemblies. Importantly, when the contents of spermine tetrahydrochloride are increased the aggregates start to agglomerate. Another approach to counteract the loss of stability due to the reduced hydrophobic interactions in pyrene-DNA conjugates with shorter sticky ends is the decrease of the ethanol content in the aqueous media, leading to a more polar medium. When the medium is more polar, hydrophobic interactions are increased. Therefore, ethanol was entirely removed to form assemblies with the pyrene-DNA conjugate with only one pyrene unit on each side **O15*O16**.

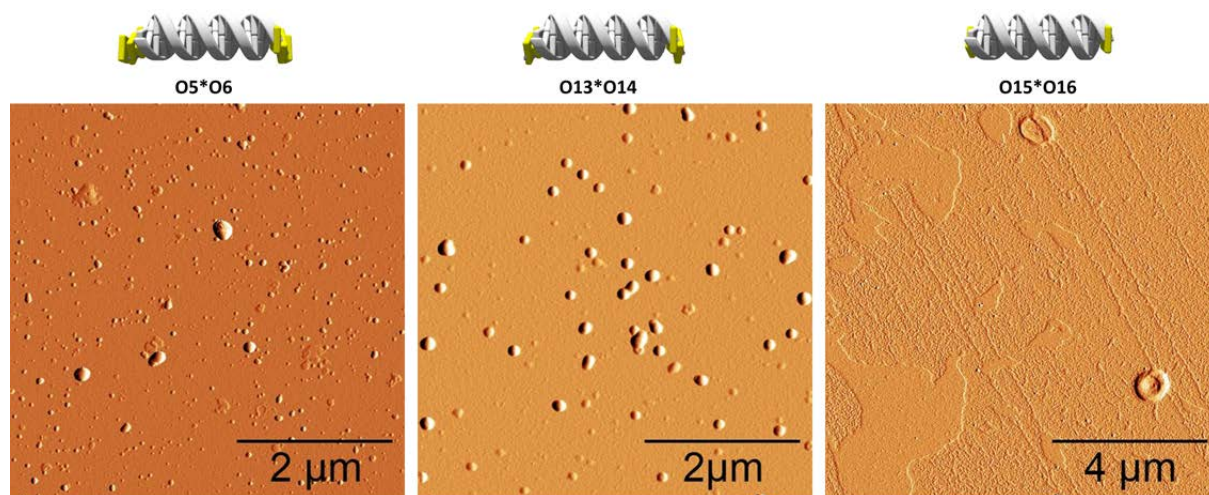


Figure 4.10: Summarized from left to right: schematic representations (top) and AFM deflection scans (bottom) of assembled pyrene-DNA conjugates with decreasing length of sticky ends: **O5*O6** (left), **O13*O14** (middle), and **O15*O16** (right). Conditions: 1 μM each single strand, 10 mM sodium phosphate buffer pH 7.2, **O5*O6**: 20 vol% ethanol and 0.03 mM spermine · 4 HCl; **O13*O14**: 20 vol% ethanol and 0.09 mM spermine · 4 HCl; and **O15*O16**: 0 vol% ethanol and 1.50 mM spermine · 4 HCl.

4.2 Conclusions and Outlook

In conclusion, AFM and UV-vis spectroscopy revealed that the concentration of spermine tetrahydrochloride and ethanol influence the self-assembly properties of pyrene-DNA conjugates. Elevated concentrations of spermine tetrahydrochloride lead to the agglomeration of aggregates. At reduced concentrations of spermine tetrahydrochloride, no nanostructures were formed. The experiments suggest that spermine tetrahydrochloride stabilizes the assemblies, and elevated concentrations of spermine tetrahydrochloride facilitate the agglomeration of the assemblies. The content of ethanol has the opposite effect. An increased ethanol content led to the formation of smaller aggregates, and more spermine tetrahydrochloride was required to form agglomerates of assemblies. Hence, ethanol has a destabilizing effect.

Furthermore, the influence of the length of sticky ends in complementary 3'-end modified pyrene-DNA conjugates was evaluated with AFM and UV-vis spectroscopy. It was found that shortening the pyrene sticky ends has a strong influence on the self-assembly behavior of pyrene-DNA conjugates. Conjugates bearing shorter sticky ends require larger quantities of spermine tetrahydrochloride to form assemblies to counteract the reduction of hydrophobic interactions. The pyrene-DNA conjugates with only one pyrene on each side self-assemble into sheets and toroids after adjusting the aqueous medium by increasing the spermine tetrahydrochloride contents and completely removing ethanol. On AFM were observed. Conjugates with two and three pyrene units self-assembled into spherical nanostructures.

In this chapter, there were always equal amounts of pyrene modifications on each side of the pyrene-DNA duplex. It would be interesting to test pyrene-DNA conjugates with an asymmetrical number of sticky ends on two sides. Asymmetric modifications could give more control over the sizes of the nanostructures due to the crowding effects on one side. Furthermore, pyrene-DNA conjugates with more than three pyrenes on each side could be investigated to verify the observed trend of increase in size depending on the length of the sticky ends.

4.3 Appendix - Chapter 4

First, the synthesis, purification, and characterization (HPLC traces and MS spectra) of the oligonucleotides **O17–O22** are described. Afterwards, the DLS measurements are presented.

4.3.1 Synthesis and Characterization of Oligonucleotides

3'-modified pyrene-DNA conjugates **O13–O16** were synthesized on an Applied Biosystems 394 DNA/RNA synthesizer applying a standard cyanoethyl phosphoramidite coupling protocol on a 1 μ mol scale. The solid-phase synthesis and purification are described in detail in chapter 8.

Afterward, the oligomers **O13–O16** were purified by reverse-phase HPLC (Shimadzu LC-20AT, ReproSil 100 C18, 5,0 μ m, 250 \times 4 mm) with a flow rate of 1 ml/min, with a detection wavelength of 260 nm at 40 °C. **O13** and **O14** were purified with solvent A: aqueous 2.1 mM triethylamine (TEA) / 25 mM 1,1,1,3,3,3-hexafluoropropan-2-ol (HFIP) pH 8 and solvent B: acetonitrile. Whereas **O15** and **O16** were purified with solvent A: aqueous 90 mM triethylammonium acetate (TEAA) at pH 7 and solvent B: acetonitrile. The following gradient was applied B [%] (t_R (min)): 5 (0), 20 (24). The respective HPLC traces are depicted in Figure 4.11.

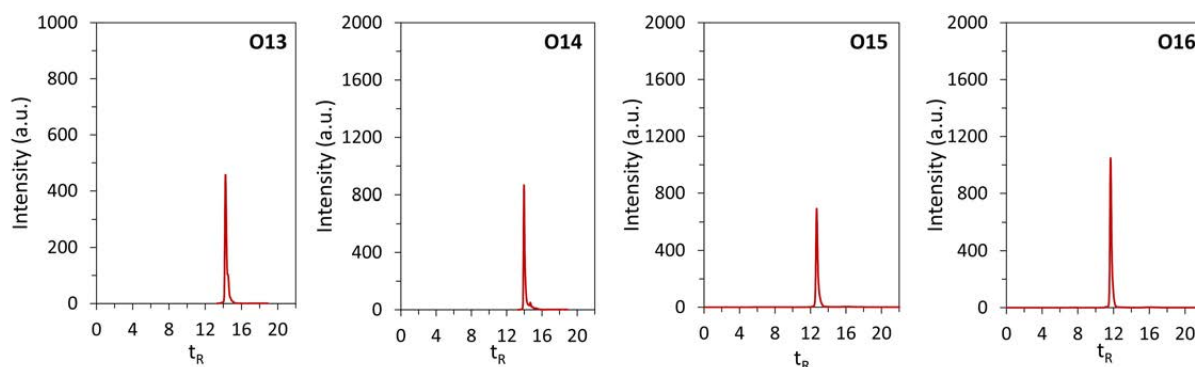


Figure 4.11: HPLC traces of pyrene-DNA conjugates **O13–O16**.

After that, the absorbance of the pyrene-DNA conjugates was measured at 260 nm to determine the concentration of the stock solutions and yields of **O13–O16**. The concentrations were determined by applying the Beer-Lambert law. The following molar absorptivities (at 260 nm) in $\text{l}\cdot\text{mol}^{-1}\cdot\text{cm}^{-1}$ were used: ϵ_A ; 15'300, ϵ_T ; 9'000, ϵ_G ; 11'700, ϵ_C ; 7'400, and $\epsilon_{2,7\text{-pyrene}}$; 32'000. The mass spectra results of **O13–O16** are listed in Table 4.1, and the mass spectra are displayed in Figure 4.12–Figure 4.19.

Table 4.1: Pyrene-DNA oligonucleotide sequences of **O13–O16**, calculated and found masses by NSI-MS, and yields.

Strand	Sequence (5'→3')	Calcd mass	Found mass	Yield [%]
O13	CAA GGT CCG ATG CAA GGA AGXX	7000.2757	7000.2711	33
O14	CTT CCT TGC ATC GGA CCT TGXX	6835.1994	6834.1947	50
O15	CAA GGT CCG ATG CAA GGA AGX	6599.1859	6599.1823	31
O16	CTT CCT TGC ATC GGA CCT TGX	6434.1096	6434.1073	36

X = 2,7-dialkynyl pyrene

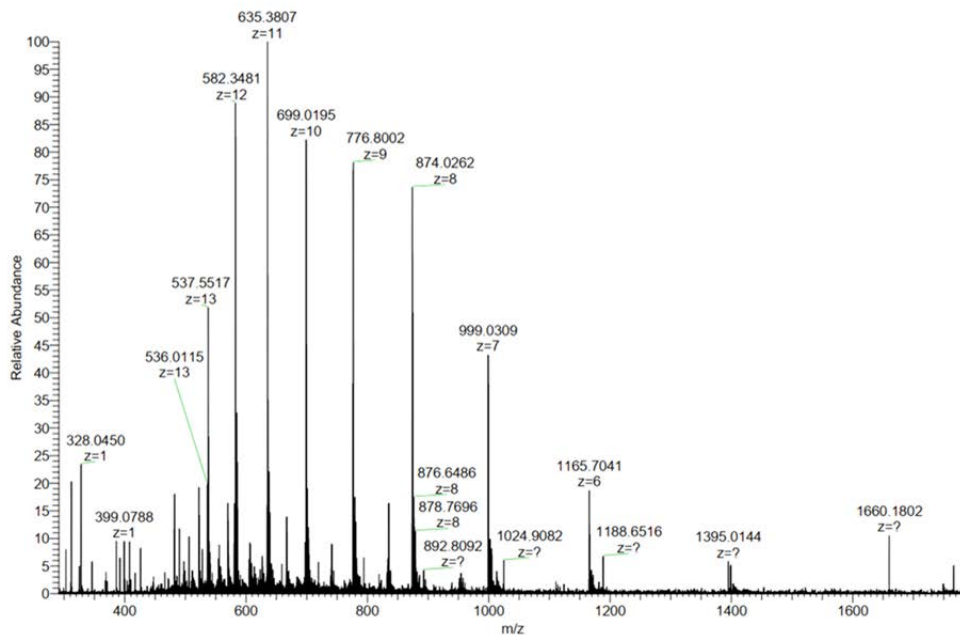


Figure 4.12: MS spectrum of O13.

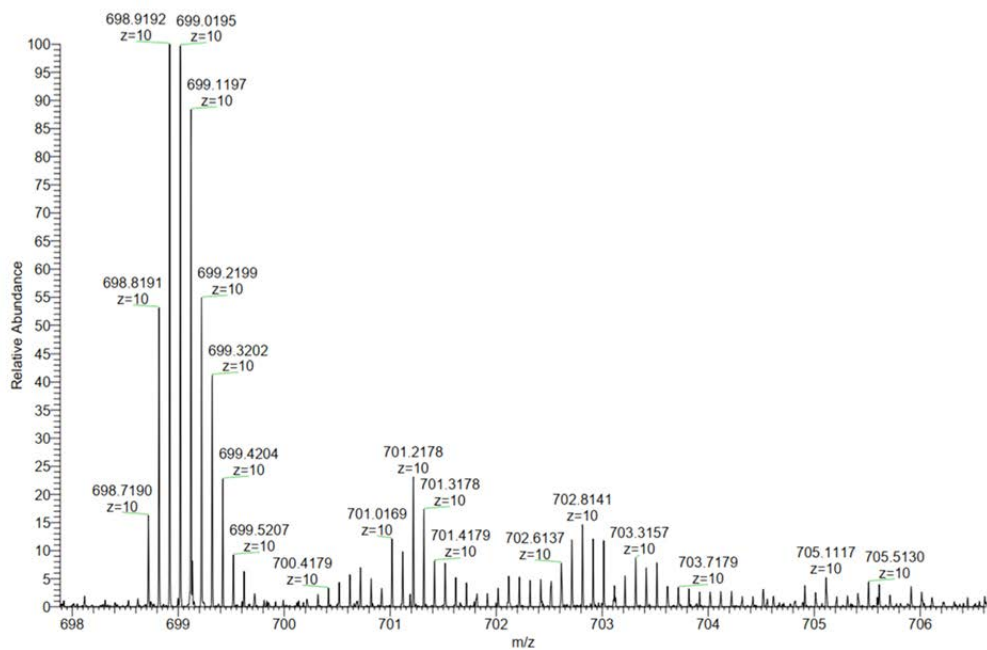


Figure 4.13: MS spectrum of O13.

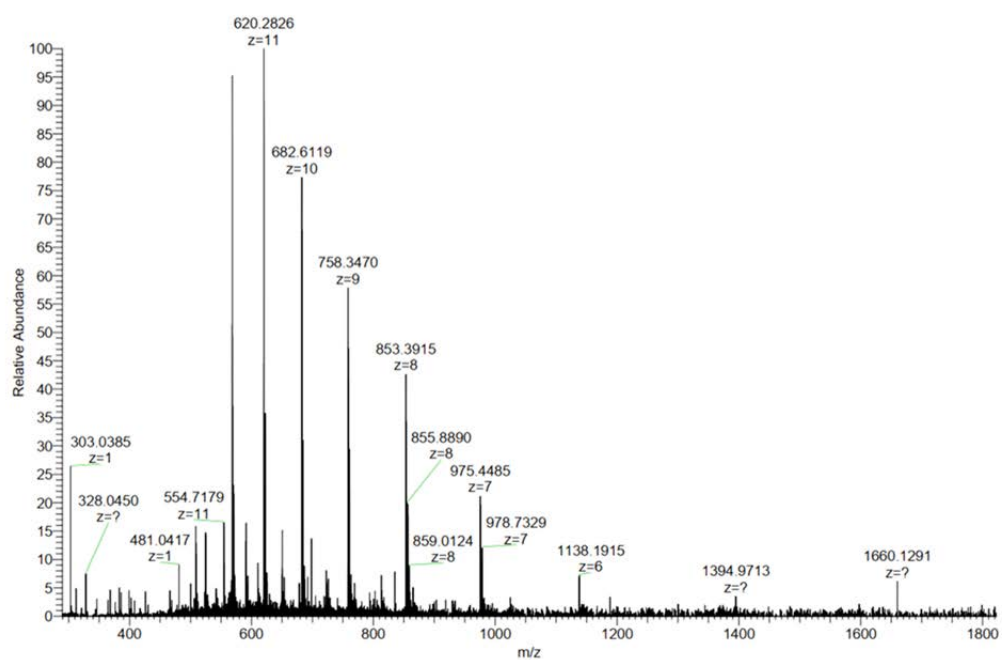


Figure 4.14: MS spectrum of O14.

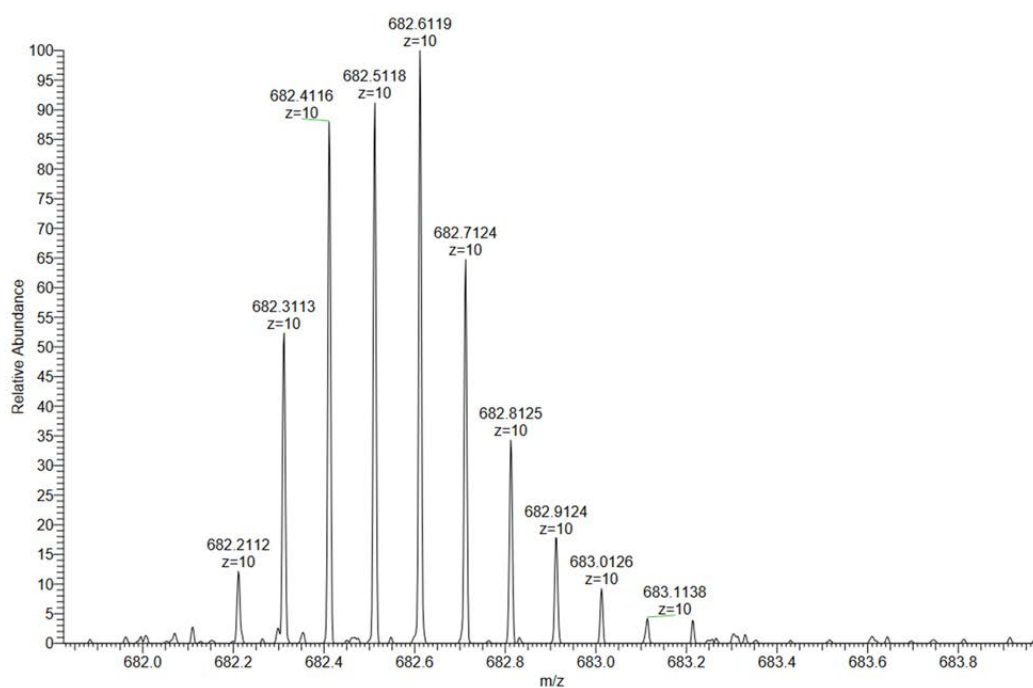


Figure 4.15: MS spectrum of O14.

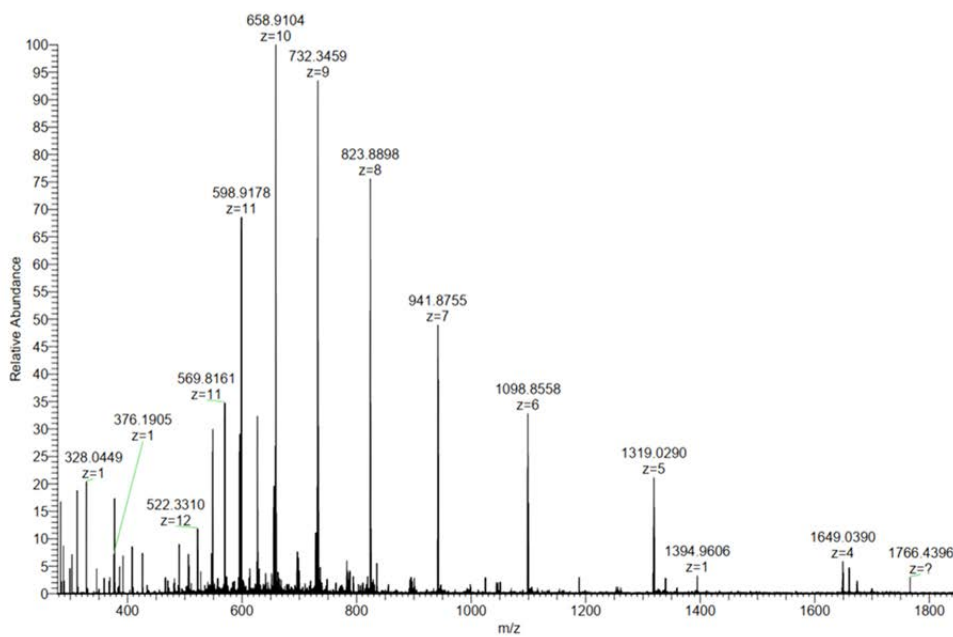


Figure 4.16: MS spectrum of O15.

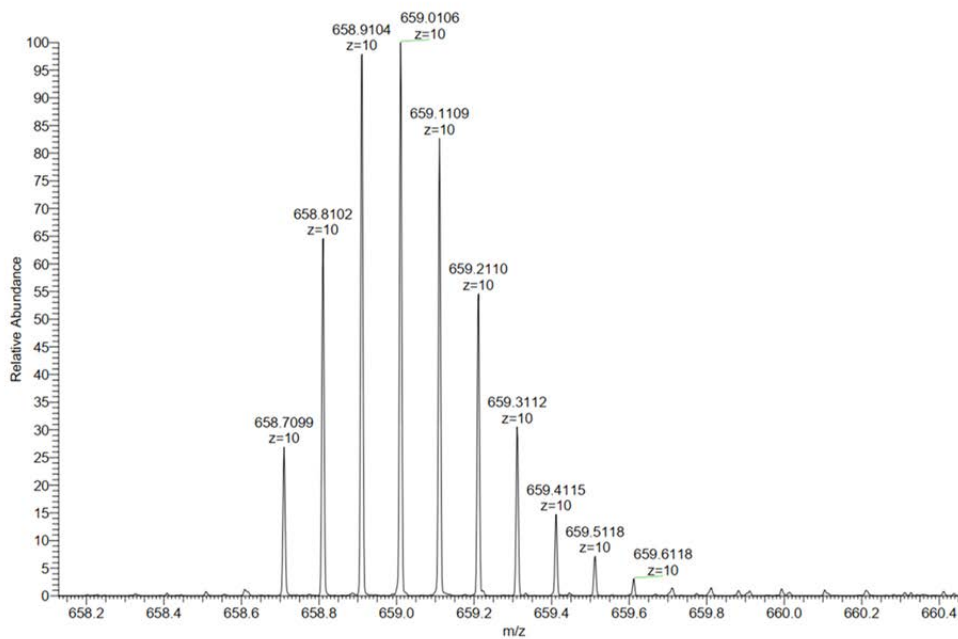


Figure 4.17: MS spectrum of O15.

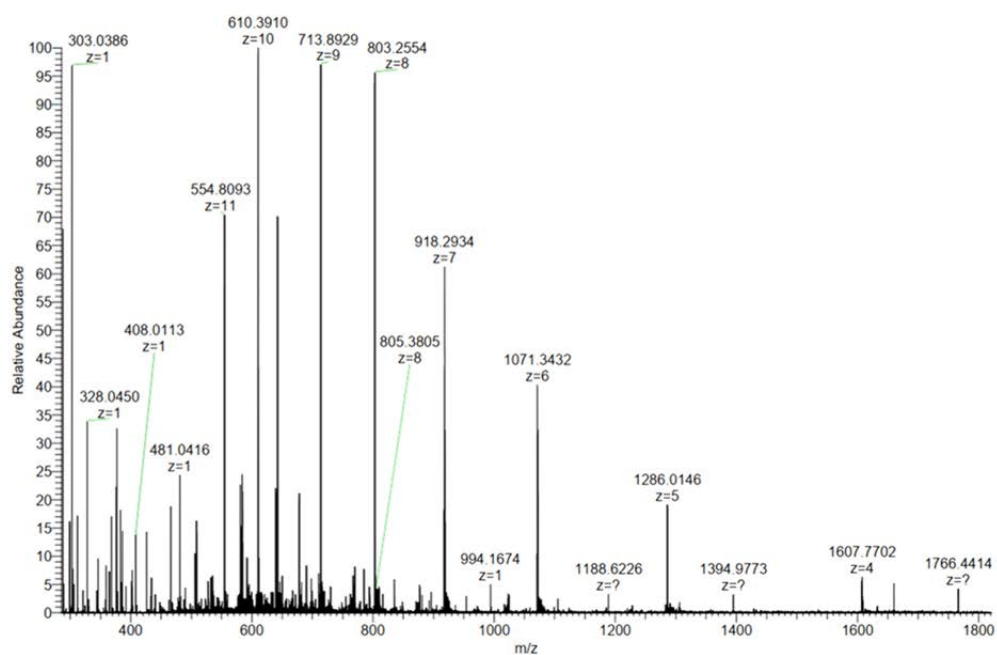


Figure 4.18: MS spectrum of O16.

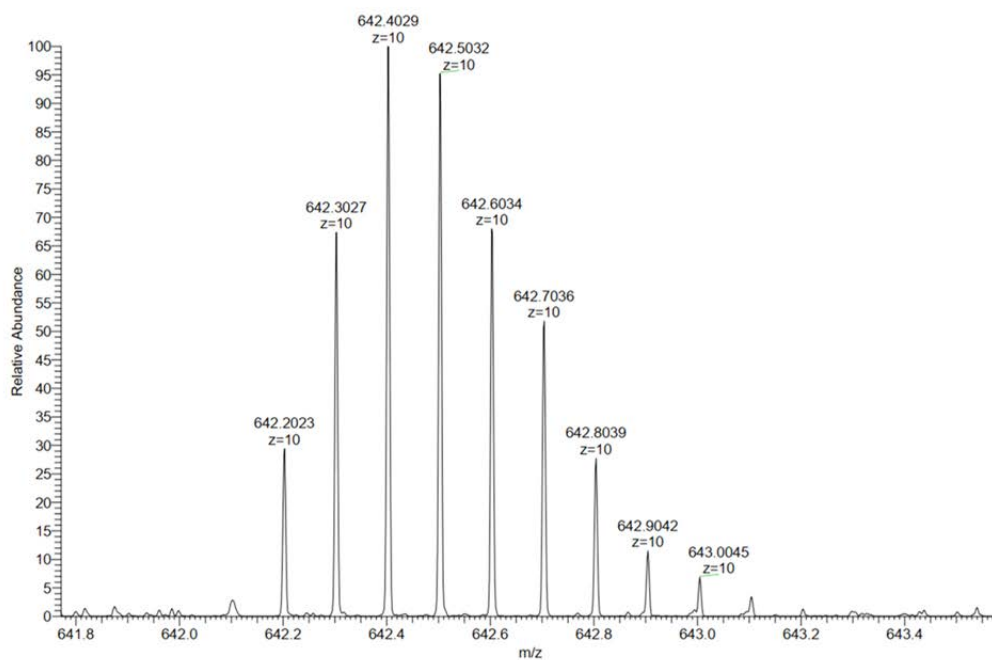


Figure 4.19: MS spectrum of O16.

4.3.2 DLS Measurement Conditions and Results

Table 4.2: Key results and measurement conditions of DLS measurement at 20 °C of a solution of **O5*O6**, and **O13*O14**. Conditions: 1 μ M each single strand, 10 mM sodium phosphate buffer pH 7.2, 0.03 mM spermine \cdot 4 HCl for **O5*O6** and 0.09 mM spermine \cdot 4 HCl for **O13*O14**, 20 vol% ethanol.

Duplex	Size Diameter with Error (nm)	Z-Average Size Diameter (nm)	PDI	PDI Width (nm)	Count Rate (kcps)	Attenuator
O5*O6	185.9 \pm 62.2	166.1	0.103	53.30	21334.9	7
O13*O14	111.9 \pm 39.52	98.82	0.111	32.96	6468.6	8

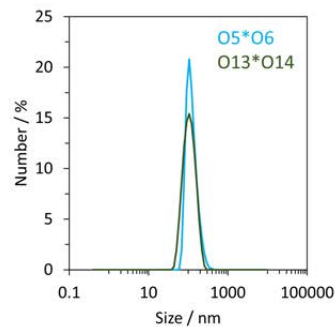


Figure 4.20: DLS measurements of **O5*O6** and **O13*O14**. Conditions: 1 μ M each single strand, 10 mM sodium phosphate buffer pH 7.2, 0.03 mM spermine \cdot 4 HCl for **O5*O6** and 0.09 mM spermine \cdot 4 HCl for **O13*O14**, 20 vol% ethanol, 20 °C.

Chapter 5

Supramolecular Assembly of 3'- and 5'-end modified Pyrene-DNA Conjugates: Influence of Number of Pyrene Modifications

In this chapter, both sides of a single DNA strand were modified with pyrene, forming a 3'- and 5'-modified pyrene-DNA conjugate. Conjugates bearing one, two, and three pyrene units on each side are compared. Pyrene-DNA conjugates with 1,6-dialkynyl pyrene and 2,7-dialkynyl pyrene were tested. In pyrene-DNA conjugates with three pyrene units on the 3' and 5'-end columnar-packed single, multilamellar, and fused vesicles, as well as agglomerates of vesicles, were observed on cryo-EM. Furthermore, cryo-EM revealed that the pyrene-conjugates with two pyrenes on each side self-assembled into smaller columnar-packed spherical objects. With the pyrene-DNA conjugates modified with one pyrene on each side, larger nanostructures were absent.

5.1 Results and Discussion

In this chapter, the supramolecular assembly of DNA duplexes, formed by an unmodified DNA 20-mer and 3'- and 5'-end pyrene-modified DNA strand containing one, two, and three pyrenes on each side, are presented. All DNA strands used in this chapter are tabulated in Figure 5.1a. The unmodified DNA strand **O7** acts as a complementary strand and was bought from a commercial supplier. **O17–O22** were prepared *via* solid-phase synthesis according to the phosphoramidite approach described in the general introduction (section 1.3) and purified by reverse-phase HPLC. Detailed experimental procedures are provided in the appendix of this chapter (section 5.3). The preparations of the 1,6- and 2,7-dialkynyl pyrene phosphoramidites were synthesized according to literature procedure.^{146,189} Their synthesis, purification, and characterization are described in the experimental section of the previous chapter (section 3.3) All oligomers listed in Figure 5.1a consist of a DNA 20-mer. **O17–O19** are modified with a 2,7-dialkynyl pyrene and **O20–O22** are modified with a 1,6-dialkynyl pyrene on the 3'- and 5'-end (chemical structure of the modification in Figure 5.1b). The amount of phosphodiester-linked pyrene units differs between the oligomers. **O17** and **O20** bear three pyrene units, **O18** and **O21** have two units, and **O19** and **O22** are modified with only one pyrene unit on each side.

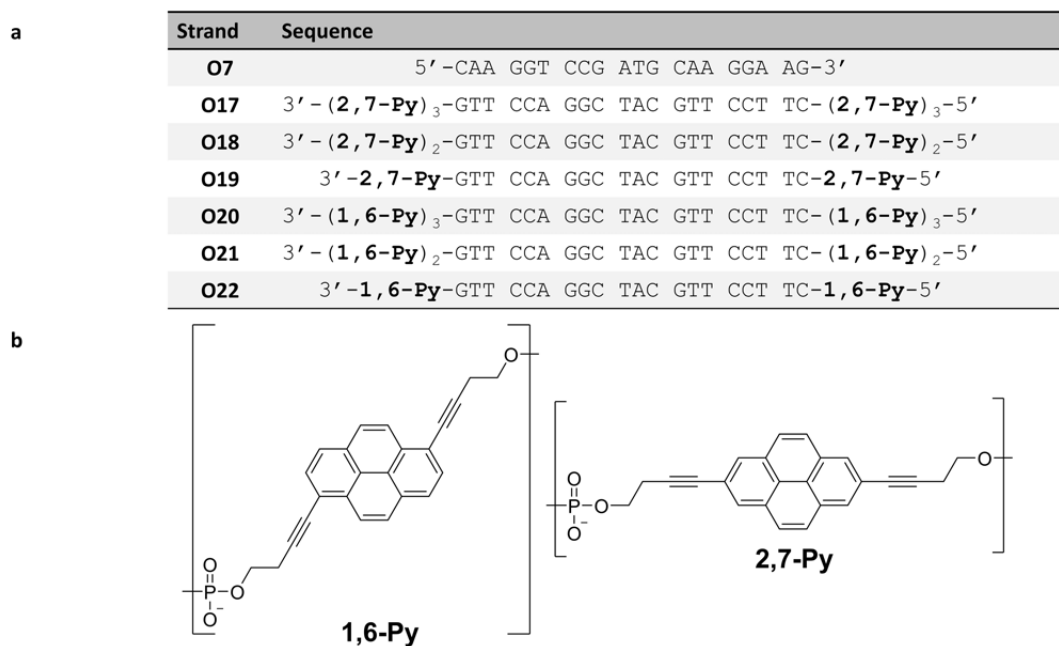


Figure 5.1: (a) DNA sequences of the 3'- and 5'-end modified 2,7- and 1,8-dialkynyl pyrene-DNA conjugates bearing three (**O17** and **O20**), two (**O18** and **O21**), and one (**O19** and **O22**) pyrene units on each side and the unmodified complementary strand **O7** and (b) the molecular structure of 1,6- and 2,7-dialkynyl pyrene.

5.1.1 Self-Assembly of 2,7-Dialkynyl Pyrene-DNA Conjugate

The temperature-dependent UV-vis absorption spectra of the pyrene-DNA conjugates **O7*O17**, **O7*O18**, and **O7*O19** were compared (Figure 5.2a–c). At 75 °C, the spectrum of **O7*O17** displays the distinctive absorption peaks for 2,7-dialkynyl pyrene (Figure 5.2a). Two maxima were found the weaker maximum at 342 nm arises from the pyrene units, the one at 270 nm originates from both the pyrene and the DNA nucleobases. Upon cooling to 20 °C, the 342 nm maximum undergoes a shift to longer wavelengths (345 nm). Simultaneously, the 270 nm band experiences a reduction due to DNA hybridization, accompanied by a shift to shorter wavelengths (268 nm). Furthermore, scattering reappears, signifying a certain degree of aggregation of the pyrene-DNA conjugates. **O7*O18** also displays the distinctive absorption peaks of 2,7-dialkynyl pyrene at 75 °C (Figure 5.2b). Two maxima were found the weaker maximum at 343 nm arises from the pyrene units, and the one at 273 nm originates from both the pyrene and the DNA nucleobases. Upon cooling to 20 °C, no shift was observed in the band with a maximum at 273 nm, but it decreased due to the base pairing of the nucleobases in the DNA. In contrast to the UV-vis spectra of **O7*O17**, scattering was not observed with **O7*O18**. However, the maxima at 343 nm shifted to longer wavelengths (345 nm), a sign of aggregation. **O7*O19** displays the distinctive absorption peaks of 2,7-dialkynyl pyrene at 75 °C (Figure 5.2c). Three maxima were identified. The two maxima at 341 nm and 284 nm are both attributed to the 2,7-dialkynyl pyrene units, the third broad maxima at 273 nm originates from both the pyrene and the DNA nucleobases. Upon cooling to 20 °C, the broad band around 273 nm and the one at 284 nm remained at their respective wavelengths but were reduced, while the maxima at 341 nm shifted to longer wavelengths (345 nm). Scattering was not observed in the UV-vis measurements of **O7*O19** after cooling to 20 °C.

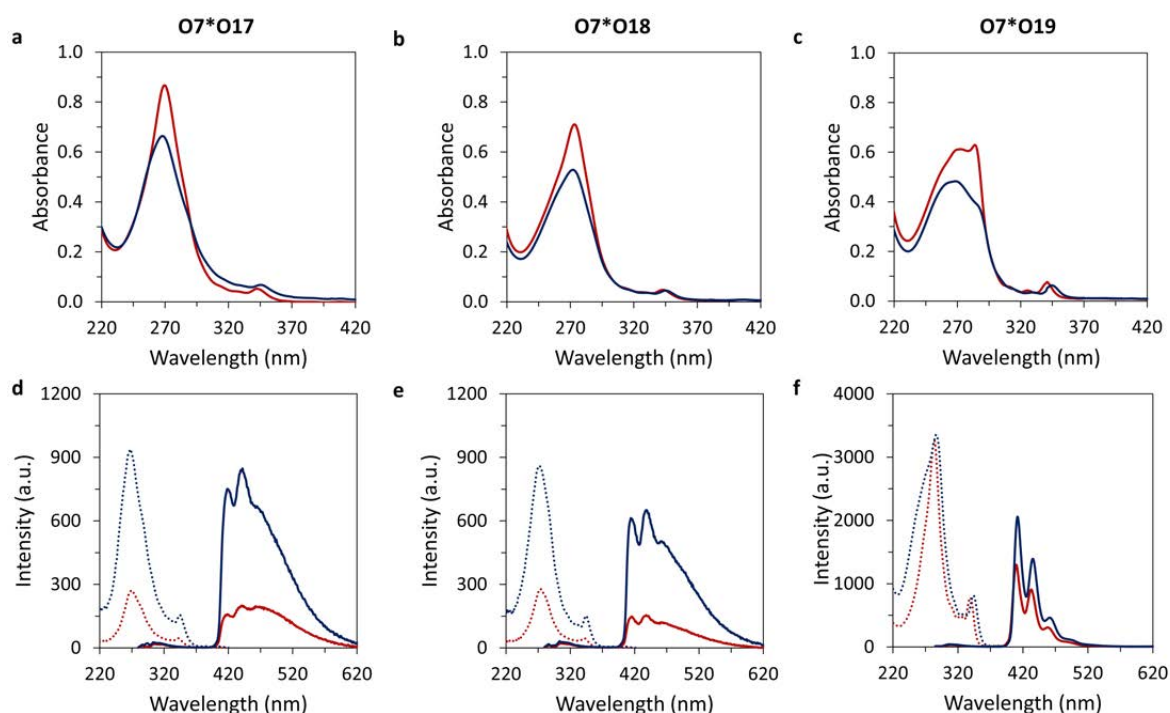


Figure 5.2: Temperature-dependent UV-vis absorption spectra (a–c) and fluorescence emission (solid line) and excitation (dashed line) spectra (d–f) of (a and d) **O7*O17**, (b and e) **O7*O18**, and (c and f) **O7*O19** (blue: 20 °C after self-assembly and red: 75 °C). Conditions: 1 μ M each single strand, 10 mM sodium phosphate buffer pH 7.2, 20 vol% ethanol, 0.03 mM spermine \cdot 4 HCl, cooling rate: 0.5 $^{\circ}$ C \cdot min $^{-1}$, $\lambda_{em.}$; 440 nm for **O7*O17** and **O7*O18** and $\lambda_{em.}$; 412 nm for **O7*O19**, and $\lambda_{ex.}$; 260 nm.

Temperature-dependent fluorescence excitation and emission spectra of the pyrene-DNA conjugates were conducted (Figure 5.2d–f). **O7*O17** and **O7*O18** displayed both monomer fluorescence (410–450 nm) and excimer fluorescence (450–625 nm) (Figure 5.2d and e). Their excitation spectra resemble well the UV-vis absorption spectra. Cooling from 75 °C to 20 °C induced a hyperchromic shift of monomer and excimer emissions. In contrast, **O7*O19** displays monomer fluorescence with three distinct maxima at 410 nm, 435 nm, and 461 nm. After cooling, a smaller hyperchromic shift of the bands is observed. The excitation spectrum of **O7*O19** closely resembles the UV-vis measurements. Interestingly, the absorption bands and excitation spectra of oligomers bearing more than one 2,7-dialkynyl pyrene on each side differ from **O7*O19**. The highest absorption band is shifted by 11–16 nm. This effect is expected to arise from the interaction between the neighboring pyrene units in **O17** and **O18**.

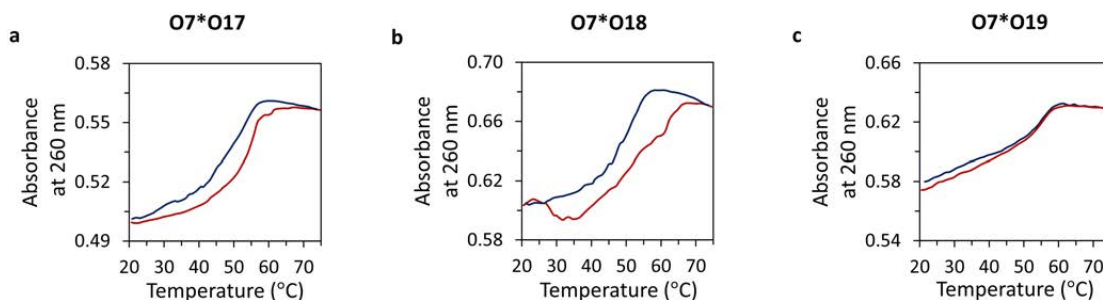


Figure 5.3: Temperature-dependent UV-vis absorbance at 260 nm of (a) **O7*O17**, (b) **O7*O18**, and (c) **O7*O19** (blue: cooling and red: heating). Conditions: 1 μM each single strand, 10 mM sodium phosphate buffer pH 7.2, 20 vol% ethanol, 0.03 mM spermine \cdot 4 HCl, cooling rate: 0.5 $^{\circ}\text{C}\cdot\text{min}^{-1}$.

Furthermore, self-assembly and disassembly were monitored by UV-vis spectroscopy, measuring the absorbance of the complementary DNA strands at 260 nm (Figure 5.3). **O7*O17** and **O7*O18** exhibited hysteresis (Figure 5.3a and b). In contrast, **O7*O19** exhibited overlaying absorbance in the cooling and heating curves (Figure 5.3c), and no hysteresis was observed.

To investigate if the length of pyrene sticky ends affects the morphology of nanostructures, AFM and cryo-EM measurements were performed. AFM measurements of **O7*O17**, **O7*O18**, and **O7*O19** were analyzed and compared (Figure 5.4 and appendix Figure 5.28). It is assumed that an increase in pyrene units in the sticky ends enhances the hydrophobicity of the conjugates, leading to the formation of larger or agglomerate nanostructures. AFM of the nanostructures after thermal self-assembly from 75 °C to 20 °C (0.5 $^{\circ}\text{C}\cdot\text{min}^{-1}$) were conducted.

AFM images of **O7*O17** showed vesicles with diameters of 50 to 150 nm (Figure 5.4, left). Besides single spherical nanostructures, some of the assemblies agglomerated. The reduction of the sticky ends by one pyrene unit **O7*O18** resulted in the formation of spherical nano-objects with similar diameters and agglomerates of spheres (Figure 5.4, middle). DLS measurements displayed an average hydrodynamic diameter of 193 ± 65 nm for **O7*O17** and 119 ± 38 nm for **O7*O18** (appendix Figure 5.35). The sizes determined by DLS are in good agreement with the observed diameters on the AFM. On AFM images of **O7*O19** (Figure 5.4, right), the pyrene-DNA conjugate with one pyrene on each side, the height profile of 0.5–1.0 nm suggests the adsorption of the DNA duplexes onto the APTES-modified mica (control measurements with no DNA showed a height of 0.2–0.4 nm on AFM, Figure 5.29). The formation of supramolecular assemblies was not observed with **O7*O19** due to the reduced amount of hydrophobic interactions among the strands. In summary, AFM images revealed that **O7*O17** and **O7*O18** form nanostructures, while nanostructures are absent with **O7*O19**.

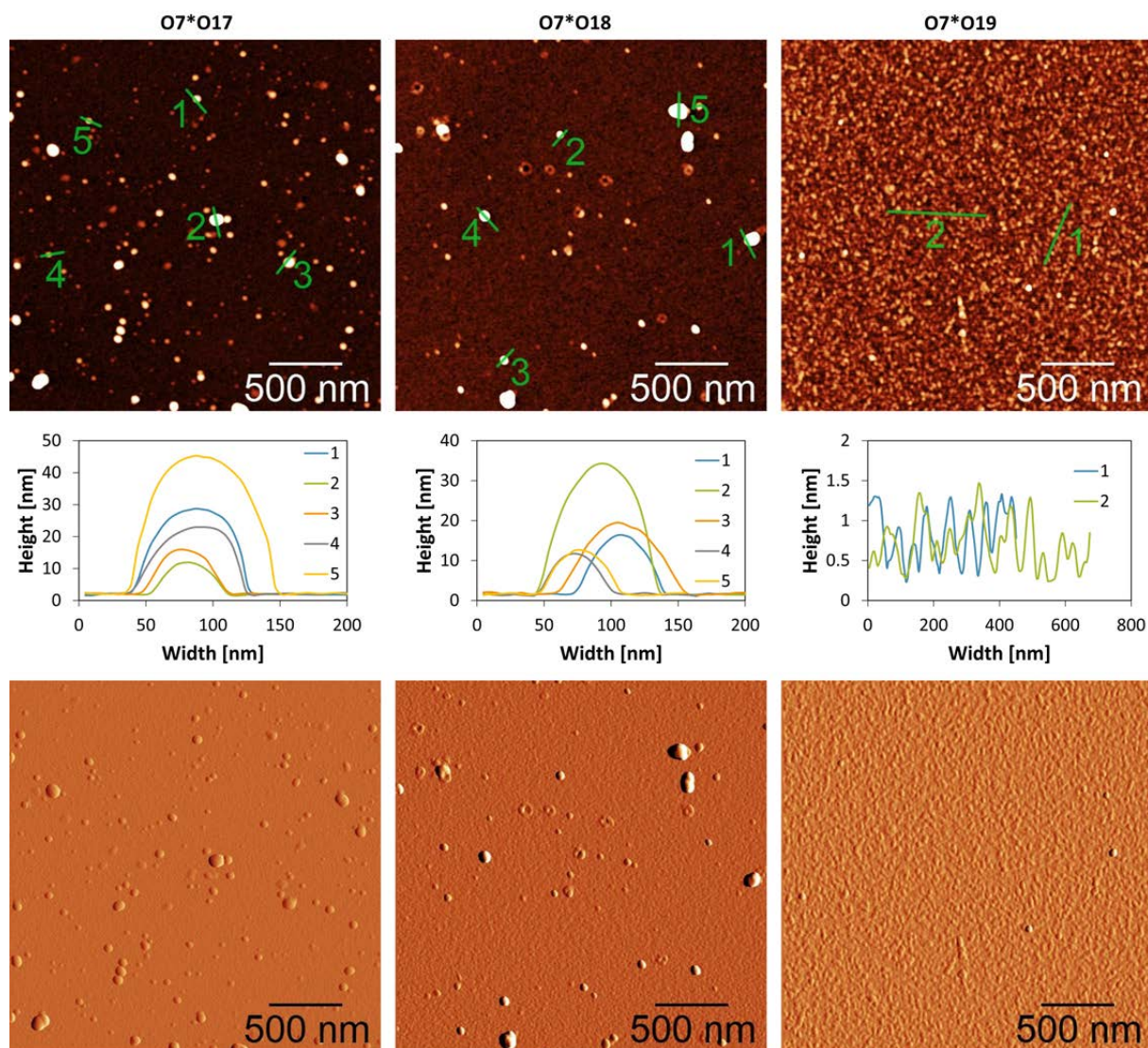


Figure 5.4: AFM scan (top) with corresponding cross sections (middle) and deflection scan of (bottom) **O7*O17** (left), **O7*O18** (middle), and **O7*O19** (right). Conditions: 1 μ M each single strand, 10 mM sodium phosphate buffer pH 7.2, 0.03 mM spermine \cdot 4 HCl, 20 vol% ethanol.

To further characterize the vesicles of cryo-EM measurements were conducted in collaboration with Prof. Dr. Benoît Zuber and Dr. Ioan Iacovache from the Institute of Anatomy of the University of Bern. Cryo-EM images of **O7*O17** revealed different morphologies of the assemblies (Figure 5.5 and appendix Figure 5.31). Single vesicles (Figure 5.5a), multilayered vesicles (Figure 5.5b), fused vesicles and agglomerates of vesicles (Figure 5.5c and Figure 5.6) were found with an average vesicle diameter of 139 ± 37 nm (Figure 5.5f). A membrane thickness of 7.6 ± 0.7 nm for the single vesicle was determined by measuring the gray values across the membranes of the vesicle in multiple images. These results propose a columnar packing, as this distance correlates well with the length of a DNA 20-mer. The columnar-packed single vesicle is schematically illustrated in Figure 5.5d, and a multilayered vesicle is depicted in Figure 5.5e.

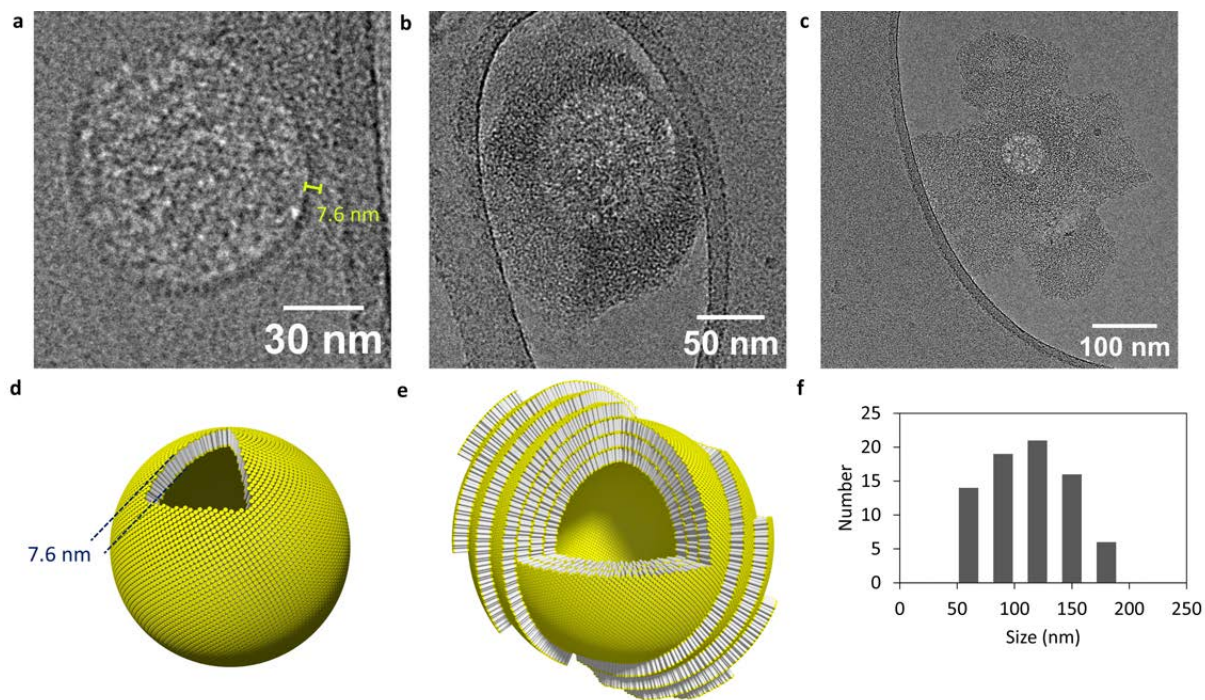


Figure 5.5: Cryo-EM images of **O7*O17** forming (a) a single vesicle, (b) a multilayered vesicle, and (c) agglomerated vesicles. (d) Schematic representation of single vesicle with measured diameter of the vesicle wall of 7.6 ± 0.7 nm, (e) schematic representation of multilayered vesicle, and (f) size distribution of vesicular diameter. Conditions: 1 μ M each single strand, 10 mM sodium phosphate buffer pH 7.2, 0.03 mM spermine \cdot 4 HCl, 20 vol% ethanol.

The agglomeration and fusing of vesicles formed by **O7*O17** have already been observed in the AFM experiments. The cryo-EM image in Figure 5.6 illustrates agglomerated and fused vesicles. The image on the left in Figure 5.6 shows non-fused vesicles (orange arrow) and vesicles that are in the fusing process (red arrow). When two vesicles formed by **O7*O17** are nearby, they tend to fuse as the pyrene overhangs (consisting of three pyrene units) on the vesicle surfaces of multiple vesicles interact *via* hydrophobic interaction.

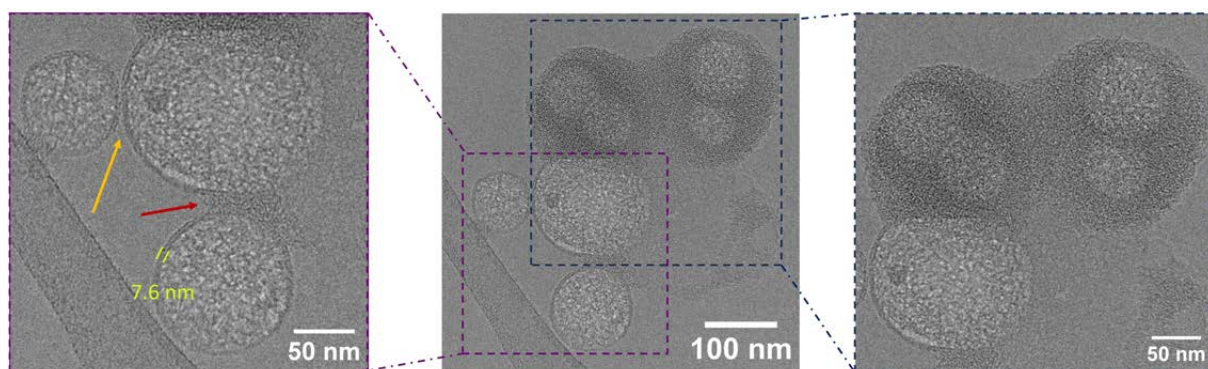


Figure 5.6: Cryo-EM images of single and agglomerated vesicles of **O7*O17**, (left) single vesicle in proximity indicated by the orange arrow, two vesicles starting to fuse indicated by the red arrow, (middle) overview image, and (right) agglomerated fused vesicles with additional layers. Conditions: 1 μ M each single strand, 10 mM sodium phosphate buffer pH 7.2, 0.03 mM spermine \cdot 4 HCl, 20 vol% ethanol.

Cryo-EM images of the pyrene-DNA conjugate with two pyrene units on each side **O7*O18** were also measured (Figure 5.7, Figure 5.5, and additional images in appendix Figure 5.32). Single spheres (Figure 5.7a) and agglomerates of spherical objects (Figure 5.7b) were observed. The nanostructures have an average diameter of 45 ± 15 nm (size distribution Figure 5.7c). They are much smaller than **O7*O17**. On the AFM images, larger structures with diameters of up to 100 nm were observed. However, these are agglomerates and have no single nanostructures. Therefore, results from AFM and cryo-EM are consistent.

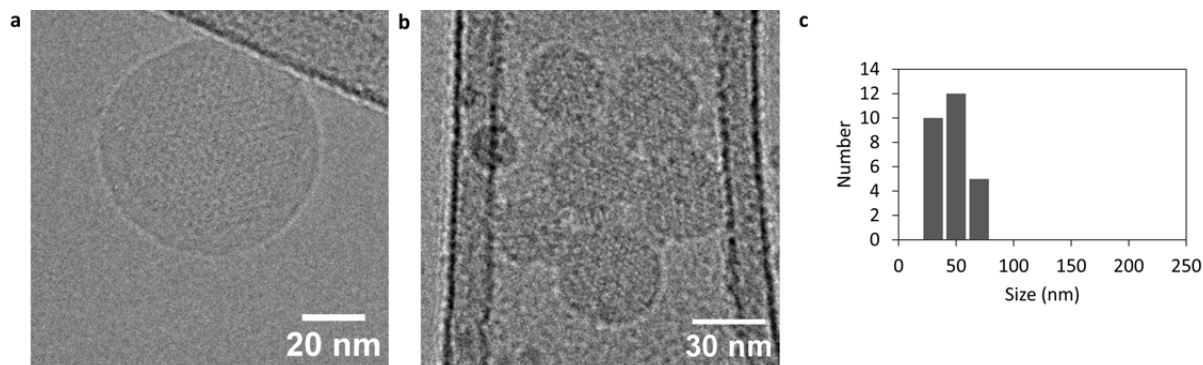


Figure 5.7: Cryo-EM images of **O7*O18** (a) single spherical nanostructures, (b) agglomerate spheres, and (c) size distribution of diameters. Conditions: 1 μ M each single strand, 10 mM sodium phosphate buffer pH 7.2, 0.03 mM spermine \cdot 4 HCl, 20 vol% ethanol.

In cryo-EM images of **O7*O18** hexagonal patterns were observed (Figure 5.8a). By filtering the images with the help of FFT (excluding the high frequencies), the visibility of the pattern was improved (Figure 5.8b). In the pattern, distances of 2.4 nm were observed in all directions (gray values in graph Figure 5.8c). The distance of 2.4 nm fits well with the width of a single DNA strand. Therefore, the pattern proposes a hexagonal columnar packing of the pyrene-DNA conjugates in the spherical object.

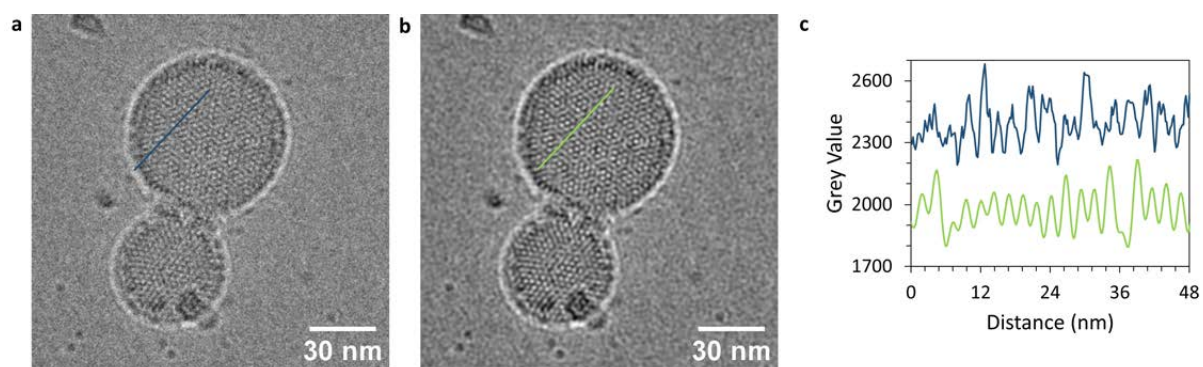


Figure 5.8: Cryo-EM images of agglomerated spherical assemblies of **O7*O18** (left), filtered version of the image (middle), and graph of gray value in the two images (blue, original, and green, filtered) with a spacing of 2.4 nm proposing columnar packing of the vesicle (right). Conditions: 1 μ M each single strand, 10 mM sodium phosphate buffer pH 7.2, 0.03 mM spermine \cdot 4 HCl, 20 vol% ethanol.

5.1.2 Self-Assembly of 1,6-Dialkynyl Pyrene-DNA Conjugate

The temperature-dependent UV-vis absorption spectra of the pyrene-DNA conjugates **O7*O20**, **O7*O21**, and **O7*O22** were compared (Figure 5.9a–c). At 75 °C, all three duplexes display the distinctive absorption peaks for 1,6-dialkynyl pyrene with maxima around at 365–368 nm and 385–388 nm. In the region between 220 and 320 nm, the pyrene absorbances overlap with those of the nucleobases. Interestingly, the pattern in the absorption bands is unequal between conjugates bearing multiple pyrene units **O7*O20** and **O7*O21** and the pyrene-DNA conjugate bearing one pyrene on each side **O7*O22**. **O7*O22** closely resembles the pattern observed in 1,6-dialkynyl pyrene-diol measured in ethanol at 20 °C at a dilute concentration (illustrated in chapter 3, Figure 3.1), whereas in **O7*O20**, **O7*O21** the two and three pyrenes nearby influence the pattern, this effect was previously described in literature for pyrene trimers.²³ Upon cooling from 75 °C to 20 °C (0.5 °C·min⁻¹), the absorbances above 320 nm exhibit a red-shift (3–4 nm), and the absorbances below 320 nm decrease. The decrease mostly originates from the pairing of the nucleobases.

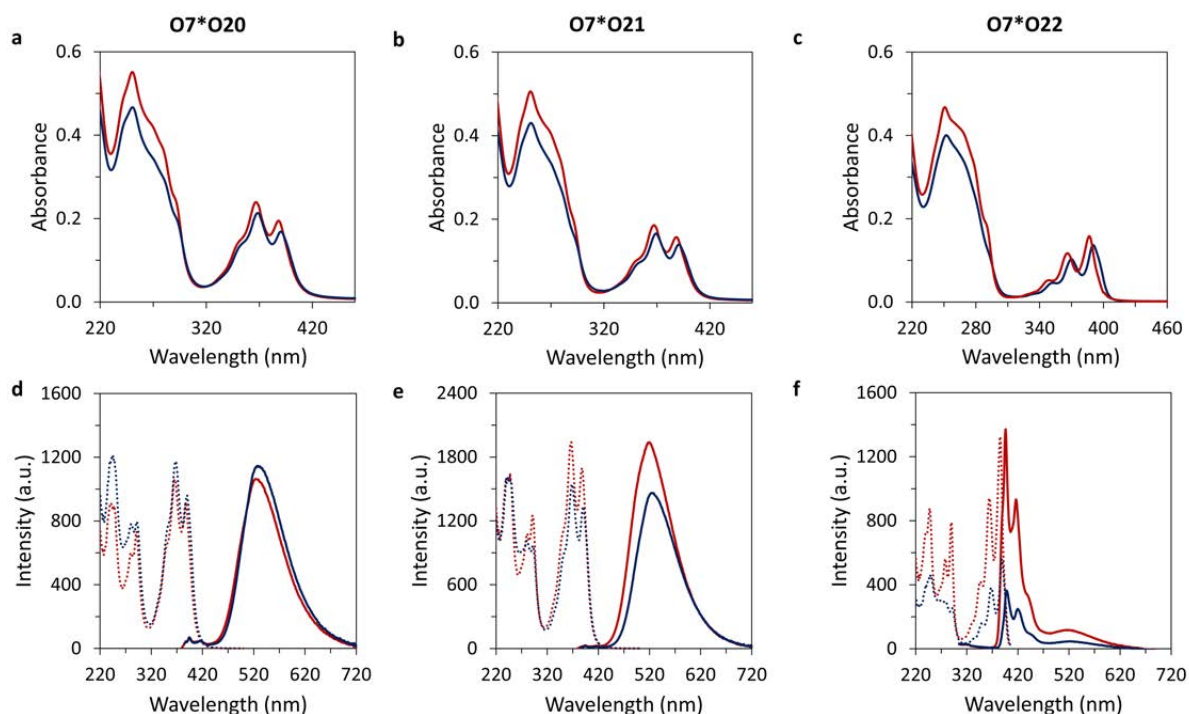


Figure 5.9: Temperature-dependent UV-vis absorption spectra (a–c) and fluorescence emission (solid line) and excitation (dashed line) spectra (d–f) of (a and d) **O7*O20**, (b and e) **O7*O21**, and (c and f) **O7*O22** (blue: 20 °C after self-assembly and red: 75 °C). Conditions: 1 μ M each single strand, 10 mM sodium phosphate buffer pH 7.2, 20% ethanol, 0.03 mM spermine · 4 HCl, cooling rate: 0.5 °C·min⁻¹, λ_{ex} : 260 nm.

Temperature-dependent fluorescence excitation and emission spectra of the pyrene-DNA conjugates were conducted (Figure 5.9d–f). **O7*O20** and **O7*O21** exhibit mostly pyrene excimer fluorescence with a maximum around 525 nm. In contrast, **O7*O22** exhibits monomer fluorescence with maxima at 396 and 418 nm and minor excimer fluorescence around 525 nm. As only one 1,6-dialkynyl pyrene unit is present on each side of the DNA duplex, the excimer fluorescence at 20 °C indicates of supramolecular interaction between a small part of the pyrene-DNA conjugates. The presence of excimer fluorescence at 75 °C is explained by the interaction of two pyrene units at the 3'- and 5'-end of a single DNA strand. The fluorescence emission of **O7*O20** shifts bathochromic and hyperchromic. In **O7*O21** and **O7*O22**, a hypochromic shift was observed after cooling to 20 °C.

To further understand the aggregation process, the absorbance at 260 nm was measured while cooling and heating the sample (Figure 5.10). The reversibility of the aggregation was validated through temperature-dependent UV-vis spectroscopy measurements, as the absorbance at 20 °C and 75 °C remained consistent before and after the heating and cooling cycles. A minor hysteresis was observed in the heating and cooling profiles of **O7*O20** and **O7*O21**. In contrast, no hysteresis was observed in **O7*O22**.

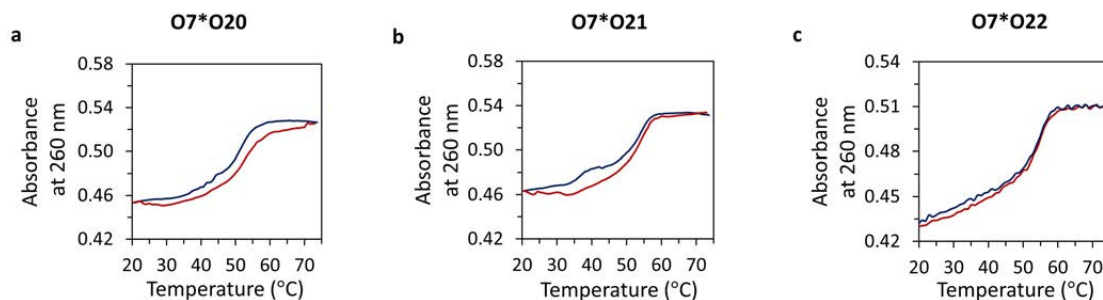


Figure 5.10: Temperature-dependent UV-vis absorbance at 260 nm of (a) **O7*O20**, (b) **O7*O21**, and (c) **O7*O22** (cooling: blue and heating: red). Conditions: 1 μ M each single strand, 10 mM sodium phosphate buffer pH 7.2, 20% ethanol, 0.03 mM spermine \cdot 4 HCl, cooling rate: 0.5 $^{\circ}$ C \cdot min $^{-1}$.

To gain further insights into the morphological changes in the assemblies based on the number of pyrene modifications and to find out if the substitution pattern on the pyrene influences the morphology, AFM, and cryo-EM measurements of **O7*O20**, **O7*O21**, and **O7*O22** were conducted. First, the AFM images of thermally self-assembled solutions of **O7*O20**, **O7*O21**, and **O7*O22** on APTES-modified mica were conducted. The conjugates were self-assembled by cooling them from 75 $^{\circ}$ C to 20 $^{\circ}$ C with a gradient of 0.5 $^{\circ}$ C \cdot min $^{-1}$. The resulting images were analyzed and compared (Figure 5.11 and appendix Figure 5.30). Then, the results of the 2,7-dialkynyl pyrene-modified conjugates (**O7*O17**, **O7*O18**, and **O7*O19**) and the 1,6-dialkynyl pyrene-modified conjugates (**O7*O20**, **O7*O21**, and **O7*O22**) are compared.

AFM images of **O7*O20** showed the formation of vesicles with diameters of 50–150 nm (Figure 5.11, left). Most vesicles were observed as single spherical nanostructures, while a few formed agglomerated. The pyrene-DNA conjugate with two 1,6-dialkynyl pyrene units **O7*O21** formed vesicles with a diameter of 50 to 150 nm (Figure 5.11, middle). Occasionally two or three vesicles were found agglomerated (Figure 5.11, middle). DLS measurements revealed an average hydrodynamic diameter of 143 ± 55 nm for **O7*O20** and 116 ± 40 nm for **O7*O21** (appendix Figure 5.35). These measurements are in good agreement with the results obtained by AFM. On AFM images of **O7*O22** (Figure 5.11, right), a few spots with a height between 4–9 nm were found, and the mica was filled with 0.5–1.5 nm high structures. As the hydrophobicity of one pyrene unit is not sufficient, most duplexes are adsorbed to the APTES-modified mica. In summary, on AFM images of **O7*O20** and **O7*O21**, supramolecular assemblies were detected. In contrast, AFM images of **O7*O22** showed adsorbed DNA duplexes. The AFM images of the three pyrene-DNA conjugates with the 1,6-dialkynyl pyrene and 2,7-dialkynyl pyrene sticky ends expressed comparable results.

To further characterize the vesicles, cryo-EM measurements of **O7*O20** and **O7*O21** were conducted. Moreover, the results of the 1,6-dialkynyl pyrene-DNA conjugate were compared to the 2,7-dialkynyl bearing **O7*O17** and **O7*O18**. Cryo-EM measurements of **O7*O20** showed the formation of single vesicles with a broad size distribution with an average diameter of 105 ± 40 nm (Figure 5.12 and appendix Figure 5.33). Similarly to the AFM, some vesicles

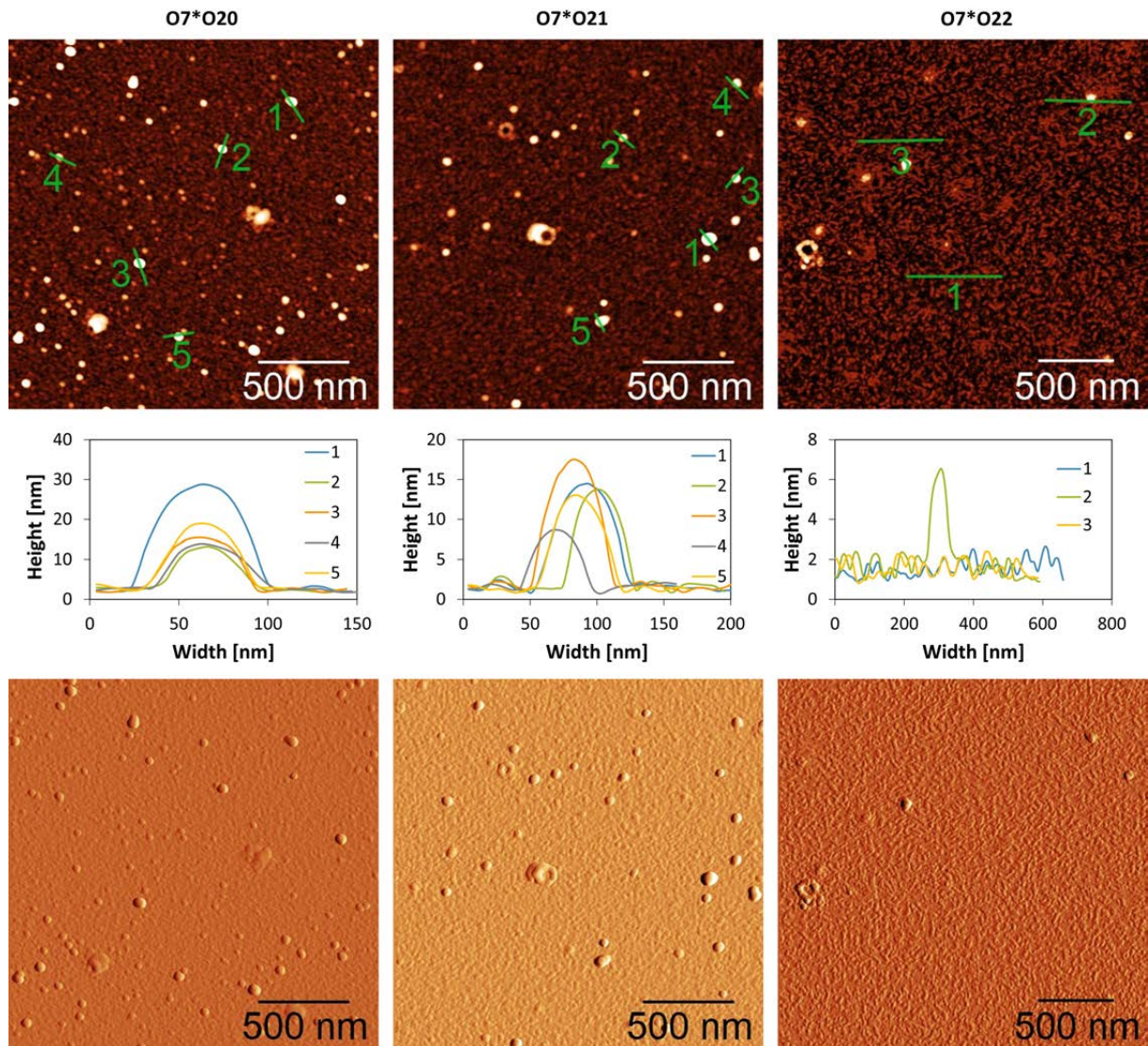


Figure 5.11: AFM scan (top) with corresponding cross sections (middle) and deflection scan of (bottom) **O7*O20** (left), **O7*O21** (middle), and **O7*O22** (right). Conditions: 1 μ M each single strand, 10 mM sodium phosphate buffer pH 7.2, 0.03 mM spermine \cdot 4 HCl, 20 vol% ethanol.

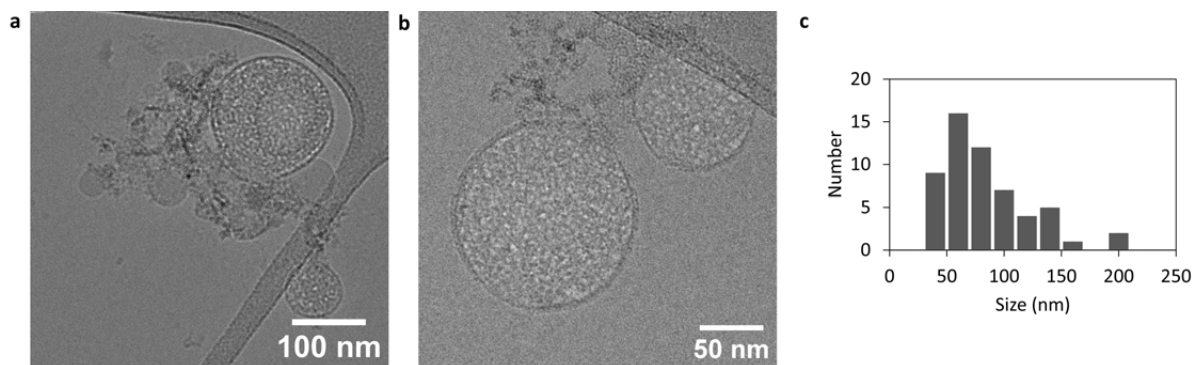


Figure 5.12: Cryo-EM images of **O7*O20** (a) agglomerates of vesicles, (b) single vesicles, and (c) size distribution of vesicular diameter. Conditions: 1 μ M each single strand, 10 mM sodium phosphate buffer pH 7.2, 0.03 mM spermine \cdot 4 HCl, 20 vol% ethanol.

agglomerated (Figure 5.12a), whereas others were found isolated. In contrast to the 2,7-dialkynyl pyrene-modified pyrene-DNA conjugate with three pyrene units on the 3'- and 5'-end (**O7*O17**), multilayered or fused vesicles were not detected in **O7*O20**. In comparison to the 2,7-dialkynyl substituted pyrene sticky-ends, hydrophobic interactions between multiple vesicles were not observed with the 1,6-dialkynyl substituted pyrenes.

Cryo-EM images of **O7*O21**, the conjugate with two pyrene units on each side were also analyzed and compared (Figure 5.13 and appendix Figure 5.34). Images of **O7*O21** showed single (Figure 5.13a) and aggregated vesicles (Figure 5.13b) with a smaller average diameter of 86 ± 20 nm. Most aggregated vesicles were found in pairs. The size and shape are comparable to the assemblies found with the 2,7-dialkynyl pyrene-DNA conjugate (**O7*O18**).

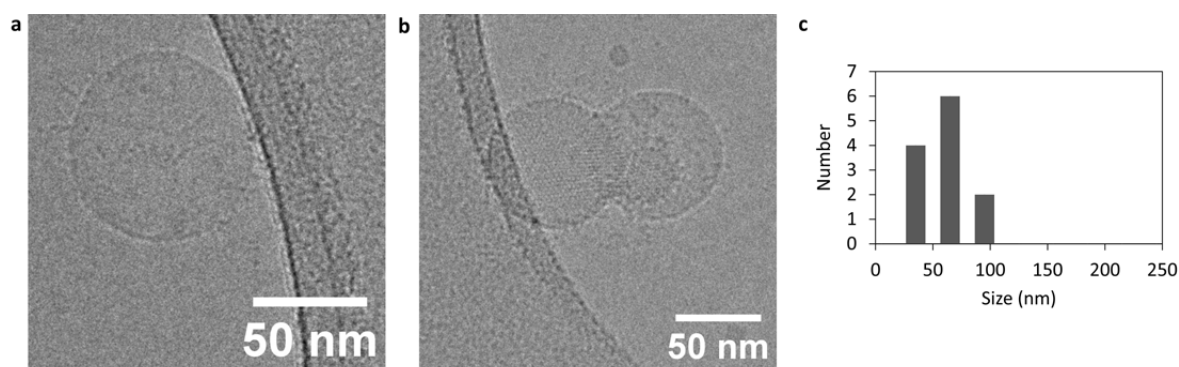


Figure 5.13: Cryo-EM images of **O7*O21** (left) and size distribution of vesicular diameter (right). Conditions: 1 μ M each single strand, 10 mM sodium phosphate buffer pH 7.2, 0.03 mM spermine \cdot 4 HCl, 20 vol% ethanol.

Similarly to the cryo-EM measurement of the 2,7-dialkynyl pyrene-DNA conjugate bearing two pyrenes on each side (**O7*O18**), a hexagonal pattern was observed in images of **O7*O21** (Figure 5.14a). FFT manipulations on the cryo-EM images improved the visibility of the hexagonal pattern (Figure 5.14b). The strongly absorbing spots on the cryo-EM image were measured to be 2.8 nm apart (Figure 5.14c). A distance of 2.8 nm is in the range of the width of a pyrene-modified DNA duplex. Therefore, these results indicate a columnar packing of the pyrene-DNA conjugates in spherical assemblies.

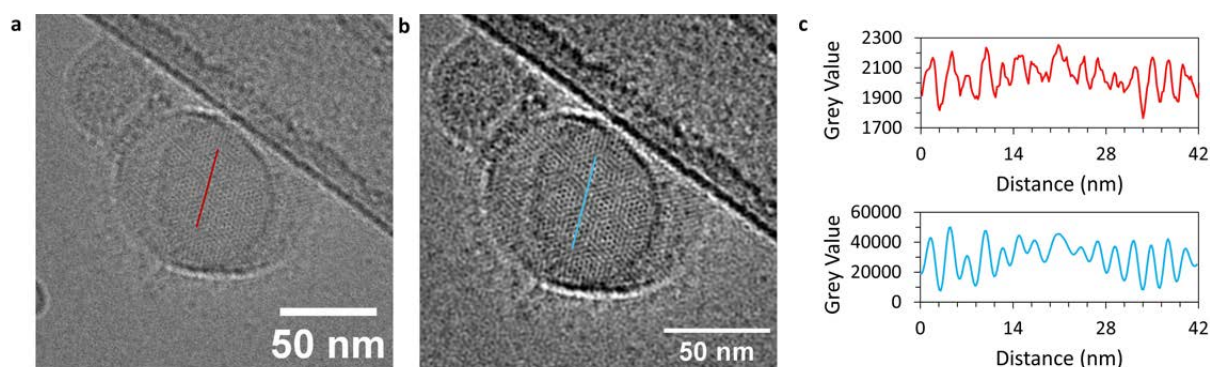
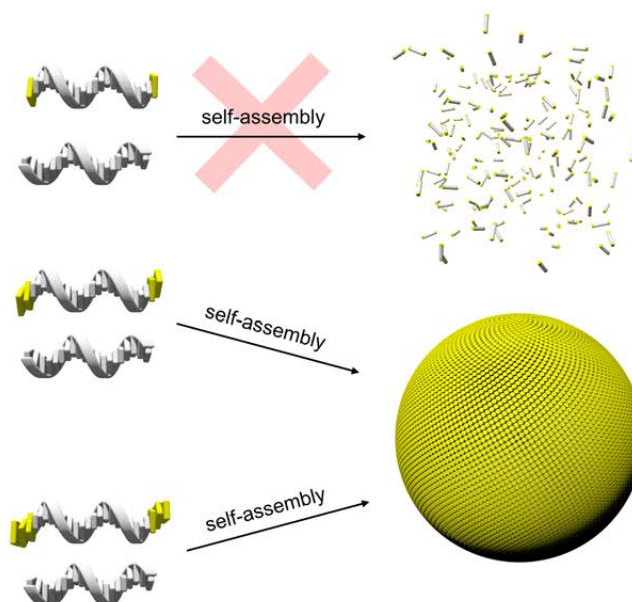


Figure 5.14: Cryo-EM images of agglomerated spherical nanostructures formed by **O7*O21** (left), a filtered version of the image (middle), and graph of gray values in the two images (red, original, and blue, filtered) with a spacing of 2.8 nm proposing columnar packing of the vesicles (right). Conditions: 1 μ M each single strand, 10 mM sodium phosphate buffer pH 7.2, 0.03 mM spermine \cdot 4 HCl, 20 vol% ethanol.

5.1.2.1 Summary 3'- and 5'-end modified DNA

In summary, pyrene-DNA conjugates bearing two and three 2,7-dialkynyl and 1,6-dialkynyl pyrene units formed vesicles, whereas unaggregated DNA duplexes were observed with the pyrene-DNA conjugates with only one pyrene on each side. Hence, a minimum of two pyrene units are required for the assembly of nanostructures. The 1,6- and 2,7-dialkynyl substitution on the pyrene had a minor influence on the assembly.



Scheme 5.1: Self-assembly of pyrene-DNA conjugates bearing one, two, and three pyrene sticky ends at 3'- and 5'-end with complementary unmodified strands.

5.2 Conclusions and Outlook

In conclusion, the influence of the length of sticky ends on 3'- and 5'-modified pyrene-DNA conjugates hybridized to an unmodified complementary strand was evaluated. The 1,6- and 2,7-dialkynyl pyrene of pyrene were tested. The two isomers showed comparable properties in temperature-dependent UV-vis spectroscopy, DLS, AFM, and cryo-EM. AFM revealed that a minimum of two pyrene units are necessary to form aggregates in the 3'- and 5'-modified pyrene-DNA conjugates. Cryo-EM, AFM, and DLS revealed that the size of the aggregates decreases the shorter the sticky ends are. AFM and cryo-EM also showed that the aggregates tend to agglomerate independent of the length of the sticky ends. Cryo-EM also showed that assemblies formed by pyrene-DNA conjugates bearing three 2,7-dialkynyl pyrenes tend to fuse if they are in proximity, whereas the ones with the 1,6-dialkynyl remained as single vesicles or agglomerates of aggregates. Hence, hydrophobic interactions of the sticky ends among multiple vesicles are more pronounced with the 2,7-dialkynyl pyrene isomer. Furthermore, cryo-EM measurements proposed a columnar packing of the pyrene-DNA conjugates inside the spherical assemblies.

To improve understanding of the supramolecular assembly of chromophore-DNA conjugates. Further hydrophobic or hydrophilic modifications to the DNA duplex could be introduced. The 3'- and 5'-end pyrene-DNA conjugates offer the possibility to hybridize it with complementary strands that are modified with additional functionalities. This approach is described in the next chapter 6.

5.3 Appendix - Chapter 5

First, the synthesis, purification, and characterization (HPLC traces and MS spectra) of the oligonucleotides **O17–O22** are described. Followed by the depiction of additional AFM and cryo-EM images. Finally, the DLS measurements are presented.

5.3.1 Synthesis and Characterization of Oligonucleotides

The 3'- and 5'-modified pyrene-DNA conjugates **O17–O22** were synthesized on an Applied Biosystems 394 DNA/RNA synthesizer applying a standard cyanoethyl phosphoramidite coupling protocol on a 1 μ mol scale. The solid-phase synthesis and purification are described in detail in chapter 8.

After that, the oligomers **O17–O22** were purified by reverse-phase HPLC (Shimadzu LC-20AT, ReproSil 100 C18, 5,0 μ m, 250 \times 4 mm) with a flow rate of 1 ml/min, with a detection wavelength of 260 nm at 50 $^{\circ}$ C. **O17–O22** were purified with solvent A: aqueous 2.1 mM triethylamine (TEA) / 25 mM 1,1,1,3,3,3-hexafluoropropan-2-ol (HFIP) pH 8 and solvent B: acetonitrile. The following gradient was applied gradients B[%] (t_R (min)) for **O17** and **O18**: 5 (0), 25 (24) and for **O19–O22** 5 (0), 30 (24). The respective HPLC traces are depicted in Figure 5.15.

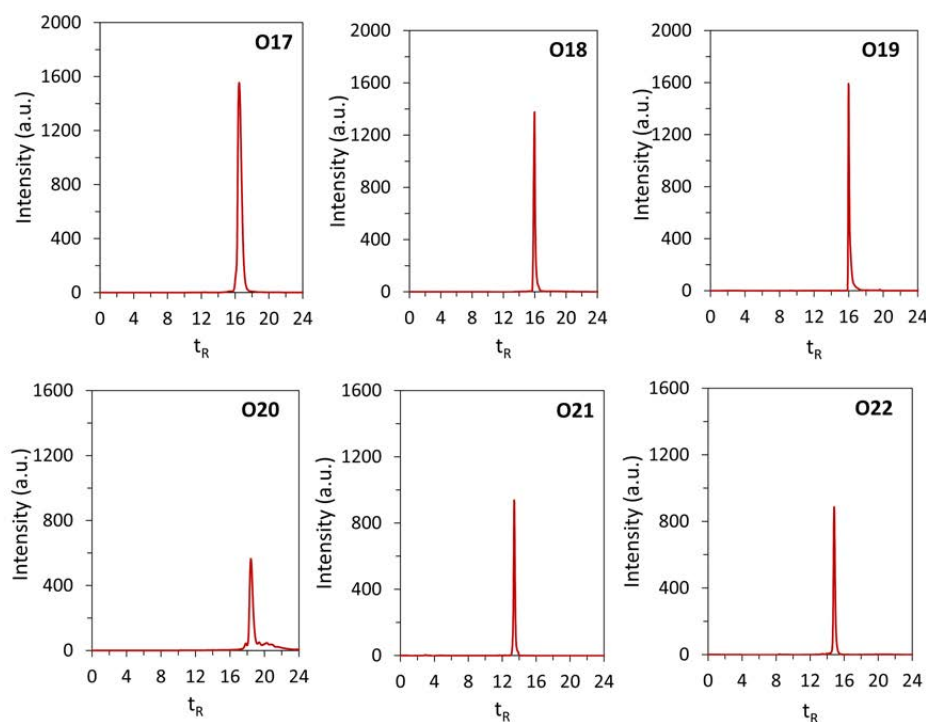


Figure 5.15: HPLC traces of pyrene-DNA conjugates **O17–O22**.

Then, the absorbance of the pyrene-DNA conjugates was measured at 260 nm to determine the concentration of the stock solutions and yields of **O17–O22**. The concentrations were determined by applying the Beer-Lambert law. The following molar absorptivities (at 260 nm) in $\text{l}\cdot\text{mol}^{-1}\cdot\text{cm}^{-1}$ were used: ϵ_{A} ; 15'300, ϵ_{T} ; 9'000, ϵ_{G} ; 11'700, ϵ_{C} ; 7'400, $\epsilon_{2,7\text{-pyrene}}$; 32'000, and $\epsilon_{1,6\text{-pyrene}}$; 20'000. The mass spectra results of **O17–O22** are listed in Table 5.1, and the mass spectra are displayed in Figure 5.16–Figure 5.27.

Table 5.1: Pyrene-DNA oligonucleotide sequences of **O17–O22**, calculated and found masses by NSI-MS, and yields.

Oligomer	Sequence (5'→3')	Calcd mass	Found mass	Yield [%]
O17	(2,7-pyrene) ₃ -CTT CCT TGC ATC GGA CCT TG-(2,7-pyrene) ₃	8436.5485	8436.5642	44
O18	(2,7-pyrene) ₂ -CTT CCT TGC ATC GGA CCT TG-(2,7-pyrene) ₂	7635.3723	7635.3865	34
O19	(2,7-pyrene) ₁ -CTT CCT TGC ATC GGA CCT TG-(2,7-pyrene) ₁	6835.1994	6835.1996	24
O20	(1,6-pyrene) ₃ -CTT CCT TGC ATC GGA CCT TG-(1,6-pyrene) ₃	8436.5485	8436.5485	17
O21	(1,6-pyrene) ₂ -CTT CCT TGC ATC GGA CCT TG-(2,7-pyrene) ₂	7635.3723 7657.3542 ^a	- 7657.3656 ^a	20
O22	(1,6-pyrene) ₁ -CTT CCT TGC ATC GGA CCT TG-(1,6-pyrene) ₁	6835.1994	6835.2025	22

^a Sodium adduct.

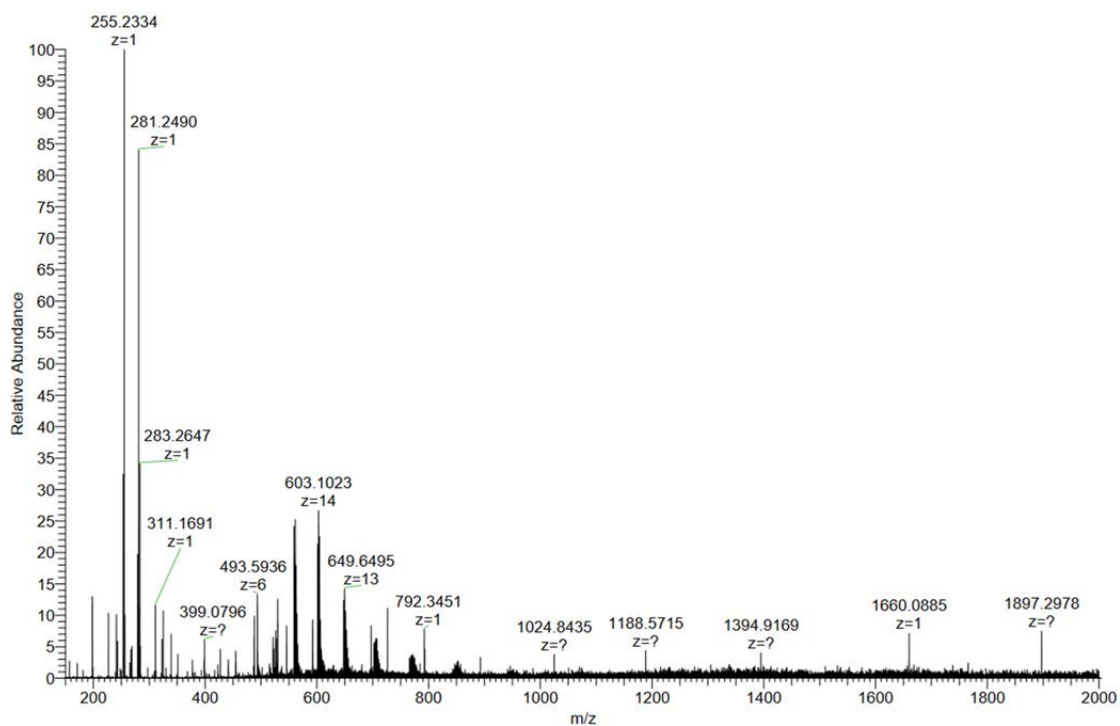


Figure 5.16: MS spectrum of O17.

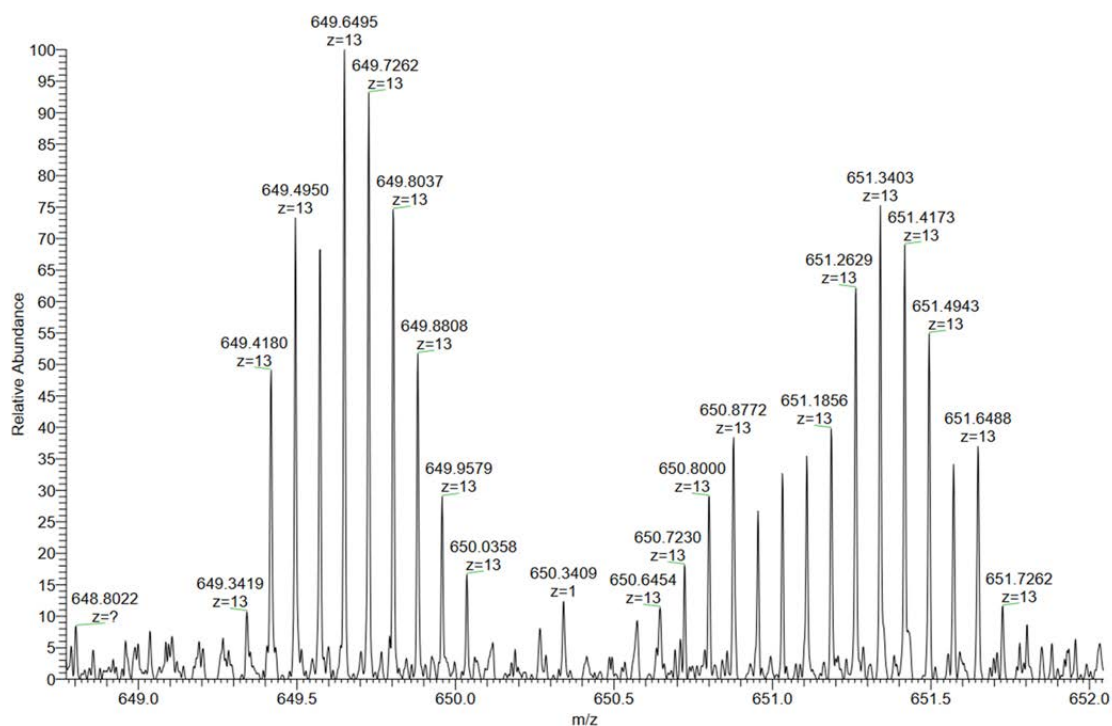


Figure 5.17: MS spectrum of O17.

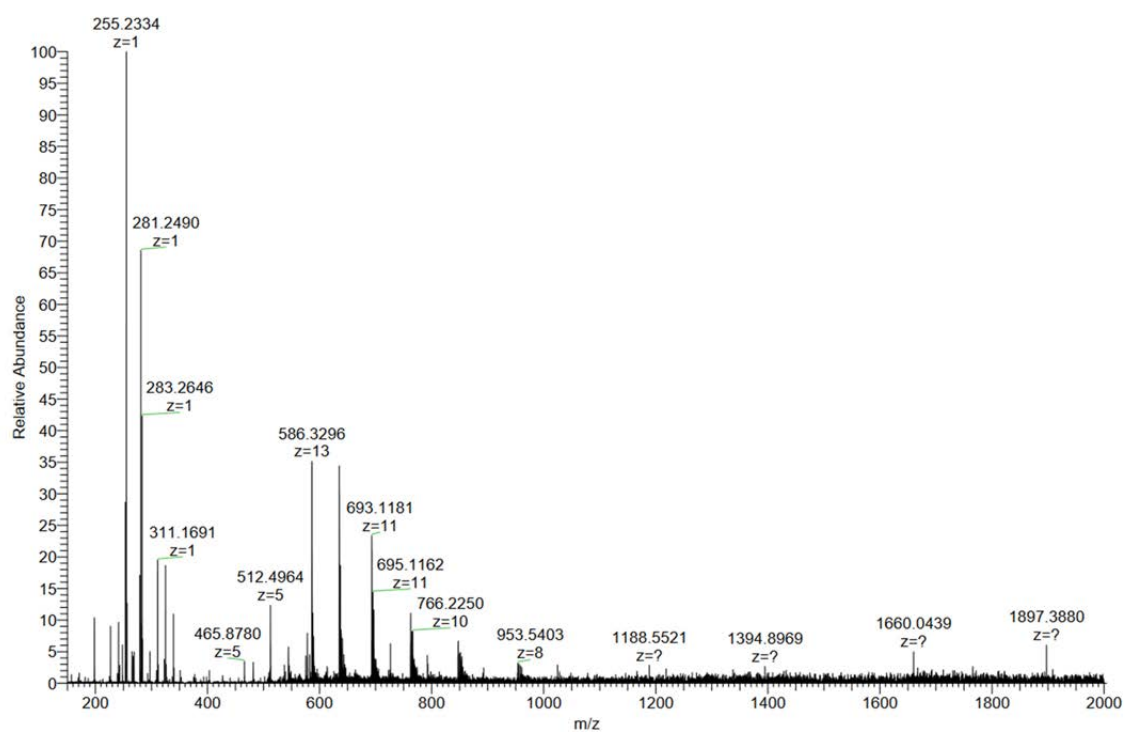


Figure 5.18: MS spectrum of O18.

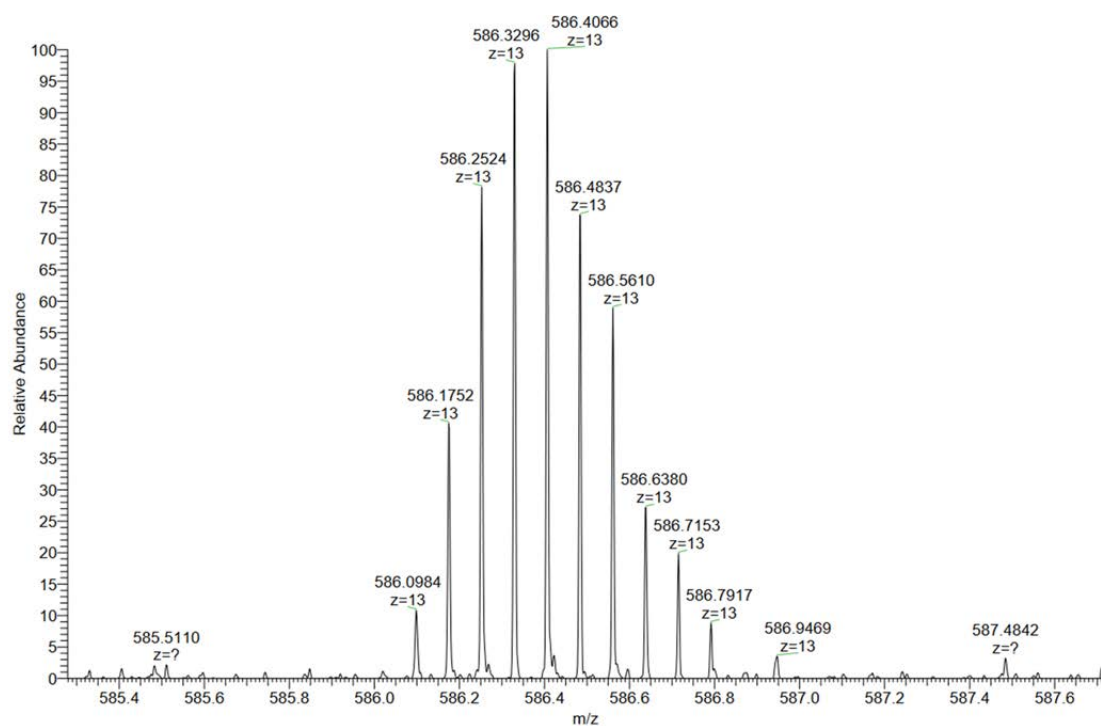


Figure 5.19: MS spectrum of O18.

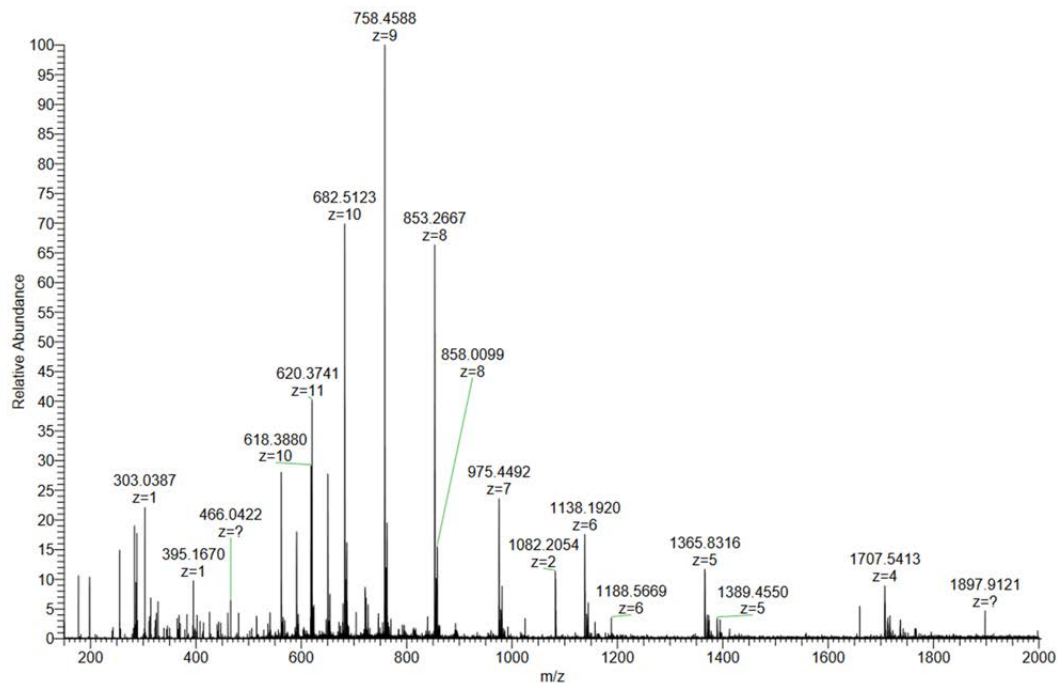


Figure 5.20: MS spectrum of O19.

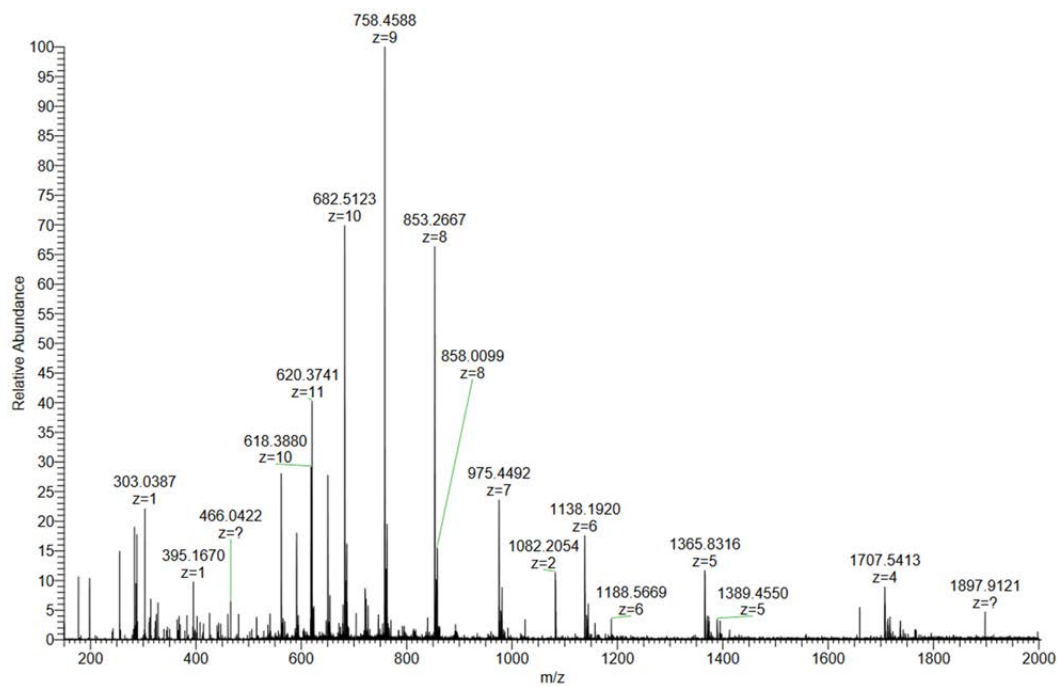
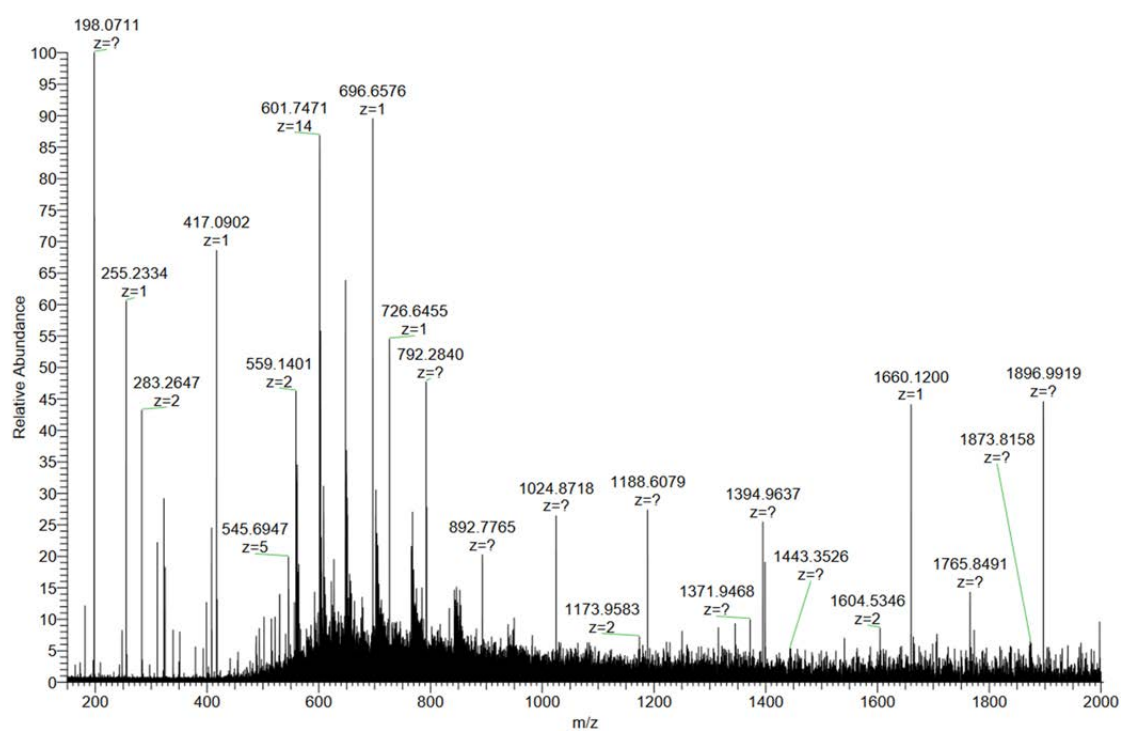
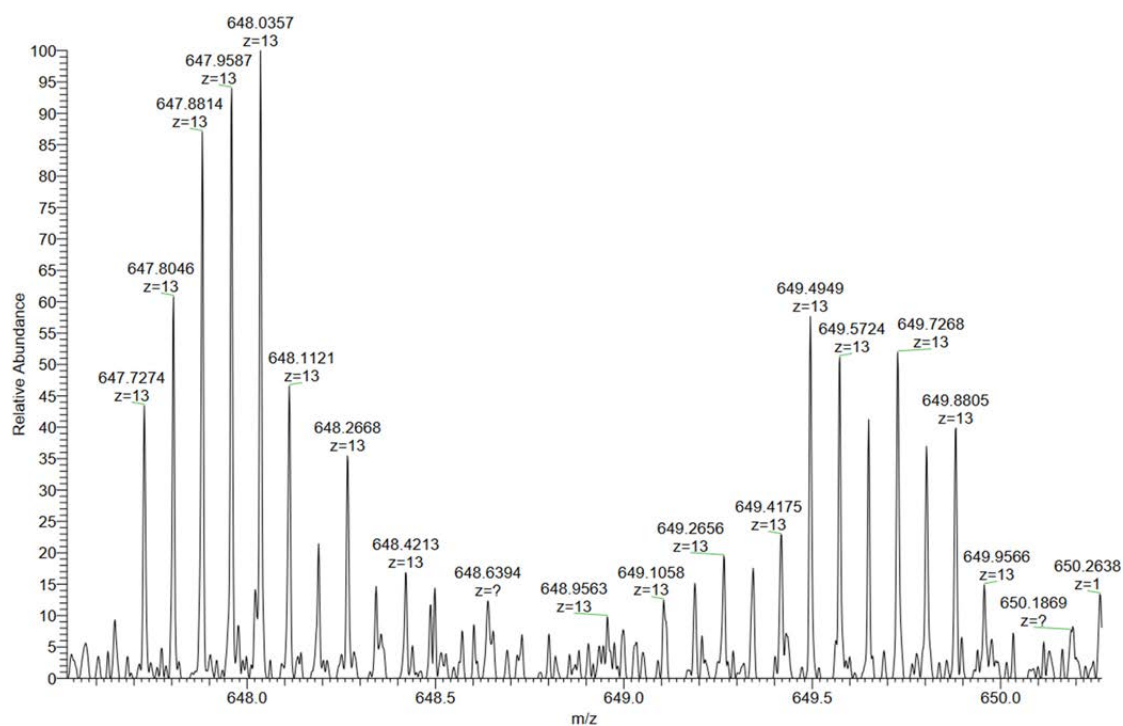


Figure 5.21: MS spectrum of O19.

Figure 5.22: MS spectrum of O₂₀.Figure 5.23: MS spectrum of O₂₀.

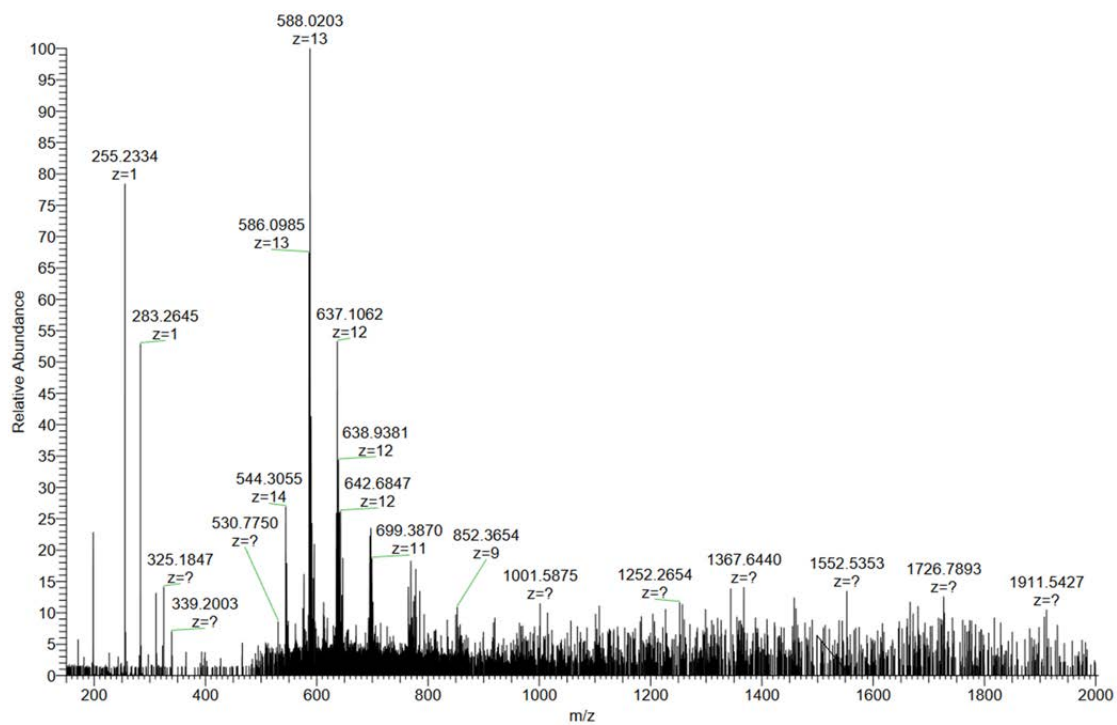


Figure 5.24: MS spectrum of O21.

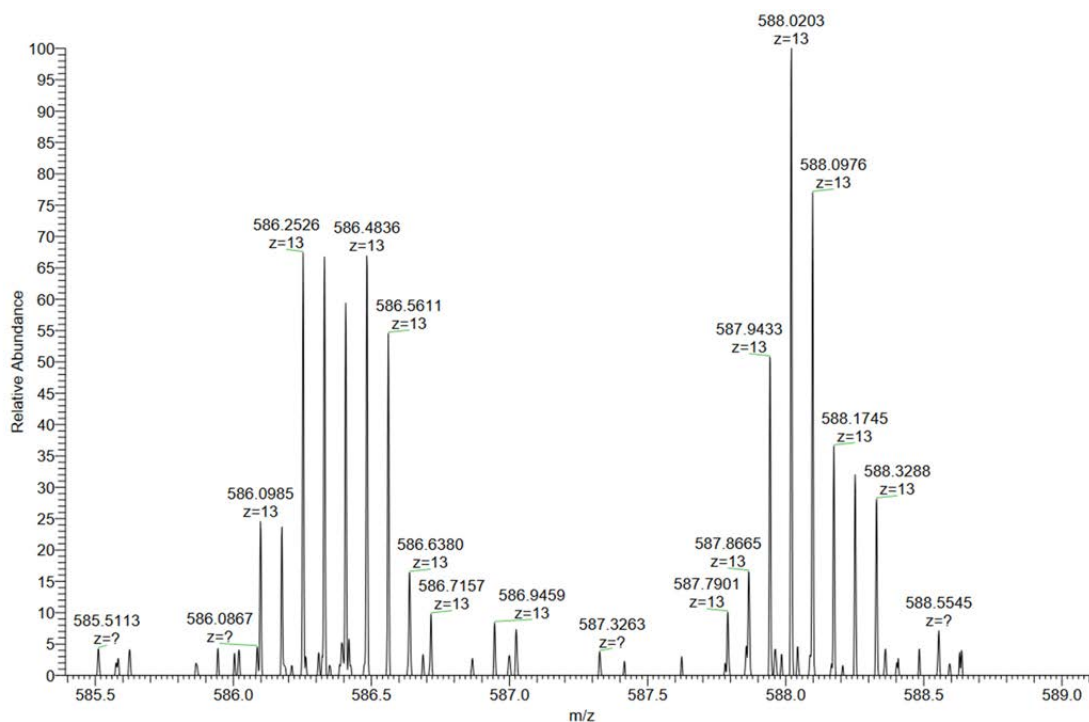


Figure 5.25: MS spectrum of O21.

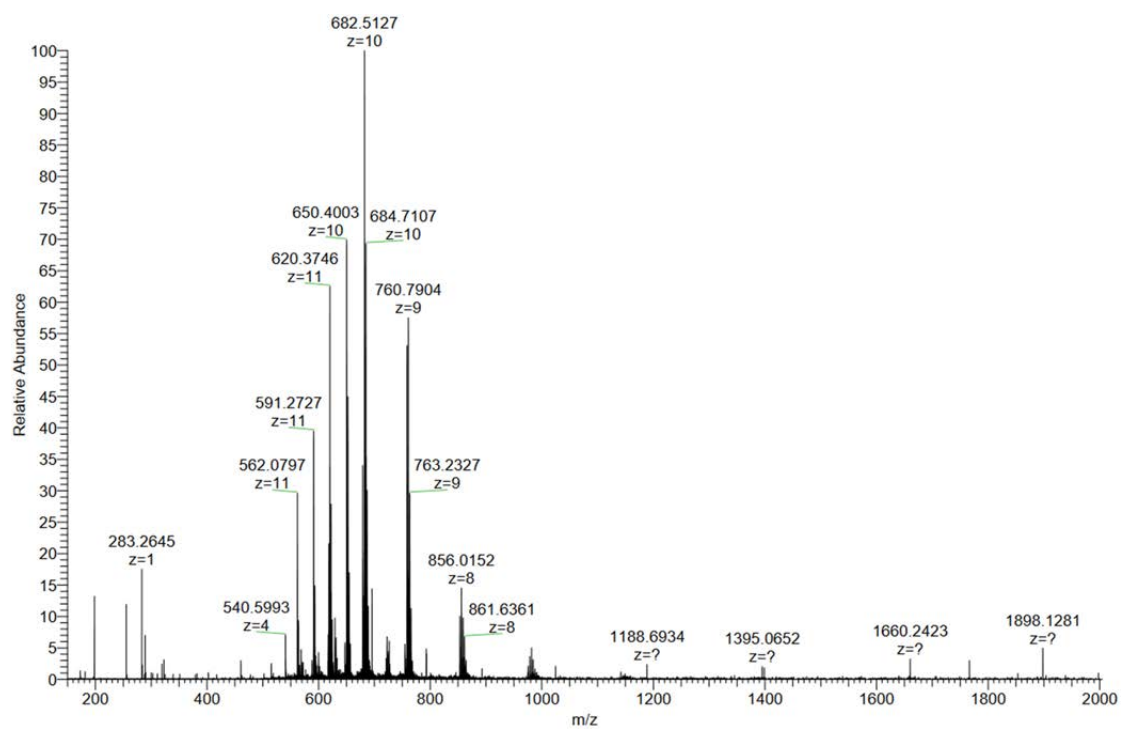


Figure 5.26: MS spectrum of O22.

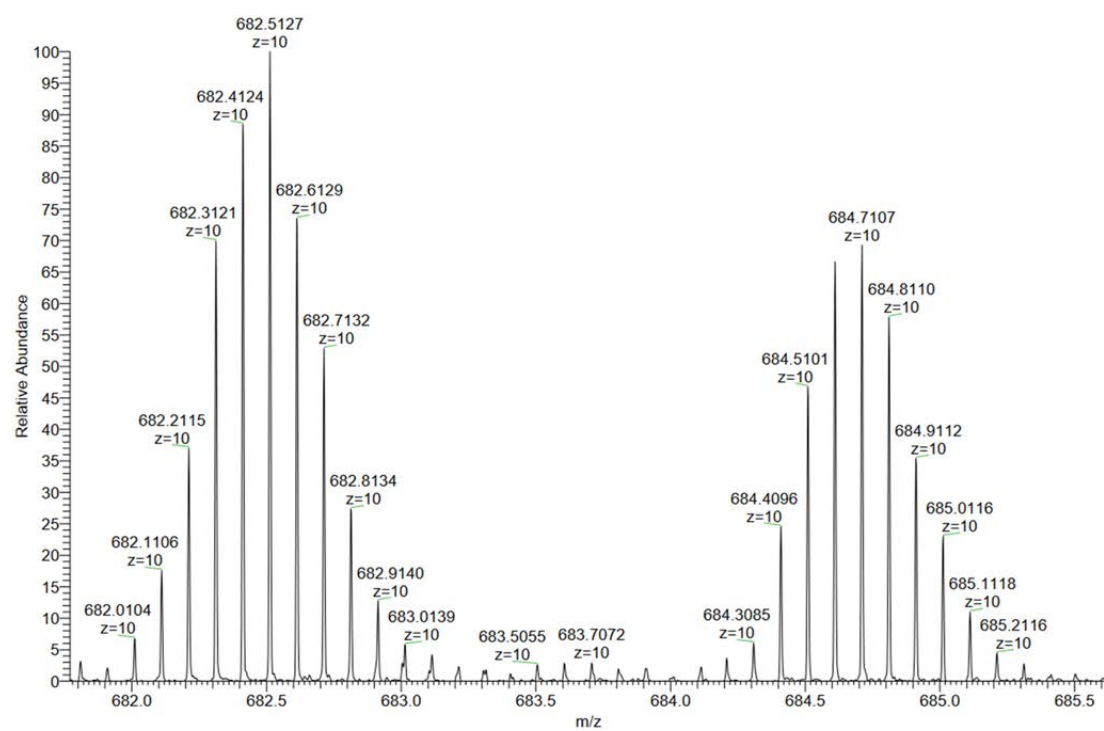


Figure 5.27: MS spectrum of O22.

5.3.2 Additional AFM

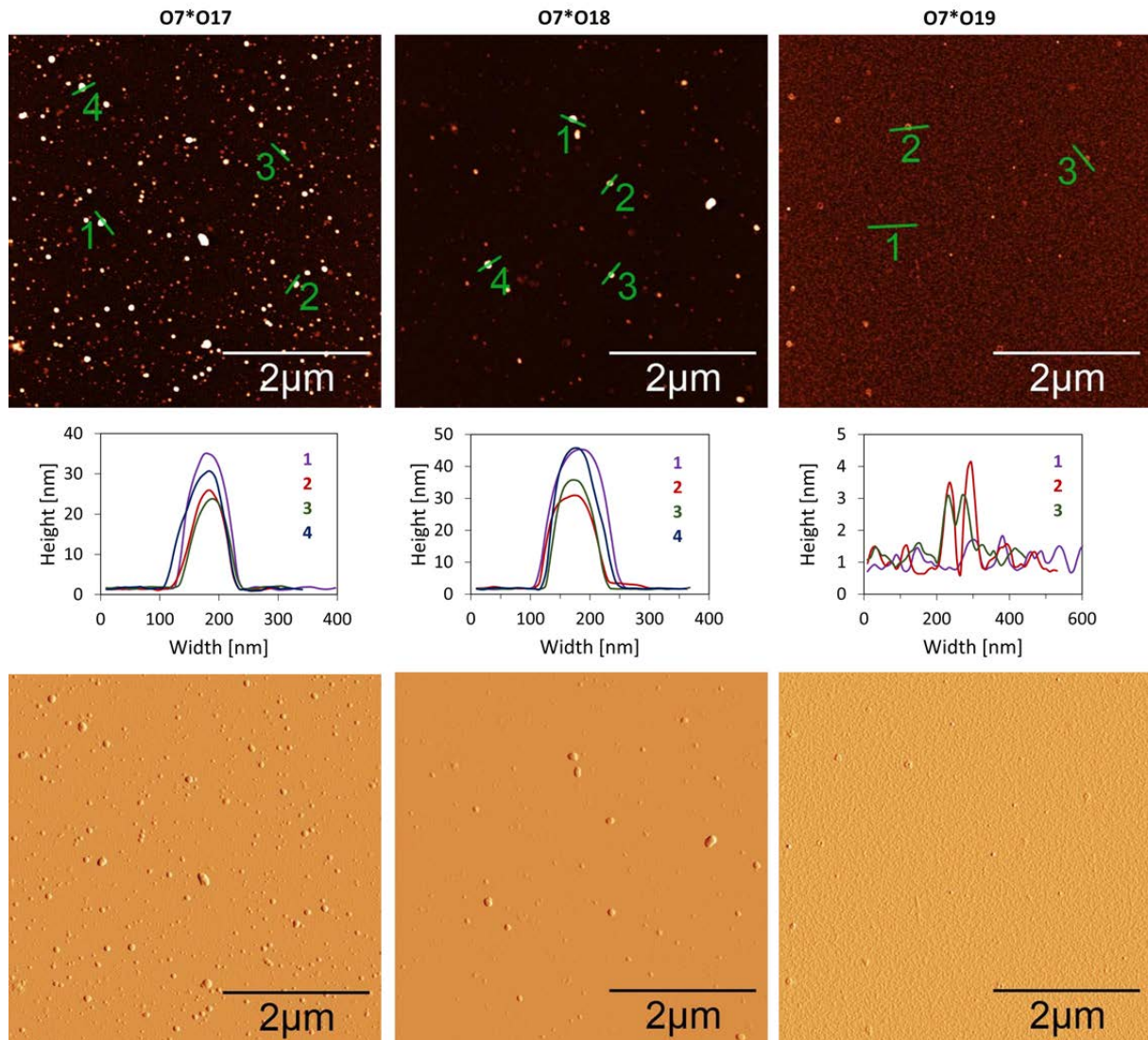


Figure 5.28: AFM scan (top) with corresponding cross sections (middle) and deflection scan of (bottom) O7*O17 (left), O7*O18 (middle), and O7*O19 (right). Conditions: 1 μM each single strand, 10 mM sodium phosphate buffer pH 7.2, 0.03 mM spermine · 4 HCl, 20 vol% ethanol.

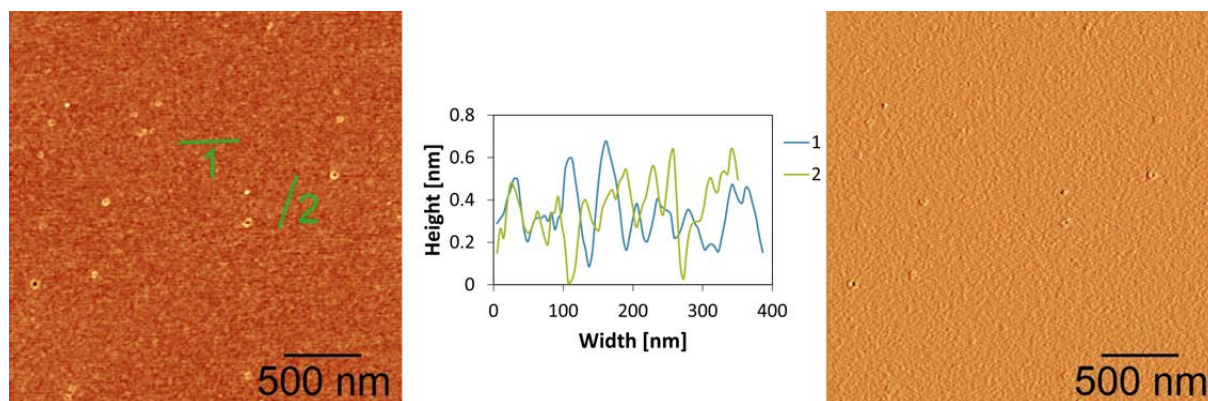


Figure 5.29: AFM scan (left) with corresponding cross sections (middle) and deflection scan of (right) of solution without oligomer. Conditions: 10 mM sodium phosphate buffer pH 7.2, 0.03 mM spermine · 4 HCl, 20 vol% ethanol.

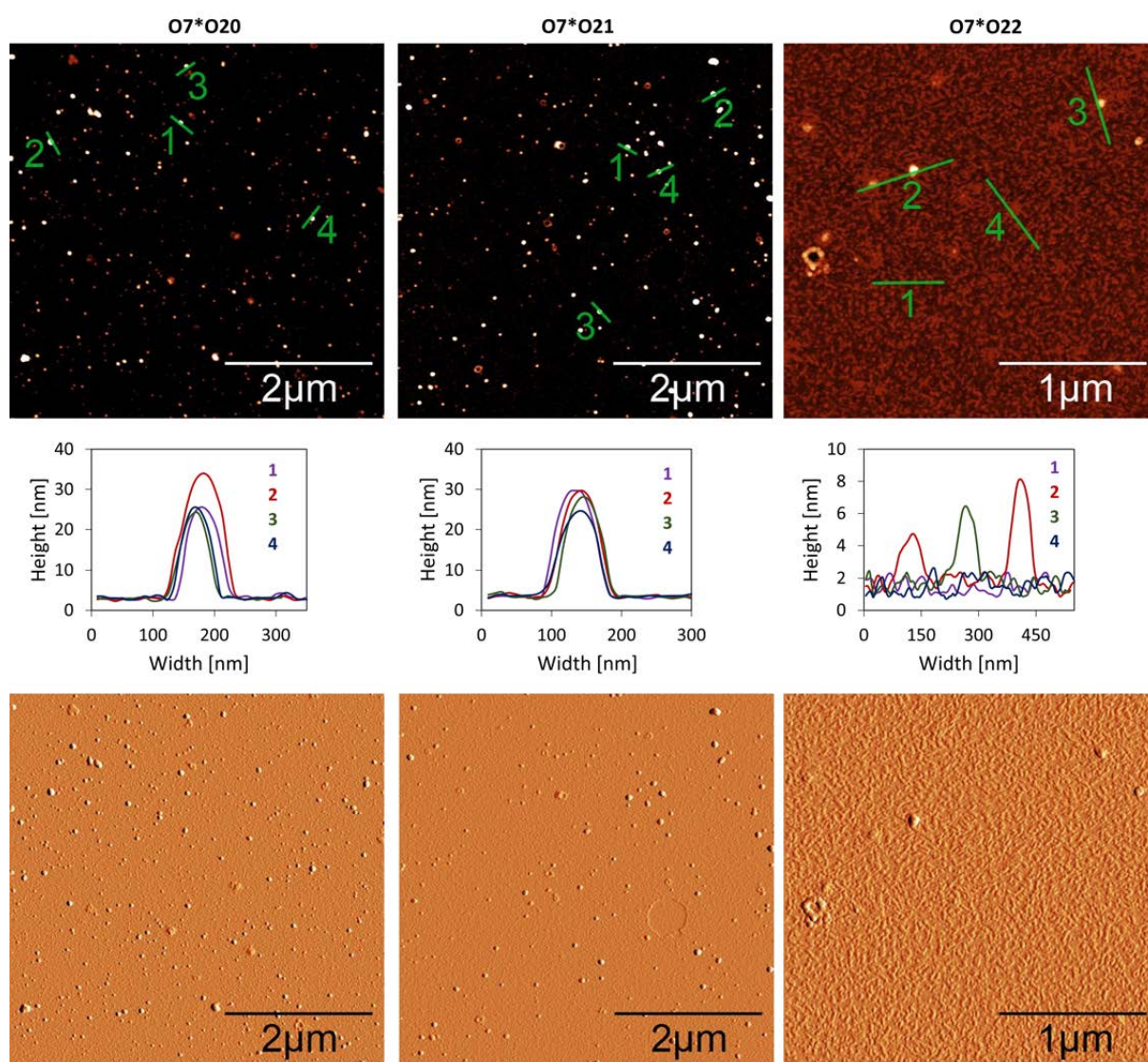


Figure 5.30: AFM scan (top) with corresponding cross sections (middle) and deflection scan of (bottom) **O7*O20** (left), **O7*O21** (middle), and **O7*O22** (right). Conditions: 1 μ M each single strand, 10 mM sodium phosphate buffer pH 7.2, 0.03 mM spermine · 4 HCl, 20 vol% ethanol.

5.3.3 Additional Cryo-EM Images

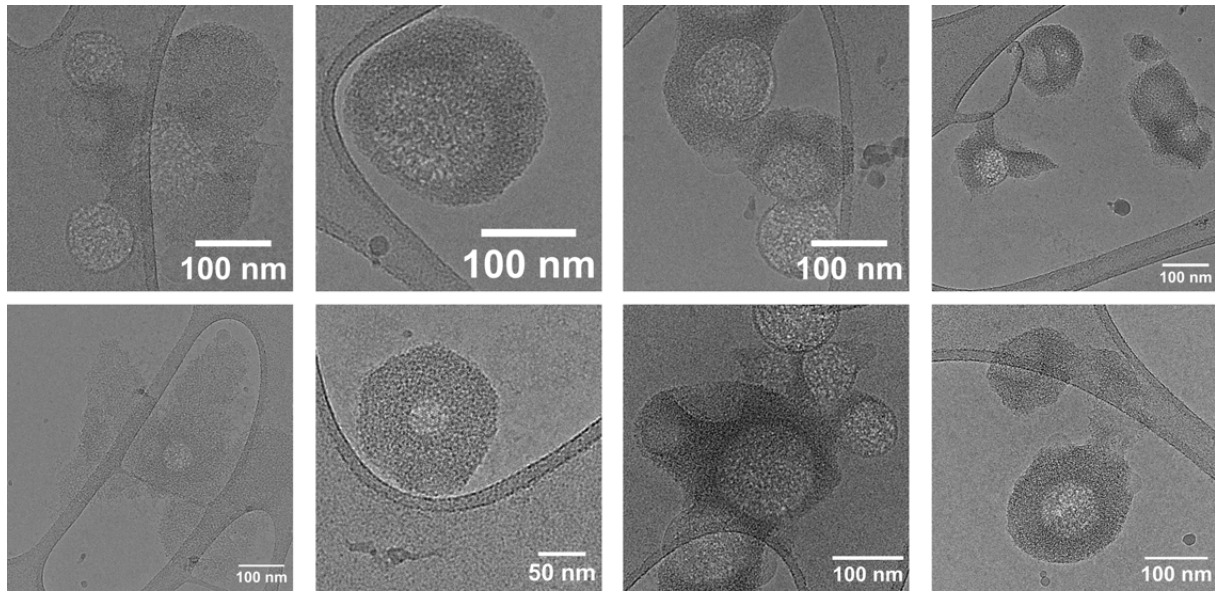


Figure 5.31: Additional cryo-EM image of self-assembled **O7*O17**. Conditions: 1 μ M **O7*O17**, 10 mM sodium phosphate buffer pH 7.2, 0.03 mM spermine \cdot 4 HCl, 20 vol% ethanol.

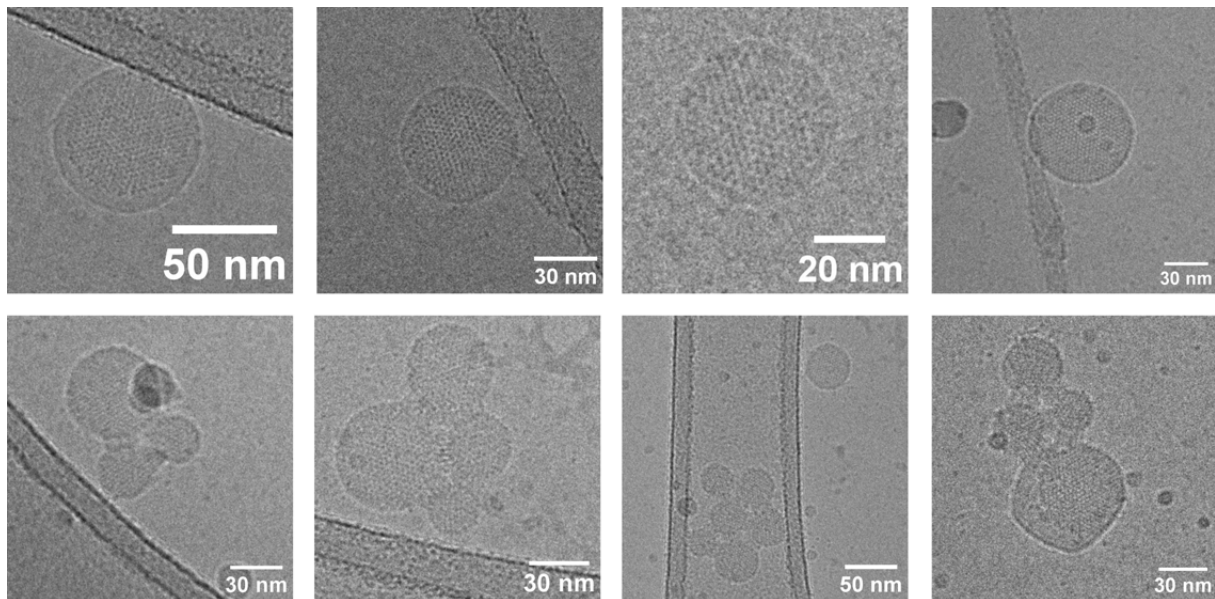


Figure 5.32: Additional cryo-EM image of self-assembled **O7*O18**. Conditions: 1 μ M **O7*O18**, 10 mM sodium phosphate buffer pH 7.2, 0.03 mM spermine \cdot 4 HCl, 20 vol% ethanol.

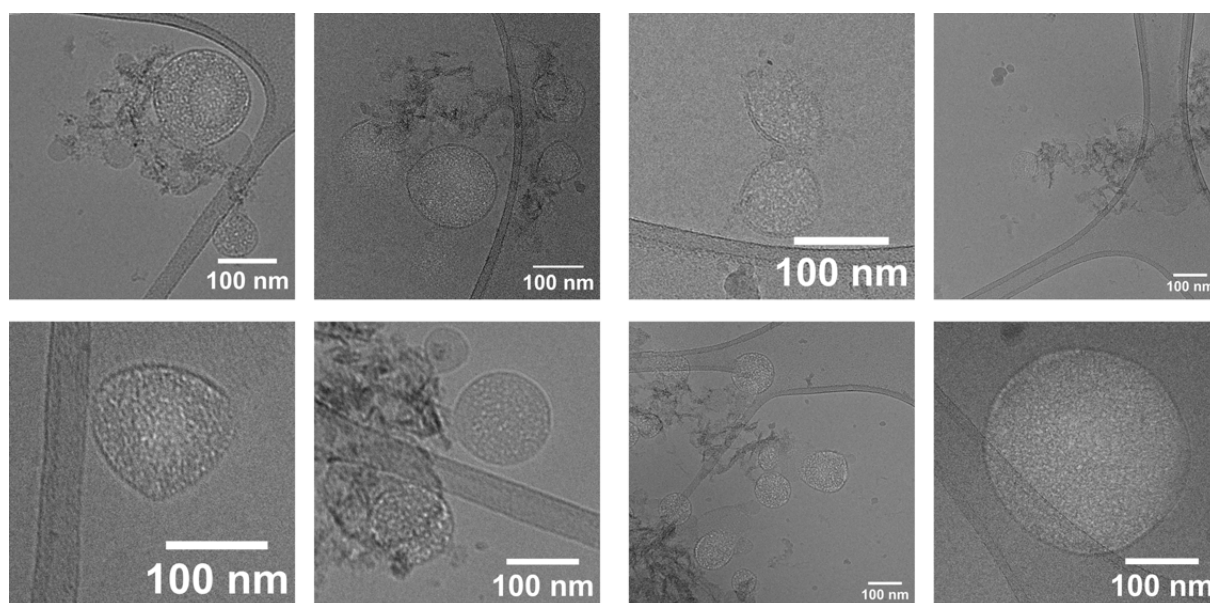


Figure 5.33: Additional cryo-EM image of self-assembled **O7*O20**. Conditions: 1 μ M **O7*O20**, 10 mM sodium phosphate buffer pH 7.2, 0.03 mM spermine \cdot 4 HCl, 20 vol% ethanol.

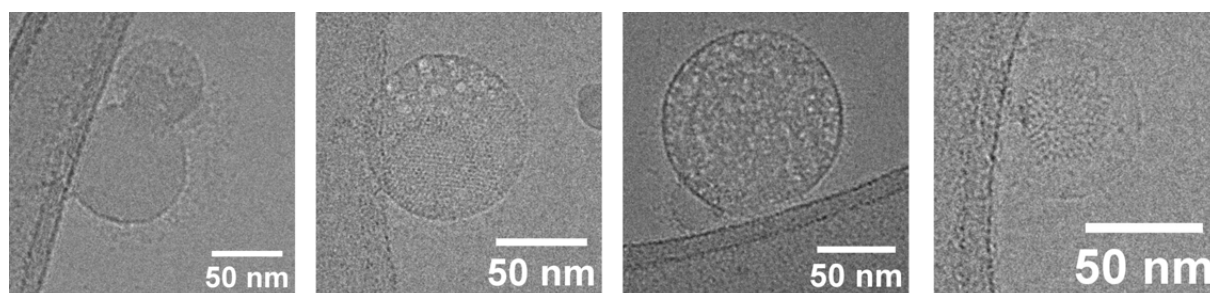


Figure 5.34: Additional cryo-EM image of self-assembled **O7*O21**. Conditions: 1 μ M **O7*O21**, 10 mM sodium phosphate buffer pH 7.2, 0.03 mM spermine \cdot 4 HCl, 20 vol% ethanol.

5.3.4 DLS Measurement Conditions and Results

Table 5.2: Key results and measurement conditions of DLS measurement at 20 °C of a solution of **O7*O17**, **O7*O18**, **O7*O20**, and **O7*O21**. Conditions: 1 μ M each single strand, 10 mM sodium phosphate buffer pH 7.2, 0.03 mM spermine \cdot 4 HCl, 20 vol% ethanol.

Duplex	Size Diameter with Error (nm)	Z-Average Size Diameter (nm)	PDI	PDI Width (nm)	Count Rate (kcps)	Attenuator
O7*O17	193.2 \pm 64.91	172.6	0.102	55.00	21579.8	7
O7*O18	119.4 \pm 37.54	107.8	0.100	34.04	8915.4	8
O7*O20	143.3 \pm 55.36	143.3	0.123	50.35	13042.6	7
O7*O21	116.3 \pm 39.56	109.5	0.205	49053	6816.5	8

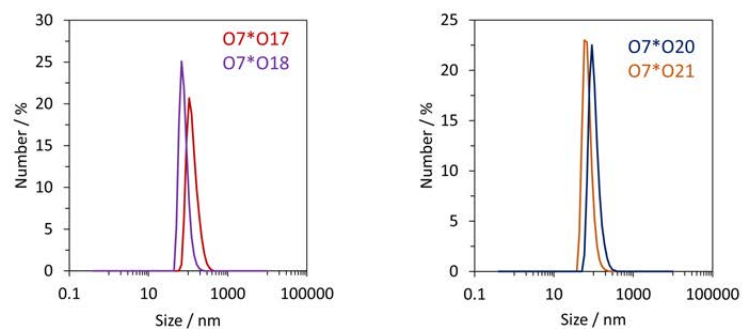


Figure 5.35: DLS measurements of **O7*O17** and **O7*O18** (left), and **O7*O20** and **O7*O21** (right). Conditions: 1 μ M each single strand, 10 mM sodium phosphate buffer pH 7.2, 0.03 mM spermine \cdot 4 HCl, 20 vol% ethanol, 20 °C.

Chapter 6

Supramolecular Self-Assembly of Terminal Functionalized 3'- and 5'-End Modified Pyrene-DNA Conjugates

In this chapter, pyrene-DNA conjugates modified with pyrene at 3'- and 5'-end are hybridized with DNA strands bearing different terminal functionalities. Firstly, we examined the influence of polyethylene glycol (PEG) linked alkyne functionalization on the supramolecular assembly. Subsequently, we investigated the effects longer PEG chains (PEG2000 and PEG5000) have on the formation of supramolecular polymers. After that, we analyzed the impact of a sterically demanding branched N-acetylgalactosamine (GalNAc) modification. It was found that the terminal modifications have a minor influence on the self-assembly of the pyrene-DNA conjugates.

6.1 Results and Discussion

The 20-mer DNA single strands used in this chapter are illustrated in Figure 6.1. The unmodified oligonucleotide **O7** and the three phosphodiester-linked 3'/5'-modified pyrene-DNA conjugates **O20** were already used in chapter 4 (see section 4.3 for details of synthesis and purification). The 5'-end alkyne-modified DNA strand **O23** was prepared *via* solid-phase synthesis using the phosphoramidite approach explained in the general introduction (section 1.3) and subsequently purified by HPLC. Detailed experimental procedures are provided in the appendix of this chapter (section 6.3). The two PEG-conjugated oligonucleotides **O24** and **O25** were synthesized using standard copper-catalyzed azide-alkyne cycloaddition (CuAAC) click chemistry, starting with the 5'-end alkyne-modified DNA single strand **O23**.²⁰⁷ **O24** has a PEG chain with a length of 2000 Da, whereas the length of **O25** is 5000 Da. Further information on the synthesis and purification of these three oligomers are also provided in the appendix of this chapter in section 6.3. Additionally, HPLC-purified 3'-end N-acetylgalactosamine (GalNAc)-modified **O26** was purchased from Microsynth (Switzerland).

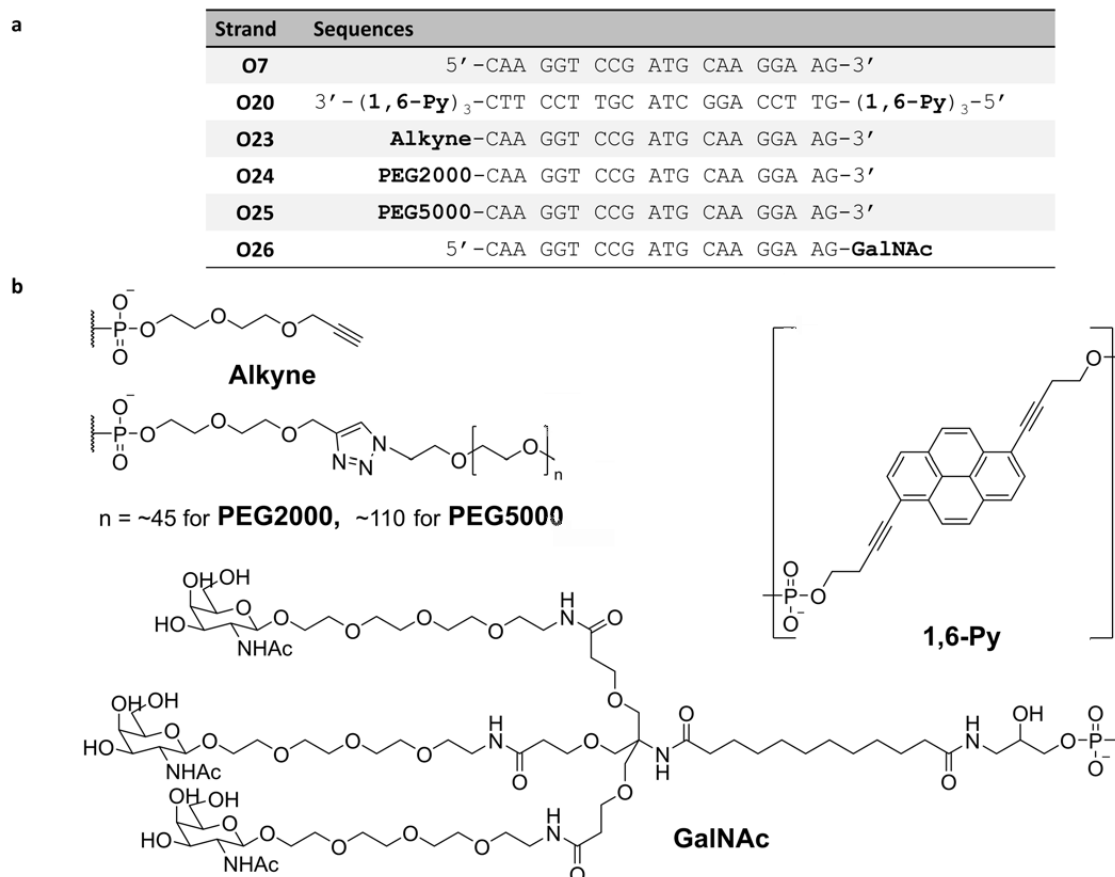


Figure 6.1: (a) DNA sequences of 3'/5'-modified 1,6-dialkynyl pyrene-DNA conjugates **O20** and the complementary unmodified **O7** and modified single strand **O23–O26**. (b) Molecular structure of 1,6-dialkynyl pyrene (**1,6-Py**), alkyne- (**Alkyne**), polyethylene glycol- (**PEG2000** and **PEG5000**), and N-acetylgalactosamine (**GalNAc**)-modification.

Hybridizing of the pyrene-DNA conjugate **O20** with any of the modified DNA single strands **O23–O26** results in duplexes featuring pyrene sticky ends on both sides, along with an extra terminal functionality derived from the complements. The key interest was to understand the influence of the terminal functionalities on the supramolecular assembly *i.e.*, changes in morphology.

The 3'- and 5'-modified pyrene-DNA conjugate **O20*O7**, which possess no additional terminal modification, serves as a control in this chapter. AFM images of **O20*O7** showed the formation of vesicles with diameters of 50–150 nm (Figure 6.2). Most vesicles were observed as single spherical nanostructures, while a few formed agglomerated.

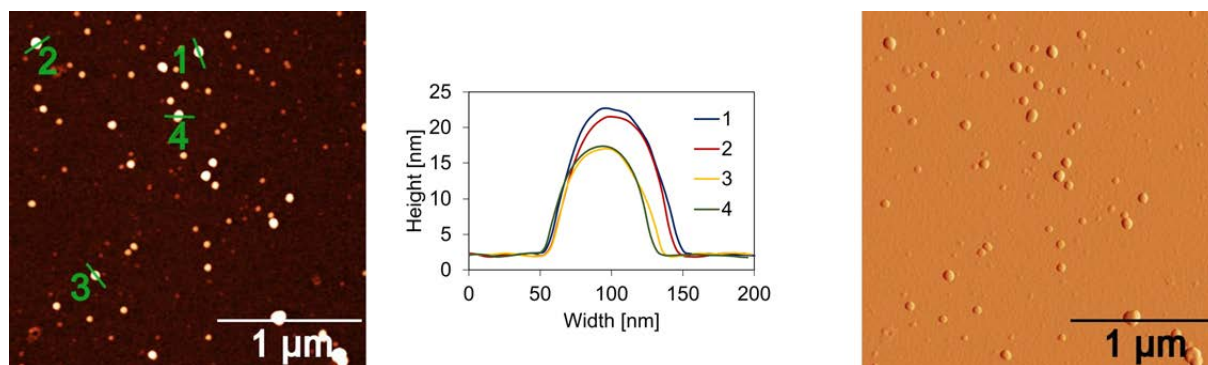


Figure 6.2: AFM scan (left) with corresponding cross sections (middle) and deflection scan (right) of assembled of **O20*O7**. Conditions: 1 μM each single strand, 10 mM sodium phosphate buffer pH 7.2, 0.03 mM spermine · 4 HCl, 20 vol% ethanol.

6.1.1 Alkyne Functionalization

Firstly, the influence of a polyethylene-linked terminal alkyne modification on the supramolecular assembly of 3'/5'-end modified pyrene-DNA conjugates was evaluated. Temperature-dependent UV-vis absorption measurements at 260 nm of **O20*O7** and **O20*O23** were conducted to assess the influence of the alkyne modification (Figure 6.3). The nucleation temperatures of **O20*O7** and **O20*O23** were found to be identical. Temperature-dependent UV-vis and fluorescence spectra of the duplexes **O20*O23** were measured. They resemble the spectra of **O20*O7** (depicted in the appendix Figure 6.18).

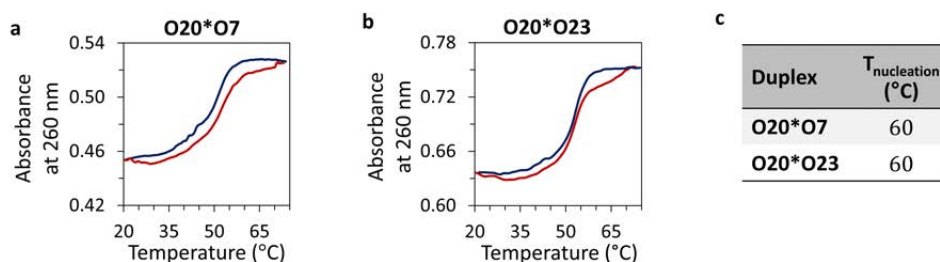


Figure 6.3: Temperature-dependent UV-vis absorbance at 260 nm (cooling: blue and heating: red) of (a) **O20*O7**, (b) **O20*O23**, and (c) table of nucleation temperatures. Conditions: 1 μM each single strand, 10 mM sodium phosphate buffer pH 7.2, 0.03 mM spermine \cdot 4 HCl, 20 vol% ethanol.

AFM measurements of **O20*O23** were performed to confirm the formation of nanostructures (Figure 6.4). AFM measurements revealed the formation of spherical supramolecular assemblies with diameters of 50 to 150 nm. The results are identical to the control **O20*O7** (Figure 6.2). AFM measurements showed that the terminal alkyne modification has no measurable effect on the morphology of the supramolecular assembly.

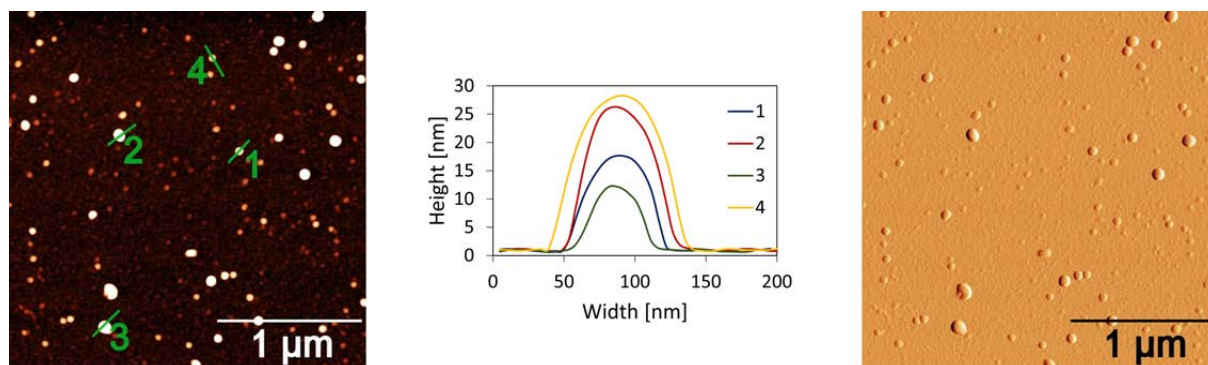


Figure 6.4: AFM scan (left) with corresponding cross sections (middle) and deflection scan (right) of assembled **O20*O23**. Conditions: 1 μM each single strand, 10 mM sodium phosphate buffer pH 7.2, 0.03 mM spermine \cdot 4 HCl, 20 vol% ethanol.

6.1.2 Effect of PEGylation

To assess the impact of DNA-PEGylation, the 3'/5'-modified pyrene-DNA duplex **O20** was hybridized with complementary PEG-modified oligonucleotides, namely **O24** and **O25**. Temperature-dependent UV-vis absorption measurements at 260 nm of **O20*O7**, **O20*O24**, and **O20*O25** indicated that PEGylation has a minor influence on the nucleation temperatures (Figure 6.5). The temperature-dependent UV-vis and fluorescence spectra of the duplexes **O20*O7**, **O20*O24**, and **O20*O25** are comparable (appendix Figure 6.19).

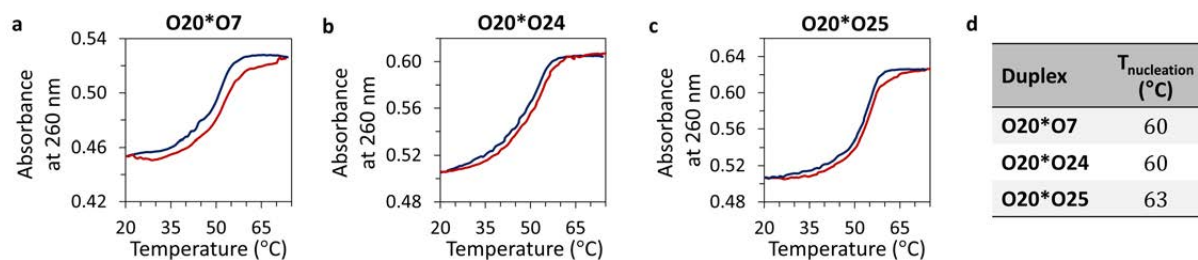


Figure 6.5: Temperature-dependent UV-vis absorbance at 260 nm (cooling: blue and heating: red) of (a) **O20*O7**, (b) **O20*O24**, (c) **O20*O25**, and (d) table of nucleation temperatures. Conditions: 1 μM each single strand, 10 mM sodium phosphate buffer pH 7.2, 0.03 mM spermine \cdot 4 HCl, 20 vol% ethanol.

AFM measurements of **O20*O7**, **O20*O24**, and **O20*O25** were carried out and compared to elucidate their structures (Figure 6.6). As mentioned earlier, AFM images of **O20*O7** revealed the formation of vesicles with diameters ranging from 50 to 150 nm (Figure 6.2). AFM measurements of the PEG-containing oligomer **O20*O24** exhibited vesicles with diameters spanning 50 to 150 nm (Figure 6.6 top). On the other hand, measurements of **O20*O25**, the oligomer with a longer PEG chain, revealed indistinct small vesicles with diameters smaller than 50 nm and undefined circular structures (Figure 6.6 bottom). The presence of poorly defined structures further suggests a lower rigidity of the PEGylated vesicles. These results show that the rigidity of the nanostructures decreases with increased PEG chain length.

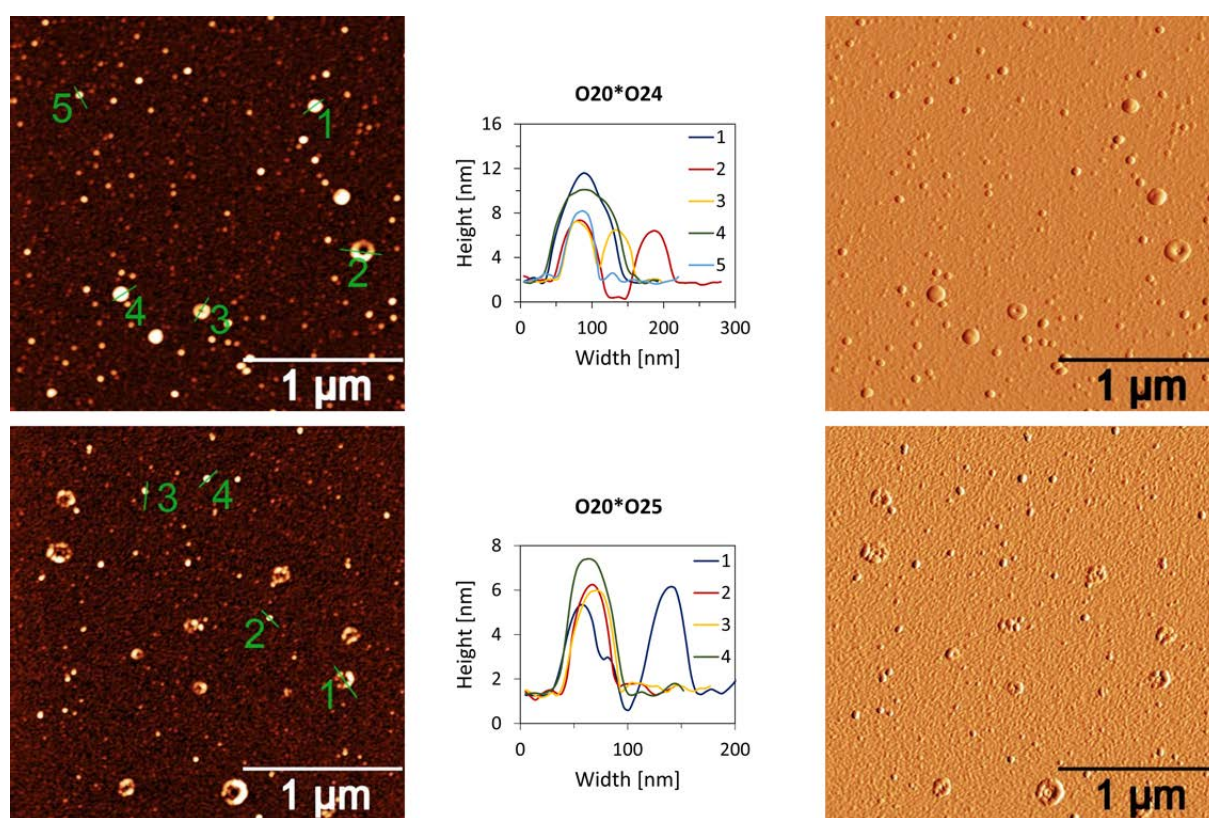


Figure 6.6: AFM scan (left) with corresponding cross sections (middle) and deflection scan of assembled (right) **O20*O24** (top) and **O20*O25** (bottom). Conditions: 1 μM each single strand, 10 mM sodium phosphate buffer pH 7.2, 0.03 mM spermine \cdot 4 HCl, 20 vol% ethanol.

6.1.3 Influence of a Branched GalNAc Moiety

In contrast to the linear PEG chains, the trivalent GalNAc moiety, characterized by its branched structure, imposes more significant steric demands. Therefore, the branched GalNAc component in the **O20*O26** duplex has the potential to induce morphological changes in the self-assembled DNA nanostructures. Moreover, the chosen triantennary GalNAc functional group holds promise for targeted drug delivery applications to the liver.^{208,209} GalNAc is promising, as it possesses an excellent binding affinity, particularly in a trivalent cluster, to the asialoglycoprotein receptor (ASGPR), which is prominently expressed in hepatocytes.

Temperature-dependent UV-vis absorption measurements at 260 nm of **O20*O7** and **O20*O26** expressed similar nucleation temperatures (Figure 6.7). The hysteresis is slightly decreased in the GalNAc-modified duplexes. Temperature-dependent UV-vis absorption and fluorescence spectra of **O20*O26** were comparable to **O20*O7** (illustrated in the appendix Figure 6.20).

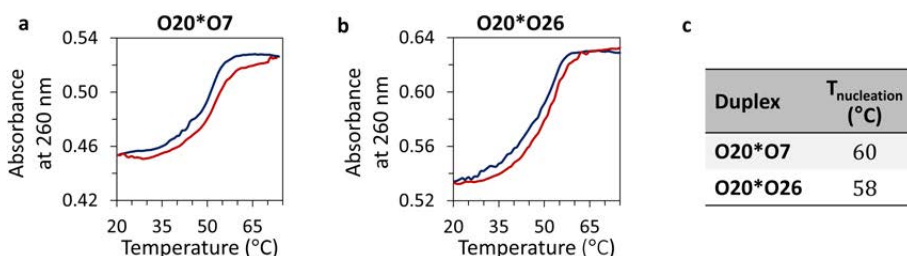


Figure 6.7: Temperature-dependent UV-vis absorbance at 260 nm (cooling: blue and heating: red) of (a) **O20*O7**, (b) **O20*O26**, and (c) table of nucleation temperatures. Conditions: 1 μM each single strand, 10 mM sodium phosphate buffer pH 7.2, 0.03 mM spermine \cdot 4 HCl, 20 vol% ethanol.

AFM measurements of **O20*O26** were conducted to determine the influence of the GalNAc moiety on self-assembly (Figure 6.8). The AFM results revealed the presence of individual spherical aggregates with diameters ranging from 50 to 150 nm. Given their resemblance to the shape of **O20*O7**, the AFM data suggests that the modification with the sterically demanding GalNAc has a minor impact on the supramolecular self-assembly.

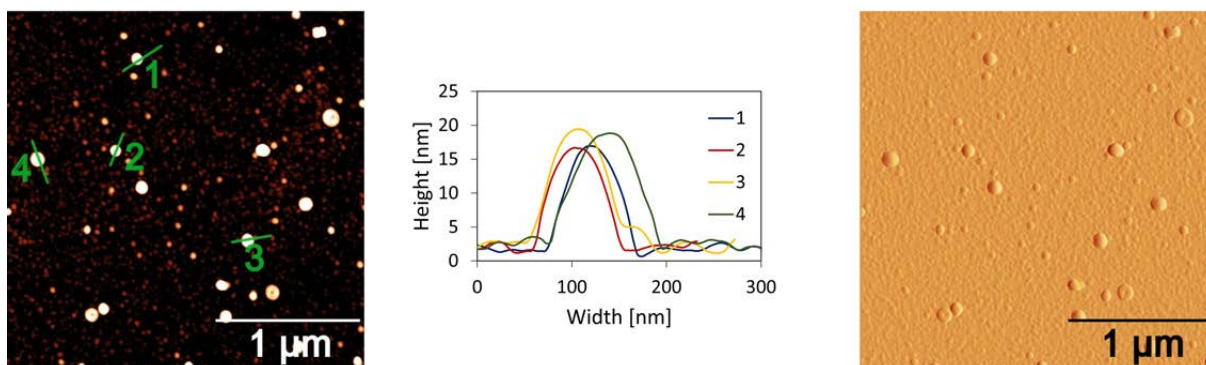


Figure 6.8: AFM scan of **O20*O26** (right) with the corresponding cross sections (middle) and deflection scan of assembled (left). Conditions: 1 μM each single strand, 10 mM sodium phosphate buffer pH 7.2, 0.03 mM spermine \cdot 4 HCl, 20 vol% ethanol.

6.2 Conclusions and Outlook

In this chapter, DNA nanostructures bearing terminal modifications were presented. The amphiphilic DNA duplexes feature hydrophobic pyrene residues at the 3'- and 5'-ends of one DNA single strand, accompanied by an additional terminal moiety on the complementary DNA strand. Introducing a PEG-linked terminal alkyne did not alter the self-assembly into spherical nanostructures. Nanostructures formed by duplexes containing longer PEG chains (PEG2000 and PEG5000) were observed to be less rigid on AFM, with decreasing rigidity as the length of the PEG chain increased. Incorporating a branched, triantennary GalNAc moiety had a negligible influence on the supramolecular assembly.

Further experiments could explore the potential of the formed nanostructures for drug delivery. DNA nanostructures containing the PEG2000 and PEG5000 are of peculiar interest, as they possess stealth properties.^{210,211} The GalNAc moiety could be assessed for specific drug delivery to liver cells due to the specific binding to the asialoglycoprotein receptor, which is dominantly in hepatocytes.

Moreover, post-assembly click chemistry could be performed with the spherical assemblies that contain a terminal alkyne modification, allowing the generation of supramolecular assemblies with further functionalities.

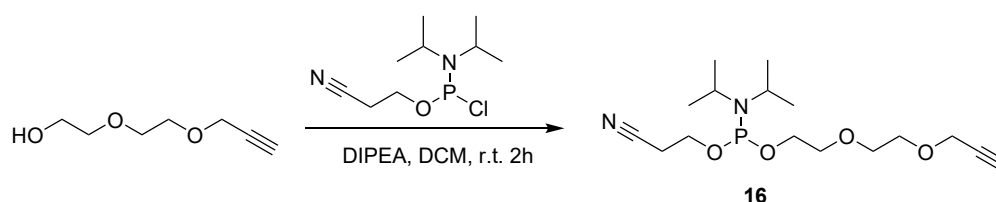
6.3 Appendix - Chapter 6

First, the organic synthesis of the alkyne-phosphoramidite (**16**) is described. Then, NMR spectra and MS results of the synthesized compounds are presented, followed by the description of the synthesis, purification, and characterization (HPLC and MS) of the oligonucleotides **O23–O25**. Finally, additional spectroscopic data are presented.

6.3.1 Organic Synthesis

2-Cyanoethyl (2-(2-(prop-2-yn-1-yloxy)ethoxy)ethyl) diisopropylphosphoramidite (**16**)

A phosphoramidite **16** bearing polyethylene glycol (PEG) chain with an alkyne at its end was synthesized according to published procedures.²¹²



Scheme 6.1: Synthesis of alkyne-phosphoramidite **16**.

2-(2-(2-Propyn-1-yloxy)ethoxy)ethanol (113 mg, 0.785 mmol, 1.00 eq.) was dissolved in anhydrous DCM (5.0 ml) and DIPEA (0.68 ml, 3.925 mmol, 5.0 eq.). 2-cyanoethyl N,N-diisopropylchlorophosphoramidite (222 mg, 0.942 mmol, 1.20 eq.) was slowly added with a syringe, and the reaction mixture was vigorously stirred at r.t. for 2 h until TLC (hexane/ethyl acetate/Et₃N 1:1:0.01) showed disappearance of starting material. After removing the solvent *in vacuo*, the product was purified by silica gel chromatography (hexane/ethyl acetate/Et₃N 1:1:0.01) and dried at high vacuum for 4 h. Phosphoramidite **16** was isolated as a colorless liquid (235 mg, 83%).

¹H-NMR (300 MHz, CDCl₃): δ 4.20 (d, *J* = 2.4 Hz, 2H), 3.88–3.58 (m, 11H), 2.65 (m, 2H), 2.42 (t, *J* = 2.4 Hz, 1H), 1.18 and 11.7 (2×d, *J* = 6.8 Hz 11H). ³¹P NMR (121.5 MHz, DMSO-*d*₆): δ 147.4. HRMS-NSI (*m/z*): [M+Na]⁺ calcd for C₁₆H₂₉N₂O₄P, 367.1757; found, 367.1762.

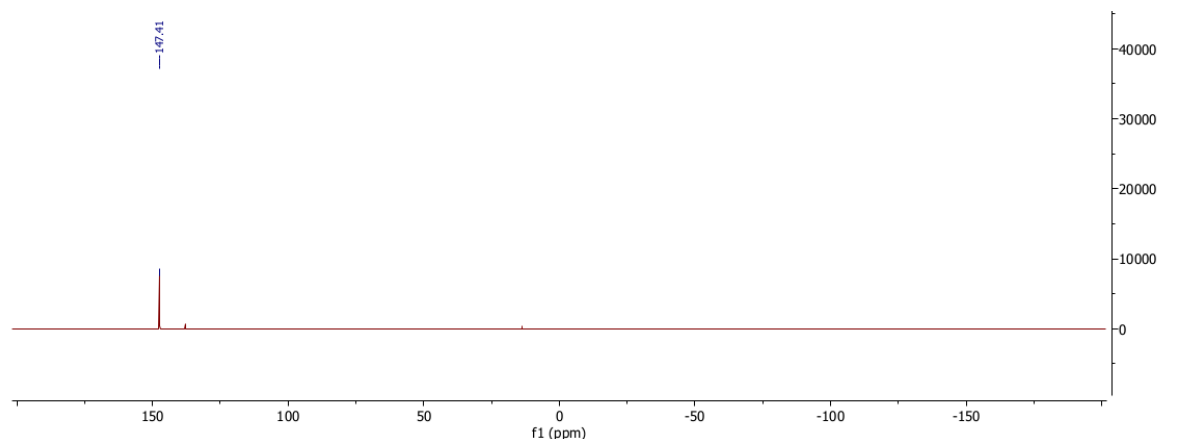


Figure 6.9: ³¹P-NMR of compound **16** in DMSO-*d*₆.

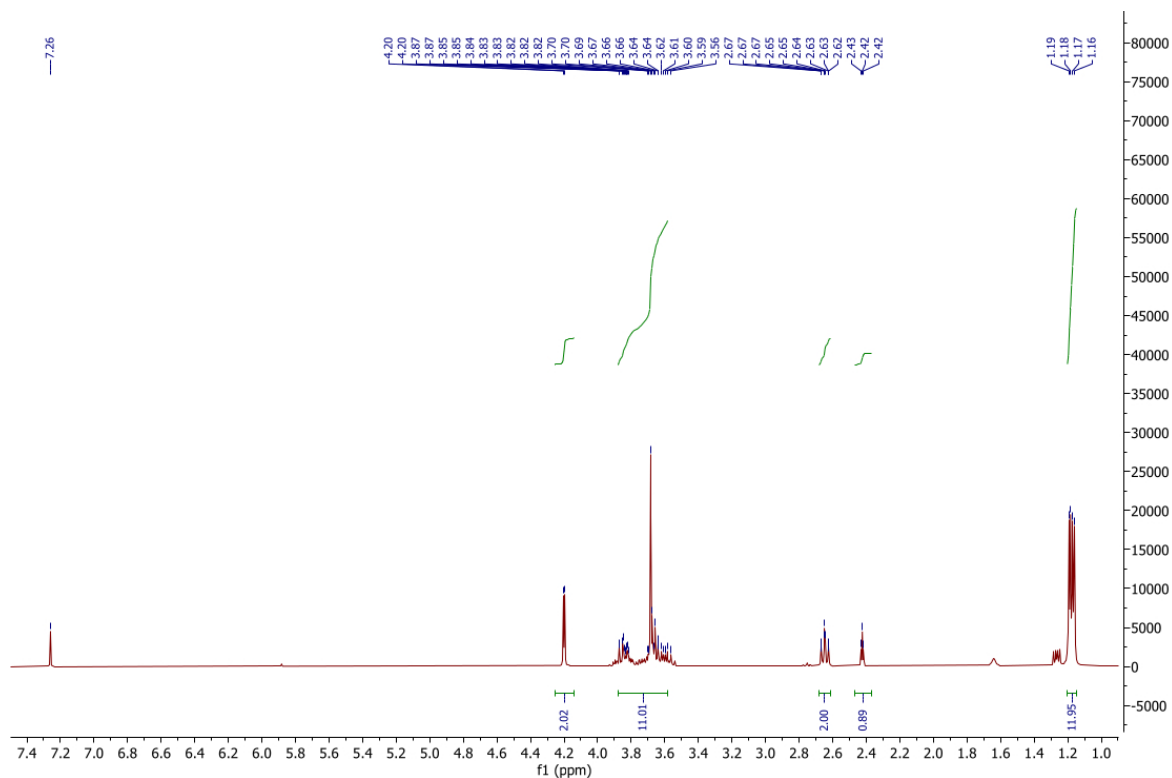


Figure 6.10: $^1\text{H-NMR}$ of compound **16** in CDCl_3 .

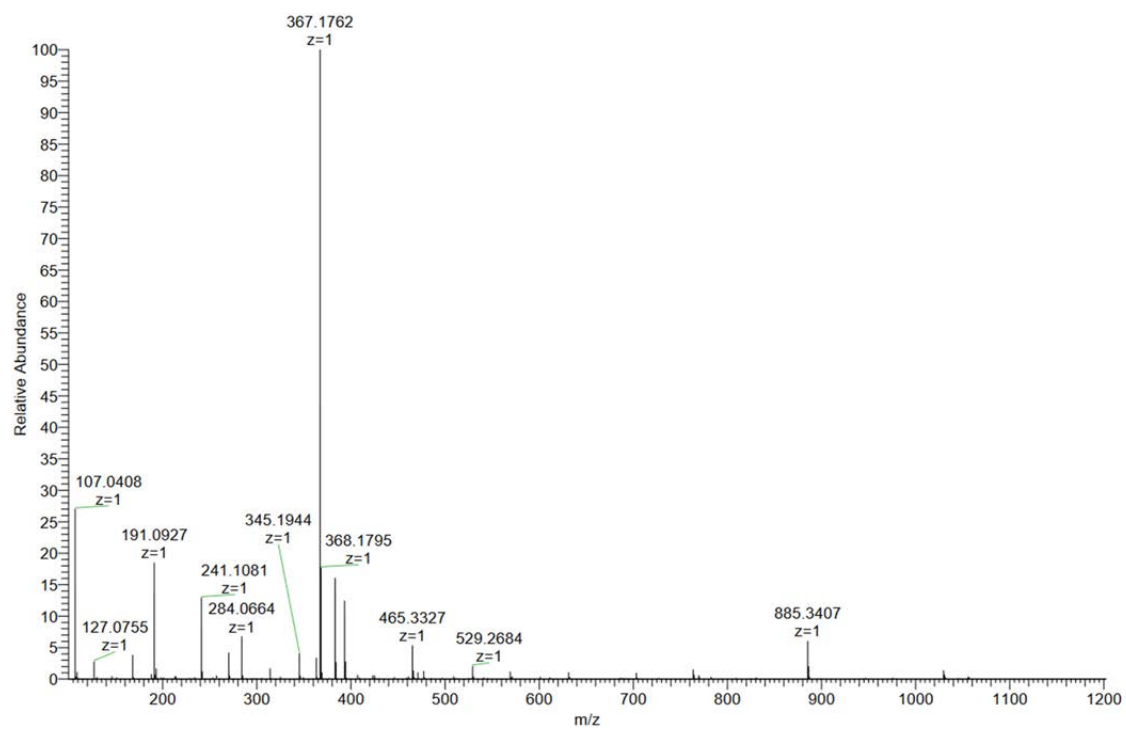


Figure 6.11: MS spectrum of **16**.

6.3.2 Synthesis and Characterization of Oligonucleotides

The 5'-modified alkyne-DNA conjugate **O23** was synthesized on an Applied Biosystems 394 DNA/RNA synthesizer applying a standard cyanoethyl phosphoramidite coupling protocol on a 1 μ mol scale. The solid-phase synthesis and purification are described in detail in chapter 8.

The oligomer **O23** was purified by reverse-phase HPLC (Shimadzu LC-20AT, ReproSil 100 C18, 5,0 μ m, 250 \times 4 mm) with a flow rate of 1 ml/min, with a detection wavelength of 260 nm. **O23** was purified at 40 $^{\circ}$ C with Solvent A: aqueous 90 mM triethylammonium acetate (TEAA); solvent B: acetonitrile; applying the gradients B [%] (t_R [min])= 5 (0), 30 (24).

The purified oligomer **O23** was dissolved in 1 ml of Milli-Q H₂O. Afterward, the absorbance was measured at 260 nm to determine the concentration of the stock solutions and yields of **O23**. The concentration was determined by applying the Beer-Lambert law. The following molar absorptivities were used (at 260 nm) in l \cdot mol⁻¹ \cdot cm⁻¹: ϵ_A ; 15'300, ϵ_T ; 9'000, ϵ_G ; 11'700, and ϵ_C ; 7'400. The results of the mass spectra of **O23** are listed in Table 6.1, the corresponding HPLC traces are depicted in Figure 6.13, and the mass spectra are displayed in Figure 6.14–Figure 6.15.

The PEG-conjugated oligomers **O24** and **O25** were formed *via* Click chemistry. A conventional copper-catalyzed azide-alkyne cycloaddition procedure was applied with a HPLC purified alkyne-modified **O23** and the corresponding mPEG azides **PEG2000N₃** and **PEG5000N₃** (illustrated in Figure 6.12).²⁰⁷ **PEG2000N₃** (with an average molecular weight of 2000 Da) and **PEG5000N₃** (with an average molecular weight of 5000 Da), yielded the PEG-DNA conjugates **O25** and **O26** with a distribution of PEG chain lengths.

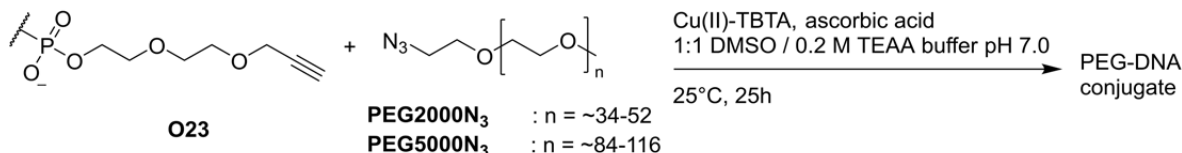


Figure 6.12: Click reaction of **O23** with PEG azides yielding PEG-DNA conjugates **O25** and **O26**.

O24 and **O25** were prepared in the following steps. A solution of alkyne-modified oligonucleotide **O23** in Milli-Q water (275 μ M) was prepared. 84 μ l of this solution was added to an Eppendorf tube. Then, 2 M triethylammonium acetate (TEAA) pH 7.0 in Milli-Q water (28 μ l) was added, followed by DMSO (116.5 μ l). The reaction mixture was vortexed and then centrifuged. A 3 mM solution of either **PEG2000N₃** (with an average molecular weight of 2000 Da) in DMSO (9.5 μ l) or **PEG5000N₃** (with an average molecular weight of 5000 Da) (9.5 μ l) in DMSO was added. The resulting solution was vortexed and then centrifuged. Then, a solution of 5 mM ascorbic acid in Milli-Q water (28 μ l) was added, the reaction mixture was vortexed briefly, centrifuged, sonicated briefly, and degassed by bubbling argon into the solution for 30 s. Promptly, a solution of 10 mM Cu(II)-TBTA (Tris(benzyltriazolylmethyl)amine) in Milli-Q water/ DMSO 45:55 (14 μ l) was added, the Eppendorf tube was flushed with argon, sealed, vortexed thoroughly, and shaken in a ThermoMixer overnight (25 $^{\circ}$ C, 500 rpm). The next day, the reaction mixture was lyophilized.

The crude oligomers **O24** and **O25** were purified by reverse-phase HPLC (Shimadzu LC-20AT, ReproSil 100 C18, 5,0 μ m, 250 \times 4 mm) at 40 $^{\circ}$ C with a flow rate of 1 ml/min, with a detection wavelength λ of 260 nm. Solvent A: 0.1 M aqueous TEAA buffer pH 7.0; solvent B: acetonitrile; B[%] (t_R (min))= 0 (0), 0 (1), 5 (2), 60 (22). The purified oligomer **O24** and **O25** were dissolved in 1 ml of Milli-Q H₂O. Thereafter, the absorbances of the pyrene-DNA conjugates

were measured at 260 nm to determine the concentration of the stock solutions and yields of **O24** and **O25**. The concentration was determined by applying the Beer-Lambert law. For the DNA nucleobases, the following molar absorptivities (at 260 nm) in $\text{L}\cdot\text{mol}^{-1}\cdot\text{cm}^{-1}$ were used: ϵ_{A} ; 15'300, ϵ_{T} ; 9'000, ϵ_{G} ; 11'700, and ϵ_{C} ; 7'400. The mass spectra results of **O24** and **O25** are listed in Table 6.1, the corresponding HPLC traces are depicted in Figure 6.13, and the mass spectra are displayed in Figure 6.16–Figure 6.17.

Table 6.1: Pyrene-DNA oligonucleotide sequences of **O23–O25**, calculated and found masses by NSI-MS, and yields.

Oligomer	Sequence (5'→3')	Calcd mass	Found mass	Yield [%]
O23	Alkyne-CAA GGT CCG ATG CAA GGA AG	6405.1338	6405.1386	28
O24	PEG2000-CAA GGT CCG ATG CAA GGA AG	8533.4098	8533.4321 ^a	45
O25	PEG5000-CAA GGT CCG ATG CAA GGA AG	11370.1060	11370.1060 ^b	70

^a PEG2000 with $n = 46$

^b PEG5000 with $n = 110$ Methanol adduct.

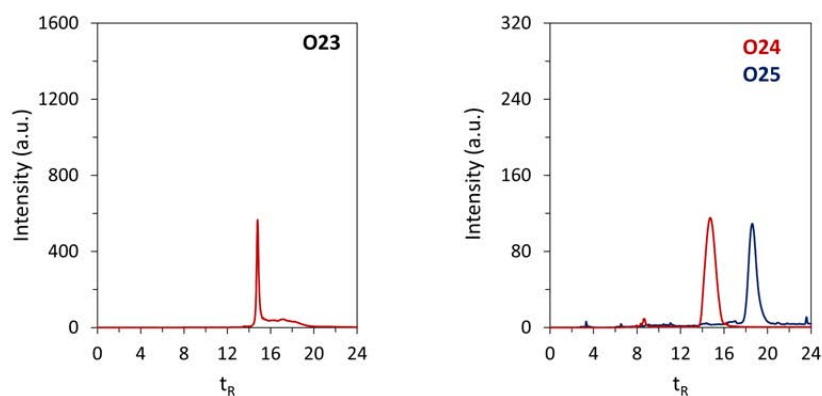


Figure 6.13: HPLC traces of pyrene-DNA conjugates **O23–O25**.

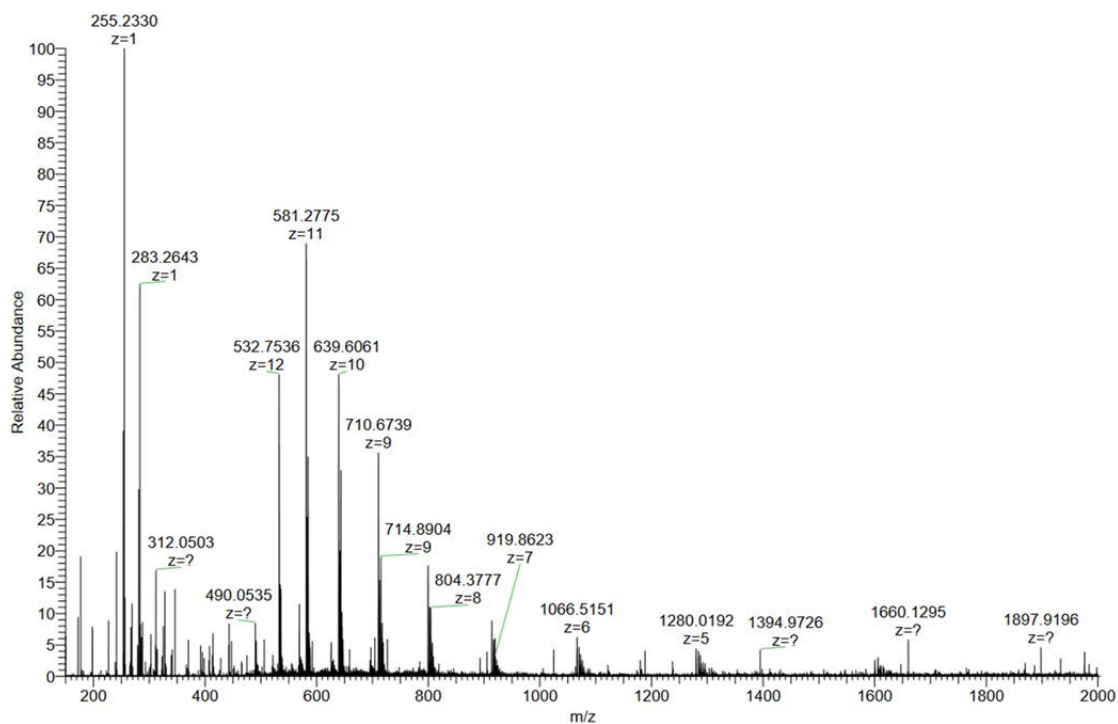


Figure 6.14: MS spectrum of O23.

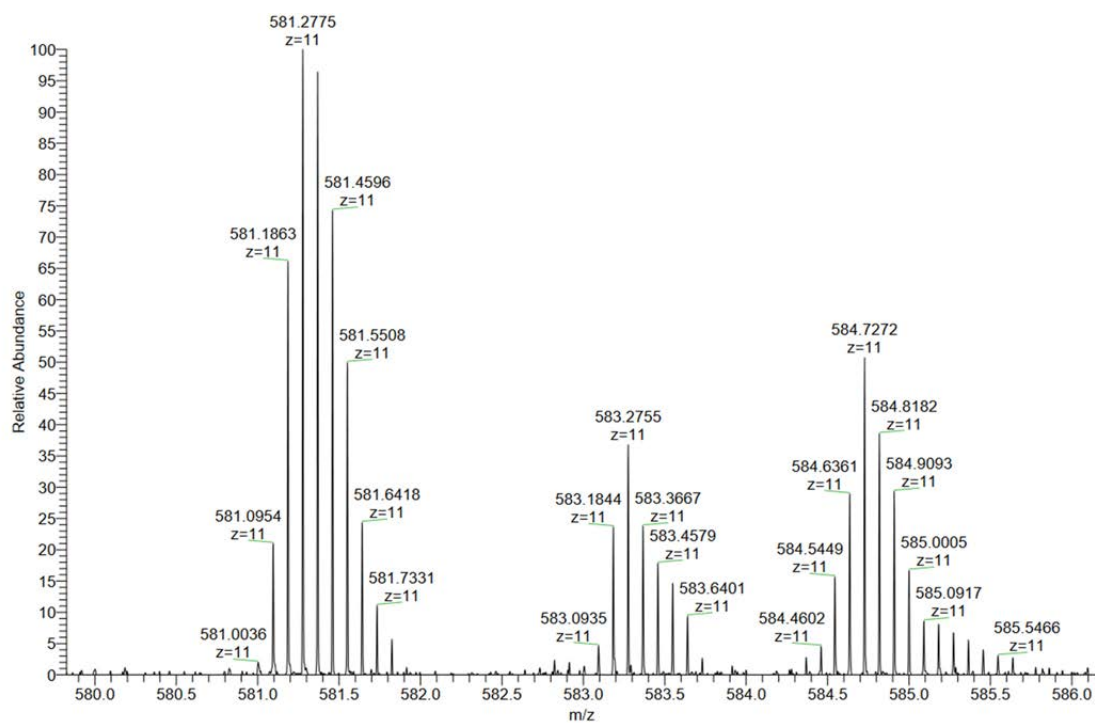


Figure 6.15: MS spectrum of O23 (zoom).

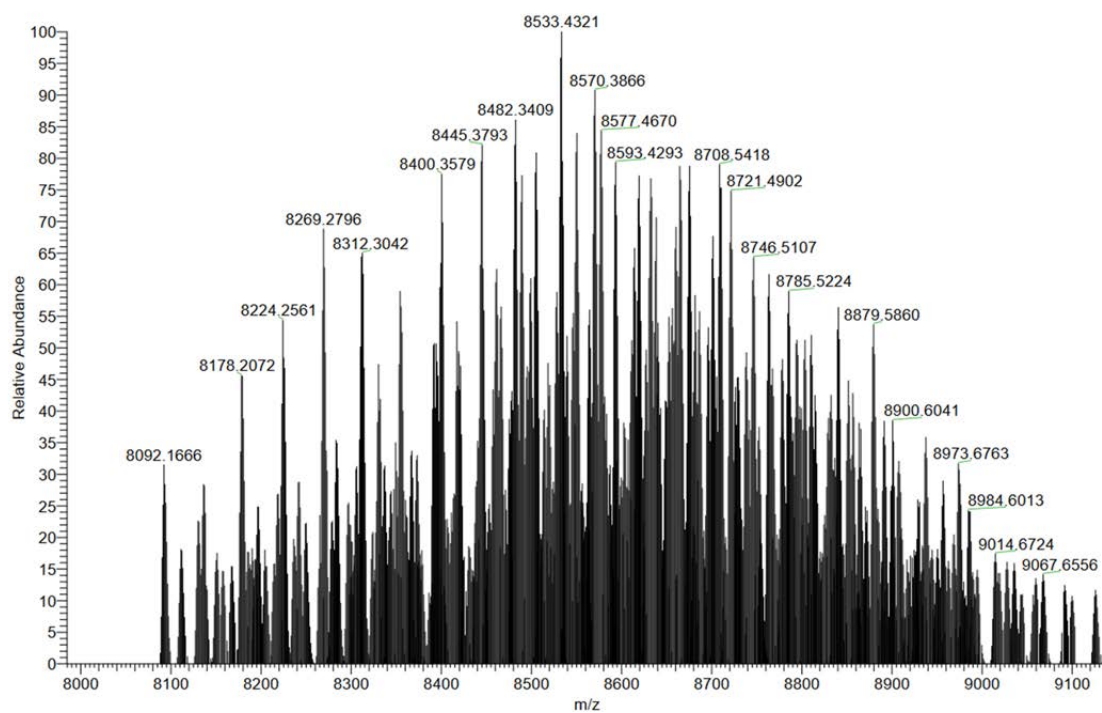


Figure 6.16: MS spectrum of O24.

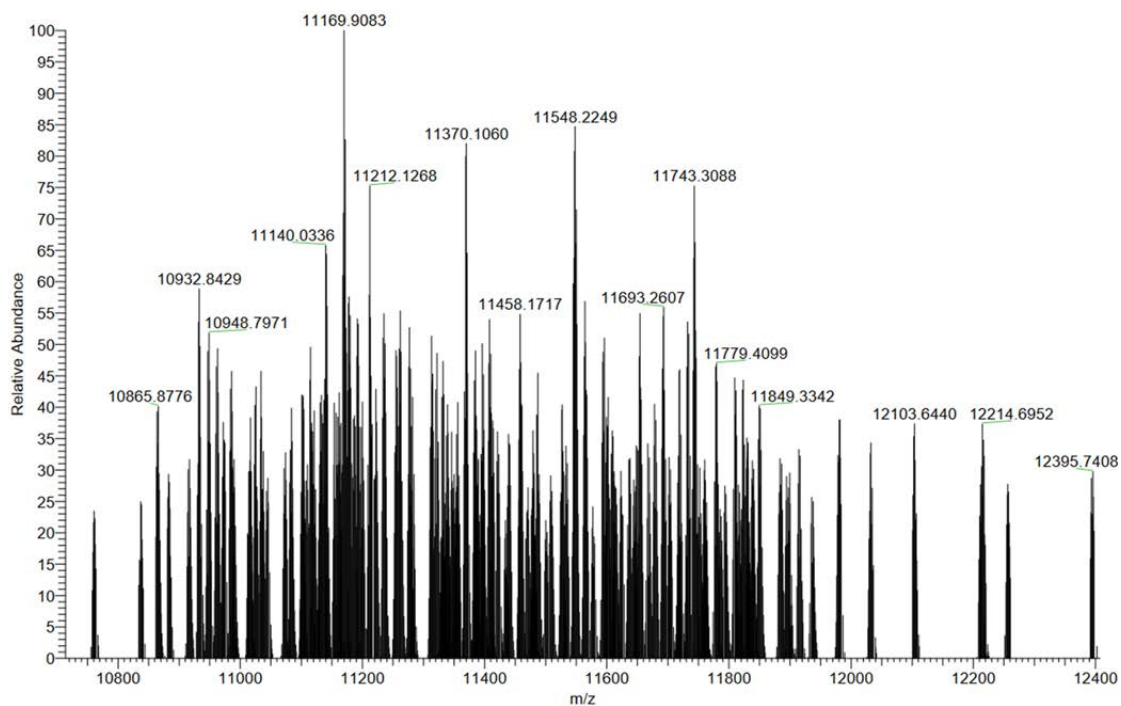


Figure 6.17: MS spectrum of O25.

6.3.3 Additional Spectroscopic Measurements

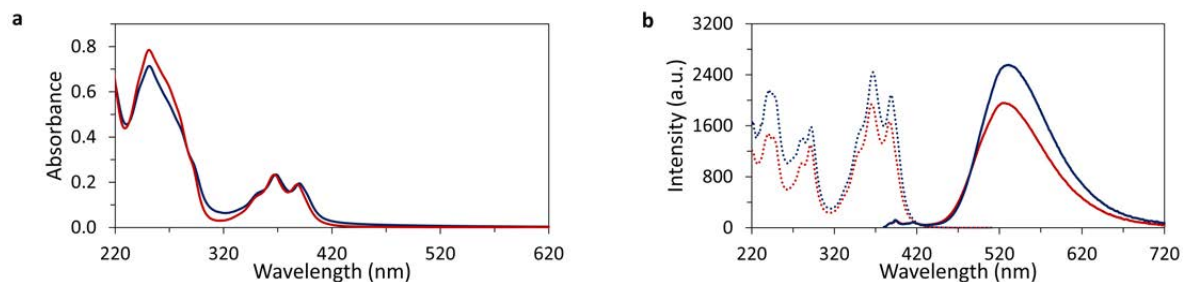


Figure 6.18: Temperature-dependent UV-vis absorption (a) and fluorescence (b) emission (solid line) and excitation (dotted line) spectra of (a) of **O20*O23** (blue 20 °C and red 75 °C). Conditions: 1 μM each single strand, 10 mM sodium phosphate buffer pH 7.2, 0.03 mM spermine \cdot 4 HCl, 20 vol% ethanol, λ_{em} . 525 nm, and λ_{ex} . 365 nm.

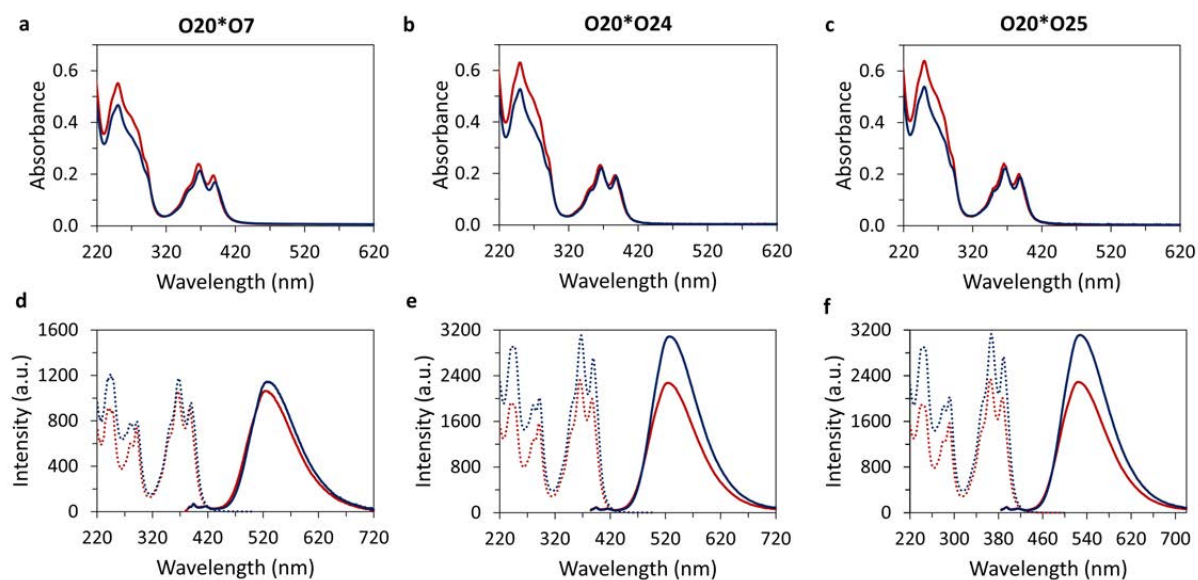


Figure 6.19: Temperature-dependent UV-vis absorption (a–c) and fluorescence (d–f) emission (solid line) and excitation (dotted line) spectra of (a and d) **O20*O7**, (b and e) **O20*O24**, and (c and f) **O20*O25** (blue 20 °C and red 75 °C). Conditions: 1 μM each single strand, 10 mM sodium phosphate buffer pH 7.2, 0.03 mM spermine \cdot 4 HCl, 20 vol% ethanol, λ_{em} . 525 nm, and for **O20*O7**: λ_{ex} . 365 nm, and for **O20*O24** and **O20*O25**: λ_{ex} . 368 nm.

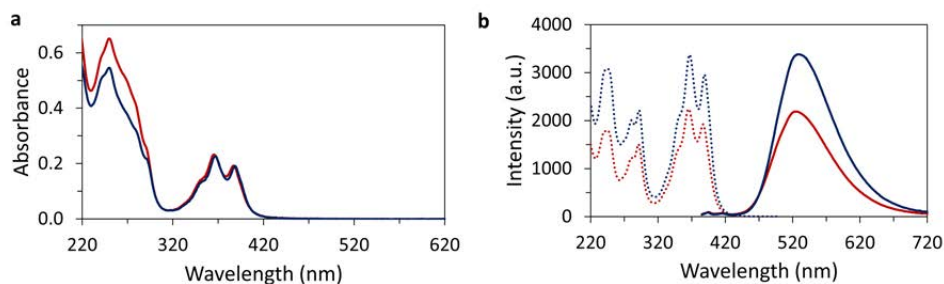


Figure 6.20: Temperature-dependent UV-vis absorption (a) and fluorescence emission (solid line) and excitation (dotted line) spectra (b) of **O20*O26** (blue 20 °C and red 75 °C). Conditions: 1 μM each single strand, 10 mM sodium phosphate buffer pH 7.2, 0.03 mM spermine \cdot 4 HCl, 20 vol% ethanol, λ_{em} . 525 nm, and λ_{ex} . 368 nm.

Chapter 7

Supramolecular Assembly of Highly Modified Phenanthrene-DNA Conjugates with Light-Harvesting Capabilities

In this chapter, an internal and 3'-end modified phenanthrene-DNA conjugate was prepared. In the internal and 3'-end modified phenanthrene-DNA conjugate, three nucleobases in the middle of the DNA strands were replaced by phenanthrene units, yielding a highly modified conjugate. As described in the introduction (1.4), previous research by our group demonstrated the assembly of 3'-end modified phenanthrene-DNA conjugates into supramolecular vesicles in the presence of spermine tetrahydrochloride.¹⁴⁶ In this chapter, the self-assembly properties of highly modified conjugates were determined. Additionally, the light-harvesting properties of the highly modified phenanthrene-DNA conjugates were evaluated.

Part of the work presented in this chapter is based on the work of Thomas Schneeberger during his master's thesis (University of Bern, Department of Chemistry, Biochemistry, and Pharmaceutical Sciences, 2022–2023)

7.1 Results and Discussion

The highly modified DNA strands (**O27–O29**) are listed in Figure 7.1a. **O27** and **O28** consist of 17 DNA nucleotides that are modified with three phosphodiester-linked 2,7-dialkynyl phenanthrene units at the 3'-ends and three 3,6-dialkynyl phenanthrenes in the middle of the strand (Figure 7.1a). **O29** is modified identically to **O28**, except for a 1,8-dialkynyl pyrene modification in the middle of the strand. Three 2,7-dialkynyl phenanthrenes were placed at the 3'-ends of the DNA to enable supramolecular assembly into spherical nanostructures, as in previous publications by our group.¹⁴⁶ The middle of the strand was modified with 3,6-dialkynyl phenanthrenes, as they have a distinctive absorption band at 330 nm that can be specifically excited and because previous publications by our groups revealed 3,6-dialkynyl phenanthrene modifications are tolerated inside a DNA duplex.^{71,72} **O27–O29** were prepared *via* solid-phase synthesis using the phosphoramidite approach explained in the general introduction (section 1.3) and were subsequently purified by HPLC. Detailed experimental procedures are provided in the appendix (section 7.3). The phenanthrene and pyrene phosphoramidites were prepared according to literature (sections 3.3 and 7.3).^{18,19,189}

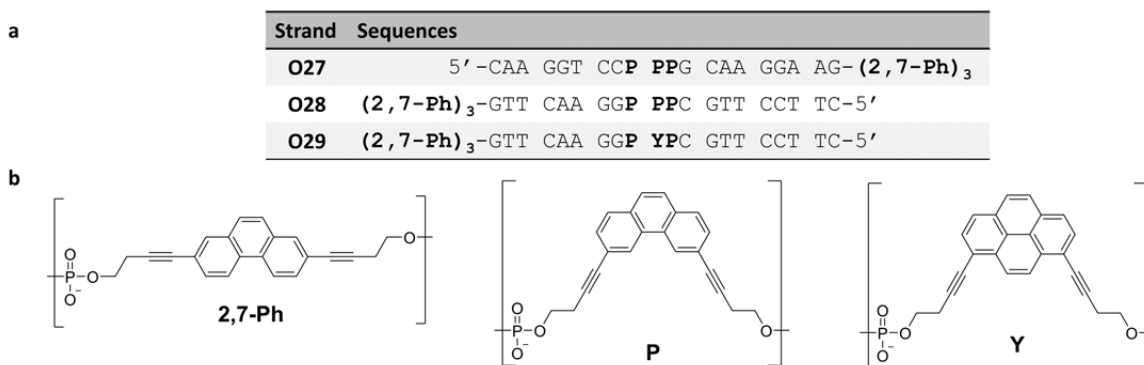


Figure 7.1: (a) DNA sequences **O27–O29** and (b) molecular structures of the phenanthrene and pyrene modifications.

7.1.1 Self-Assembly of Highly Modified Phenanthrene-DNA Conjugates

The self-assembly process of the highly modified phenanthrene-DNA conjugates was followed by temperature-dependent UV-vis absorption. Temperature-dependent UV-vis absorption spectra of the phenanthrene-DNA conjugate **O27*O28** are depicted in Figure 7.2a. The spectra of the single strands at 75 °C and the supramolecular assemblies at 20 °C after thermal assembly (0.5 °C·min⁻¹) display the distinctive absorption peaks of the DNA and the two phenanthrene isomers. The band between 325 and 340 nm is solely attributed to the 3,6-dialkynyl phenanthrenes. Upon cooling, this band is red-shifted by 1 nm and broadened. The peak with a maximum at 318 nm is a combination of 2,7-dialkynyl phenanthrene and 3,6-dialkynyl phenanthrene. Upon cooling, the maximum is red-shifted by 1 nm to 319 nm. The broad band between 250 and 280 nm is a combination of the absorbance of the DNA bases and the two phenanthrene isomers. After cooling to 20 °C, a hypochromic shift was observed in this band. The hypochromicity is attributed to the base pairing of the nucleobases. The bands in Figure 7.2a were assigned according to the UV-vis absorption measurements of the 2,7-dialkynyl phenanthrenediol and the 3,6-dialkynyl phenanthrenediol (appendix, Figure 7.12). Temperature-dependent UV-vis absorption measurements of the pyrene containing **O27*O29** can be found in the appendix (Figure 7.13).

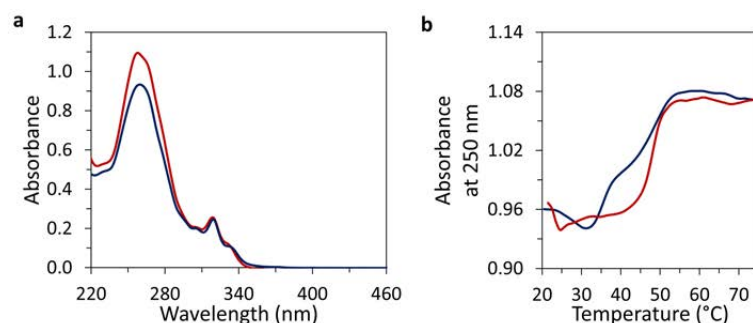


Figure 7.2: (a) Temperature-dependent UV-vis absorbance spectra of **O27*O28** (red 75 °C and blue 20 °C) and (b) absorbance at 250 nm (cooling-heating curves) of **O27*O28** during the cooling (blue) and heating (red). Conditions: 1 μ M each single strand, 10 mM sodium phosphate buffer pH 7.2, 0.10 mM spermine \cdot 4 HCl, 20 vol% ethanol.

Furthermore, the self-assembly and disassembly were monitored by temperature-dependent UV-vis spectroscopy, measuring the absorbance of the complementary DNA strands at 250 nm (Figure 7.2b). A nucleation temperature of 52 °C was measured for **O27*O28**, and hysteresis was observed.

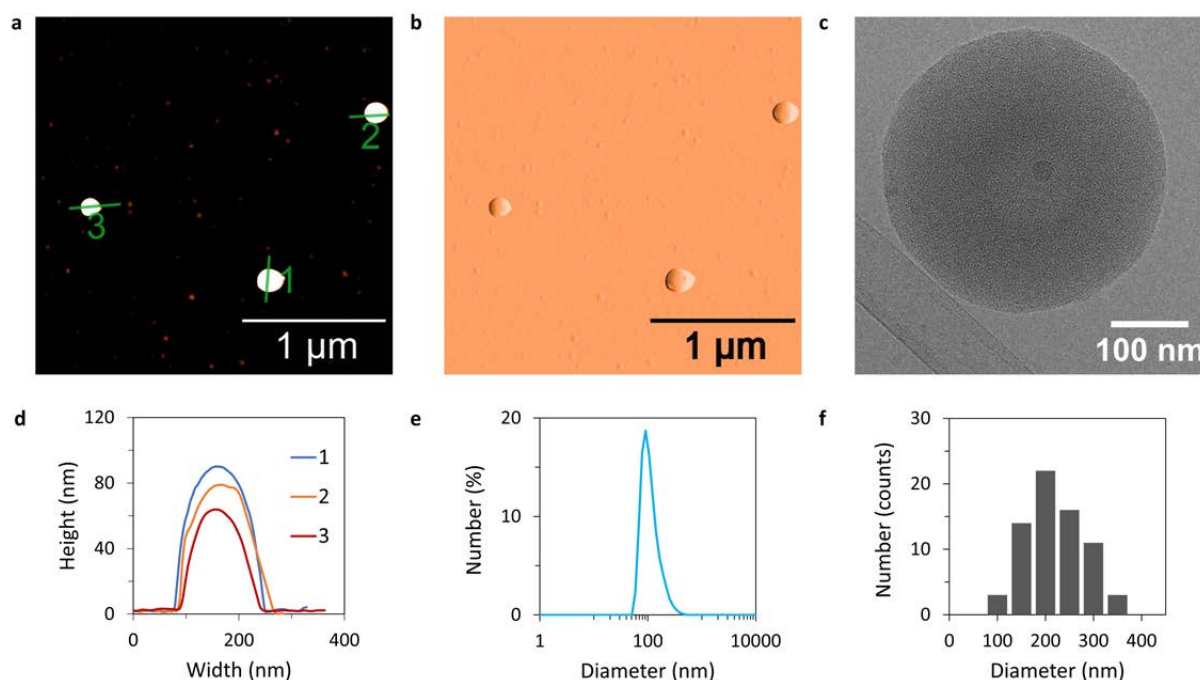


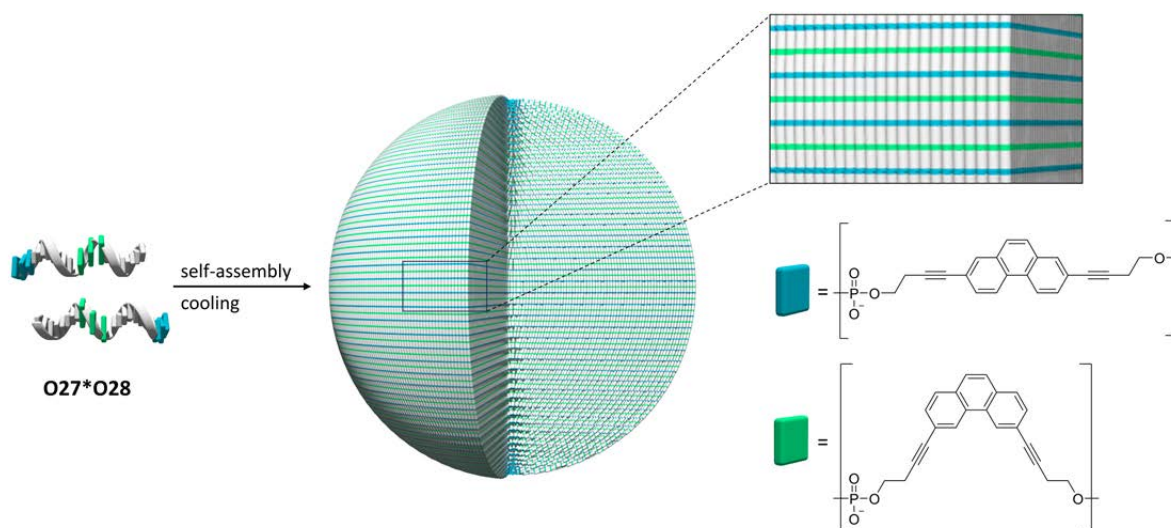
Figure 7.3: (a) AFM scan, (b) AFM deflection scan, (c) cryo-EM image, (d) cross sections corresponding to AFM scan, (e) DLS measurement, and (f) distributions of diameters in cryo-EM measurements of **O27*O28**. Conditions: 1 μ M each single strand, 10 mM sodium phosphate buffer pH 7.2, 0.10 mM spermine \cdot 4 HCl, 20 vol% ethanol.

To determine the morphology and size of the assemblies, AFM, DLS, and cryo-EM measurements of **O27*O28** were conducted. AFM measurement of thermally assembled **O27*O28** on APTES-modified mica showed the formation of spherical nanostructures with an average diameter of 237 ± 81 nm (Figure 7.3). In contrast to the pyrene-DNA conjugates described in the previous chapters, assemblies formed by the phenanthrene-DNA conjugates were solely detected as single spherical objects. Agglomeration of the aggregates was not observed on AFM. DLS experiments were performed to confirm the diameters measured by AFM. The

DLS experiments are in good agreement with the AFM data. The nanostructures expressed diameters of 230 ± 89 nm in DLS (Figure 7.3c and appendix Table 7.6). To validate the findings of AFM and DLS, cryo-EM of **O27*O28** was performed (Figure 7.3 and appendix Figure 7.14). Cryo-EM measurements revealed single spherical nanostructures with an average diameter of 271 ± 63 nm. The sizes measured by cryo-EM are in good agreement with the DLS and AFM measurements in (Table 7.1, and appendix Figure 7.15–Figure 7.18). All cryo-EM images exhibited high electron density inside the spherical nanostructures, and clear layers were absent on their surfaces. The high electron density inside the nanostructures indicates that the nanostructures are filled, as illustrated in Scheme 7.1.

Table 7.1: Average diameters of the spherical nanostructures based on AFM, DLS, and cryo-EM.

Strand	AFM (nm)	DLS (nm)	Cryo-EM (nm)
O27*O28	237 ± 81	230 ± 89	271 ± 63
O27*O29	257 ± 103	224 ± 98	254 ± 78

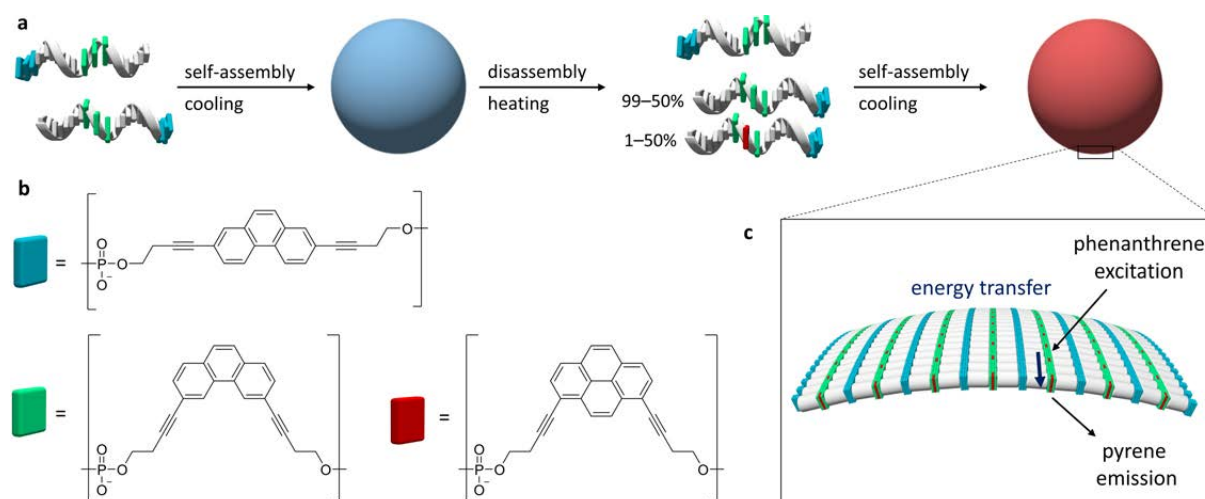


Scheme 7.1: Schematic representation of the self-assembly of **O27*O28** into a spherical filled nanostructure and chemical composition of the phenanthrene modifications.

7.1.2 Light-Harvesting Experiments of Highly Modified Phenanthrene-DNA Conjugates

To investigate the light-harvesting properties of the self-assembled nanostructures formed by **O27*O28**, they were doped with different amounts of **O27*O29** while keeping the concentration of phenanthrene-DNA conjugates constant (Scheme 7.2 and Figure 7.4). **O29** is complementary to **O27** and bears a 1,8-dialkynyl pyrene acceptor in the middle of the strand. We chose to decorate the DNA strand with 3,6-dialkynyl phenanthrene donor and 1,8-dialkynyl pyrene acceptor, as they show good light-harvesting properties.^{18,71} In this work, the 3,6-dialkynyl phenanthrene was excited selectively at 330 nm to minimize the absorption of the 2,7-dialkynyl phenanthrene units (phenanthrenediol absorbances in appendix Figure 7.12).

Excitation of the 3,6-dialkynyl phenanthrene in self-assembled **O27*O28** at 330 nm led to phenanthrene fluorescence (maxima at 383 nm and 398 nm, black curve in Figure 7.4a). After excitation of the 3,6-dialkynyl phenanthrene in assemblies with **O29**, pyrene-phenanthrene exciplex fluorescence at 395–595 nm was observed (colored graphs in Figure 7.4a). The intensity



Scheme 7.2: A general overview of the doping experiments. (a) From left to right: self-assembly of **O27*O28** to form spherical nanostructures (75 °C to 20 °C, 0.5 °C·min⁻¹) serving as control, disassembly of the nanostructures by heating to 75 °C, exchange of 1–50% **O28** with **O29**, followed by self-assembly by cooling to 20 °C forming doped spherical nanostructures. (b) Chemical structures of the pyrene and phenanthrene modification and (c) illustration of the energy transfer in the spherical nanostructures (for clarity, only one layer illustrated).

of the exciplex fluorescence increased with increasing amounts of 1,8-dialkynyl pyrene containing **O29**, whereas the 3,6-dialkynyl pyrene emission at 383 nm decreased (Figure 7.4b). Importantly, a decrease of the phenanthrene emission is expected, as the amount of 3,6-dialkynyl phenanthrene is decreased with every **O28** that is exchanged by **O29** (**O28** contains three 3,6-dialkynyl phenanthrenes, whereas **O29** contains only two). Therefore, the expected decrease was calculated and added to the intensities (gray dots in Figure 7.4b). The present decrease is clearly more pronounced than the corrected. Hence, the decrease in phenanthrene emission indicates excitation energy transfer from the 3,6-dialkynyl phenanthrene to the pyrene-phenanthrene exciplex.

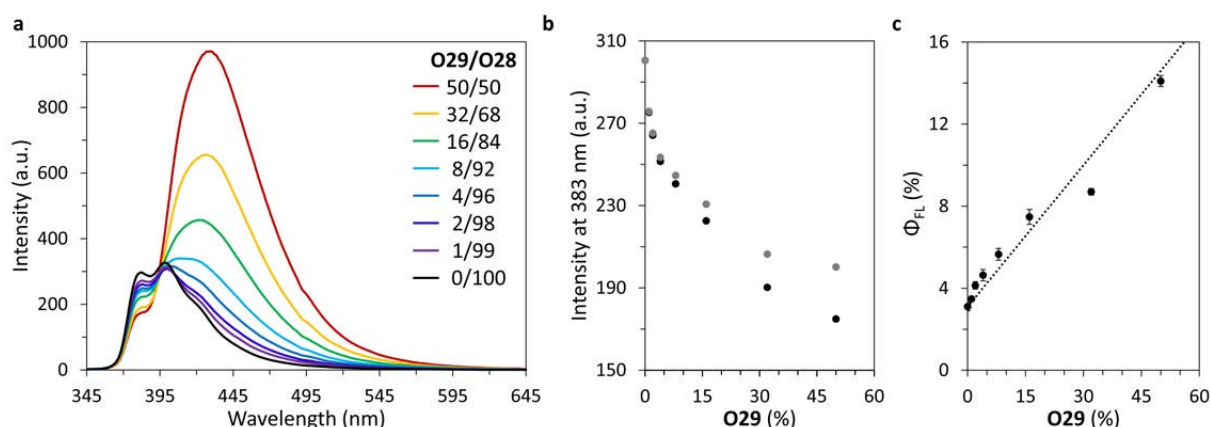


Figure 7.4: (a) Fluorescence emission spectra of self-assembled **O27*O28** at 20 °C (black) and **O27** with 1–0.5 μ M of **O28** and 0–0.5 μ M **O29** (colored), (b) fluorescence intensities at 383 nm with different amounts of **O29** and **O28** (black dots) and 3,6-dialkynyl phenanthrene reduction corrected fluorescence intensity (gray dots), and (c) fluorescence quantum yields of assemblies containing different amounts of **O29** and expected quantum yield (dashed line). Conditions: 1 μ M **O27**, 1.0–0.5 μ M **O28**, 0–0.5 μ M **O29**, 10 mM sodium phosphate buffer pH 7.2, 0.10 mM spermine · 4 HCl, 20 vol% ethanol, $\lambda_{ex.}$: 330 nm.

Table 7.2: Fluorescence quantum yields (Φ_{Fl}) and FRET efficiencies (E_{FRET}) of nanostructures formed by **O27*O28** with 0–0.5 μM **O29** instead of **O28**. Averages of three measurements with standard deviation.

O29 (μM)	Φ_{Fl} (%)	E_{FRET} (%)
-	3.1 ± 0.2	
0.01	3.5 ± 0.1	8.0 ± 1.4
0.02	4.1 ± 0.3	11.3 ± 1.6
0.04	4.6 ± 0.4	14.7 ± 1.6
0.08	5.7 ± 0.4	16.6 ± 2.0
0.16	7.5 ± 0.5	19.3 ± 2.5
0.32	8.7 ± 0.2	23.5 ± 2.3
0.50	14.1 ± 0.3	21.2 ± 2.3

As expected, the quantum yield and FRET efficiencies of the assemblies rose with increasing contents of **O29** (Figure 7.4c and Table 7.2, equations 8.2 in general methods chapter 8). Based on the FRET efficiency, the number of 3,6-dialkynyl phenanthrene units involved in FRET was determined (equation 8.3 in general methods chapter 8). The calculation showed that 47–49 individual phenanthrene units are involved in the excitation of one pyrene acceptor. This corresponds to 3,6-dialkynyl phenanthrenes present on 8–9 DNA duplexes. In addition, Förster radii were determined (Table 7.3, equations 8.4 in general methods chapter 8). Commonly, an orientation factor κ^2 of 2/3 is used to predict donor-acceptor distances for FRET measurements. The value of 2/3 describes freely rotating chromophores in solution. However, this approximation seems inappropriate here, as the phenanthrene and pyrene units are stacked inside a DNA duplex. Tilting and rolling of the chromophores inside the DNA duplex is restricted. Therefore, the average orientation factor in the assemblies is between 2/3 and 1. And the Förster radius is between 2.7 and 2.9 nm (Table 7.3). The calculated Förster radii propose a columnar packing inside the nanostructures, as this is the only possible arrangement where enough 3,6-dialkynyl phenanthrenes are placed in sufficiently close proximity to the 1,6-dialkynyl pyrenes.

Table 7.3: Förster Radii (R_0) depending on orientation factor κ^2 .

Orientation	κ^2	R_0 (nm)
Orthogonal	0	-
Random	0.67	2.73
Parallel	1.00	2.92
Colinear	4.00	3.68

7.2 Conclusions and Outlook

In this chapter, the self-assembly of amphiphilic 3'-end and internally modified phenanthrene-DNA conjugates into nanostructures was demonstrated. AFM, DLS, and cryo-EM revealed that the highly modified phenanthrene-DNA conjugates self-assemble into columnar-filled spherical nanostructures with diameters of 200–300 nm.

The formed nanostructures express light-harvesting capabilities. Fluorescence spectroscopy revealed that excitation of the 3,6-dialkynyl phenanthrene units, in the presence of the 1,8-dialkynyl pyrene containing DNA strands, leads to FRET from the 3,6-dialkynyl phenanthrene to a pyrene-phenanthrene exciplex. Light-harvesting experiments showed that 8–9 DNA duplex participate in exciting one pyrene-phenanthrene exciplex.

Subsequent experiments could investigate the limits regarding the extent of modifications, such as replacing more than three nucleobases with additional chromophores. This exploration could facilitate the determination of the maximum number of chromophores that can be integrated while still permitting the formation of DNA nanostructures.

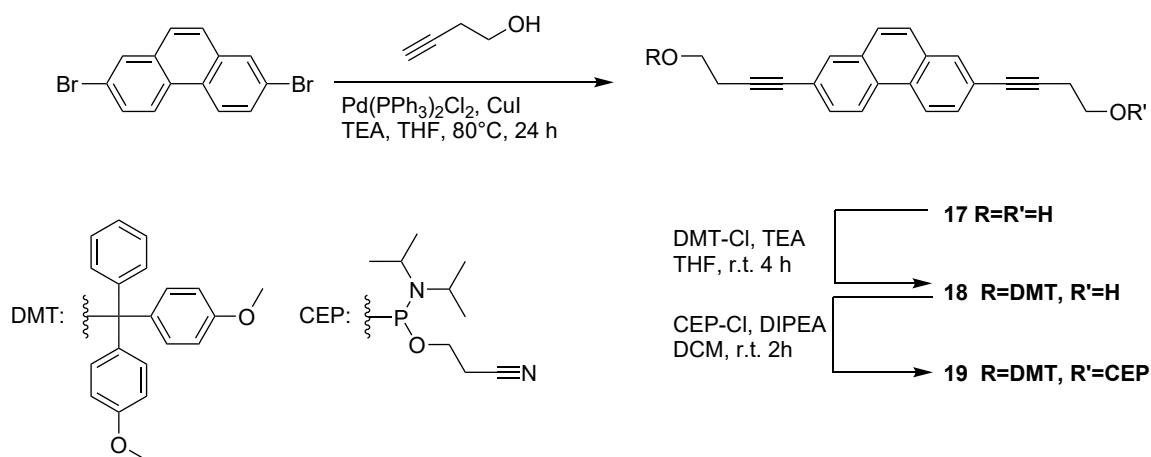
Another major interest lies in achieving light-harvesting energy transfer within the sticky ends rather than the middle of the strand by incorporating an acceptor unit into the sticky ends.

7.3 Appendix - Chapter 7

First, the organic synthesis of 2,7- and 3,6-dialkynyl phenanthrene phosphoramidites and the 2,7-phenanthrene solid support will be described. Then, the solid-phase oligomer synthesis and their characterization are described. All synthetic steps were performed by Thomas Schneeberger as part of his Master's thesis.

7.3.1 Organic Synthesis

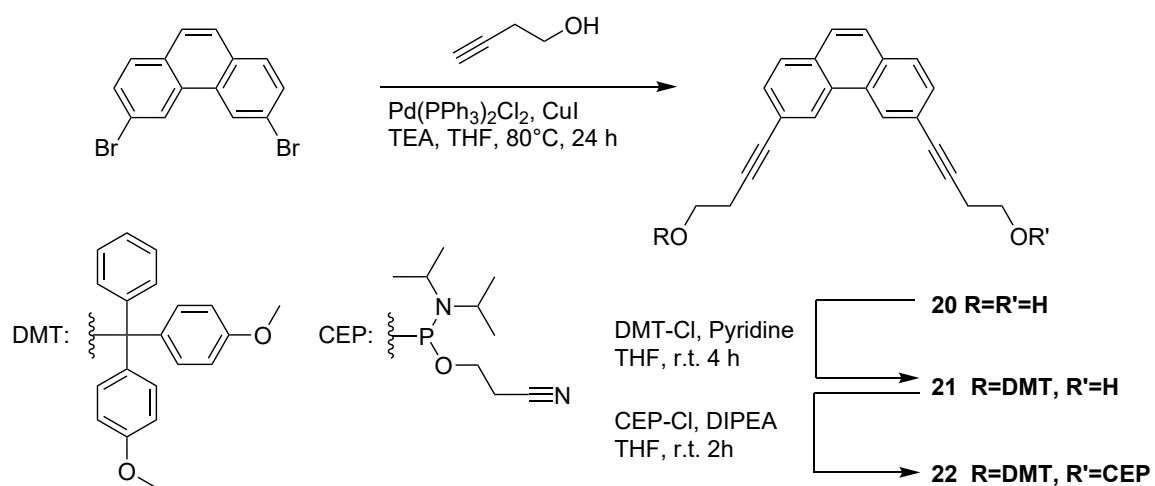
The 2,7-dialkynyl phenanthrene phosphoramidite **19** was synthesized according to a three-step procedure reported previously by our group (Scheme 7.3).¹⁹ Similarly, 3,6-dialkynyl phenanthrene phosphoramidite **22** was synthesized following a reported three-step procedure (Scheme 7.4).¹⁸ The synthesis of 1,8-dialkynyl pyrene phosphoramidite is described in the appendix of chapter 3 (3.3).



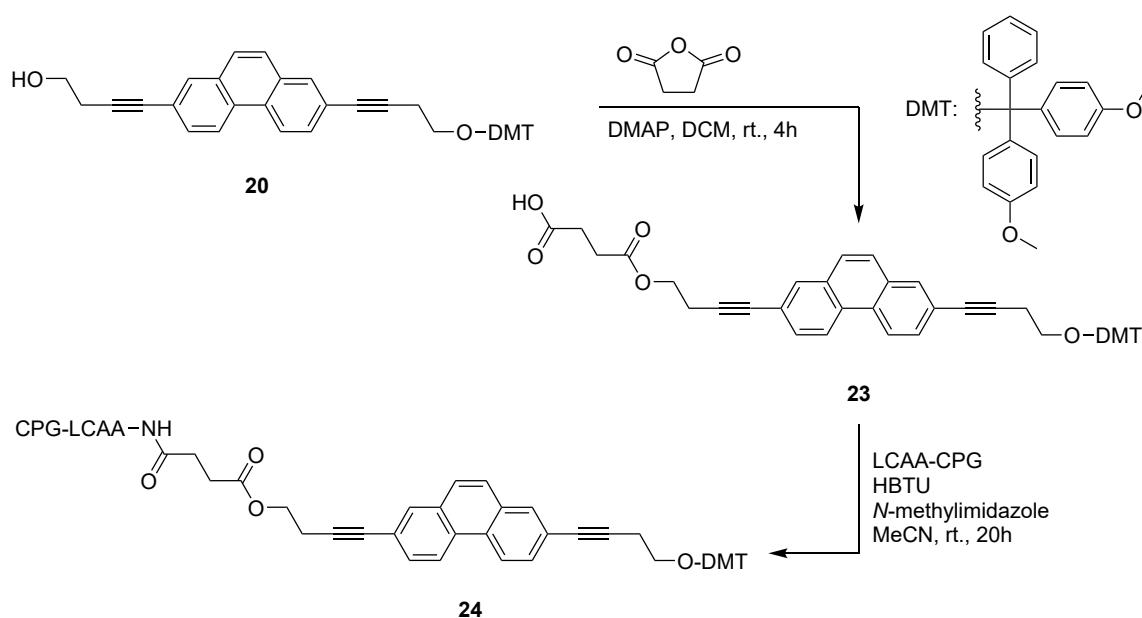
Scheme 7.3: A general overview of synthesis of the 2,7-dialkynyl phenanthrene diol **17**, the mono-protected phenanthrene **18** and 2,7-phenanthrene phosphoramidite **19**.

In the first step, the commercially available 2,7-dibromophenanthrene was coupled *via* palladium-catalyzed Sonogashira coupling with 3-butynol resulting in the formation of the dialkynyl phenanthrene diol **17**. In the second step, **17** was tritylated on one side using one equivalent of 4,4'-dimethoxytrityl chloride (DMT-Cl), yielding the mono-protected compound **18**. In the third step, the remaining alcohol of mono-protected **18** was reacted with 2-cyanoethyl N,N-bis(1-methylethyl)phosphoramidite chloride (CEP-Cl), forming the 2,7-dialkynyl phenanthrene phosphoramidite **19**. First, the commercially available 3,6-dibromo phenanthrene was alkynated *via* palladium-catalyzed Sonogashira coupling with 3-butynol forming the diol **20**. Then **20** was mono-protected with 4,4'-dimethoxytrityl chloride, yielding the mono-protected phenanthrene **21**. The 3,6-dialkynyl phenanthrene phosphoramidite **22** was formed by reacting **21** and 2-cyanoethyl N,N-bis(1-methylethyl)phosphoramidite chloride.

The solid-support bound 2,7-dialkynyl pyrene **24** was synthesized in two steps according to reported literature (Scheme 7.5).¹⁹ First, the mono-protected phenanthrene **20** was reacted with succinic anhydride forming **23**. Then, **23** was coupled to a long chain alkylamine-controlled pore glass solid support, forming the final product **24**.



Scheme 7.4: A general overview of synthesis of the 3,6-phenanthrene diol **20**, the mono-protected phenanthrene **21** and 2,7-phenanthrene phosphoramidite **22**.



Scheme 7.5: A general overview of synthesis of the succinated phenanthrene **23** and the solid support bound phenanthrene **24**.

7.3.2 Synthesis and Characterization of Oligonucleotides

The phenanthrene and pyrene-phenanthrene-DNA conjugates **O27–O29** were synthesized on an Applied Biosystems 394 DNA/RNA synthesizer with a 1 μM standard cyanoethyl phosphoramidite coupling protocol. The solid-phase synthesis and purification are described in detail in chapter 8.

Afterwards, the conjugates **O27–O29** were purified by reverse-phase HPLC (Shimadzu LC-20AT, ReproSil 100 C18, 5,0 μm , 250 \times 4 mm) at 50 $^\circ\text{C}$ with a flow rate of 1 ml/min, λ : 260 nm. Solvent A: aqueous 2.1 mM triethylamine (TEA) / 25 mM 1,1,1,3,3,3-hexafluoropropan-2-ol (HFIP) pH 8; solvent B: acetonitrile; applying the gradients B [%] (t_{R} [min])= 10 (0), 25 (24).

The purified oligomers **O27–O29** were dissolved in 1 ml of Milli-Q H_2O . Afterward, the absorbance of the conjugates was measured at 260 nm to determine the concentration of the stock solutions and yields of **O27–O29**. The Beer-Lambert law was applied to determine the concentrations. For the DNA nucleobases, phenanthrene, and pyrene modifications the following molar absorption coefficients (at 260 nm) in $\text{l}\cdot\text{mol}^{-1}\cdot\text{cm}^{-1}$ were used: ϵ_{A} ; 15'300, ϵ_{T} ; 9'000, ϵ_{G} ; 11'700, ϵ_{C} ; 7'400, $\epsilon_{3,6\text{-phenanthrene}}$; 56'000, $\epsilon_{2,7\text{-phenanthrene}}$; 47'000, and $\epsilon_{1,8\text{-pyrene}}$; 30'000. The results of mass spectra of **O27–O29** are listed in Table 7.4, the corresponding HPLC traces are depicted in Figure 7.5, and the mass spectra are displayed in Figure 7.6–Figure 7.11.

Table 7.4: Phenanthrene- and pyrene-phenanthrene-DNA oligonucleotide sequences of **O27–O29**, calculated and found masses by NSI-MS, and yields.

Strand	Sequence (5'→3')	Calcd mass	Found mass	Yield [%]
O27	CAA GGT CCP PPG CAA GGA AG-(2,7-Ph) ₃	7510.4653	7510.4630	18
O28	CTT CCT TGC PPP GGA CCT TG-(2,7-Ph) ₃	7385.3951	7385.3497	4
O29	CTT CCT TGC PYP GGA CCT TG-(2,7-Ph) ₃	7409.3951	7409.3932	20

P = 3,6-dialkynyl phenanthrene, and **Y** = 1,8-dialkynyl pyrene.

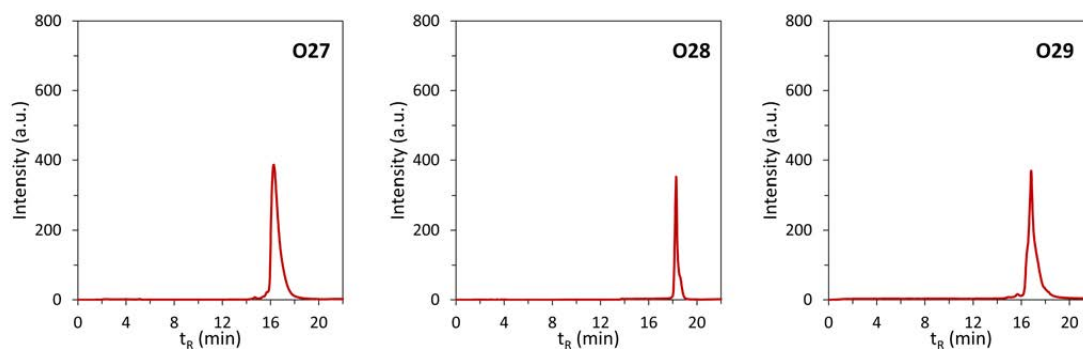


Figure 7.5: HPLC traces of phenanthrene-DNA conjugates **O27–O29**.

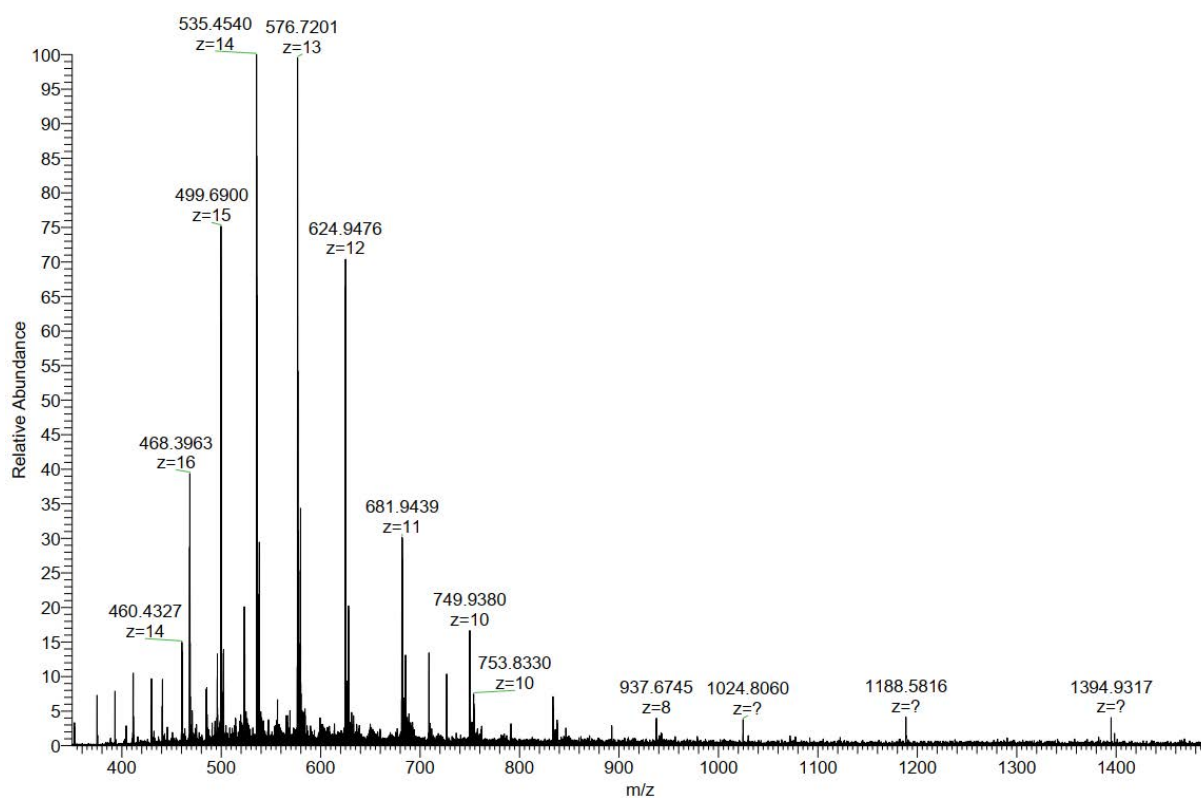


Figure 7.6: MS spectrum of O27.

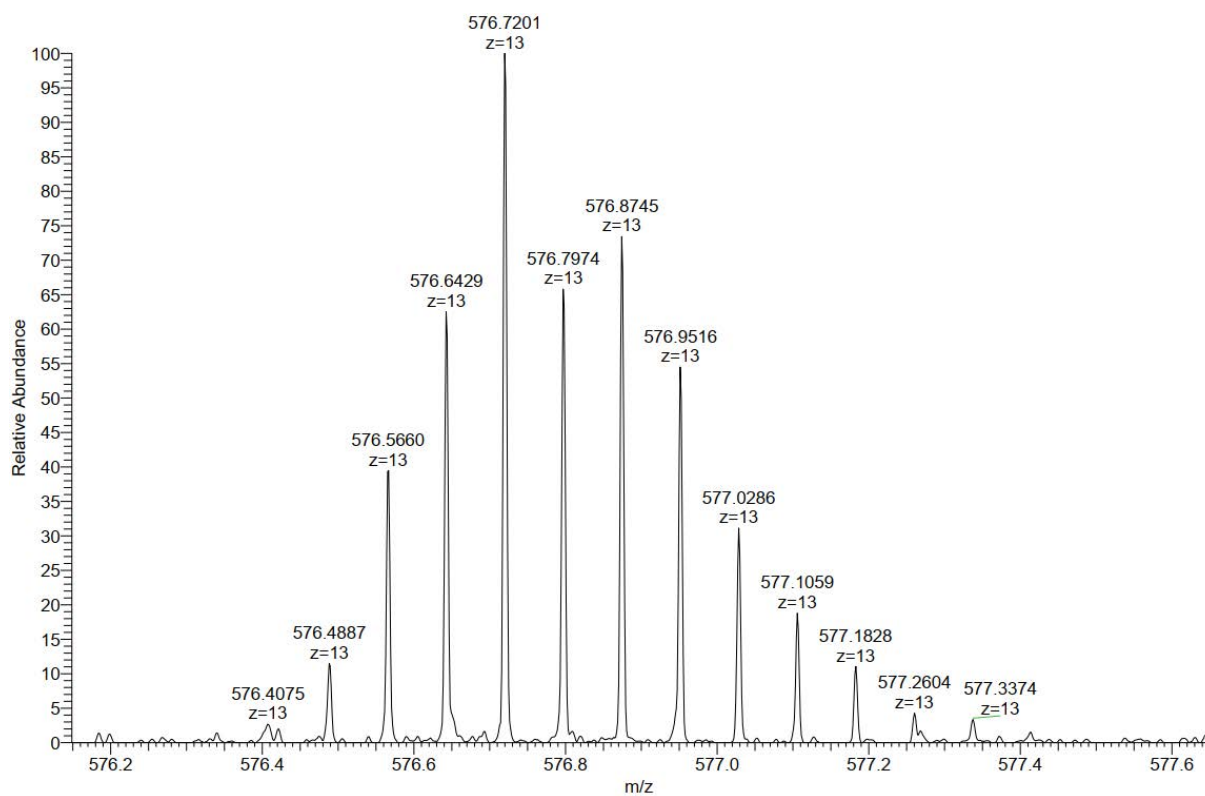
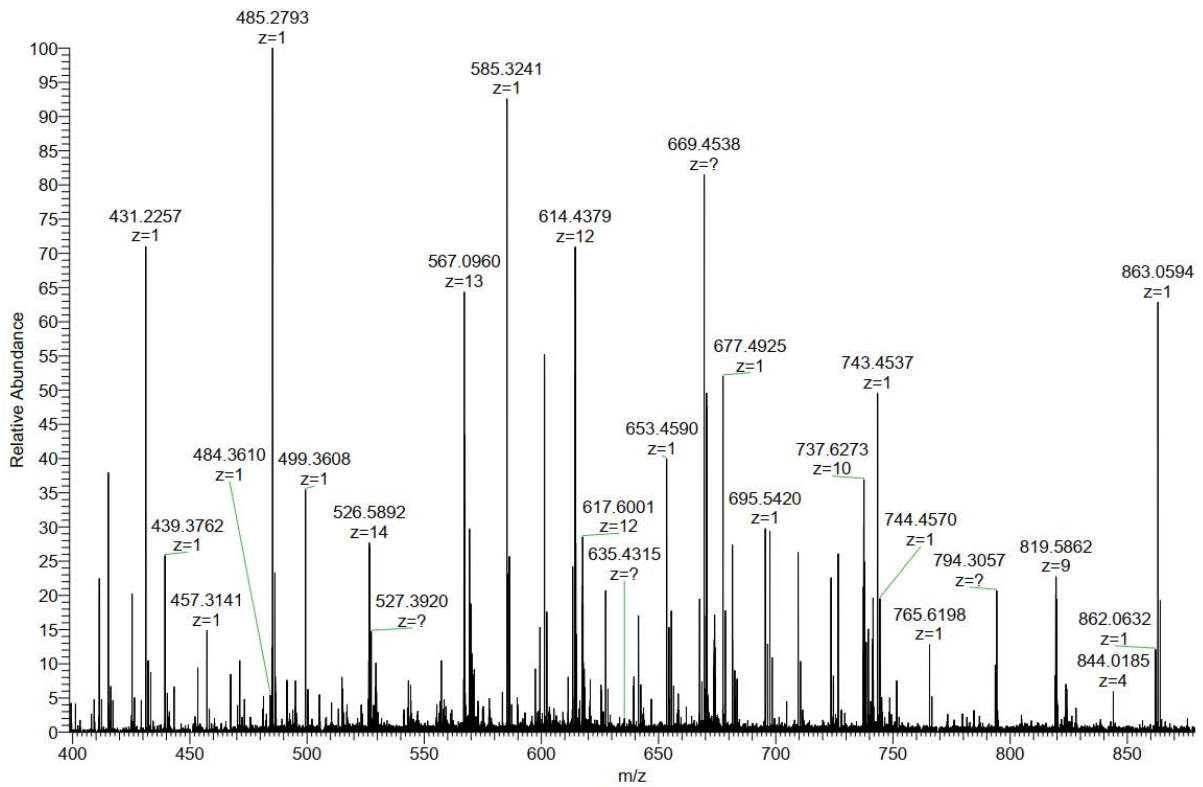
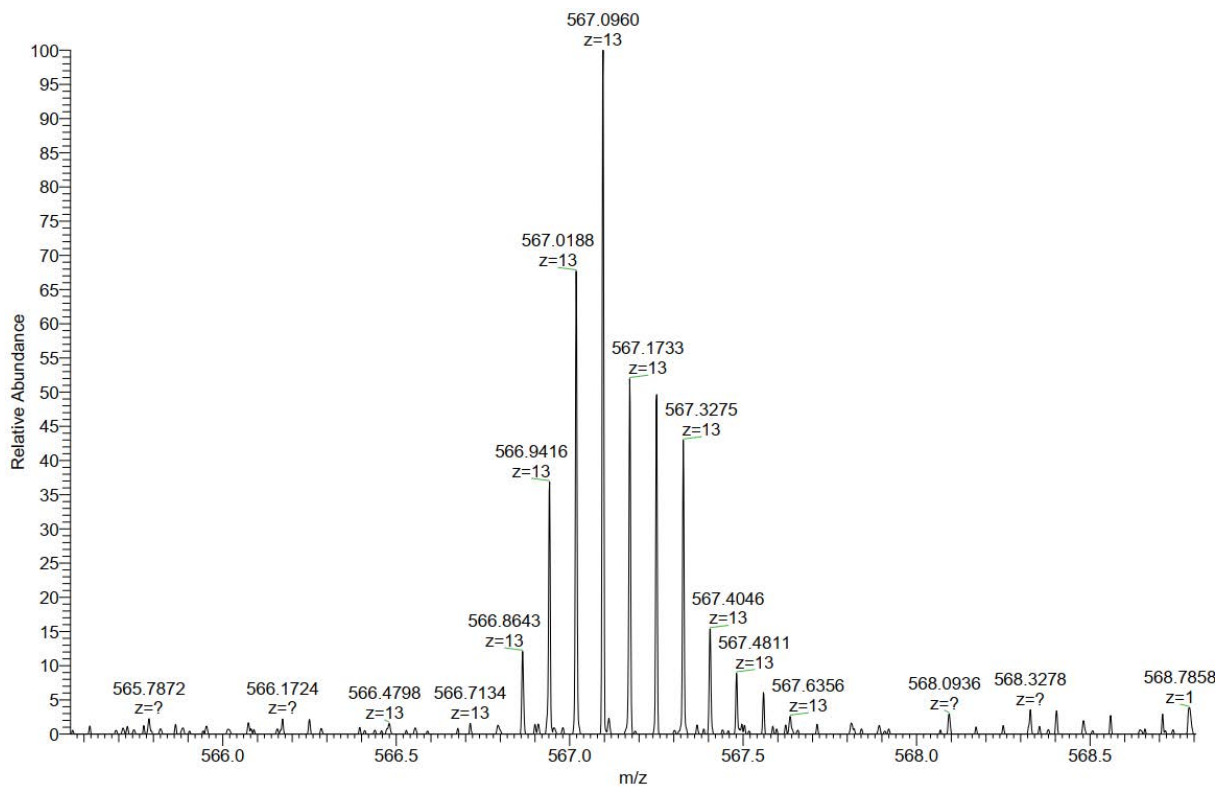


Figure 7.7: Zoomed MS spectrum of O27.

Figure 7.8: MS spectrum of O₂₈.Figure 7.9: Zoomed MS spectrum of O₂₈.

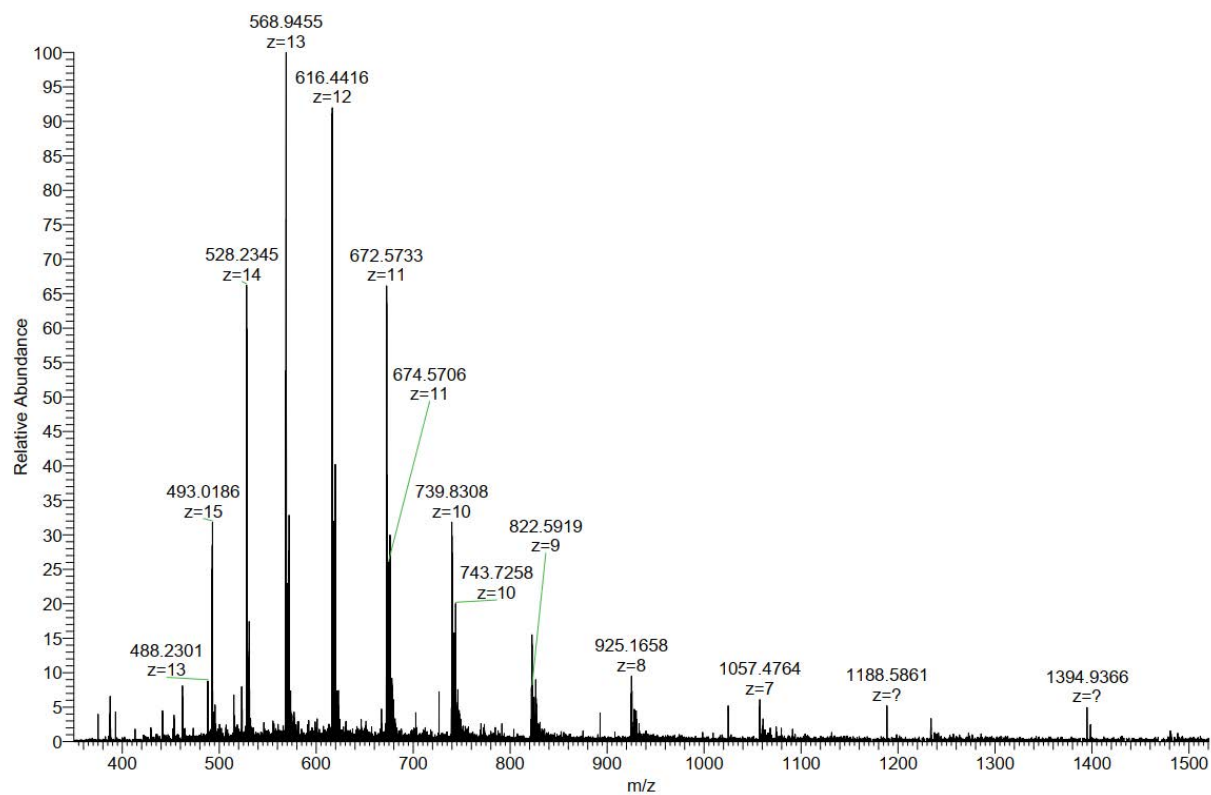


Figure 7.10: MS spectrum of O29.

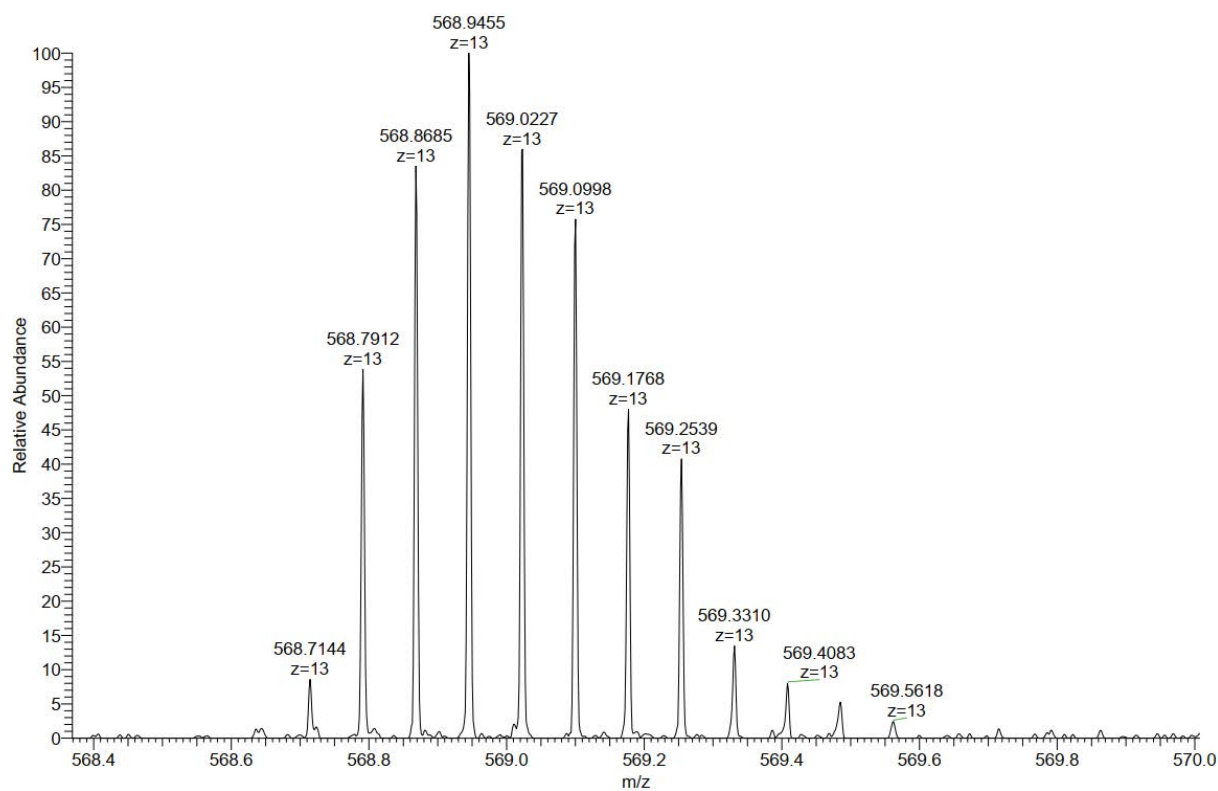


Figure 7.11: Zoomed MS spectrum of O29.

7.3.3 Spectroscopic Characterization of Pyrene and Phenanthrene Diols

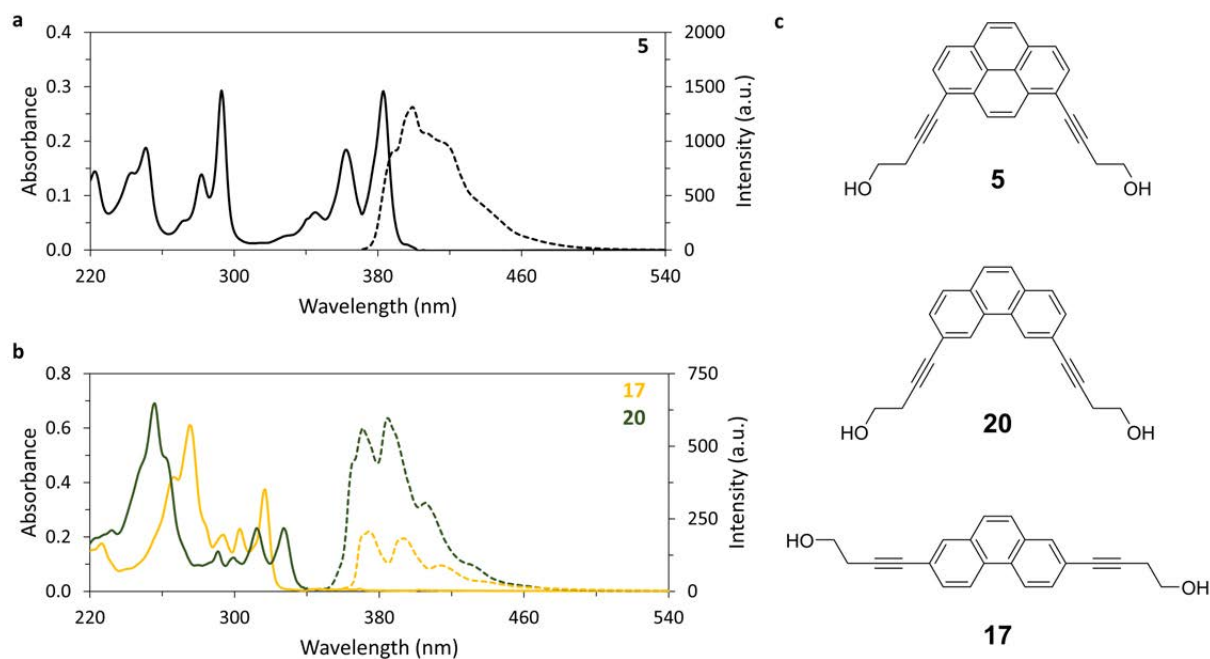


Figure 7.12: UV-Vis absorption (solid) and fluorescence emission (dashed) spectra of (a) 1,8-dialkynyl pyrene **5** and (b) 2,7-dialkynyl phenanthrene **17** and 3,6-dialkynyl phenanthrene **20** diols in ethanol. (c) Illustrations of the chemical structures of the three diols. Conditions: 6 μ M diols in ethanol, 20 $^{\circ}$ C, λ_{ex} . 293 nm for **5** and 310 nm for **17** and **20**, excitation slit width 1.0 nm, and emission slit width 2.5 nm.

Table 7.5: Pyrene and phenanthrene-absorption maxima of: **5**, **17**, and **20** in ethanol.

λ_{max} 5 , nm (ϵ , mol $^{-1}$ cm $^{-1}$ L)	λ_{max} 17 , nm (ϵ , mol $^{-1}$ cm $^{-1}$ L)	λ_{max} 20 , nm (ϵ , mol $^{-1}$ cm $^{-1}$ L)
383 (49000)	317 (61000)	327 (38000)
361 (31000)	303 (38000)	312 (38000)
345 (12000)	294 (3400)	299 (20000)
293 (49000)	275 (100000)	291 (24000)
282 (23000)	267 (69000)	255 (112000)
250 (31000)	-	-

7.3.4 Additional Spectroscopic and Microscopic Measurements

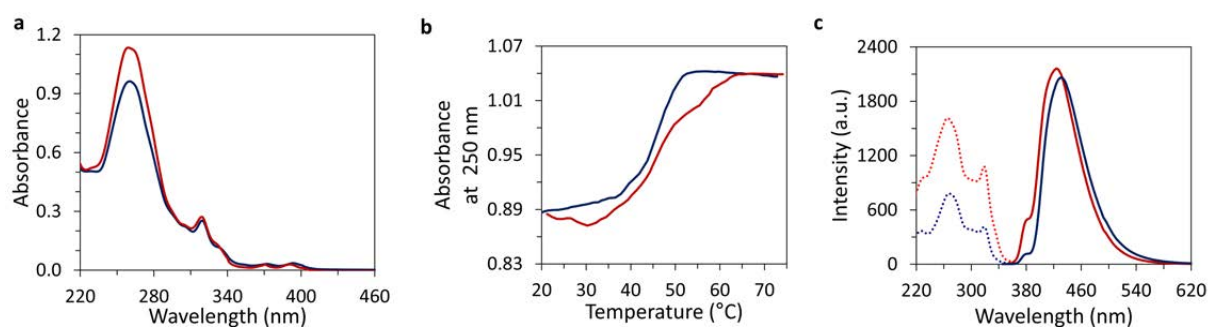


Figure 7.13: (a) Temperature-dependent UV-vis absorbance spectra of **O27*O29** (red 75 °C and blue 20 °C after self-assembly), (b) absorbance at 250 nm (cooling-heating curves) of **O27*O29** during the cooling (blue) and heating (red), and (c) temperature-dependent fluorescence emission (solid) and excitation (dotted) spectra of **O27*O29** before assembly at 75 °C (red) and after cooling (0.5 °C·min⁻¹) to 20 °C (blue). Conditions: 1 μM each single strand, 10 mM sodium phosphate buffer pH 7.2, 0.10 mM spermine · 4 HCl, 20 vol% ethanol, λ_{ex} 330 nm, and λ_{em} 380 nm.

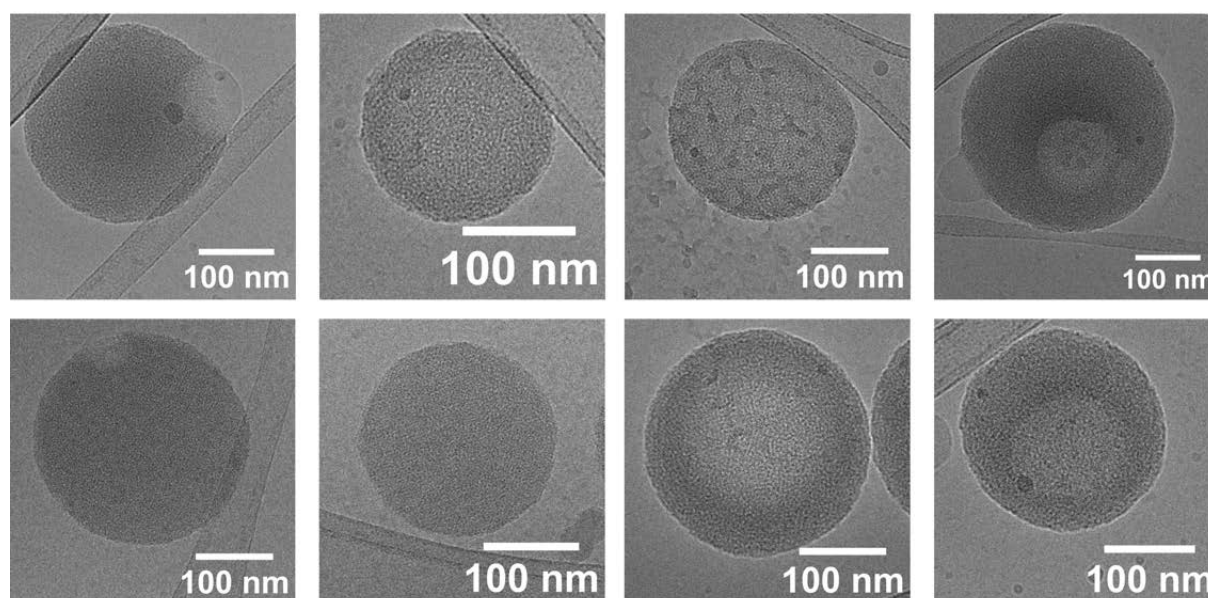


Figure 7.14: Cryo-EM images of **O27*O28**. Conditions: 1 μM each single strand, 10 mM sodium phosphate buffer pH 7.2, 0.10 mM spermine · 4 HCl, 20 vol% ethanol.

Table 7.6: Key results and measurement conditions of DLS measurement at 20 °C of a solution of **O27*O28** and **O27*O29**. Conditions: 1 μM each single strand, 10 mM sodium phosphate buffer pH 7.2, 0.10 mM spermine \cdot 4 HCl, 20 vol% ethanol, 20 °C.

Duplex	Size Diameter with Error (nm)	Z-Average Size Diameter (nm)	PDI	PDI Width (nm)	Count Rate (kcps)	Attenuator
O27*O30	229.9 \pm 88.75	208.2	0.184	89.27	17985.3	7
O27*O29	223.7 \pm 97.68	183.9	0.171	75.96	18154.7	7

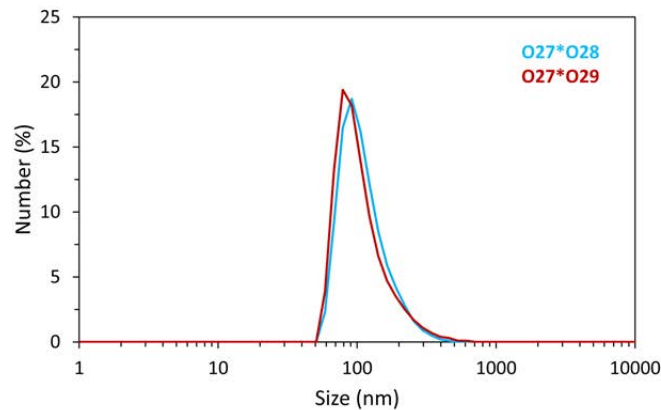


Figure 7.15: DLS measurements of **O27*O28** and **O27*O29**. Conditions: 1 μM each single strand, 10 mM sodium phosphate buffer pH 7.2, 0.10 mM spermine \cdot 4 HCl, 20 vol% ethanol, 20 °C.

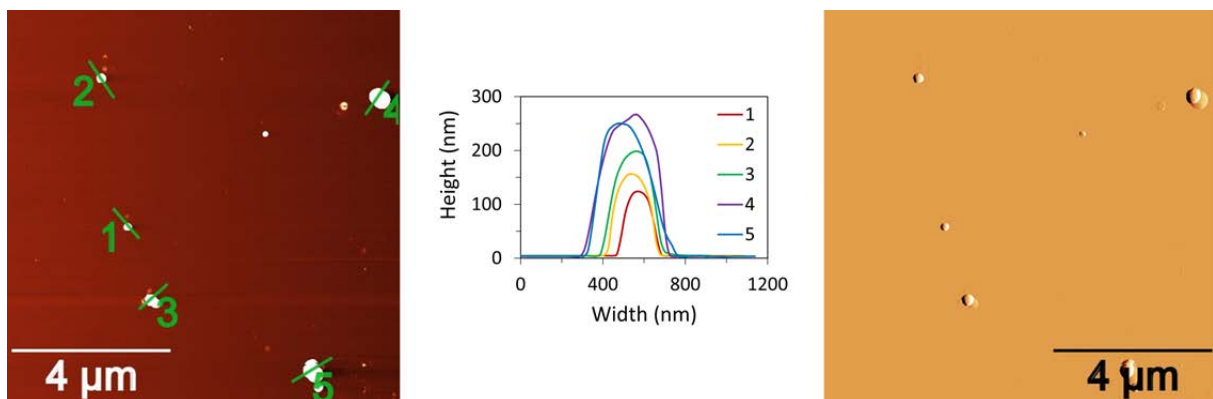


Figure 7.16: AFM scan (left) with corresponding cross sections (middle) and deflection scan of (right) **O27*O29**. Conditions: 1 μM each single strand, 10 mM sodium phosphate buffer pH 7.2, 0.10 mM spermine \cdot 4 HCl, 20 vol% ethanol.

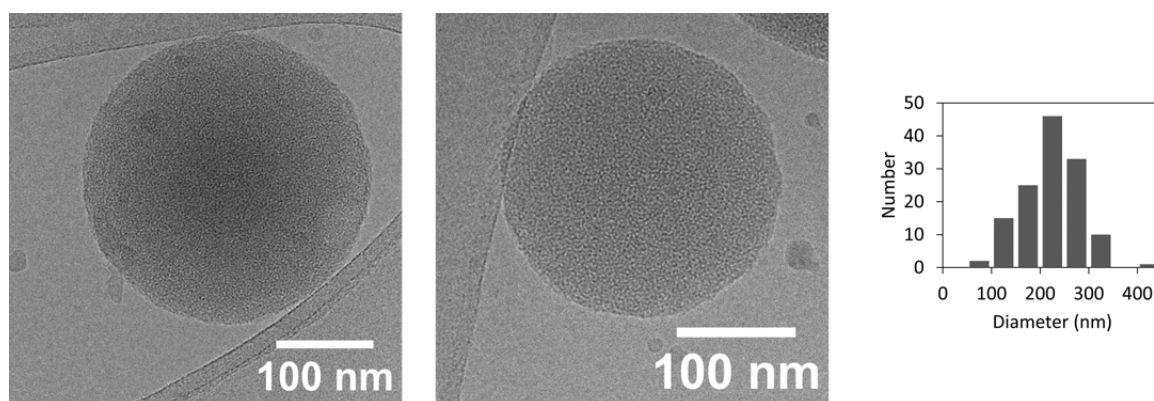


Figure 7.17: (right) Cryo-EM measurements of **O27*O29** and (left) size distribution of nanostructures (diameters). Conditions: 1 μ M each single strand, 10 mM sodium phosphate buffer pH 7.2, 0.10 mM spermine \cdot 4 HCl, 20 vol% ethanol.

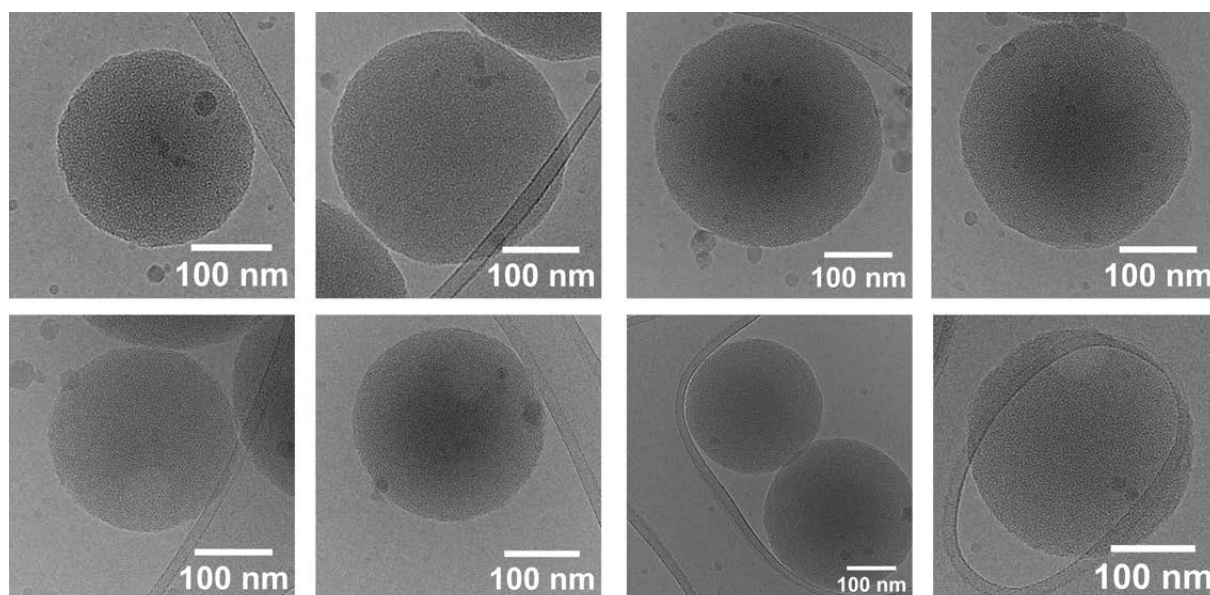


Figure 7.18: Cryo-EM images of **O27*O29**. Conditions: 1 μ M each single strand, 10 mM sodium phosphate buffer pH 7.2, 0.10 mM spermine \cdot 4 HCl, 20 vol% ethanol.

7.3.5 Additional Light-Harvesting Experiments

A second light harvesting experiment was conducted. In this experiment, **O27*O28** was doped with different amounts of **O29** single strands. Excitation of the 3,6-dialkynyl phenanthrene in self-assembled **O27*O28** led to phenanthrene fluorescence with maxima at 383 nm and 398 nm (black curve in Figure 7.19a). In contrast, in the **O29** doped nanostructures of **O27*O28**, a phenanthrene-pyrene exciplex fluorescence was observed at 395–595 nm (colored graphs in Figure 7.19a). The intensity of the exciplex fluorescence increases with increasing amounts of **O29**. In addition, the phenanthrene emission decreased with increasing amounts of **O29**, indicating an energy transfer from the 3,6-dialkynyl phenanthrene to the phenanthrene-pyrene exciplex *via* FRET (Figure 7.19b). As expected, the doping experiments expressed a steady increase in the fluorescence quantum yield (Φ_{FL}) with increasing amounts of **O29** (Figure 7.19c and Table 7.7).

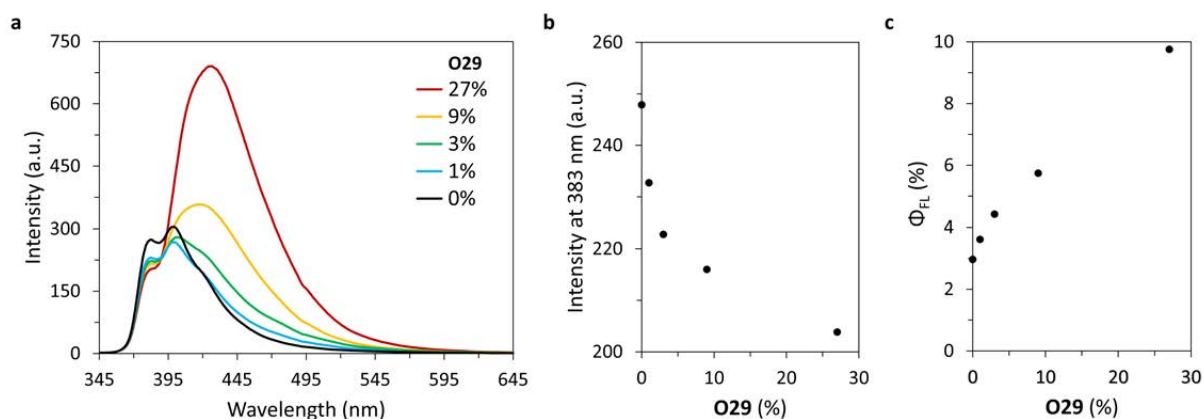


Figure 7.19: (a) Fluorescence emission spectra of self-assembled **O27*O28** at 20 °C (black) and nanostructures of **O27*O28** doped with 1–27% **O29** (colored), (b) fluorescence intensities at 383 nm with differing amounts of **O29**, and (c) fluorescence quantum yields of assemblies containing different amounts of **O29** (black dots) and calculated fluorescence quantum yield of duplexes in case of no light-harvesting from strand to strand (dotted line). Conditions: 1 μM **O27** and μM **O28**, 0–0.27 μM **O29**, 10 mM sodium phosphate buffer pH 7.2, 0.10 mM spermine \cdot 4 HCl, 20 vol% ethanol, λ_{ex} 330 nm.

The FRET efficiencies of the assemblies formed by **O27*O28** with different contents of **O29** were calculated, and the FRET efficiency increases with increasing **O29** contents (equations 8.2 in general methods section chapter 8). Based on the FRET efficiency, the number of 3,6-dialkynyl phenanthrene units involved in FRET was determined (equation 8.3 in general methods section chapter 8). The calculation showed that 60 individual 3,6-dialkynyl phenanthrene units are involved in the excitation of one pyrene. In other words, the excitation energy of the 3,6-dialkynyl phenanthrene units present on 10 to 11 DNA duplexes is transferred to one pyrene.

Table 7.7: Fluorescence quantum yields (Φ_{FL}) and FRET efficiencies (E_{FRET}) of **O27*O28** doped with different amounts of **O29**. Averages of three measurements with standard deviation.

O29 (μM)	Φ_{FL} (%)	E_{FRET} (%)
-	3.1 ± 0.2	
0.01	3.6 ± 0.1	9.9 ± 1.9
0.03	4.4 ± 0.1	14.9 ± 1.9
0.09	5.7 ± 0.5	18.4 ± 1.9
0.27	9.8 ± 0.2	23.4 ± 2.0

Chapter 8

Overall Conclusions and Outlook

In conclusion, 3'- and 3'/5'-end modified pyrene-DNA conjugates, as well as 3'-end and internally modified phenanthrene-DNA conjugates, self-assemble into spherical nanostructures, confirming previous observations made with phenanthrene- and TPE-DNA conjugates.^{146,163–165} Alternations in the morphologies of supramolecular assemblies were observed depending on the substitution pattern of the pyrene sticky ends. The pyrene-DNA conjugates with 1,6- and 1,8-dialkynyl pyrene isomers assemble into columnar-packed multilamellar vesicles, and spherical aggregates are formed by the 2,7-dialkynyl pyrene isomer. Furthermore, the size of the DNA nanostructures depends on the number of pyrene units present in the sticky ends. By shortening the sticky ends from three to two pyrenes, the size of the nanostructures decreased. The pyrene-DNA conjugates with one pyrene on each side self-assemble only at increased concentrations of spermine tetrahydrochloride and reduced ethanol content. In contrast to the diverse architectures formed upon terminal functionalization of TPE-DNA conjugates, terminal functionalization of 3'-/5'-end modified pyrene-DNA conjugated yields almost identical spherical nanostructures.¹⁶⁵ Contrary internal modifications of phenanthrene-DNA conjugates led to substantial morphological changes, while previously published 3'-ends modified phenanthrene-DNA conjugates formed vesicles.¹⁴⁶ Internally and 3'-end modified phenanthrene-DNA conjugates formed larger filled spherical nanostructures. Finally, all assemblies of pyrene- and phenanthrene-DNA conjugates demonstrate light-harvesting capabilities.

The self-assembly of chromophore-DNA conjugates into spherical nanostructures was observed, irrespective of the hydrophobic unit, proposing that any hydrophobic chromophore forms DNA nanostructures. In future experiments, different hydrophobic moieties could be assessed. Furthermore, the number of chromophores inside and on the sticky ends could be increased to determine the boundaries of the presented system.

The resistance of 3'-/5'-end modified pyrene-DNA conjugates to morphological changes upon terminal modification renders them promising candidates for drug delivery applications, and therefore, further experiments are of interest. Apart from drug delivery applications, the light-harvesting capabilities of the nanostructures are of great interest. Additional experiments using two-pulse fluorescence-detected coherent spectroscopy and four-pulse fluorescence-detected coherent spectroscopy could give more detailed information on the energy transfer mechanisms involved.

Abbreviations

2D	Two-dimensional
3D	Three-dimensional
AIE	Aggregation induced emission
AFM	Atomic force microscopy
ARS	Analytical research and services
APTES	(3-Aminopropyl)triethoxysilane
ASGPR	Asialoglycoprotein receptor
calcd	Calculated
CEP	2-Cyanoethyl N,N-diisopropylchlorophosphoramidite
CPG	Controlled pore glass
cryo-EM	Cryogenic electron microscopy
Cy	Cyanine
CuAAC	Copper-catalyzed azide-alkyne cycloaddition
d	Doublet
DCBP	Department of Chemistry, Biochemistry and Pharmaceutical Sciences
DCI	4,5-dicyanoimidazole
DCM	Dichloromethane
DIPA	Diisopropylamine
DIPEA	N,N-Diisopropylethylamine
DLS	Dynamic light scattering
DMAP	4-(Dimethylamino)pyridine
DMSO	Dimethyl sulfoxide
DMT	4,4'-Dimethoxytrityl
DNA	Deoxyribonucleic acid
Et ₃ N	Triethylamine
EET	Excitation energy transfer
FFT	Fast Fourier transform
FRET	Förster resonance energy transfer
GalNAc	<i>N</i> -Acetylgalactosamine
h	hours
HBTU	(2-(1H-benzotriazol-1-yl)-1,1,3,3-tetramethyluronium hexafluorophosphate
HFIP	1,1,1,3,3,3-Hexafluoropropan-2-ol
HPLC	High performance liquid chromatography
Hz	Herz
kcps	kilo counts per second
l	liters
LCAA	Long chain alkylamino
LHC	Light-harvesting complex
m	Multiplet
MeCN	Acetonitrile

mPEG	Poly(ethylene glycol) monomethyl ether
HRMS	High resolution mass spectrometry
MS	Mass spectrometry
NMR	Nuclear magnetic resonance
NSI	Nano electrospray ionization
PEG	Polyethylene glycol
PAH	Polycyclic aromatic hydrocarbon
PDI	Polydispersity index
ppm	Parts per million
PSD	Particle size distribution
RNA	Ribonucleic acid
r.t.	Room temperature
ref	reference
s	Singlet
SAXS	Small-angle x-ray scattering
SNF	Swiss National Science Foundation
Sp	Spermine tetrahydrochloride
t	Triplet
TALOS	Three-dimensional algorithmically-generated library of DNA Origami Shapes
TBTA	Tris(benzyltriazolylmethyl)amine
TEA	Triethylamine
TEAA	Triethylamine acetate
TEM	Transmission electron microscopy
TFA	Trifluoroacetic acid
THF	Tetrahydrofuran
TLC	Thin layer chromatography
TPE	Tetraphenylethylene
UV-vis	Ultraviolet-visible
WAXS	Wide-angle X-ray scattering

General Methods

Organic Synthesis

Unless otherwise stated, all chemicals and solvents were purchased from commercial sources and were used without further purification. Technical grade ethyl acetate, heptane, and hexane were purified by vacuum distillation on a Büchi Rotavapor R-220 before use. TLCs were conducted on silica gel ALUGRAM[®] Xtra SIL G/UV₂₅₄ (Macherey-Nagel). Flash column chromatography was performed on Sigma Aldrich silica gel, pore size 60 Å, 230–400 mesh particle size. The water was used from a Milli-Q system.

NMR

All NMR spectra were recorded on a Bruker Avance III HD 300 GA spectrometer at 300.13 MHz or a Bruker Avance III HD 400 IOCSP1 at 400.13 MHz, respectively. All compounds were characterized by ¹H-NMR. Chemical shifts are reported in parts per million (ppm) and are referenced to the residual solvent peaks DMSO-*d*₆, ¹H = 2.50 ppm; and CDCl₃, ¹H = 7.26 ppm. Coupling constants (*J*) are given in hertz (Hz). Peak multiplicities are described in the following way: s, singlet; d, doublet; t, triplet; m, multiplet. ³¹P NMR were recorded on a Bruker Avance III HD 300 GA spectrometer at 121.5 MHz.

MS

Mass spectra were measured by the *Analytical Research and Services (ARS)* team of the *Department of Chemistry and Biochemistry* (University of Bern) on a *Thermo Fisher LTQ Orbitrap XL* using Nano Electrospray Ionization (NSI).

Solid-Phase Synthesis

The oligomers were synthesized on an Applied Biosystems 394 DNA/RNA synthesizer applying a standard cyanoethyl phosphoramidite coupling protocol on a 1 μmol scale. The following pyrene: **3**, **8**, and **9**; alkyne: **16**, phenanthrene: **19** and **22**; and nucleobases: **C-Ac**, **T**, **A-Bz**, and **G-DMF** phosphoramidites were used (Figure 8.1). A 0.3 M solution of ethylthiotetrazol in MeCN was used as an activator, and a 3 weight% solution of trichloroacetic acid (TCA) in DCM was used for the detritylation step. Two capping agents A and B were used and mixed *in situ* to perform the capping step A: a solution 10 vol% 2,6-lutidine, and 10 vol% acetic anhydride in THF and B: 16 vol% 1-methylimidazol in THF, and for the oxidation a solution of 0.02 M iodine in 70 vol% THF, 20 vol% pyridine and 10 vol% water was used. Between the steps, the solid supports were washed with MeCN or DCM.

A coupling time of 30 seconds was used for all modifications. All phosphoramidites were dissolved in anhydrous acetonitrile, forming a 0.1 M solution. The solid-phase synthesis was started with a pyrene-, guanine-, or phenanthrene-modified long chain alkylamine controlled pore glass (LCAA-CPG) solid supports **11**, **13**, **15**, **24**, or the commercially available guanine-modified solid support (Figure 8.2). After the oligonucleotide synthesis, the oligomers were cleaved from the solid-support and deprotected with aqueous NH_4OH (28–30%) at 55 °C overnight. The respective supernatants were collected, and the glass beads were washed three times with a solution of ethanol and Milli-Q H_2O (1:1, 4×1 ml), and the crude oligonucleotides were lyophilized three times.

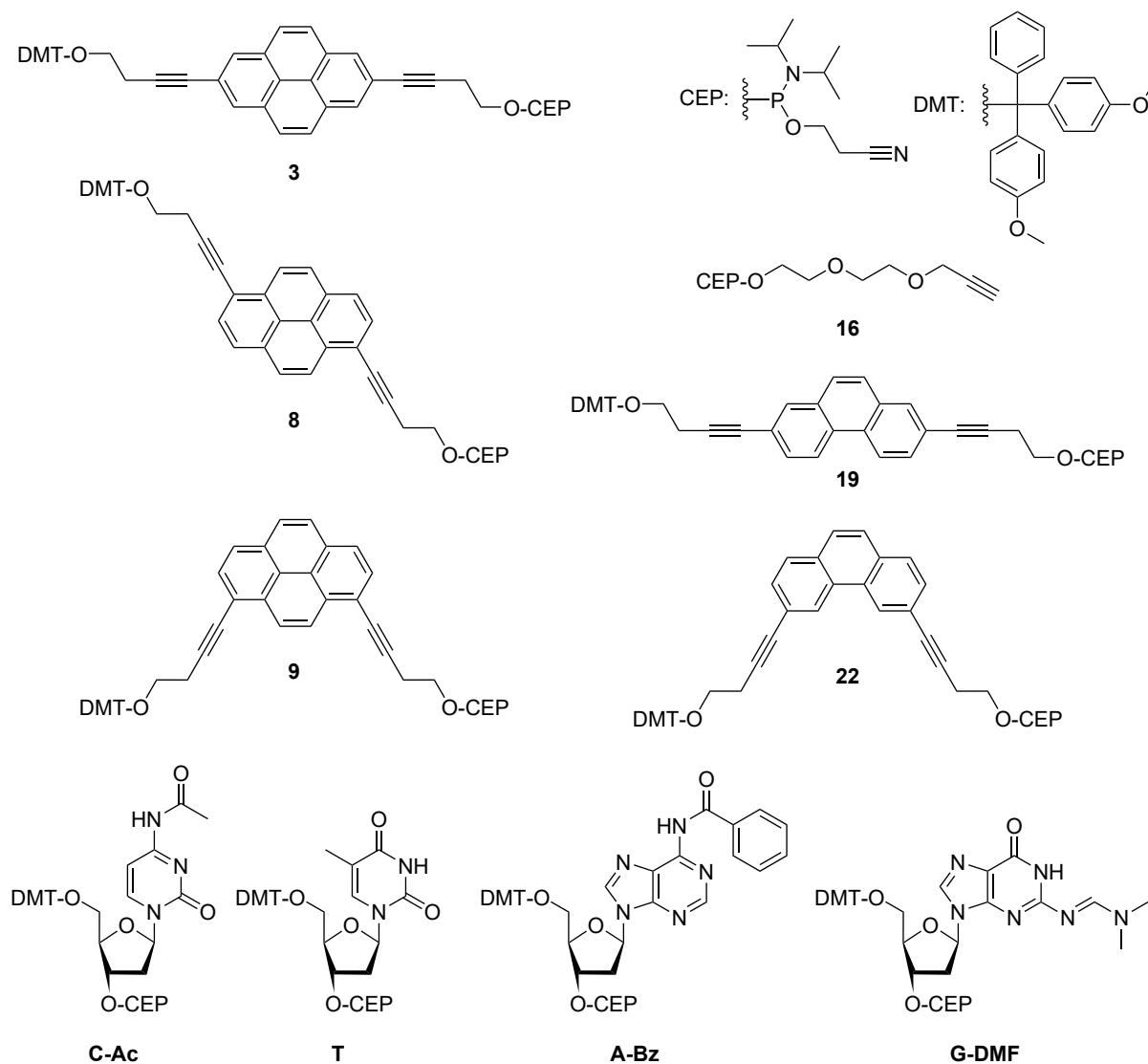


Figure 8.1: Chemical formula of all phosphoramidites used in this thesis. The pyrene phosphoramidites: **3**, **8**, and **9**; the alkyne phosphoramidite: **16**, the phenanthrene phosphoramidites: **19** and **22**; and the phosphoramidites of the nucleobases: **C-Ac**, **T**, **A-Bz**, and **G-DMF**.

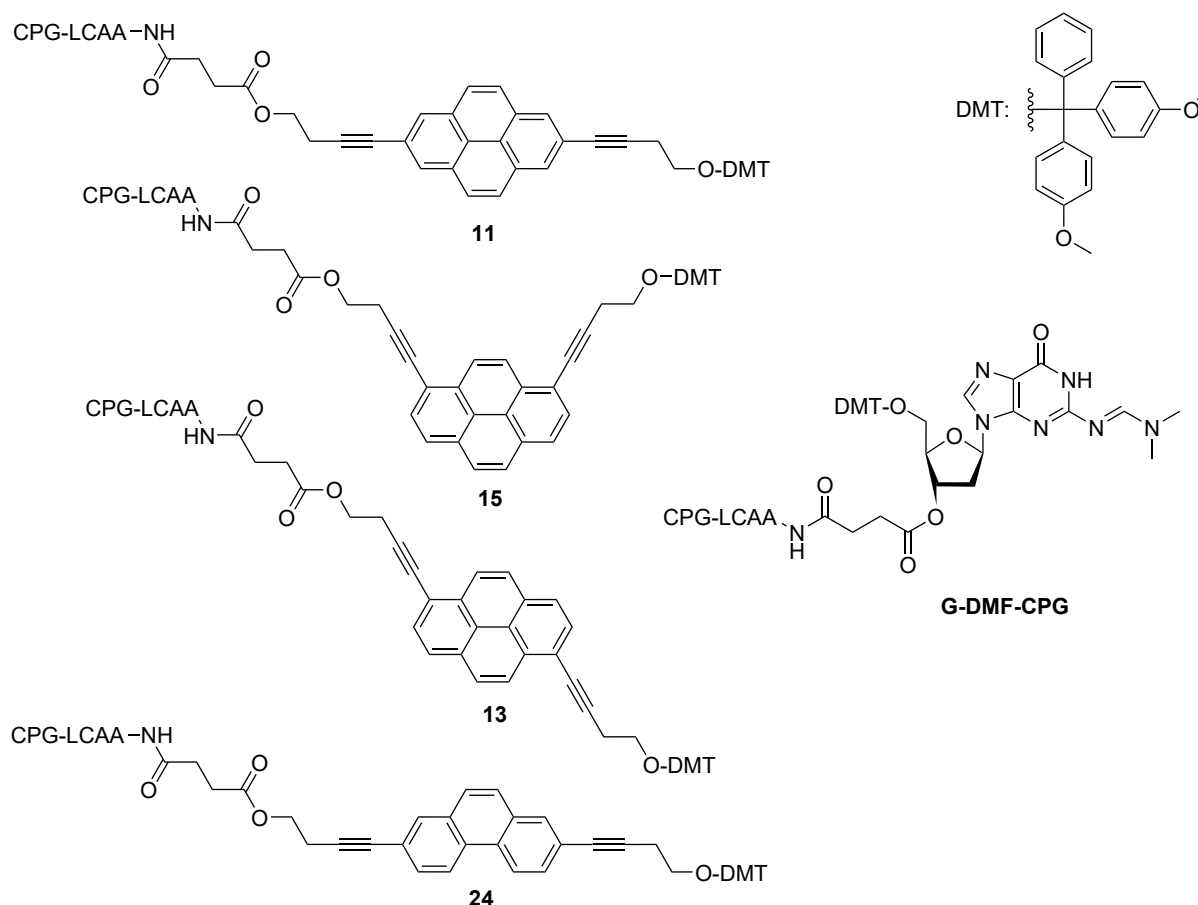


Figure 8.2: Chemical structures of the solid support bound **11**, **13**, **15**, **24**, and **G-DMF-CPG**.

HPLC

All oligomers were purified by reverse-phase HPLC (Shimadzu LC-20AT, ReproSil 100 C18, 5,0 μm , 250 \times 4 mm) at 40 $^{\circ}\text{C}$ or 50 $^{\circ}\text{C}$ with a flow rate of 1 $\text{ml} \cdot \text{min}^{-1}$, with a UV-vis detector at a detection wavelength λ of 260 nm. The solvents and gradients are described in the individual chapters. After the purification, the oligomers were dissolved in 1 ml of Milli-Q water. The absorbances of the oligomers were measured at 260 nm to determine the concentration of the stock solutions and yields. The concentrations were determined by applying the Beer-Lambert law. The following molar absorptivities (at 260 nm) in $\text{l} \cdot \text{mol}^{-1} \cdot \text{cm}^{-1}$ were used: ϵ_{A} ; 15'300, ϵ_{T} ; 9'000, ϵ_{G} ; 11'700, ϵ_{C} ; 7'400, $\epsilon_{2,7\text{-pyrene}}$; 32'000, 1,8-pyrene; 30'000, $\epsilon_{1,6\text{-pyrene}}$; 20'000, $\epsilon_{3,6\text{-phenanthrene}}$; 56'000, and $\epsilon_{2,7\text{-phenanthrene}}$; 47'000,.

UV-Vis and Fluorescence Spectroscopy

Spectroscopic data were measured from at least five min thermally equilibrated samples at the corresponding temperature. UV-Vis spectra were recorded on a Jasco V-730 spectrophotometer using quartz cuvettes with an optical path of 1 cm. Fluorescence spectra were collected on a Jasco spectrophotometer FP-8300 using an excitation and emission slit of 2.5 nm (unless otherwise noted).

Supramolecular Assembly

Supramolecular assembly proceeded via thermal disassembly and reassembly: the sample solution was heated to 75 °C, followed by a controlled cooling of 0.5 °C/min to 20 °C in a Jasco V-730 spectrophotometer or Jasco spectrophotometer FP-8300 equipped with a Peltier thermostat.

DLS

DLS experiments were conducted on a Malvern Zetasizer Nano Series instrument (Malvern Instruments) ($\lambda = 633$ nm) in particle size distribution (PSD) mode (number value) at 20 °C, equilibrated for 5 minutes.

AFM

AFM experiments were performed on a Nanosurf FlexAFM instrument at ambient conditions in tapping mode. Tap190Al-G cantilevers from Budget-Sensors, Innovative Solutions Bulgaria Ltd. were used. AFM samples were prepared on APTES-modified mica sheets (Glimmer “V1”, 20 mm x 20 mm, G250-7, Plano GmbH) according to published procedures.²¹³ Mica sheets were freshly cleaved with ShamrockTM labeling tape and mounted with tape on top of a desiccator (3 l). After that, the desiccator was purged with argon. 30 μ l of APTES and 10 μ l triethylamine acetate (TEAA) was pipetted into two separate caps of an Eppendorf tube. Both Eppendorf tube caps were placed at the bottom of the desiccator below the mica sheets, the desiccator was closed, and the mica sheets were left overnight in the desiccator. Afterward, the sample solutions (20 μ l) were pipetted onto the APTES-modified mica sheet. After an adsorption time of 10 min, the mica sheet was rinsed with Milli-Q water (2 ml), followed by drying under a stream of argon.

TEM

5 μ l of the sample solution was pipetted on copper holey carbon grids (300 mesh, Agar Scientific). After 2 min of adsorption, the solution was blotted (KIMTECH Scientific precision wipes). Then the grid was dipped into 30 μ l of Mili-Q water before the solution was blotted again. This washing step was repeated once. Afterwards, the grid was dipped into UA-Zero staining solution (Agar Scientific) and blotted. The grid was dipped again into the staining solution and blotted after 30 seconds. TEM images were recorded on a Tecnai Spirit using an operating voltage of 80 kV and with either an Olympus-SIS Veleta CCD camera or an FEI Eagle CCD camera.

Cryo-EM

Cryo-electron microscopy samples were prepared using the FEI Vitrobot Mark 4 at room temperature with 100% humidity. For the images, copper lacey carbon grids were used. These grids were glow discharged (air -10 mA for 20 seconds). A 3 μ l sample solution was pipetted onto the grids and blotted for 3 seconds before being plunged into liquid ethane. The prepared sample grids were stored in liquid nitrogen.

Imaging was performed using a Gatan 626 cryo holder on an FEI Tecnai F20 microscope in nanoprobe mode. Due to the sensitive nature of the sample, imaging settings were adjusted to ensure a low total electron dose (less than 20 $e^-/\text{\AA}^2$) using EPU software.

Distance measurements were conducted using Fiji software.^{214,215} The multi-point tool was utilized to set measurement marks on the images. After obtaining the x- and y-values from the marked points, distances between the marks were calculated. The reported distances are presented as mean values along with their corresponding standard deviations.

Fluorescence Quantum Yield

Fluorescence quantum yields (Φ_{FL}) were determined according to published procedures²¹⁶ relative to quinine sulfate (in 0.5 M sulfuric acid) as a standard.²¹⁷ The equation 8.1 was used to determine the fluorescence quantum yield of the sample $\Phi_{F(X)}$, where $\Phi_{F(S)}$ is the quantum yield of the standard, A_S the absorbance of the standard at the excitation wavelength, A_X the absorbance of the sample at the excitation wavelength, F_S the integral of the fluorescence emission of the standard, F_X the integral of the fluorescence emission of the sample, n_s the refractive index of the standard, and n_X the refractive index of the sample at 20 °C.

$$\Phi_{F(X)} = \left(\frac{A_S}{A_X} \right) \left(\frac{F_X}{F_S} \right) \left(\frac{n_X}{n_S} \right)^2 \Phi_{F(S)} \quad (8.1)$$

FRET Efficiency

The FRET efficiency (E_{FRET}) was calculated according to the equation 8.2 where F_{DA} and F_D are the integrated areas of fluorescence emission of the donor in the presence and absence of the acceptor.

$$E_{FRET} = 1 - \frac{F_{DA}}{F_D} \quad (8.2)$$

Number of Donors involved in FRET

The Number of Donors involved in FRET was calculated according to the equation 8.3 where E_{FRET} is the FRET efficiency (equation: 8.2), c_A is the concentrations of the acceptor, and c_D is the concentration of the donor.

$$N_{Donor} = \frac{E_{FRET} \cdot c_D}{c_A} \quad (8.3)$$

Förster Radius

The Förster Radius R_0 , which is the distance at which energy transfer is 50% efficient, was calculated according to the equation 8.4 where κ^2 is the orientation factor, Φ_D the quantum yield of the donor fluorescence, n the refractive index of the medium, and J the degree of spectral overlap between normalized donor fluorescence spectrum and acceptor absorption spectrum.

$$R_0 = 0.2108 \cdot (\kappa^2 \Phi_D n^{-4} J)^{1/6} \quad (8.4)$$

With the absence of structural information, a κ^2 value of 2/3 is often chosen. This limiting situation is valid when the molecular dipoles are rapidly rotating at a speed much faster than the FRET rate.

The degree of spectral overlap between normalized donor fluorescence spectrum and acceptor absorption spectrum J was calculated according to the equation 8.5 where λ is a sampled wavelength, $F_D(\lambda)$ is the fluorescence emission of the donor at a given wavelength normalized to unity, and ϵ_A is the extinction coefficient of the acceptor at the maximum (**O9**: 150'000 M⁻¹cm⁻¹ and **O11**: 2500'000 M⁻¹cm⁻¹).

$$J = \int_0^\infty F_D(\lambda) \epsilon_A(\lambda) \lambda^4 d\lambda \quad (8.5)$$

Bibliography

- [1] Lehn, J.-M. Toward Self-Organization and Complex Matter. *Science* **2002**, *295*, 2400–2403.
 - [2] Bäumer, N.; Castellanos, E.; Soberats, B.; Fernández, G. Bioinspired Crowding Directs Supramolecular Polymerisation. *Nat. Commun.* **2023**, *14*, 1084.
 - [3] Brunsveld, L.; Folmer, B. J. B.; Meijer, E. W.; Sijbesma, R. P. Supramolecular Polymers. *Chem. Rev.* **2001**, *101*, 4071–4098.
 - [4] Leenders, C. M. A.; Baker, M. B.; Pijpers, I. A. B.; Lafleur, R. P. M.; Albertazzi, L.; Palmans, A. R. A.; Meijer, E. W. Supramolecular Polymerisation in Water; Elucidating the Role of Hydrophobic and Hydrogen-Bond Interactions. *Soft Matter* **2016**, *12*, 2887–2893.
 - [5] Boekhoven, J.; Hendriksen, W. E.; Koper, G. J. M.; Eelkema, R.; Van Esch, J. H. Transient Assembly of Active Materials Fueled by a Chemical Reaction. *Science* **2015**, *349*, 1075–1079.
 - [6] Krieg, E.; Bastings, M. M. C.; Besenius, P.; Rybtchinski, B. Supramolecular Polymers in Aqueous Media. *Chem. Rev.* **2016**, *116*, 2414–2477.
 - [7] Aida, T.; Meijer, E. W.; Stupp, S. I. Functional Supramolecular Polymers. *Science* **2012**, *335*, 813–817.
 - [8] Campanella, A.; Döhler, D.; Binder, W. H. Self-Healing in Supramolecular Polymers. *Macromol. Rapid Commun.* **2018**, *39*, 1700739.
 - [9] Schill, J.; Rosier, B. J. H. M.; Gumí Audenis, B.; Magdalena Estirado, E.; Greef, T. F. A.; Brunsveld, L. Assembly of Dynamic Supramolecular Polymers on a DNA Origami Platform. *Angew. Chem.* **2021**, *133*, 7690–7694.
 - [10] Dumele, O.; Chen, J.; Passarelli, J. V.; Stupp, S. I. Supramolecular Energy Materials. *Adv. Mater.* **2020**, *32*, 1907247.
 - [11] Van Gemert, G. M. L.; Peeters, J. W.; Söntjens, S. H. M.; Janssen, H. M.; Bosman, A. W. Self-Healing Supramolecular Polymers In Action. *Macromol. Chem. Phys.* **2012**, *213*, 234–242.
 - [12] Lutz, J.-F.; Lehn, J.-M.; Meijer, E. W.; Matyjaszewski, K. From Precision Polymers to Complex Materials and Systems. *Nat. Rev. Mater.* **2016**, *1*, 16024.
 - [13] Cordier, P.; Tournilhac, F.; Soulié-Ziakovic, C.; Leibler, L. Self-Healing and Thermoreversible Rubber from Supramolecular Assembly. *Nature* **2008**, *451*, 977–980.
 - [14] Vázquez-González, M.; Willner, I. Stimuli-Responsive Biomolecule-Based Hydrogels and Their Applications. *Angew. Chem. Int. Ed.* **2020**, *59*, 15342–15377.
-

- [15] Magdalena Estirado, E.; Mason, A. F.; Alemán García, M. A.; Van Hest, J. C. M.; Brunsveld, L. Supramolecular Nanoscaffolds within Cytomimetic Protocells as Signal Localization Hubs. *J. Am. Chem. Soc.* **2020**, *142*, 9106–9111.
- [16] Ball, P. Water as an Active Constituent in Cell Biology. *Chem. Rev.* **2008**, *108*, 74–108.
- [17] Grabicki, N.; Dumele, O.; Sai, H.; Powers-Riggs, N. E.; Phelan, B. T.; Sangji, M. H.; Chapman, C. T.; Passarelli, J. V.; Dannenhoffer, A. J.; Wasielewski, M. R.; Stupp, S. I. Polymorphism and Optoelectronic Properties in Crystalline Supramolecular Polymers. *Chem. Mater.* **2021**, *33*, 706–718.
- [18] Winiger, C. B.; Li, S.; Kumar, G. R.; Langenegger, S. M.; Häner, R. Long-Distance Electronic Energy Transfer in Light-Harvesting Supramolecular Polymers. *Angew. Chem. Int. Ed.* **2014**, *53*, 13609–13613.
- [19] Bösch, C. D.; Langenegger, S. M.; Häner, R. Light-Harvesting Nanotubes Formed by Supramolecular Assembly of Aromatic Oligophosphates. *Angew. Chem. Int. Ed.* **2016**, *55*, 9961–9964.
- [20] Nussbaumer, A. L.; Studer, D.; Malinovskii, V. L.; Häner, R. Amplification of Chirality by Supramolecular Polymerization of Pyrene Oligomers. *Angew. Chem. Int. Ed.* **2011**, *50*, 5490–5494.
- [21] Malinovskii, V. L.; Nussbaumer, A. L.; Häner, R. Oligopyrenotides: Chiral Nanoscale Templates for Chromophore Assembly. *Angew. Chem. Int. Ed.* **2012**, *51*, 4905–4908.
- [22] Vybornyi, M.; Rudnev, A. V.; Langenegger, S. M.; Wandlowski, T.; Calzaferri, G.; Häner, R. Formation of Two-Dimensional Supramolecular Polymers by Amphiphilic Pyrene Oligomers. *Angew. Chem. Int. Ed.* **2013**, *52*, 11488–11493.
- [23] Vybornyi, M.; Rudnev, A.; Häner, R. Assembly of Extra-Large Nanosheets by Supramolecular Polymerization of Amphiphilic Pyrene Oligomers in Aqueous Solution. *Chem. Mater.* **2015**, *27*, 1426–1431.
- [24] Vybornyi, M.; Bur-Cecilio Hechevarria, Y.; Glauser, M.; Rudnev, A. V.; Häner, R. Tubes or Sheets: Divergent Aggregation Pathways of an Amphiphilic 2,7-Substituted Pyrene Trimer. *Chem. Commun.* **2015**, *51*, 16191–16193.
- [25] Jevric, J.; Langenegger, S. M.; Häner, R. Layered Assembly of Cationic and Anionic Supramolecular Polymers. *Chem. Commun.* **2021**, *57*, 6648–6651.
- [26] Jevric, J.; Langenegger, S. M.; Häner, R. Light-Harvesting Supramolecular Polymers: Energy Transfer to Various Polyaromatic Acceptors: Light-Harvesting Supramolecular Polymers: Energy Transfer to Various Polyaromatic Acceptors. *Eur. J. Org. Chem.* **2020**, *2020*, 4677–4680.
- [27] Yu, H.; Häner, R. Solution-Phase Synthesis of 1D Tubular Polymers via Preorganization–Polymerization. *Chem. Commun.* **2016**, *52*, 14396–14399.
- [28] Yu, H.; Sabetti, M.; Häner, R. Formation of Supramolecular Nanotubes by Self-assembly of a Phosphate-linked Dimeric Anthracene in Water. *Chem. Asian J.* **2018**, *13*, 968–971.
- [29] Markova, L.; Probst, M.; Häner, R. Assembly and Functionalization of Supramolecular Polymers from DNA-conjugated Squaraine Oligomers. *RSC Adv.* **2020**, *10*, 44841–44845.
- [30] Markova, L. I.; Malinovskii, V. L.; Patsenker, L. D.; Häner, R. Synthesis and Properties of Squaraine-Modified DNA. *Org. Biomol. Chem.* **2012**, *10*, 8944.
-

- [31] Münich, P. W.; Pfäffli, M.; Volland, M.; Liu, S.-X.; Häner, R.; Guldi, D. M. Amphiphilic Anthanthrene Trimers That Exfoliate Graphite and Individualize Single Wall Carbon Nanotubes. *Nanoscale* **2020**, *12*, 956–966.
- [32] Häner, R.; Vybornyi, O.; Liu, S.-X. Stimuli-responsive Supramolecular Polymers from Amphiphilic Phosphodiester-linked Azobenzene Trimers. *Angew. Chem. Int. Ed.* **2021**, anie.202108745.
- [33] De Greef, T. F. A.; Smulders, M. M. J.; Wolffs, M.; Schenning, A. P. H. J.; Sijbesma, R. P.; Meijer, E. W. Supramolecular Polymerization. *Chem. Rev.* **2009**, *109*, 5687–5754.
- [34] Wang, H.; Mills, J.; Sun, B.; Cui, H. Therapeutic Supramolecular Polymers: Designs and Applications. *Prog. Polym. Sci.* **2024**, *148*, 101769.
- [35] Dhiman, S.; Sarkar, A.; George, S. J. Bioinspired Temporal Supramolecular Polymerization. *RSC Adv.* **2018**, *8*, 18913–18925.
- [36] Franklin, R. E.; Gosling, R. G. Molecular Configuration in Sodium Thymonucleate. *Nature* **1953**, *171*, 740–741.
- [37] Watson, J. D.; Crick, F. H. C. Molecular Structure of Nucleic Acids: A Structure for Deoxyribose Nucleic Acid. *Nature* **1953**, *171*, 737–738.
- [38] Wilkins, M. H. F.; Stokes, A. R.; Wilson, H. R. Molecular Structure of Nucleic Acids: Molecular Structure of Deoxypentose Nucleic Acids. *Nature* **1953**, *171*, 738–740.
- [39] Matteucci, M. D.; Caruthers, M. H. Synthesis of Deoxyoligonucleotides on a Polymer Support. *J. Am. Chem. Soc.* **1981**, *103*, 3185–3191.
- [40] Stulz, E., Clever, G. H., Eds. *DNA in Supramolecular Chemistry and Nanotechnology*; John Wiley & Sons, Ltd: Chichester, UK, 2014.
- [41] Fuertes, M. A.; Cepeda, V.; Alonso, C.; Pérez, J. M. Molecular Mechanisms for the B-Z Transition in the Example of Poly[d(G-C)-d(G-C)] Polymers. A Critical Review. *Chem. Rev.* **2006**, *106*, 2045–2064.
- [42] Hartmann, B.; Lavery, R. DNA Structural Forms. *Quart. Rev. Biophys.* **1996**, *29*, 309–368.
- [43] Blackburn, G. M., Ed. *Nucleic Acids in Chemistry and Biology*, 3rd ed.; RSC Pub: Cambridge, UK, 2006.
- [44] Yakovchuk, P. Base-Stacking and Base-Pairing Contributions into Thermal Stability of the DNA Double Helix. *Nucleic Acids Res.* **2006**, *34*, 564–574.
- [45] Guckian, K. M.; Schweitzer, B. A.; Ren, R. X.-F.; Sheils, C. J.; Tahmassebi, D. C.; Kool, E. T. Factors Contributing to Aromatic Stacking in Water: Evaluation in the Context of DNA. *J. Am. Chem. Soc.* **2000**, *122*, 2213–2222.
- [46] Luo, R.; Gilson, H. S.; Potter, M. J.; Gilson, M. K. The Physical Basis of Nucleic Acid Base Stacking in Water. *Biophys. J.* **2001**, *80*, 140–148.
- [47] Krall, J. B.; Nichols, P. J.; Henen, M. A.; Vicens, Q.; Vögeli, B. Structure and Formation of Z-DNA and Z-RNA. *Molecules* **2023**, *28*, 843.
- [48] Malinovskii, V. L.; Wenger, D.; Häner, R. Nucleic Acid-Guided Assembly of Aromatic Chromophores. *Chem. Soc. Rev.* **2010**, *39*, 410–422.
-

- [49] Garo, F.; Häner, R. A DNA-Based Light-Harvesting Antenna. *Angew. Chem. Int. Ed.* **2012**, *51*, 916–919.
- [50] Vybornyi, M.; Nussbaumer, A. L.; Langenegger, S. M.; Häner, R. Assembling Multiporphyrin Stacks Inside the DNA Double Helix. *Bioconjugate Chem.* **2014**, *25*, 1785–1793.
- [51] Khorev, O.; Bösch, C. D.; Probst, M.; Häner, R. Observation of the Rare Chrysene Excimer. *Chem. Sci.* **2014**, *5*, 1506–1512.
- [52] Winiger, C. B.; Langenegger, S. M.; Calzaferri, G.; Häner, R. Formation of Two Homochromophoric H-Aggregates in DNA-Assembled Alternating Dye Stacks. *Angew. Chem.* **2015**, *5*.
- [53] Ensslen, P.; Wagenknecht, H.-A. One-Dimensional Multichromophore Arrays Based on DNA: From Self-Assembly to Light-Harvesting. *Acc. Chem. Res.* **2015**, *48*, 2724–2733.
- [54] Nakamura, M.; Matsui, Y.; Takada, T.; Yamana, K. Chromophore Arrays Constructed in the Major Groove of DNA Duplexes Using a Post-Synthetic Strategy. *ChemistrySelect* **2019**, *4*, 1525–1529.
- [55] Zhou, X.; Mandal, S.; Jiang, S.; Lin, S.; Yang, J.; Liu, Y.; Whitten, D. G.; Woodbury, N. W.; Yan, H. Efficient Long-Range, Directional Energy Transfer through DNA-Templated Dye Aggregates. *J. Am. Chem. Soc.* **2019**, *141*, 8473–8481.
- [56] Teo, Y. N.; Kool, E. T. DNA-Multichromophore Systems. *Chem. Rev.* **2012**, *112*, 4221–4245.
- [57] Gorman, J. *et al.* Deoxyribonucleic Acid Encoded and Size-Defined π -Stacking of Perylene Diimides. *J. Am. Chem. Soc.* **2022**, *144*, 368–376.
- [58] Hara, Y.; Fujii, T.; Kashida, H.; Sekiguchi, K.; Liang, X.; Niwa, K.; Takase, T.; Yoshida, Y.; Asanuma, H. Coherent Quenching of a Fluorophore for the Design of a Highly Sensitive In-Stem Molecular Beacon. *Angew. Chem.* **2010**, *122*, 5634–5638.
- [59] Ghufran Rafique, M.; Remington, J. M.; Clark, F.; Bai, H.; Toader, V.; Perepichka, D. F.; Li, J.; Sleiman, H. F. Two-Dimensional Supramolecular Polymerization of DNA Amphiphiles Is Driven by Sequence-Dependent DNA-Chromophore Interactions. *Angew. Chem. Int. Ed.* **2023**, *62*, e202217814.
- [60] Burns, J. R.; Wood, J. W.; Stulz, E. A Porphyrin-DNA Chiroptical Molecular Ruler With Base Pair Resolution. *Front. Chem.* **2020**, *8*, 113.
- [61] Hart, S. M.; Chen, W. J.; Banal, J. L.; Bricker, W. P.; Dodin, A.; Markova, L.; Vyborna, Y.; Willard, A. P.; Häner, R.; Bathe, M.; Schlau-Cohen, G. S. Engineering Couplings for Exciton Transport Using Synthetic DNA Scaffolds. *Chem* **2021**, *7*, 752–773.
- [62] Duncan, K. M.; Kellis, D. L.; Huff, J. S.; Barclay, M. S.; Lee, J.; Turner, D. B.; Davis, P. H.; Yurke, B.; Knowlton, W. B.; Pensack, R. D. Symmetry Breaking Charge Transfer in DNA-Templated Perylene Dimer Aggregates. *Molecules* **2022**, *27*, 6612.
- [63] Zhou, X.; Satyabola, D.; Liu, H.; Jiang, S.; Qi, X.; Yu, L.; Lin, S.; Liu, Y.; Woodbury, N. W.; Yan, H. Two-Dimensional Excitonic Networks Directed by DNA Templates as an Efficient Model Light-Harvesting and Energy Transfer System. *Angew. Chem. Int. Ed.* **2022**, *61*, e202211200.
-

- [64] Hart, S. M.; Banal, J. L.; Castellanos, M. A.; Markova, L.; Vyborna, Y.; Gorman, J.; Häner, R.; Willard, A. P.; Bathe, M.; Schlau-Cohen, G. S. Activating Charge-Transfer State Formation in Strongly-Coupled Dimers Using DNA Scaffolds. *Chem. Sci.* **2022**, *13*, 13020–13031.
- [65] Hart, S. M.; Gorman, J.; Bathe, M.; Schlau-Cohen, G. S. Engineering Exciton Dynamics with Synthetic DNA Scaffolds. *Acc. Chem. Res.* **2023**, *56*, 2051–2061.
- [66] Hart, S. M.; Wang, X.; Guo, J.; Bathe, M.; Schlau-Cohen, G. S. Tuning Optical Absorption and Emission Using Strongly Coupled Dimers in Programmable DNA Scaffolds. *J. Phys. Chem. Lett.* **2022**, *13*, 1863–1871.
- [67] Garo, F.; Häner, R. Influence of a GC Base Pair on Excitation Energy Transfer in DNA-Assembled Phenanthrene π -Stacks. *Bioconjugate Chem.* **2012**, *23*, 2105–2113.
- [68] Probst, M.; Langenegger, S. M.; Häner, R. A Modular LHC Built on the DNA Three-Way Junction. *Chem. Commun.* **2014**, *50*, 159–161.
- [69] Ensslen, P.; Gärtner, S.; Glaser, K.; Colsmann, A.; Wagenknecht, H.-A. A DNA-Fullerene Conjugate as a Template for Supramolecular Chromophore Assemblies: Towards DNA-Based Solar Cells. *Angew. Chem. Int. Ed.* **2016**, *55*, 1904–1908.
- [70] Bui, H.; Díaz, S. A.; Fontana, J.; Chiriboga, M.; Veneziano, R.; Medintz, I. L. Utilizing the Organizational Power of DNA Scaffolds for New Nanophotonic Applications. *Adv. Optical Mater.* **2019**, *7*, 1900562.
- [71] Bösch, C. D.; Abay, E.; Langenegger, S. M.; Nazari, M.; Cannizzo, A.; Feurer, T.; Häner, R. DNA-Organized Light-Harvesting Antennae: Energy Transfer in Polyaromatic Stacks Proceeds through Interposed Nucleobase Pairs. *Helv. Chim. Acta* **2019**, *102*, 1–6.
- [72] Bürki, N.; Grossenbacher, E.; Cannizzo, A.; Feurer, T.; Langenegger, S. M.; Häner, R. DNA-organized Artificial LHCs – Testing the Limits of Chromophore Segmentation. *Org. Biomol. Chem.* **2020**, *18*, 6818–6822.
- [73] Mass, O. A.; Wilson, C. K.; Roy, S. K.; Barclay, M. S.; Patten, L. K.; Terpetschnig, E. A.; Lee, J.; Pensack, R. D.; Yurke, B.; Knowlton, W. B. Exciton Delocalization in Indolenine Squaraine Aggregates Templated by DNA Holliday Junction Scaffolds. *J. Phys. Chem. B* **2020**, *124*, 9636–9647.
- [74] Devaux, A.; Calzaferri, G.; Belser, P.; Cao, P.; Brühwiler, D.; Kunzmann, A. Efficient and Robust Host–Guest Antenna Composite for Light Harvesting. *Chem. Mater.* **2014**, *26*, 6878–6885.
- [75] Madsen, M.; Gothelf, K. V. Chemistries for DNA Nanotechnology. *Chem. Rev.* **2019**, *119*, 6384–6458.
- [76] Takezawa, Y.; Kanemaru, D.; Kudo, N.; Shionoya, M. Phenanthroline-Modified DNA Three-Way Junction Structures Stabilized by Interstrand 3 : 1 Metal Complexation. *Dalton Trans.* **2023**, *52*, 11025–11029.
- [77] Appukutti, N.; Serpell, C. J. High Definition Polyphosphoesters: Between Nucleic Acids and Plastics. *Polym. Chem.* **2018**, *9*, 2210–2226.
- [78] Ramezani, H.; Dietz, H. Building Machines with DNA Molecules. *Nat. Rev. Genet.* **2020**, *21*, 5–26.
-

- [79] Hu, Y.; Niemeyer, C. M. From DNA Nanotechnology to Material Systems Engineering. *Adv. Mater.* **2019**, *31*, 1806294.
- [80] Marth, G.; Hartley, A. M.; Reddington, S. C.; Sargisson, L. L.; Parcollet, M.; Dunn, K. E.; Jones, D. D.; Stulz, E. Precision Templated Bottom-Up Multiprotein Nanoassembly through Defined Click Chemistry Linkage to DNA. *ACS Nano* **2017**, *11*, 5003–5010.
- [81] Wilner, O. I.; Willner, I. Functionalized DNA Nanostructures. *Chem. Rev.* **2012**, *112*, 2528–2556.
- [82] Kwon, Y.-W.; Lee, C. H.; Choi, D.-H.; Jin, J.-I. Materials Science of DNA. *J. Mater. Chem.* **2009**, *19*, 1353–1380.
- [83] Bathe, M.; Rothmund, P. W. K. DNA Nanotechnology: A Foundation for Programmable Nanoscale Materials. *MRS Bulletin* **2017**, *42*, 882–888.
- [84] Lehninger, A. L.; Nelson, D. L.; Cox, M. M. *Lehninger Principles of Biochemistry*, 6th ed.; W.H. Freeman: New York, 2013.
- [85] Agrawal, S., Ed. *Protocols for Oligonucleotides and Analogs: Synthesis and Properties*; Methods in Molecular Biology v. 20; Humana Press: Totowa, N.J, 1993.
- [86] Merrifield, B. Solid Phase Synthesis. *Science* **1986**, *232*, 341–347.
- [87] Adinolfi, M.; Barone, G.; De Napoli, L.; Iadonisi, A.; Piccialli, G. Use of Controlled Pore Glass in Solid Phase Oligosaccharide Synthesis. Application to the Semiautomated Synthesis of a Glyconucleotide Conjugate. *Tetrahedron Lett.* **1998**, *39*, 1953–1956.
- [88] McCollum, C.; Andrus, A. An Optimized Polystyrene Support for Rapid, Efficient Oligonucleotide Synthesis. *Tetrahedron Lett.* **1991**, *32*, 4069–4072.
- [89] Adams, S. P.; Kavka, K. S.; Wykes, E. J.; Holder, S. B.; Galluppi, G. R. Hindered Dialkylamino Nucleoside Phosphite Reagents in the Synthesis of Two DNA 51-Mers. *J. Am. Chem. Soc.* **1983**, *105*, 661–663.
- [90] Dahl, B. H.; Nielsen, J.; Dahl, O. Mechanistic Studies on the Phosphoramidite Coupling Reaction in Oligonucleotide Synthesis. I. Evidence for Nucleophilic Catalysis by Tetrazole and Rate Variations with the Phosphorus Substituents. *Nucleic Acids Res.* **1987**, *15*, 1729–1743.
- [91] Seeman, N. C. Nucleic Acid Junctions and Lattices. *J. Theor. Biol.* **1982**, *99*, 237–247.
- [92] Seeman, N.; Kallenbach, N. Design of Immobile Nucleic Acid Junctions. *Biophys. J.* **1983**, *44*, 201–209.
- [93] Kallenbach, N. R.; Ma, R.-I.; Seeman, N. C. An Immobile Nucleic Acid Junction Constructed from Oligonucleotides. *Nature* **1983**, *305*, 829–831.
- [94] Seeman, N. C. DNA in a Material World. *Nature* **2003**, *421*, 427–431.
- [95] Jones, M. R.; Seeman, N. C.; Mirkin, C. A. Programmable Materials and the Nature of the DNA Bond. *Science* **2015**, *347*, 1260901–1260901.
- [96] Winfree, E.; Liu, F.; Wenzler, L. A.; Seeman, N. C. Design and Self-Assembly of Two-Dimensional DNA Crystals. *Nature* **1998**, *394*, 539–544.
- [97] Tikhomirov, G.; Petersen, P.; Qian, L. Fractal Assembly of Micrometre-Scale DNA Origami Arrays with Arbitrary Patterns. *Nature* **2017**, *552*, 67–71.
-

- [98] Macfarlane, R. J.; Lee, B.; Jones, M. R.; Harris, N.; Schatz, G. C.; Mirkin, C. A. Nanoparticle Superlattice Engineering with DNA. *Science* **2011**, *334*, 204–208.
- [99] Seeman, N. C. DNA Nanotechnology at 40. *Nano Lett.* **2020**, *20*, 1477–1478.
- [100] Zheng, J.; Birktoft, J. J.; Chen, Y.; Wang, T.; Sha, R.; Constantinou, P. E.; Ginell, S. L.; Mao, C.; Seeman, N. C. From Molecular to Macroscopic via the Rational Design of a Self-Assembled 3D DNA Crystal. *Nature* **2009**, *461*, 74–77.
- [101] Wei, B.; Dai, M.; Yin, P. Complex Shapes Self-Assembled from Single-Stranded DNA Tiles. *Nature* **2012**, *485*, 623–626.
- [102] Li, Z.; Zheng, M.; Liu, L.; Seeman, N. C.; Mao, C. 5'-Phosphorylation Strengthens Sticky-End Cohesions. *J. Am. Chem. Soc.* **2021**, *143*, 14987–14991.
- [103] Douglas, S. M.; Dietz, H.; Liedl, T.; Högberg, B.; Graf, F.; Shih, W. M. Self-Assembly of DNA into Nanoscale Three-Dimensional Shapes. *Nature* **2009**, *459*, 414–418.
- [104] He, Y.; Ye, T.; Su, M.; Zhang, C.; Ribbe, A. E.; Jiang, W.; Mao, C. Hierarchical Self-Assembly of DNA into Symmetric Supramolecular Polyhedra. *Nature* **2008**, *452*, 198–201.
- [105] Lin, C.; Liu, Y.; Yan, H. Designer DNA Nanoarchitectures. *Biochem.* **2009**, *48*, 1663–1674.
- [106] Rothemund, P. W. K. Folding DNA to Create Nanoscale Shapes and Patterns. *Nature* **2006**, *440*, 297–302.
- [107] Dey, S.; Fan, C.; Gothelf, K. V.; Li, J.; Lin, C.; Liu, L.; Liu, N.; Nijenhuis, M. A. D.; Saccà, B.; Simmel, F. C.; Yan, H.; Zhan, P. DNA Origami. *Nat Rev Methods Primers* **2021**, *1*, 13.
- [108] Feldkamp, U.; Niemeyer, C. M. Rational Design of DNA Nanoarchitectures. *Angew. Chem. Int. Ed.* **2006**, *45*, 1856–1876.
- [109] Wang, P.; Meyer, T. A.; Pan, V.; Dutta, P. K.; Ke, Y. The Beauty and Utility of DNA Origami. *Chem* **2017**, *2*, 359–382.
- [110] Tørring, T.; Voigt, N. V.; Nangreave, J.; Yan, H.; Gothelf, K. V. DNA Origami: A Quantum Leap for Self-Assembly of Complex Structures. *Chem. Soc. Rev.* **2011**, *40*, 5636.
- [111] Douglas, S. M.; Marblestone, A. H.; Teerapittayanon, S.; Vazquez, A.; Church, G. M.; Shih, W. M. Rapid Prototyping of 3D DNA-origami Shapes with caDNAo. *Nucleic Acids Res.* **2009**, *37*, 5001–5006.
- [112] Williams, S.; Lund, K.; Lin, C.; Wonka, P.; Lindsay, S.; Yan, H. In *DNA Computing*; Goel, A., Simmel, F. C., Sosík, P., Eds.; Springer Berlin Heidelberg: Berlin, Heidelberg, 2009; Vol. 5347; pp 90–101.
- [113] Andersen, E. S.; Dong, M.; Nielsen, M. M.; Jahn, K.; Lind-Thomsen, A.; Mamdouh, W.; Gothelf, K. V.; Besenbacher, F.; Kjems, J. DNA Origami Design of Dolphin-Shaped Structures with Flexible Tails. *ACS Nano* **2008**, *2*, 1213–1218.
- [114] Doye, J. P. K.; Fowler, H.; Prešern, D.; Bohlin, J.; Rovigatti, L.; Romano, F.; Šulc, P.; Wong, C. K.; Louis, A. A.; Schreck, J. S.; Engel, M. C.; Matthies, M.; Benson, E.; Poppleton, E.; Snodin, B. E. K. In *DNA and RNA Origami*; Valero, J., Ed.; Springer US: New York, NY, 2023; Vol. 2639; pp 93–112.
-

- [115] Matthies, M.; Agarwal, N. P.; Poppleton, E.; Joshi, F. M.; Šulc, P.; Schmidt, T. L. Triangulated Wireframe Structures Assembled Using Single-Stranded DNA Tiles. *ACS Nano* **2019**, *2*, 1839–1848.
- [116] Benson, E.; Mohammed, A.; Gardell, J.; Masich, S.; Czeizler, E.; Orponen, P.; Högberg, B. DNA Rendering of Polyhedral Meshes at the Nanoscale. *Nature* **2015**, *523*, 441–444.
- [117] Veneziano, R.; Ratanalert, S.; Zhang, K.; Zhang, F.; Yan, H.; Chiu, W.; Bathe, M. Designer Nanoscale DNA Assemblies Programmed from the Top Down. *Science* **2016**, *352*, 1534–1534.
- [118] Jun, H.; Shepherd, T. R.; Zhang, K.; Bricker, W. P.; Li, S.; Chiu, W.; Bathe, M. Automated Sequence Design of 3D Polyhedral Wireframe DNA Origami with Honeycomb Edges. *ACS Nano* **2019**, *13*, 2083–2093.
- [119] de Llano, E.; Miao, H.; Ahmadi, Y.; Wilson, A. J.; Beeby, M.; Viola, I.; Barisic, I. Adenita: Interactive 3D Modelling and Visualization of DNA Nanostructures. *Nucleic Acids Res.* **2020**, *48*, 8269–8275.
- [120] Wagenbauer, K. F.; Sigl, C.; Dietz, H. Gigadalton-Scale Shape-Programmable DNA Assemblies. *Nature* **2017**, *552*, 78–83.
- [121] Jun, H.; Wang, X.; Bricker, W. P.; Jackson, S.; Bathe, M. *Rapid Prototyping of Wireframe Scaffolded DNA Origami Using ATHENA*; Preprint, 2020.
- [122] McLaughlin, C. K.; Hamblin, G. D.; Sleiman, H. F. Supramolecular DNA Assembly. *Chem. Soc. Rev.* **2011**, *40*, 5647.
- [123] Stulz, E. DNA Architectonics: Towards the Next Generation of Bio-inspired Materials. *Chem. Eur. J.* **2012**, *18*, 4456–4469.
- [124] Stulz, E. Porphyrin-Modified DNA as Construction Material in Supramolecular Chemistry and Nano-architectonics. *Chimia* **2015**, *69*, 678.
- [125] Stulz, E. Nanoarchitectonics with Porphyrin Functionalized DNA. *Acc. Chem. Res.* **2017**, *50*, 823–831.
- [126] Brady, R. A.; Brooks, N. J.; Cicuta, P.; Di Michele, L. Crystallization of Amphiphilic DNA C-Stars. *Nano Lett.* **2017**, *17*, 3276–3281.
- [127] Fabrini, G.; Minard, A.; Brady, R. A.; Di Antonio, M.; Di Michele, L. Cation-Responsive and Photocleavable Hydrogels from Noncanonical Amphiphilic DNA Nanostructures. *Nano Lett.* **2022**, *22*, 602–611.
- [128] Walczak, M.; Brady, R. A.; Mancini, L.; Contini, C.; Rubio-Sánchez, R.; Kaufhold, W. T.; Cicuta, P.; Di Michele, L. Responsive Core-Shell DNA Particles Trigger Lipid-Membrane Disruption and Bacteria Entrapment. *Nat. Commun.* **2021**, *12*, 4743.
- [129] Yang, H.; Duan, Z.; Liu, F.; Zhao, Z.; Liu, S. Cucurbit[7]Uril-Based Supramolecular DNA Nanogel for Targeted Codelivery of Chemo/Photodynamic Drugs. *ACS Macro Lett.* **2023**, *12*, 295–301.
- [130] Borum, R. M.; Moore, C.; Mantri, Y.; Xu, M.; Jokerst, J. V. Supramolecular Loading of DNA Hydrogels with Dye-Drug Conjugates for Real-Time Photoacoustic Monitoring of Chemotherapy. *Adv. Sci.* **2023**, *10*, 2204330.
- [131] Hendrikse, S. I. S.; Gras, S. L.; Ellis, A. V. Opportunities and Challenges in DNA-Hybrid Nanomaterials. *ACS Nano* **2019**, *13*, 8512–8516.
-

- [132] Burns, J. R.; Stulz, E.; Howorka, S. Self-Assembled DNA Nanopores That Span Lipid Bilayers. *Nano Lett.* **2013**, *13*, 2351–2356.
- [133] Burns, J. R.; Göpfrich, K.; Wood, J. W.; Thacker, V. V.; Stulz, E.; Keyser, U. F.; Howorka, S. Lipid-Bilayer-Spanning DNA Nanopores with a Bifunctional Porphyrin Anchor. *Angew. Chem.* **2013**, *125*, 12291–12294.
- [134] Göpfrich, K.; Li, C.-Y.; Mames, I.; Bhamidimarri, S. P.; Ricci, M.; Yoo, J.; Mames, A.; Ohmann, A.; Winterhalter, M.; Stulz, E.; Aksimentiev, A.; Keyser, U. F. Ion Channels Made from a Single Membrane-Spanning DNA Duplex. *Nano Lett.* **2016**, *16*, 4665–4669.
- [135] Gu, R.; Lamas, J.; Rastogi, S. K.; Li, X.; Brittain, W.; Zauscher, S. Photocontrolled Micellar Aggregation of Amphiphilic DNA-azobenzene Conjugates. *Colloids Surf. B* **2015**, *135*, 126–132.
- [136] Whitfield, C. J.; Zhang, M.; Winterwerber, P.; Wu, Y.; Ng, D. Y. W.; Weil, T. Functional DNA-Polymer Conjugates. *Chem. Rev.* **2021**, *121*, 11030–11084.
- [137] De Lambert, B.; Chaix, C.; Charreyrex, M.-T.; Laurent, A.; Aigoui, A.; Perrin-Rubens, A.; Pichot, C. Polymer-Oligonucleotide Conjugate Synthesis from an Amphiphilic Block Copolymer. Applications to DNA Detection on Microarray. *Bioconjugate Chem.* **2005**, *16*, 265–274.
- [138] Vyborna, Y.; Vybornyi, M.; Häner, R. Pathway Diversity in the Self-Assembly of DNA-Derived Bioconjugates. *Bioconjugate Chem.* **2016**, *27*, 2755–2761.
- [139] Wijnands, S. P.; Meijer, E. W.; Merckx, M. DNA-Functionalized Supramolecular Polymers: Dynamic Multicomponent Assemblies with Emergent Properties. *Bioconjugate Chem.* **2019**, *30*, 1905–1914.
- [140] Zhang, Y.; Peng, R.; Xu, F.; Ke, Y. Hierarchical Self-Assembly of Cholesterol-DNA Nanorods. *Bioconjugate Chem.* **2019**, *30*, 1845–1849.
- [141] Kim, C.-J.; Park, J.-e.; Hu, X.; Albert, S. K.; Park, S.-J. Peptide-Driven Shape Control of Low-Dimensional DNA Nanostructures. *ACS Nano* **2020**, *14*, 2276–2284.
- [142] Patwa, A.; Gissot, A.; Bestel, I.; Barthélémy, P. Hybrid Lipid Oligonucleotide Conjugates: Synthesis, Self-Assemblies and Biomedical Applications. *Chem. Soc. Rev.* **2011**, *40*, 5844.
- [143] Vyborna, Y.; Vybornyi, M.; Rudnev, A. V.; Häner, R. DNA-Grafted Supramolecular Polymers: Helical Ribbon Structures Formed by Self-Assembly of Pyrene-DNA Chimeric Oligomers. *Angew. Chem. Int. Ed.* **2015**, *54*, 7934–7938.
- [144] Vyborna, Y.; Vybornyi, M.; Häner, R. From Ribbons to Networks: Hierarchical Organization of DNA-Grafted Supramolecular Polymers. *J. Am. Chem. Soc.* **2015**, *137*, 14051–14054.
- [145] Vybornyi, M.; Vyborna, Y.; Häner, R. Silica Mineralization of DNA-inspired 1D and 2D Supramolecular Polymers. *ChemistryOpen* **2017**, *6*, 488–491.
- [146] Bösch, C. D.; Jevric, J.; Bürki, N.; Probst, M.; Langenegger, S. M.; Häner, R. Supramolecular Assembly of DNA-Phenanthrene Conjugates into Vesicles with Light-Harvesting Properties. *Bioconjugate Chem.* **2018**, *29*, 1505–1509.
- [147] Casero, R. A.; Woster, P. M. Recent Advances in the Development of Polyamine Analogues as Antitumor Agents. *J. Med. Chem.* **2009**, *52*, 4551–4573.
-

- [148] Van Dam, L. Polyamine-Nucleic Acid Interactions and the Effects on Structure in Oriented DNA Fibers. *Nucleic Acids Res.* **2002**, *30*, 419–428.
- [149] Thomas*, T.; Thomas, T. J. Polyamines in Cell Growth and Cell Death: Molecular Mechanisms and Therapeutic Applications. *CMLS, Cell. Mol. Life Sci.* **2001**, *58*, 244–258.
- [150] Bloomfield, V. A. DNA Condensation by Multivalent Cations. *Biopolymers* **1997**, *44*, 269–282.
- [151] Iacomino, G.; Picariello, G.; D’Agostino, L. DNA and Nuclear Aggregates of Polyamines. *Biochim Biophys Acta Mol Cell Res* **2012**, *1823*, 1745–1755.
- [152] Zinchenko, A. A.; Yoshikawa, K.; Baigl, D. DNA-Templated Silver Nanorings. *Adv. Mater.* **2005**, *17*, 2820–2823.
- [153] Egli, M. DNA-Cation Interactions. *Chem. Biol.* **2002**, *9*, 277–286.
- [154] Mozdzan, M.; Szemraj, J.; Rysz, J.; Stolarek, R. A.; Nowak, D. Anti-Oxidant Activity of Spermine and Spermidine Re-Evaluated with Oxidizing Systems Involving Iron and Copper Ions. *Int. J. Biochem. Cell Biol.* **2006**, *38*, 69–81.
- [155] Seiler, N.; Raul, F. Polyamines and Apoptosis. *J. Cell. Mol. Med.* **2005**, *9*, 623–642.
- [156] Igarashi, K.; Kashiwagi, K. Polyamines: Mysterious Modulators of Cellular Functions. *Biochem. Biophys. Res. Commun.* **2000**, *271*, 559–564.
- [157] Raspaud, E.; Chaperon, I.; Leforestier, A.; Livolant, F. Spermine-Induced Aggregation of DNA, Nucleosome, and Chromatin. *Biophys. J.* **1999**, *77*, 1547–1555.
- [158] Feuerstein, B. G.; Williams, L. D.; Basu, H. S.; Marton, L. J. Implications and Concepts of Polyamine-nucleic Acid Interactions. *J. Cell. Biochem.* **1991**, *46*, 37–47.
- [159] Lächelt, U.; Wagner, E. Nucleic Acid Therapeutics Using Polyplexes: A Journey of 50 Years (and Beyond). *Chem. Rev.* **2015**, *115*, 11043–11078.
- [160] Chen, Z.; Lv, Z.; Sun, Y.; Chi, Z.; Qing, G. Recent Advancements in Polyethyleneimine-Based Materials and Their Biomedical, Biotechnology, and Biomaterial Applications. *J. Mater. Chem. B* **2020**, *8*, 2951–2973.
- [161] Ma, K.; Mi, C.-L.; Cao, X.-X.; Wang, T.-Y. Progress of Cationic Gene Delivery Reagents for Non-Viral Vector. *Appl. Microbiol. Biotechnol.* **2021**, *105*, 525–538.
- [162] Santana-Armas, M. L.; Tros De Ilarduya, C. Strategies for Cancer Gene-Delivery Improvement by Non-Viral Vectors. *Int. J. Pharm.* **2021**, *596*, 120291.
- [163] Rothenbühler, S.; Iacovache, I.; Langenegger, S. M.; Zuber, B.; Häner, R. Supramolecular Assembly of DNA-constructed Vesicles. *Nanoscale* **2020**, *12*, 21118–21123.
- [164] Rothenbühler, S.; Gonzalez, A.; Iacovache, I.; Langenegger, S. M.; Zuber, B.; Häner, R. Tetraphenylethylene–DNA Conjugates: Influence of Sticky Ends and DNA Sequence Length on the Supramolecular Assembly of AIE-active Vesicles. *Org. Biomol. Chem.* **2022**, *20*, 3703–3707.
- [165] Rothenbühler, S.; Iacovache, I.; Langenegger, S. M.; Zuber, B.; Häner, R. Complex DNA Architectonics–Self-Assembly of Amphiphilic Oligonucleotides into Ribbons, Vesicles, and Asterosomes. *Bioconjugate Chem.* **2023**, *34*, 70–77.
- [166] Blankenship, R. E. *Molecular Mechanisms of Photosynthesis*; John Wiley & Sons, 2021.
-

- [167] Croce, R.; Van Amerongen, H. Natural Strategies for Photosynthetic Light Harvesting. *Nat Chem Biol* **2014**, *10*, 492–501.
- [168] Wasielewski, M. R. Photoinduced Electron Transfer in Supramolecular Systems for Artificial Photosynthesis. *Chem. Rev.* **1992**, *92*, 435–461.
- [169] Aratani, N.; Kim, D.; Osuka, A. Discrete Cyclic Porphyrin Arrays as Artificial Light-Harvesting Antenna. *Acc. Chem. Res.* **2009**, *42*, 1922–1934.
- [170] Sakai, N.; Matile, S. Multistep Organic Synthesis of Modular Photosystems. *Beilstein J. Org. Chem.* **2012**, *8*, 897–904.
- [171] McConnell, I.; Li, G.; Brudvig, G. W. Energy Conversion in Natural and Artificial Photosynthesis. *Chem. Biol.* **2010**, *17*, 434–447.
- [172] Maity, A.; Dey, A.; Gangopadhyay, M.; Das, A. Water Induced Morphological Transformation of a Poly(Aryl Ether) Dendron Amphiphile: Helical Fibers to Nanorods, as Light-Harvesting Antenna Systems. *Nanoscale* **2018**, *10*, 1464–1473.
- [173] Rao, K. V.; Datta, K. K. R.; Eswaramoorthy, M.; George, Subi. J. Light-Harvesting Hybrid Assemblies. *Chem. Eur. J.* **2012**, *18*, 2184–2194.
- [174] Xiao, T.; Zhong, W.; Zhou, L.; Xu, L.; Sun, X.-Q.; Elmes, R. B.; Hu, X.-Y.; Wang, L. Artificial Light-Harvesting Systems Fabricated by Supramolecular Host–Guest Interactions. *Chin Chem Lett* **2019**, *30*, 31–36.
- [175] Van Grondelle, R. Excitation Energy Transfer, Trapping and Annihilation in Photosynthetic Systems. *Biochim Biophys Acta Bioenerg* **1985**, *811*, 147–195.
- [176] Förster, T. Zwischenmolekulare Energiewanderung Und Fluoreszenz. *Ann. Phys.* **1948**, *437*, 55–75.
- [177] Benatto, L.; Mesquita, O.; Rosa, J. L.; Roman, L. S.; Koehler, M.; Capaz, R. B.; Candiotto, G. FRET–Calc: A Free Software and Web Server for Förster Resonance Energy Transfer Calculation. *Comput. Phys. Commun.* **2023**, *287*, 108715.
- [178] Wang, H.; Yue, B.; Xie, Z.; Gao, B.; Xu, Y.; Liu, L.; Sun, H.; Ma, Y. Controlled Transition Dipole Alignment of Energy Donor and Energy Acceptor Molecules in Doped Organic Crystals, and the Effect on Intermolecular Förster Energy Transfer. *Phys. Chem. Chem. Phys.* **2013**, *15*, 3527.
- [179] Hillisch, A.; Lorenz, M.; Diekmann, S. Recent Advances in FRET: Distance Determination in Protein–DNA Complexes. *Curr. Opin. Struct. Biol.* **2001**, *11*, 201–207.
- [180] Dexter, D. L. A Theory of Sensitized Luminescence in Solids. *J. Chem. Phys* **1953**, *21*, 836–850.
- [181] Collini, E. Spectroscopic Signatures of Quantum-Coherent Energy Transfer. *Chem. Soc. Rev.* **2013**, *42*, 4932.
- [182] Olaya-Castro, A.; Scholes, G. D. Energy Transfer from Förster–Dexter Theory to Quantum Coherent Light-Harvesting. *Int Rev Phys Chem* **2011**, *30*, 49–77.
- [183] Van Der Meer, B. W. In *FRET – Förster Resonance Energy Transfer*, 1st ed.; Medintz, I., Hildebrandt, N., Eds.; Wiley, 2013; pp 23–62.
-

- [184] Engel, G. S.; Calhoun, T. R.; Read, E. L.; Ahn, T.-K.; Mančal, T.; Cheng, Y.-C.; Blankenship, R. E.; Fleming, G. R. Evidence for Wavelike Energy Transfer through Quantum Coherence in Photosynthetic Systems. *Nature* **2007**, *446*, 782–786.
- [185] Strümpfer, J.; Şener, M.; Schulten, K. How Quantum Coherence Assists Photosynthetic Light-Harvesting. *J. Phys. Chem. Lett.* **2012**, *3*, 536–542.
- [186] Dutta, P. K.; Varghese, R.; Nangreave, J.; Lin, S.; Yan, H.; Liu, Y. DNA-Directed Artificial Light-Harvesting Antenna. *J. Am. Chem. Soc.* **2011**, *133*, 11985–11993.
- [187] Crawford, A. G.; Dwyer, A. D.; Liu, Z.; Steffen, A.; Beeby, A.; Pålsson, L.-O.; Tozer, D. J.; Marder, T. B. Experimental and Theoretical Studies of the Photophysical Properties of 2- and 2,7-Functionalized Pyrene Derivatives. *J. Am. Chem. Soc.* **2011**, *133*, 13349–13362.
- [188] Rothenbühler, S. DNA Architectonics: Self-Assembly of Amphiphilic Oligonucleotides into Supramolecular Nanostructures. Ph.D. thesis, University of Bern, Bern, 2022.
- [189] Bittermann, H.; Siegemund, D.; Malinovskii, V. L.; Häner, R. Dialkynylpyrenes: Strongly Fluorescent, Environment-Sensitive DNA Building Blocks. *J. Am. Chem. Soc.* **2008**, *130*, 15285–15287.
- [190] Ji, S.; Yang, J.; Yang, Q.; Liu, S.; Chen, M.; Zhao, J. Tuning the Intramolecular Charge Transfer of Alkynylpyrenes: Effect on Photophysical Properties and Its Application in Design of OFF-ON Fluorescent Thiol Probes. *J. Org. Chem.* **2009**, *74*, 4855–4865.
- [191] Ronson, T. K.; League, A. B.; Gagliardi, L.; Cramer, C. J.; Nitschke, J. R. Pyrene-Edged $\text{Fe}^{\text{II}}_4\text{L}_6$ Cages Adaptively Reconfigure During Guest Binding. *J. Am. Chem. Soc.* **2014**, *136*, 15615–15624.
- [192] Goldstein, R.; Stryer, L. Cooperative Polymerization Reactions. Analytical Approximations, Numerical Examples, and Experimental Strategy. *Biophys. J.* **1986**, *50*, 583–599.
- [193] Smulders, M. M. J.; Nieuwenhuizen, M. M. L.; de Greef, T. F. A.; van der Schoot, P.; Schenning, A. P. H. J.; Meijer, E. W. How to Distinguish Isodesmic from Cooperative Supramolecular Polymerisation. *Chem. Eur. J.* **2010**, *16*, 362–367.
- [194] Zhao, D.; Moore, J. S. Nucleation–Elongation: A Mechanism for Cooperative Supramolecular Polymerization. *Org. Biomol. Chem.* **2003**, *1*, 3471–3491.
- [195] Jonkheijm, P.; Van Der Schoot, P.; Schenning, A. P. H. J.; Meijer, E. W. Probing the Solvent-Assisted Nucleation Pathway in Chemical Self-Assembly. *Science* **2006**, *313*, 80–83.
- [196] Korevaar, P. A.; George, S. J.; Markvoort, A. J.; Smulders, M. M. J.; Hilbers, P. A. J.; Schenning, A. P. H. J.; De Greef, T. F. A.; Meijer, E. W. Pathway Complexity in Supramolecular Polymerization. *Nature* **2012**, *481*, 492–496.
- [197] Dubochet, J.; Adrian, M.; Chang, J.-J.; Homo, J.-C.; Lepault, J.; McDowell, A. W.; Schultz, P. Cryo-Electron Microscopy of Vitrified Specimens. *Quart. Rev. Biophys.* **1988**, *21*, 129–228.
- [198] Adrian, M.; Ten Heggeler-Bordier, B.; Wahli, W.; Stasiak, A. Z.; Stasiak, A.; Dubochet, J. Direct Visualization of Supercoiled DNA Molecules in Solution. *EMBO J.* **1990**, *9*, 4551–4554.
-

- [199] Dubochet, J.; McDowell, A. VITRIFICATION OF PURE WATER FOR ELECTRON MICROSCOPY. *J. Microsc.* **1981**, *124*, 3–4.
- [200] Wang, Q.; Irobalieva, R. N.; Chiu, W.; Schmid, M. F.; Fogg, J. M.; Zechiedrich, L.; Pettitt, B. M. Influence of DNA Sequence on the Structure of Minicircles under Torsional Stress. *Nucleic Acids Res.* **2017**, *45*, 7633–7642.
- [201] Unwin, P.; Henderson, R. Molecular Structure Determination by Electron Microscopy of Unstained Crystalline Specimens. *J. Mol. Biol.* **1975**, *94*, 425–440.
- [202] Teo, Y. N.; Kool, E. T. Polyfluorophore Excimers and Exciplexes as FRET Donors in DNA. *Bioconjugate Chem.* **2009**, *20*, 2371–2380.
- [203] Aparin, I. O.; Sergeeva, O. V.; Mishin, A. S.; Khaydukov, E. V.; Korshun, V. A.; Zatsepin, T. S. Excimer-FRET Cascade in Dual DNA Probes: Open Access to Large Stokes Shift, Enhanced Acceptor Light up, and Robust RNA Sensing. *Anal. Chem.* **2020**, *92*, 7028–7036.
- [204] Adeyemi, O. O.; Malinovskii, V. L.; Biner, S. M.; Calzaferri, G.; Häner, R. Photon Harvesting by Excimer-Forming Multichromophores. *Chem. Commun.* **2012**, *48*, 9589.
- [205] Berney, C.; Danuser, G. FRET or No FRET: A Quantitative Comparison. *Biophys. J.* **2003**, *84*, 3992–4010.
- [206] Dawlaty, J. M.; Ishizaki, A.; De, A. K.; Fleming, G. R. Microscopic Quantum Coherence in a Photosynthetic-Light-Harvesting Antenna. *Phil. Trans. R. Soc. A.* **2012**, *370*, 3672–3691.
- [207] Presolski, S. I.; Hong, V. P.; Finn, M. Copper-Catalyzed Azide–Alkyne Click Chemistry for Bioconjugation. *Curr. protoc. chem. biol.* **2011**, *3*, 153–162.
- [208] Monestier, M.; Charbonnier, P.; Gateau, C.; Cuillel, M.; Robert, F.; Lebrun, C.; Mintz, E.; Renaudet, O.; Delangle, P. ASGPR-Mediated Uptake of Multivalent Glycoconjugates for Drug Delivery in Hepatocytes. *Chembiochem* **2016**, *17*, 590–594.
- [209] Willoughby, J. L. *et al.* Evaluation of GalNAc-siRNA Conjugate Activity in Pre-clinical Animal Models with Reduced Asialoglycoprotein Receptor Expression. *Mol. Ther.* **2018**, *26*, 105–114.
- [210] Stefanick, J. F.; Ashley, J. D.; Kiziltepe, T.; Bilgicer, B. A Systematic Analysis of Peptide Linker Length and Liposomal Polyethylene Glycol Coating on Cellular Uptake of Peptide-Targeted Liposomes. *ACS Nano* **2013**, *7*, 2935–2947.
- [211] Gref, R.; Lück, M.; Quellec, P.; Marchand, M.; Dellacherie, E.; Harnisch, S.; Blunk, T.; Müller, R. ‘Stealth’ Corona-Core Nanoparticles Surface Modified by Polyethylene Glycol (PEG): Influences of the Corona (PEG Chain Length and Surface Density) and of the Core Composition on Phagocytic Uptake and Plasma Protein Adsorption. *Colloids Surf. B* **2000**, *18*, 301–313.
- [212] Gerland, B.; Goudot, A.; Pourceau, G.; Meyer, A.; Dugas, V.; Cecioni, S.; Vidal, S.; Souteyrand, E.; Vasseur, J.-J.; Chevolot, Y.; Morvan, F. Synthesis of a Library of Fucosylated Glycoclusters and Determination of Their Binding toward *Pseudomonas Aeruginosa* Lectin B (PA-IIL) Using a DNA-Based Carbohydrate Microarray. *Bioconjugate Chem.* **2012**, *23*, 1534–1547.
- [213] Shlyakhtenko, L. S.; Gall, A. A.; Lyubchenko, Y. L. In *Cell Imaging Techniques*; Taatjes, D. J., Roth, J., Eds.; Humana Press: Totowa, NJ, 2012; Vol. 931; pp 295–312.
-

- [214] Schindelin, J. *et al.* Fiji: An Open-Source Platform for Biological-Image Analysis. *Nat Methods* **2012**, *9*, 676–682.
- [215] Linkert, M. *et al.* Metadata Matters: Access to Image Data in the Real World. *J. Cell Biol.* **2010**, *189*, 777–782.
- [216] Fery-Forgues, S.; Lavabre, D. Are Fluorescence Quantum Yields So Tricky to Measure? A Demonstration Using Familiar Stationery Products. *J. Chem. Educ.* **1999**, *76*, 1260.
- [217] Melhuish, W. H. QUANTUM EFFICIENCIES OF FLUORESCENCE OF ORGANIC SUBSTANCES: EFFECT OF SOLVENT AND CONCENTRATION OF THE FLUORESCENT SOLUTE. *J. Phys. Chem.* **1961**, *65*, 229–235.

Declaration of Consent

Erklärung

gemäss Art. 18 PromR Phil.-nat. 2019

Name/Vorname: Thiede Jan

Matrikelnummer: 15-124-811

Studiengang: PhD in Chemie und Molekulare Wissenschaften

Bachelor Master Dissertation

Titel der Arbeit: Supramolecular Self-Assembly of Pyrene-Modified Amphiphilic DNA Nanostructures

LeiterIn der Arbeit: Professor Dr. Robert Häner

Ich erkläre hiermit, dass ich diese Arbeit selbständig verfasst und keine anderen als die angegebenen Quellen benutzt habe. Alle Stellen, die wörtlich oder sinngemäss aus Quellen entnommen wurden, habe ich als solche gekennzeichnet. Mir ist bekannt, dass andernfalls der Senat gemäss Artikel 36 Absatz 1 Buchstabe r des Gesetzes über die Universität vom 5. September 1996 und Artikel 69 des Universitätsstatuts vom 7. Juni 2011 zum Entzug des Dokortitels berechtigt ist. Für die Zwecke der Begutachtung und der Überprüfung der Einhaltung der Selbständigkeitserklärung bzw. der Reglemente betreffend Plagiate erteile ich der Universität Bern das Recht, die dazu erforderlichen Personendaten zu bearbeiten und Nutzungshandlungen vorzunehmen, insbesondere die Doktorarbeit zu vervielfältigen und dauerhaft in einer Datenbank zu speichern sowie diese zur Überprüfung von Arbeiten Dritter zu verwenden oder hierzu zur Verfügung zu stellen.

Bern, 14.02.2024

Ort/Datum



Unterschrift

Curriculum Vitae

Personal Information

Name: Jan Thiede
Date of Birth: 26.11.1995
Place of Origin: Lucerne
E-mail: jan.thiede@bluewin.ch

Education

2020–2024 PhD with Prof. Dr. Robert Häner, University of Bern
2019–2020 Master in Chemistry and Molecular Sciences, University of Bern
2015–2019 Bachelor in Chemistry and Molecular Sciences, University of Bern

Publication

J. Thiede, S. Rothenbühler, I. Iacovache, S. M. Langenegger, B. Zuber, and R. Häner
Supramolecular Assembly of Pyrene-DNA Conjugates: Influence of Pyrene Substitution Pattern and Implications for Artificial LHCs
Org. Biomol. Chem. **2023**, 21, 7908–7912. DOI: 10.1039/d3ob01375h

P. Melle, J. Thiede, D. A. Hey, and M. Albrecht
Highly Efficient Transfer Hydrogenation Catalysis with Tailored Pyridylidene Amide Pincer Ruthenium Complexes
Chem.-Eur. J. **2020**, 58, 13226–13234. DOI: 10.1002/chem.202001145

Academic Works

Synthesis and Characterisation of Metallo-Porphyrin Dyads and Spiropran Derivatives,
2020 (Master Thesis)

Fine Tuning Mesoionic PYA Complexes-Utilizing Para Substituents for E-Density Variations and Improved Catalytic Activity, **2018** (Bachelor Thesis)
